Characterization of intracellular Zn^{2+} dynamics and Zn^{2+}-dependent gene expression in primary dissociated hippocampal neurons

by

Lynn Sanford
B.A., Pomona College, 2009

A thesis submitted to the Faculty of the Graduate School of the University of Colorado in partial fulfillment of the requirement for the degree of Doctor of Philosophy

Department of Biochemistry

2019

This thesis entitled:

Characterization of intracellular Zn^{2+} dynamics and Zn^{2+}-dependent gene expression in primary dissociated hippocampal neurons

written by Lynn Sanford

has been approved for the Department of Biochemistry

_____

Amy E. Palmer

_____

Natalie Ahn

Date_____

The final copy of this thesis has been examined by the signatories, and we find that both the content and the form meet acceptable presentation standards of scholarly work in the above mentioned discipline.

IACUC protocols #1407.01 and #2547

Sanford, Lynn (Ph.D., Biochemistry)

Characterization of intracellular Zn^{2+} dynamics and Zn^{2+}-dependent gene expression in primary dissociated hippocampal neurons

Thesis directed by Professor Amy E. Palmer

Ionic zinc (Zn^{2+}) is an essential cofactor in many proteins, but labile (non-protein bound) Zn^{2+} also functions as a signaling ion in many cell types. In specific neurons of the brain and nervous system, Zn^{2+} is highly enriched and operates as a neurotransmitter that modulates neuronal signaling. Zn^{2+} has crucial physiological roles in memory consolidation and sensory processing, yet abnormal levels of Zn^{2+} have been observed to be pathological in neurological disorders ranging from Alzheimer's Disease to depression. Both extracellular and intracellular Zn^{2+} are necessary for neuronal signaling, but little is known about the dynamics of intracellular Zn^{2+} during neuronal stimulation and how intracellular Zn^{2+} influences signaling in physiological or pathological processes. We employed fluorescence imaging with genetically encoded and small molecule Zn^{2+} sensors to quantify intracellular Zn^{2+} dynamics during different stimulations in primary dissociated hippocampal neurons. We found that Zn^{2+} rose transiently during both chemical and electrical stimulation, although there were differences in peak Zn^{2+} concentrations depending on the stimulus used. Furthermore, we perturbed intracellular Zn^{2+} signaling to explore Zn^{2+}-dependent changes in gene expression through global mRNA sequencing of hippocampal neurons. Our RNA-Seq results indicated that mild stimulation with potassium chloride induced Zn^{2+}-dependent expression of genes related to synaptic growth and signaling, while more intensive stimulation with

glutamate promoted Zn^{2+}-dependent expression of genes involved in endoplasmic reticulum stress. Our results therefore show distinct differences in the role of Zn^{2+} signaling during potassium chloride and glutamate stimulation of neurons, which may reflect differences between physiological and pathological Zn^{2+} signaling. In future studies we aim to elucidate the underlying signaling mechanisms behind these differences.

Acknowledgments

I would first like to thank my original supporters, my parents, who taught me to be strong, kind, and thoughtful. I could not have succeeded in graduate school without their love and encouragement. My brother David, too, has been a source of inspiration, advice, and endless hours of fun. I also thank the rest of my family, especially Dave Sanford for many an intellectual discussion, Liz Hengeveld and Pat Wetzel for love, laughs, and advice, and Jennifer Brent for welcoming me into her incredibly big heart.

My friends have been essential for my happiness and well-being over the last decade. I particlarly want to thank Irene Toro Martinez for hugs and inspiration, Sarah McQuate for boundless fun and good food, Andrew Fabry for always making me smile, Lara Janiszewski and Andy Janiszewski for long talks and good movies, Anne Huntzicker for dragging me outdoors with enthusiasm, and Josh Harris for lots of encouragement.

For helping me develop my scientific skills and curiosity, I would like to acknowledge my Pomona College professors Jonathan Wright and Bruce Telzer, and especially E.J. Crane III. I am also incredibly grateful for everyone who mentored me during my time at OHSU, particularly Allison Gregory, Penny Hogarth, Moon Yoon, Weihong Xiong, and most of all Susan Hayflick. You all are incredible people.

I could not be here today without my wonderful Palmer Lab labmates, who were always there through thick and thin. I especially want to thank Kelsie Anson, Yu Han, and Lara Janiszewski for their help and discussion about everything neurons

and sequencing. Thank you to my awesome CU biochemistry graduate student class, particularly Elina Ly for the great lunches and nerd talk, and my IQ Biology student class, who are some fabulous people. I would also like to thank Kim Kelley, Pamela Williamson, and Kristin Powell for administrative advice. I am immensely grateful to Andrea Stith and Amber McDonnell for seamlessly integrating me into the IQ Biology program, and for much guidance and support.

Thank you to all of the biochemistry faculty that have guided me during my time at CU, particularly Natalie Ahn and Debbie Wuttke for convincing me to come here for graduate school and for advice along the way, and Robin Dowell and Mary Allen for excellent and fun bioinformatics training and recommendations. Thank you to Joel Kralj and Matthew Kennedy for providing helpful suggestions as part of my thesis committee. I am immensely grateful to everyone in the core facilities, especially Theresa Nahreini, Nicole Kethley, Jamie Prior Kershner, Amber Scott, the IT team, and the wonderful Joe Dragavon. I could never have done research without you.

None of my graduate school career would have been possible without my amazing mentor, Amy Palmer, who has gently guided and encouraged me through a multitude of scientific storms. Thank you for always seeing me as a well-rounded person and for supporting my ideas, my experiments, and my dreams.

Finally, I could not have made it through this experience without my wife, Essie, and my kid, Dax, who are the coolest people in the world. Essie has always been my rock, my light, my champion, and my girl, and I am incredibly fortunate to have had her as a constant sympathetic ear during graduate school. Dax, meanwhile, has brought me such laughter, joy, and inspiration in his short time on this earth, and he gets more incredible every day. Thank you, my amazing family. I love you.

Contents

Appendix

Tables

Figures

Chapter 1

Introduction

1.1 Publication status and author contributions

This work is unpublished. L.S. and A.E.P. wrote the manuscript.

1.2 Zn^{2+} in biology and human health

Living organisms, despite their incredible diversity, require a standard set of chemical components to function. Among the essential elements of life are seven transition metals, of which iron (Fe) and zinc (Zn) are most abundant among eukaryotes[1]. Ionic zinc (Zn^{2+}) is an electronically stable and redox-inert species in biological systems that can act as a strong Lewis acid[2], and these properties have enabled cells to utilize Zn^{2+} as a cofactor in a wide variety of different proteins[3,4]. Enzymes that bind Zn^{2+} as a catalytic cofactor, such as carbonic anhydrase, are the primary Zn^{2+}-containing proteins in prokaryotic organisms[3,5]. In addition to many Zn^{2+}-containing enzymes, eukaryotic organisms also use Zn^{2+} as a structural component in thousands of proteins, most notably the large class of transcription factors known as zinc fingers[6–9]. Current estimates indicate that the protein products of up to 3,000 genes in the human genome may bind Zn^{2+} through a number of different architectures[10–13]. The diversity of function among these proteins is evidence that Zn^{2+} is directly or indirectly involved in a majority of cellular processes.

The necessity for cells and organisms to maintain proper levels of Zn^{2+} is evident in the many links that have been drawn between Zn^{2+} disequilibrium and disease states. Zn^{2+} deficiency is a widespread concern, with around 20% of the global population at risk of suboptimal nutritional Zn^{2+} intake[14]. Severe Zn^{2+} deficiency can lead to physical and mental development retardation, dermatitis, sensory deficits, problems with blood sugar balance, abnormal sperm development, and susceptibility to infection[15,16]. Nutritional Zn^{2+} deficiency is often caused or exacerbated by mutations in specific Zn^{2+} transporters that are important for intestinal epithelial cell Zn^{2+} uptake[17–19], epidermal health[20], pancreatic development[21], growth hormone secretion[22–24], and cell differentiation in different organs[25–27]. Zn^{2+} transporters, Zn^{2+} buffering proteins, or abnormally high or low levels of Zn^{2+} have also been linked to many other non-developmental diseases, including a wide array of neurological disorders[28–38], hypertension[39], deafness[40], chronic obstructive pulmonary disease[41], several types of cancer[25,42,43], and diabetes[44–51]. While in some of these diseases mechanistic links have been discovered between Zn^{2+} disequilibrium and pathology[52–58], in many cases these links remain unknown.

Proper Zn^{2+} homeostasis, in addition to mitigating human genetic diseases, is relevant for immune response to pathogens. As Zn^{2+} is an essential element that can be toxic at high levels, modulation of Zn^{2+} by host immune cells to either starve or poison pathogens can be an effective strategy for pathogen clearance[59–65]. Additionally, Zn^{2+} is implicated as a modulator of immune cell signaling, both physiologically and pathologically[66–70], although how it functions in these signaling pathways is still unclear.

1.3 Zn^{2+} buffering and signaling

In order to successfully supply Zn^{2+} to all of its binding partners while limiting Zn^{2+} toxicity[71], cells have evolved rigorous Zn^{2+} buffering systems. Zn^{2+}-sensing transcription factors, such as Zur in *Escherichia coli*[72], Zap1 in *Saccharomyces cerevisiae*[73], and MTF1 in higher eukaryotes[73,74], mediate transcription of select Zn^{2+} transporters and Zn^{2+} buffering proteins upon elevation of intracellular Zn^{2+} concentrations. In vertebrates, members of the Zn Transporter (ZnT) and Zrt- and Irt-Like Protein (ZIP) families canonically manage Zn^{2+} transport across cellular membranes[75–77]. The 10 ZnTs, which transfer Zn^{2+} out of the cytosol, and the 14 ZIPs, which transport Zn^{2+} into the cytosol, are differentially expressed across cell types and localize to different cellular regions in order to transfer Zn^{2+} among subcellular compartments[78]. The Zn^{2+} present in cells is mostly bound by proteins, although some exists in a more labile form, as a hydrated ion or transiently bound to small molecules such as negatively charged amino acids, glutathione, and other anions[79,80]. Cytosolic labile Zn^{2+} has been quantified to be between about 80 pM and 800 pM in a number of cell types[81–83]. Additionally, small proteins called metallothioneins (MTs) are highly expressed in cells and reversibly bind Zn^{2+} and other metal ions[78,84,85]. Metallothioneins act as important cytosolic Zn^{2+} buffering proteins and chaperones that can deliver Zn^{2+} to essential binding partners[86,87]. Zn^{2+} transporters, metallothioneins, and the Zn^{2+}-binding proteome all function to maintain the tight balance of intracellular labile Zn^{2+} necessary for proper biological function.

While the Zn^{2+} buffer maintains a steady concentration of labile Zn^{2+} in most healthy eukaryotic cells at any given time, a number of cell types have been shown to experience dynamic changes in Zn^{2+} in order to perform physiological functions[88,89]. Neurons are by far the most studied of these cell types, and background knowledge

of Zn^{2+} involvement in neuronal signaling, which is the focus of this thesis, will be covered in detail in later sections. Other important biological processes that have been shown to rely on transient changes in intracellular labile Zn^{2+} include insulin secretion[90,91], differentiation of colonocytes and B-cells[92,93], polarization and activation of macrophages and T-cells[94–96], contractility of cardiomyocytes[97–99], egg division[100,101], and fertilization[102,103]. In some of these cases, Zn^{2+}-binding signaling molecules have been identified, such as the Zn^{2+}-specific G protein-coupled receptor GPR39[93,104,105], protein tyrosine phosphatases[106–110], or stress-related proteins such as caspases or Hsp33[111,112]. In other systems, Zn^{2+} has been shown to influence the mitogen-activated protein kinase (MAPK)[113–116], Akt[42], and nuclear factor kappa-light-chain-enhancer of activated B cells (NF-κB)[117] signaling pathways, but specific binding factors have not been established. Generally, there is still very little mechanistic data on how Zn^{2+} modulates signaling pathways in different cell types to regulate physiological responses.

1.4 Tools for measuring Zn^{2+} in cells

Measuring steady-state levels and dynamic changes in cellular Zn^{2+} is essential for understanding its physiological and pathological roles in cells. While for much of the twentieth century radiographic detection of Zn^{65} and histological stains such as the Timm's stain were commonly used methods to investigate zinc distribution in organisms and tissues[118,119], in the past two decades fluorescence microscopy has been the primary method for tracking cellular Zn^{2+}. Two major classes of fluorescent Zn^{2+} sensors exist: small molecule fluorescent sensors and genetically encoded fluorescent sensors. Small molecule fluorescent sensors consist of a fluorophore linked to a Zn^{2+}-binding chemical moiety. While there are a few small molecule Zn^{2+} sensors that are

in the red region of the spectrum[120–122], or are ratiometric via dual-emission[123–125] or Förster resonance energy transfer (FRET) mechanisms[126,127], most of the sensors that have been widely used and best characterized are single-wavelength intensiometric green sensors[128–132]. Good small molecule sensors have the advantages of brightness, large dynamic range, and easy application to different model systems (such as cells or tissues slices)[129,133]. One major caveat in the use of small molecule sensors, however, is that they have the potential to perturb the Zn^{2+} buffer, depending on affinity, binding kinetics, and concentration[134–137]. Additionally, many small molecule sensors are membrane-permeable and tend to localize non-specifically in cells or aggregate in subcellular compartments, which can limit their applicability[81,129,137–139]. Despite these disadvantages, however, a small molecule fluorescent dye is often the most robust sensor that can be applied to a system.

The other main type of sensor for measuring Zn^{2+} in cells is a genetically encoded sensor, consisting of one or two fluorescent proteins and a protein-derived Zn^{2+}-binding domain[140]. Sensor platforms exist using one green fluorescent protein for intensiometric measurements[141–143] or two fluorescent proteins for FRET or bioluminescence resonance energy transfer (BRET) measurements[144–151]. These sensors, especially the FRET sensors, are attractive tools because their expression is tunable, they can be targeted to a specific subcellular compartment, they are capable of ratiometric quantification, and they are relatively non-perturbing to the Zn^{2+} buffer[81]. Genetically encoded sensors do have the major limitations that they are difficult to use in cells that resist transfection, and they are dimmer and more readily perturbed by environmental pH and redox conditions than small molecule fluorophores, which impedes their use in the secretory pathway and extracellular

space[152]. If experimentally possible, however, genetically encoded sensors are our sensors of choice for robust intracellular measurement of Zn^{2+}.

1.5 Zn^{2+} in the brain and neuronal synapses

Refined labile Zn^{2+} staining techniques in the latter part of the twentieth century led to the discovery that many neurons contain Zn^{2+} in axon termini, and within these termini Zn^{2+} specifically appears to be concentrated into synaptic vesicles[119,153,154]. Further study identified Zn^{2+}-containing neurons (sometimes termed "zincergic") as subsets of neurons in the hippocampus[119,155,156], frontal and somatosensory cortexes[156–158], visual cortex[159,160], olfactory bulb[156,161], amygdala[156,162], cerebellum[161,163], dorsal cochlear nucleus[164,165], spinal cord[166–169], retina[170,171], and peripheral nerves[172]. In animals, synaptic Zn^{2+} is scarce before birth but accumulates over time, reaching a steady state at around 1 month in mice and gradually declining in aging animals[173–177]. Neurons containing synaptic Zn^{2+} also express ZnT3 (*Slc30a3)*, a Zn^{2+}-specific transporter that shuttles Zn^{2+} into synaptic vesicles[178–183], and in almost all cases show increased mRNA and protein expression of the primarily brain-localized metallothionein isoform MT-III (*Mt3*)[161,184–186] and the plasma membrane Zn^{2+} exporter ZnT1 (*Slc30a1*)[187–191]. These zincergic neurons therefore have the molecular machinery to regulate the dynamic changes in Zn^{2+} necessary to employ it as a signaling ion.

Normal neurotransmitter-mediated neuronal signaling consists of an action potential (a Na^+/K^+-driven membrane depolarization/repolarization event) traveling down an axon to a presynaptic terminal, where depolarization opens voltage-gated Ca^{2+} channels, and the resulting Ca^{2+} influx mediates synaptic vesicle fusion with the plasma membrane to release neurotransmitters into the synapse[192].

Neurotransmitters then bind to specific receptors on postsynaptic neurons to either induce or prevent postsynaptic depolarization[193]. The excitatory neurotransmitter glutamate binds to postsynaptic glutamate receptors, including the ion channel N-methyl-D-aspartate (NMDA)-type and α-amino-3-hydroxy-5-methyl-4-isoxazolepropionic acid (AMPA)-type receptors and non-ion channel G protein-coupled receptors, to induce depolarization and signaling in postsynaptic neurons[194].

While Zn^{2+} is considered a neurotransmitter, its mechanism of action in synapses is to modulate receptors for other neurotransmitters rather than directly induce postsynaptic potentials (Figure 1). Although a few studies have raised the possibility of synaptic vesicle Zn^{2+} being present in inhibitory neurons containing the neurotransmitters gamma-aminobutyric acid (GABA) or glycine[169,195,196], most zinc-containing neurons have been identified as glutamatergic (stimulatory) neurons, with Zn^{2+} and glutamate packaged together in synaptic vesicles (Figure 1.1A)[197–199]. Upon neuronal stimulation, vesicles release Zn^{2+} and glutamate into the synapse (Figure 1.1B)[200–210], where a peak concentration of Zn^{2+} under normal physiological stimulation conditions is currently estimated to reach 5-110 nM, with strong stimulation inducing rises up to about 1 μM and pathological stimulation potentially causing higher concentrations[208,210–212]. Many studies of the effects of synaptic/extracellular Zn^{2+} use concentrations far in excess of these based on an early estimate of synaptic Zn^{2+} reaching 300 μM[213], but these studies are unlikely to describe any Zn^{2+}-related effects that would be observed *in vivo*.

Synaptic Zn^{2+} has been shown to interact with a wide array of synaptic proteins, although the physiological nature of some of these interactions is unclear. Extensive evidence illustrates that Zn^{2+} inhibits the NMDA-type glutamate receptor (NMDAR) via a high affinity (IC_{50} 10-30 nM) allosteric site on its GluN2A subunit[214–225] (Figure

1.1B). While Zn^{2+} released during single excitation events does not appear to affect synaptic transmission (possibly due to insufficient synaptic Zn^{2+} concentrations or slow kinetics)[211,223,226], stimulation bursts of zincergic neurons significantly reduce postsynaptic NMDAR potentiation[223,227]. Similarly to the NMDAR, allosteric high-

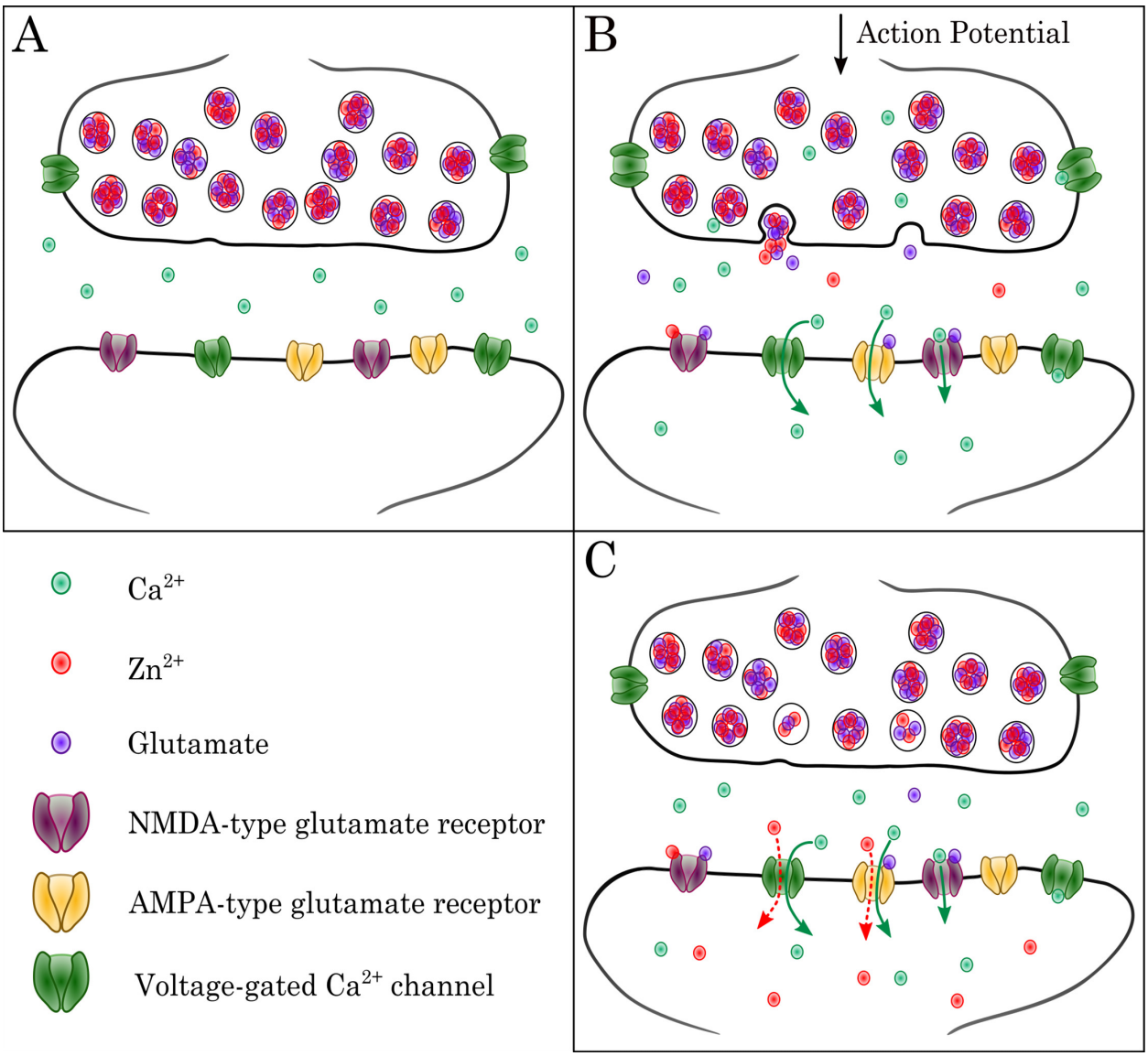

Figure 1.1: Zn^{2+} in neuronal synapses. (A) In resting neurons, Zn^{2+} is packed into synaptic vesicles with glutamate. As an action potential reaches the synapse (B), extracellular Ca^{2+} is internalized into the presynaptic terminal and facilitates fusion of synaptic vesicles. Glutamate and Zn^{2+} are released into the synapse and bind to postsynaptic receptors. On glutamatergic neurons, Zn^{2+} specifically inhibits NMDA-type glutamate receptors. (C) After excitation, Zn^{2+} transiently increases intracellularly due to potential translocation from the synapse or release from intracellular stores.

affinity Zn^{2+}-binding sites have been identified on inhibitory neurotransmitter receptors, namely the glycine receptor (EC_{50} 15 nM)[228–232] and the α/ß subunits of the $GABA_A$ receptor (IC_{50} 90 nM)[233–236]. Zn^{2+} binding to the glycine receptor enhances its activity by increasing its affinity for glycine, but Zn^{2+} inhibits the activity of the $GABA_A$ receptor, thus providing more evidence of the complexity of Zn^{2+} signaling in neuronal circuits. In addition to these well-studied receptor binding sites, evidence also exists that Zn^{2+} may modulate the activity of AMPA-type glutamate receptors (AMPARs)[218,237–242], kainate-type glutamate receptors[243,244], $GABA_B$ receptors[245], $ß_2$-andrenergic receptors[246], nicotinic acetylcholine receptors[247], serotonin receptors[248], neurotransmitter transporters[249–252], potassium transporters/channels[253–257], calcium transporters/channels[258–262], or other synaptic proteins[263,264]. Most of these studies found interactions that occur at higher levels of exogenous Zn^{2+} (> 1 μM), and thus are likely irrelevant for physiological synaptic processes, but they may be pertinent in pathological conditions.

1.6 Intracellular Zn^{2+} signaling in neurons

In addition to specifically interacting with postsynaptic receptors, labile Zn^{2+} has been shown to increase in postsynaptic cells upon stimulation (Figure 1.1C)[131,204,265–267]. One possible mechanism for this intracellular increase is translocation from the synapse, as Zn^{2+} can permeate different Ca^{2+} channels, including AMPARs[265,268–273], NMDARs[272,274], and voltage-gated Ca^{2+} channels (VGCCs)[272,275]. Of these, AMPARs have been shown to be most permeable to Zn^{2+}, and thus would likely be the primary mediators of Zn^{2+} translocation from the synapse[272,276]. Zn^{2+}-specific plasma membrane importers, including ZIP1, ZIP3, and ZIP4, are also likely present at synapses[277–280], although this localization has not been explicitly tested. Another

mechanism by which intracellular labile Zn^{2+} might increase is by stimulation-specific perturbations of Zn^{2+} buffering molecules that release a portion of the intracellularly bound Zn^{2+} into the labile Zn^{2+} pool. Two likely modulators of the Zn^{2+} buffer are reactive oxygen species (ROS)[89] and pH[281]. While ROS have been studied extensively in pathological conditions such as excitoxicity (see section 1.7) and in a somewhat more limited fashion in physiological development of neuronal polarity and plasticity[282], little is known about how physiological stimulation of neurons might dynamically change cellular ROS levels, and whether any such perturbations could affect the Zn^{2+} buffer. Alternatively, neurons are well known to acidify upon excitation[283–288], and in cultured neurons this acidification has been implicated in Zn^{2+} release from intracellular ligands[281,289,290]. Neurons in these studies, however, showed substantially more of a pH drop than the mild acidification seen in more *in situ/in vivo* systems[284,287,288], so the extent of pH-dependent Zn^{2+} mobilization in tissue under physiological conditions is unclear. It is therefore still ambiguous whether observed stimulation-dependent intracellular increases in labile Zn^{2+} may be mediated by a subset of these mechanisms (translocation from the synapse, ROS perturbation, or acidification), or by all three.

The difficulty in triangulating the source of neuronal intracellular Zn^{2+} dynamics is partially due to lack of rigorous quantification of these transients in the literature. Most studies of intracellular Zn^{2+} transients have utilized perturbing or low-affinity probes to detect changes[204,265,290], which has limited even approximate quantification. To address this gap in knowledge, we used fluorescence imaging to quantify Zn^{2+} changes in neurons under different mild to moderate stimulation conditions (see sections 2.3.1, 2.3.4, and 3.3.1). While approximate, these measurements will inform our understanding of the causes and downstream effects of intracellular Zn^{2+} signals.

1.7 Zn^{2+} in physiological neuron function

The regions of the brain that are most highly enriched in zincergic neurons are those related to memory encoding (hippocampus, amygdala, frontal cortex), and sensory processing (visual cortex, dorsal cochlear cortex, somatosensory cortex, olfactory bulb, retina). Accordingly, many *in vivo* studies have established synaptic vesicular Zn^{2+} and neuronal Zn^{2+} signaling as essential in a variety of memory- and sensory-related behaviors. Global Zn^{2+} deficiency, in addition to causing problems in brain development[291], causes impairment in spatial memory in animals[292,293]. These findings parallel a plethora of studies in which global or regional-specific Zn^{2+} chelation diminishes spatial memory, object recognition memory, exploratory behavior, fear consolidation, and odor response[294–299]. ZnT3 knockout (ZnT3 KO) mice, which lack the synaptic vesicle Zn^{2+} transporter and correspondingly have no synaptic vesicular Zn^{2+} [300], provide further evidence that these behavioral deficits arise specifically from synaptic Zn^{2+} signaling. While these mice have no major developmental difficulties[301], partially due to compensatory mechanisms[302], they have been seen to perform worse than wild-type mice on tasks related to spatial memory, associative memory, fear conditioning, motor learning, stress response, and discrimination of textures and audio stimuli, often in a sex- or age-dependent manner[303–309]. Additionally, alteration of external stimuli through whisker manipulation, visual deprivation, and environment enrichment can dramatically alter the patterns of zincergic neurons in associated brain regions of rodents and monkeys[310–319]. Synaptic Zn^{2+} is therefore well-established as a physiologically relevant and dynamically changing signaling ion *in vivo*.

On a cellular level, the effects of Zn^{2+} signaling on neuronal potentiation (perpetuating an action potential across a chemical synapse) range from modulating

postsynaptic excitation[232,320–323] to tuning presynaptic neurotransmitter release[324–328] to affecting Ca^{2+} trafficking and intracellular signaling pathways[266,293,326,329–338] to stabilizing cytoskeletal and structural components of the postsynaptic density[339–345]. As Zn^{2+} is clearly involved in memory development, many studies have focused on the role of Zn^{2+} in synaptic plasticity and long-term potentiation (LTP), a process by which repeated stimulation of specific neurons dynamically alters synapse physiology to facilitate further stimulation[346]. LTP is thought to be essential for memory formation, and involves many different signaling components. Presynaptic LTP, common in the zincergic mossy fiber synapses of the hippocampus, primarily escalates neurotransmitter release to increase synaptic signaling[347]. Endogenous synaptic Zn^{2+} facilitates this presynaptic LTP, possibly through increasing Ca^{2+} influx or through influencing postsynaptic retrograde signaling through the receptor tyrosine kinase TrkB[202,302,337,348–350]. Postsynaptic LTP, on the other hand, is mediated by altering neurotransmitter receptor density on the synapse and transcriptionally upregulating synaptic proteins and signaling components[351]. This form of LTP is most well-studied in the hippocampal Schaffer collateral synapses, and while both endogenous and exogenous Zn^{2+} have been shown to promote postsynaptic LTP[294,352–359], its mechanism of action is unclear. Furthermore, it is not fully established how synaptic Zn^{2+} and intracellular Zn^{2+} signaling both contribute to Zn^{2+}-dependent LTP induction. Some studies investigating LTP and postsynaptic signaling have focused on the importance of synaptic Zn^{2+} interacting with NMDARs, AMPARs, or Zn^{2+}-specific G protein-coupled receptor GPR39[242,308,335,336,355,357], while others indicate that intracellular Zn^{2+} signals may be responsible for modulation of Shank-mediated postsynaptic AMPAR density[359], BDNF/Src/TrkB signaling[337,338,360], downstream nitric oxide synthase (NOS)/p38 signaling[356], or downstream

MAPK/CREB signaling[293,332–334]. Zn^{2+} may therefore have many roles in LTP and synaptic plasticity, or specific roles in specific brain areas, but how these functions connect is still uncertain.

Much of the work concerning the physiological role of Zn^{2+} in neurons, especially in relation to how Zn^{2+} may affect intracellular signaling, has taken a targeted approach to investigating Zn^{2+}-dependent cellular changes by concentrating on specific signaling proteins or pathways. This focused approach is also characteristic of the larger field investigating Zn^{2+} signaling in other cell types. As a complementary approach, we analyzed global Zn^{2+}-dependent gene expression changes upon neuronal stimulation with potassium chloride (section 2.3.5). In combination with Zn^{2+} imaging, we were able to characterize specific Zn^{2+}-dependent gene upregulation and potential signaling pathways upon a modest change in intracellular Zn^{2+}.

1.8 Zn^{2+} in neurological disorders and excitotoxicity

The importance of Zn^{2+} to human health and to the medical field has grown substantially in the past two decades, partially due to advances in our understanding of its physiological function, but mostly due to an expanding body of work linking cellular and synaptic Zn^{2+} to many neurodegenerative diseases and disorders. In Alzheimer's disease (AD), elevated Zn^{2+} levels, ZnT3, or Zn^{2+} homeostasis proteins are evident in brains of AD mouse models and human patients[361–367], often linked to degenerating neurons that have higher Aß plaque load[368,369]. Mice with perturbed brain Zn^{2+} buffers also show different incidence of AD pathologies[370–372]. On a biochemical level, Zn^{2+} stabilizes Aß aggregates, possibly through interfering with proper dimerization or through interactions with the unstructured tail of the protein[58,373–378], and synaptic Zn^{2+} and Aß may have a synergistic effect on perturbing

synaptic transmission[340,379,380]. Although not as widely reported, similar pathologies and coincidence of Zn^{2+} in protein aggregates have also been seen in Parkinson's disease[36,381–384] and amyotrophic lateral sclerosis (ALS)[385–387], indicating that elevated Zn^{2+} may also influence the progression of these diseases. In contrast, global Zn^{2+} deficiency and mutations in vesicular Zn^{2+}-related proteins have been implicated in schizophrenia[388], autism[389,390], and depression[391–393], and Zn^{2+} is being explored as a clinical antidepressant[394–399]. A more thorough understanding of physiological and pathological Zn^{2+} function would benefit potential therapeutic development for all of these disorders[400].

In addition to (and sometimes overlapping with) neurological disorders, another major source of neuronal injury is excitotoxicity, which can arise from stroke/ischemia, traumatic brain injury, epileptic seizures, or other insults[401]. Excitotoxicity is generally considered to be excessive release of glutamate from glutamatergic synapses, which then causes spreading neuronal over-activation and intracellular stress/death signaling[402]. As many glutamatergic synapses also contain Zn^{2+}, it has long been recognized that Zn^{2+} likely plays a role in excitotoxic cascades. Ischemia, seizures, and traumatic brain injury (TBI) all can lead to a rapid depletion of intracellular Zn^{2+} and rise in extracellular Zn^{2+}, sometimes followed by a rise in cytosolic Zn^{2+} of surrounding neurons[403–408]. A large body of work has described the effects of Zn^{2+} perturbations on the pathology of excitotoxicity/ischemic insults in animals or tissues, with strongly paradoxical results. One set of experiments describes Zn^{2+} as neuroprotective, as assessed by greater cell death upon Zn^{2+} chelation or Zn^{2+} deficiency[409–415], less cell death/greater cell recovery upon Zn^{2+} supplementation[416–422], or greater susceptibility of ZnT3 KO mice to injury/seizures[423–426]. Another collection of studies postulates Zn^{2+} as a toxic agent,

due to cell death upon addition of exogenous Zn^{2+} during injury[416,427–431], neuroprotective effect of Zn^{2+} chelation[432–449], or neuroprotection of ZnT3 KO or other Zn^{2+}-buffering protein-related mouse models[280,450–453]. These studies vary widely in the methods they use to induce ischemia, injury, or seizures, and they also diverge in the brain region of the insult. In general, most of the experiments in which Zn^{2+} is shown to be neuroprotective are in the hippocampal region, with Zn^{2+}-related inhibition of NMDARs postulated as the primary mode of protection[409,416]. This pattern is not uniformly true, however, indicating that much is still unclear about how Zn^{2+} participates in excitotoxic cascades.

A main downstream component of excitotoxic cell death is oxidative stress, which has canonically been thought to be primarily mediated by intracellular Ca^{2+} [402]. Zn^{2+}, however, has also been shown to be an important factor in a feed-forward loop of reactive oxygen species/reactive nitrogen species (ROS/RNS) generation[57,454–460]. Intracellular rise in ROS/RNS will effectively mobilize Zn^{2+} from intracellular proteins, particularly metallothioneins, due to the abundance of redox-sensitive cysteines at Zn^{2+} binding sites[461–469]. Pathological increases in cytosolic Zn^{2+} can then induce Zn^{2+} movement into mitochondria, where it inhibits NADPH oxidase, leading to further ROS generation[57,470–477]. Whether extracellular Zn^{2+} translocation into neurons occurs to exacerbate this process during excitoxicity is ambiguous, but excessive glutamate stimulation/Ca^{2+} influx is sufficient to instigate the Zn^{2+}/ROS cycle[469]. Some signaling proteins, including Akt[478], HSP70[479], and poly(ADP ribose) polymerase (PARP)[480], have been implicated in mediating Zn^{2+}-dependent oxidative stress responses in neurons, but it is unclear how Zn^{2+} plays a role in this signaling. Furthermore, in addition to its function in exacerbating ROS proliferation, Zn^{2+} has been implicated in neuroprotective and anti-apoptotic signaling during oxidative

stress[117,481,482], but whether there is a threshold of Zn^{2+} that differentiates these roles is unknown.

In order to more fully understand Zn^{2+}-dependent intracellular signaling mechanisms during glutamate stimulation of neurons, we analyzed global gene expression and hundreds of protein phosphorylation states (see sections 3.3.4 and 3.3.5). Even in our mild stimulation conditions, we found evidence of Zn^{2+}-dependent endoplasmic reticulum-localized stress and potentially anti-apoptotic signaling, although there was little indication of oxidative stress. We are currently further investigating and validating these results, but we hope to provide important insight into how Zn^{2+} may modulate cell stress during glutamate toxicity.

Chapter 2

Characterization of neuronal intracellular and synaptic Zn^{2+} and Zn^{2+}-dependent gene expression

2.1 Publication status and author contributions

Sanford, L., Carpenter, M. C. & Palmer, A. E. Intracellular Zn^{2+} transients modulate global gene expression in dissociated rat hippocampal neurons. *Scientific Reports* **9**, 9411 (2019).

L.S. and A.E.P. designed the study and wrote the manuscript. L.S. collected and analyzed all imaging and sequencing data. M.C. collected and analyzed *in vitro* FRET sensor data. All authors reviewed the manuscript.

2.2 Introduction

Zinc (Zn^{2+}) is an essential trace element that is increasingly suggested to play a signaling role in a variety of different cell types. Transient Zn^{2+} increases have been linked to many aspects of neuronal regulation and physiology[242,302,483,484], pro-inflammatory signaling in monocytes[70], oocyte maturation[485], and modulation of Ca^{2+} release in cardiomyocytes[97]. In some cases, researchers have identified specific Zn^{2+}-sensing proteins, such as neurotransmitter receptors or phosphatases[110,486–488], or Zn^{2+}-dependent regulation of signaling pathways, including Zn^{2+} modulation of the mitogen-activated protein kinase (MAPK) pathway[115,332]. However, there is still no unified mechanistic insight into how Zn^{2+} fluctuations induce changes in cellular physiology. Using dissociated hippocampal neurons as a model system, we present

here the first global sequencing-based examination of potential downstream targets of Zn^{2+} signals.

Zn^{2+} is concentrated into glutamate-containing synaptic vesicles in subsets of neurons throughout the brain and is heavily enriched in the hippocampus[178]. Electrophysiology studies in brain slices have demonstrated that Zn^{2+} is released upon neuronal activation and modulates postsynaptic glutamate receptors[208,302,484]. Transient increases in Zn^{2+} have been observed inside neurons after stimulation, possibly as a result of translocation of Zn^{2+} from the synapse or release of Zn^{2+} from intracellular stores[212,266,289]. Both synaptic and intracellular Zn^{2+} signals contribute to regulation of short- and long-term plasticity in different areas of the brain[208,242,354,489], and genetic or pharmacological manipulation of hippocampal Zn^{2+} leads to learning and memory deficits in rodents[294,305,490]. However, the cellular mechanisms underlying Zn^{2+}-dependent neuronal remodeling are largely unclear.

In order to gain further insight into downstream effects of neuronal Zn^{2+} signaling, we performed RNA-Seq on dissociated hippocampal neuron cultures. While synaptic Zn^{2+} has been primarily characterized in brain slices or *in vivo* in rodent brains[208,300], cultured neurons allow for uniform stimulation of a more homogenous population of cells than brain tissue. Furthermore, single-cell fluorescence imaging permits more robust quantification of intracellular Zn^{2+} dynamics than can be accomplished in tissue, giving us the ability to define a stimulation-induced Zn^{2+} signal and investigate its downstream consequences. The extent of synaptic Zn^{2+} mobilization in neuron cultures would inform any analysis of Zn^{2+}-dependent global changes. Unfortunately, while dissociated hippocampal neurons have been shown to both release Zn^{2+} and exhibit cytosolic Zn^{2+} dynamics upon intensive glutamate stimulation[210,289], no rigorous characterization of synaptic Zn^{2+} or synaptic Zn^{2+}

machinery has been performed in these cultures.

In this work, we aimed to quantify cytosolic Zn^{2+} in dissociated hippocampal neurons under resting and mild stimulation conditions, characterize the synaptic Zn^{2+} pools in these neurons, and determine the transcriptional effects of cytosolic Zn^{2+} signals. We found that dissociated neurons accumulate the synaptic transporter ZnT3 (*Slc30a3*), responsible for loading Zn^{2+} into synaptic vesicles, although we were unable to confirm the presence of synaptic Zn^{2+} due to limitations of existing tools. However, we did find that stimulation of neurons with a short KCl treatment generated modest Zn^{2+} signals that increased 3-fold in the presence of low levels of exogenous Zn^{2+}. Further, we observed robust Zn^{2+}-dependent differential expression of 931 genes, many of which are related to neuronal physiology and synaptic modulation. To our knowledge, this is the first large-scale experiment to identify transcriptional changes of Zn^{2+} signals in a mammalian system, and these results can provide possible mechanistic insight into Zn^{2+}-dependent neuronal plasticity.

2.3 Results

2.3.1 Quantification of resting neuronal Zn^{2+}

In order to rigorously define the overall Zn^{2+} status of dissociated hippocampal neuron cultures, we first characterized resting neuronal cytosolic and synaptic Zn^{2+}. We used a genetically encoded Zn^{2+} Förster Resonance Energy Transfer (FRET) sensor to quantify cytosolic labile Zn^{2+} under resting conditions in neuronal cultures (Figures 2.1A, 2.2). We observed a resting fractional saturation for our sensor of 0.21 ± 0.02, which corresponds to an approximate Zn^{2+} concentration of 60 pM ± 40 pM (Figure 2.1B). It should be noted that this estimate is based on an *in vitro* FRET sensor K_d of 5.3 nM (Figures 2.1B, 2.3), which may be altered in cells. Nevertheless,

this Zn^{2+} concentration is comparable to that observed in other cell types[81,152] and also is in accordance with previous measurements in neurons[81].

A

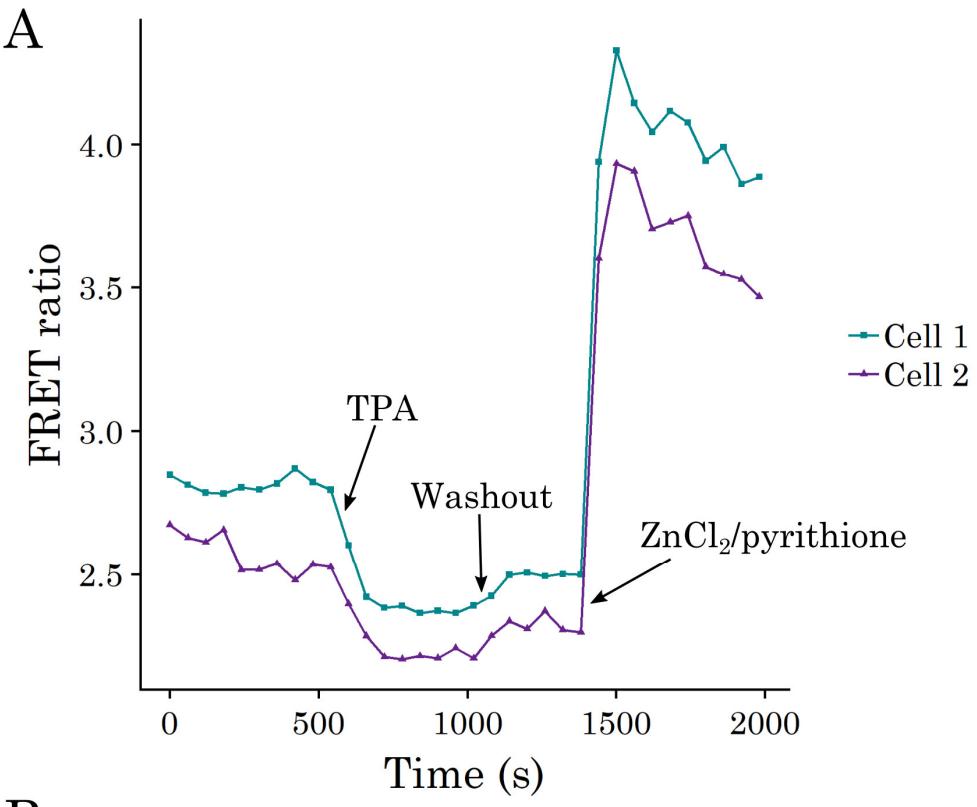

B

ZapCV2 sensor *in vitro* K_d	5.3 nM ± 1.1 nM
ZapCV2 sensor *in vitro* Hill coefficient	0.29 ± 0.02
Resting neuron fractional saturation	0.21 ± 0.02
Approximate resting neuron [Zn^{2+}]	60 pM ± 40 pM

Figure 2.1: Genetically encoded Zn^{2+} FRET sensor measurements in resting neurons. (A) Sample traces from a typical FRET sensor calibration. Each trace is derived from a region of interest in two separate cells within one field of view. Resting FRET ratios were observed, followed by treatment with 10 µM TPA and subsequently 10 µM $ZnCl_2$/2.5 µM pyrithione to determine minimum and maximum FRET ratios, respectively. (B) Quantification of Zn^{2+} based on the *in vitro* binding parameters of the sensor. Errors correspond to standard error of the mean. n = 14 cells from 6 separate biological replicates derived from 2 separate cell preparations.

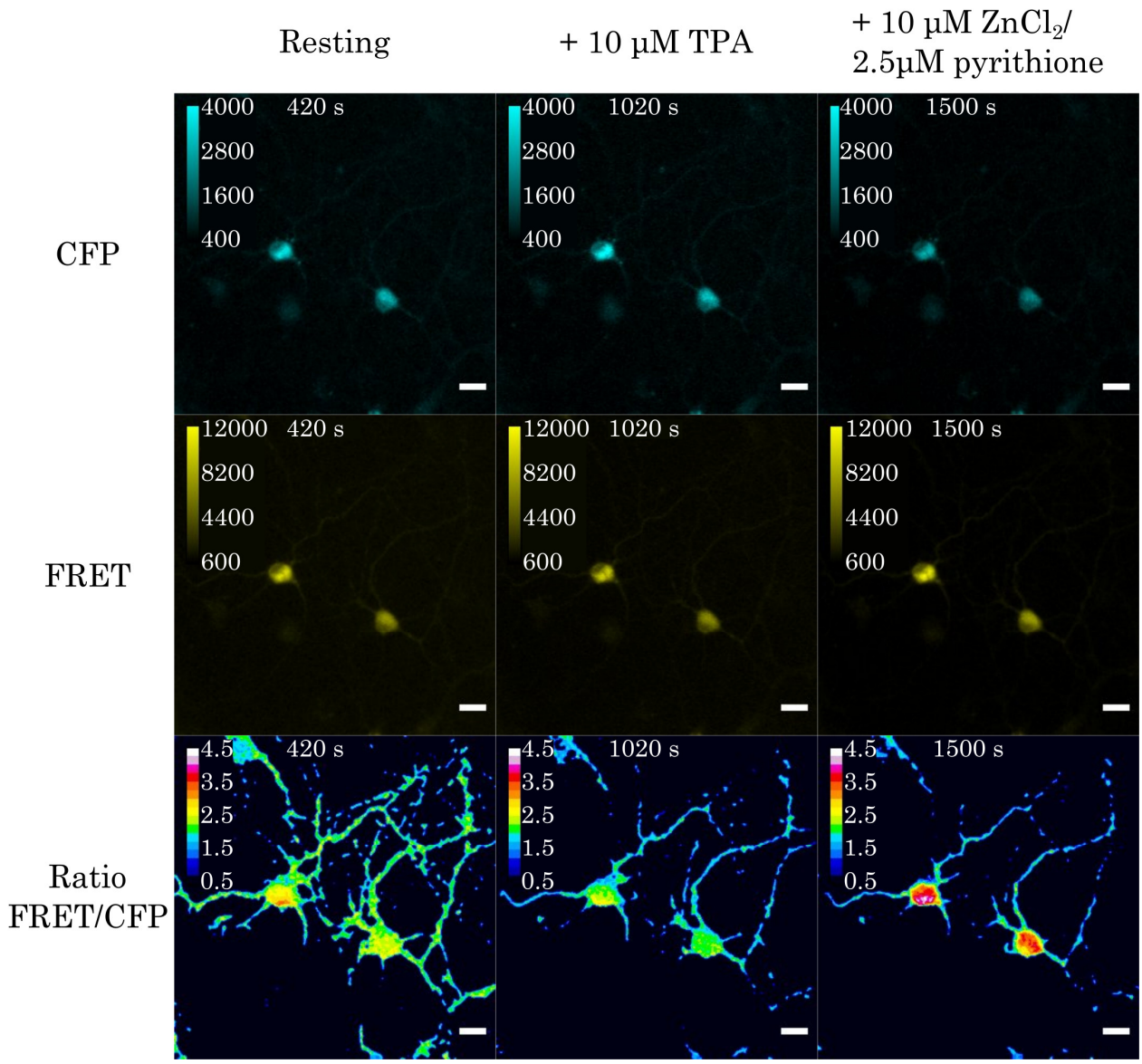

Figure 2.2: Representative images of cells expressing Zn^{2+} sensor ZapCV2. CFP and FRET channels are shown with corresponding pixel intensity scales, along with ratio images of relevant neuronal areas within the field of view. Resting images were taken before exogenous Zn^{2+} perturbation, 10 µM TPA treatment shows unbound sensor (higher CFP intensity, lower FRET intensity, lower ratio), and 10 µM $ZnCl_2$/2.5 µM pyrithione treatment shows fully bound sensor (lower CFP intensity, higher FRET intensity, higher ratio). Cells and times correspond to the traces in Figure 2.1A. Scale bars = 20 µm.

2.3.2 Characterization of ZnT3 in dissociated neurons

There are two main logical possibilities for how cytosolic Zn^{2+} signals can be generated. One is that intracellular, protein-bound stores of Zn^{2+} are mobilized upon

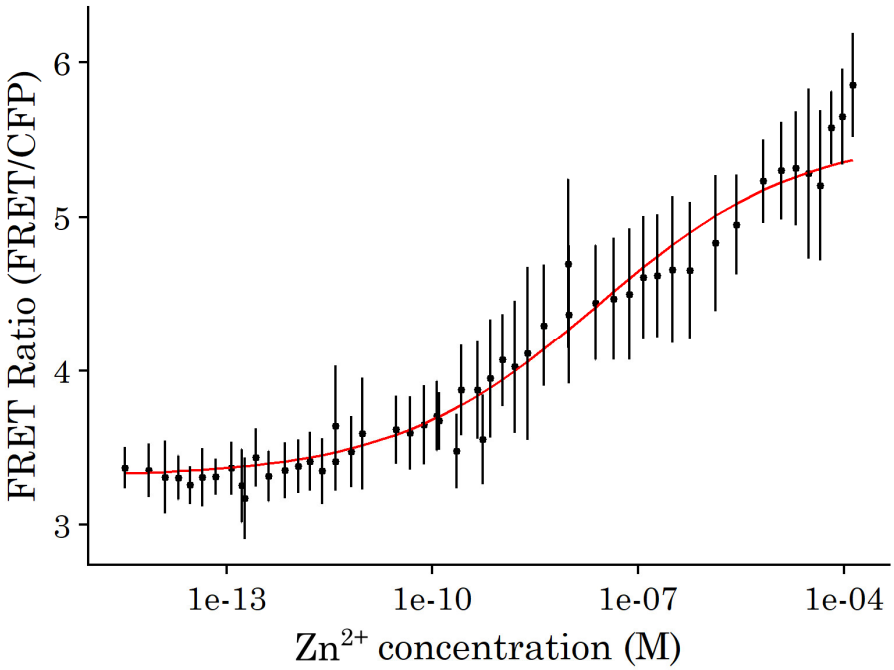

Figure 2.3: *In vitro* binding curve for genetically encoded Zn^{2+} sensor ZapCV2. Sensor protein was expressed and purified from *E. coli*, and sensor fluorescence (Excitation: 420 nm, donor emission: 475 nm, acceptor emission: 529 nm) was measured in different buffered Zn^{2+} concentrations. The binding curve shown yielded the parameters K_d = 5.3 nM ± 1.1 nM and Hill coefficient n = 0.29 ± 0.02. Error bars indicate the standard deviation of measurements, and parameter error values correspond to standard error.

stimulation. The second is that Zn^{2+} is released from synaptic vesicles into the synapse upon stimulation and subsequently translocates across the plasma membrane into the cytosol of postsynaptic or presynaptic neurons. The latter possibility depends upon the presence of ZnT3 and concentration of Zn^{2+} into synaptic vesicles. To determine whether dissociated neuron cultures have the machinery for synaptic vesicle Zn^{2+} sequestration, we investigated whether the synaptic vesicle Zn^{2+} transporter ZnT3 (*Slc30a3*) was expressed in cultures (Figures 2.4 – 2.8). *Slc30a3* mRNA and synaptic Zn^{2+} are barely detectable in embryonic brain slices, with both increasing substantially after birth[173,300]. Accordingly, *Slc30a3* mRNA was not evident in our cells upon isolation (Day *in vitro* 0, DIV 0) as measured by RT-qPCR, but was present at all other timepoints (Figure 2.4). ZnT3 protein was observed by

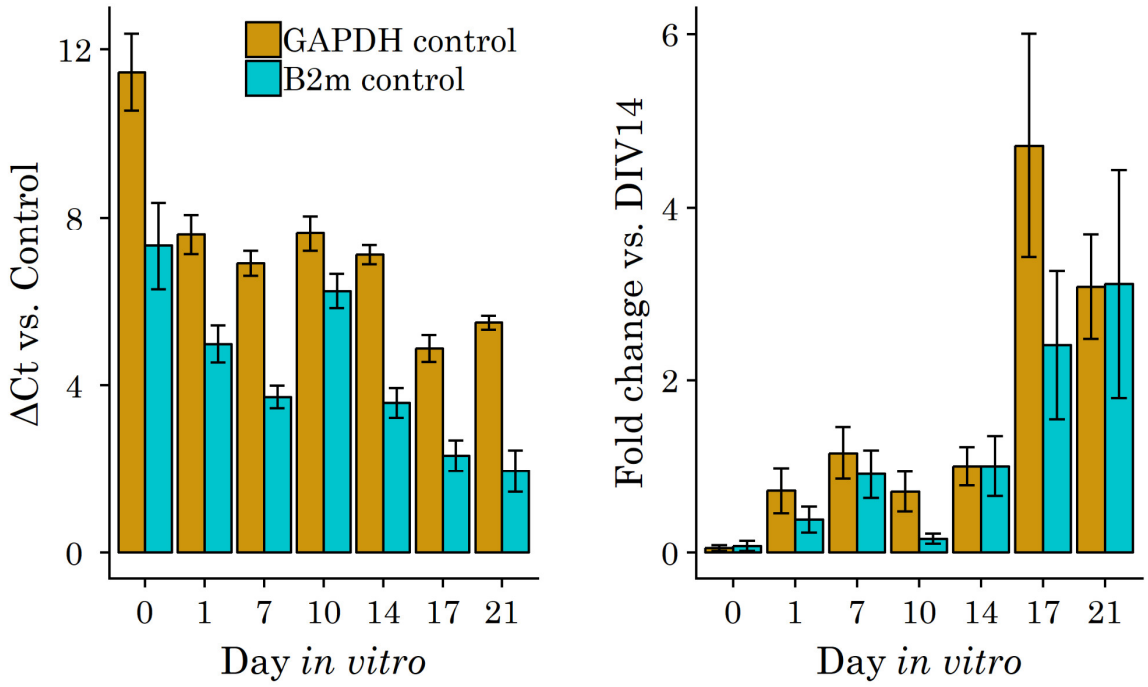

Figure 2.4: RNA expression of Zn^{2+} transporter ZnT3 in cultured neurons. RT-qPCR for the ZnT3 gene *Slc30a3* in neuron cultures at day *in vitro* (DIV) 0, 1, 7, 10, 14, 17, and 21. ΔCt values were generated by normalizing threshold cycle values (Ct) to either GAPDH or beta-2-microglobulin (B2m) as internal controls. Fold changes were calculated with respect to the DIV14 timepoint. 3-4 technical replicates were run on 1 biological replicate for DIV 0, 1, 17, and 21, and 3-4 technical replicates were run on each of 2 biological replicates from 2 separate neuron preparations for DIV 7, 10, and 14. Error bars represent standard deviations, propagated from technical replicate standard deviations. Data reveal that ZnT3 mRNA is not expressed at DIV 0 but is expressed at all other timepoints tested.

immunofluorescence, with robust expression after DIV 1 (Figures 2.5A, 2.6). By DIV 10, ZnT3 staining showed a synaptic pattern, colocalizing with presynaptic marker Synapsin1/2 and lying adjacent to postsynaptic protein Homer1 (Figures 2.5B, 2.7). Co-incubating samples with the ZnT3 antibody and a ZnT3-derived peptide abolished staining (Figure 2.8). This evidence indicates that ZnT3 is expressed and correctly localized in dissociated neuron culture.

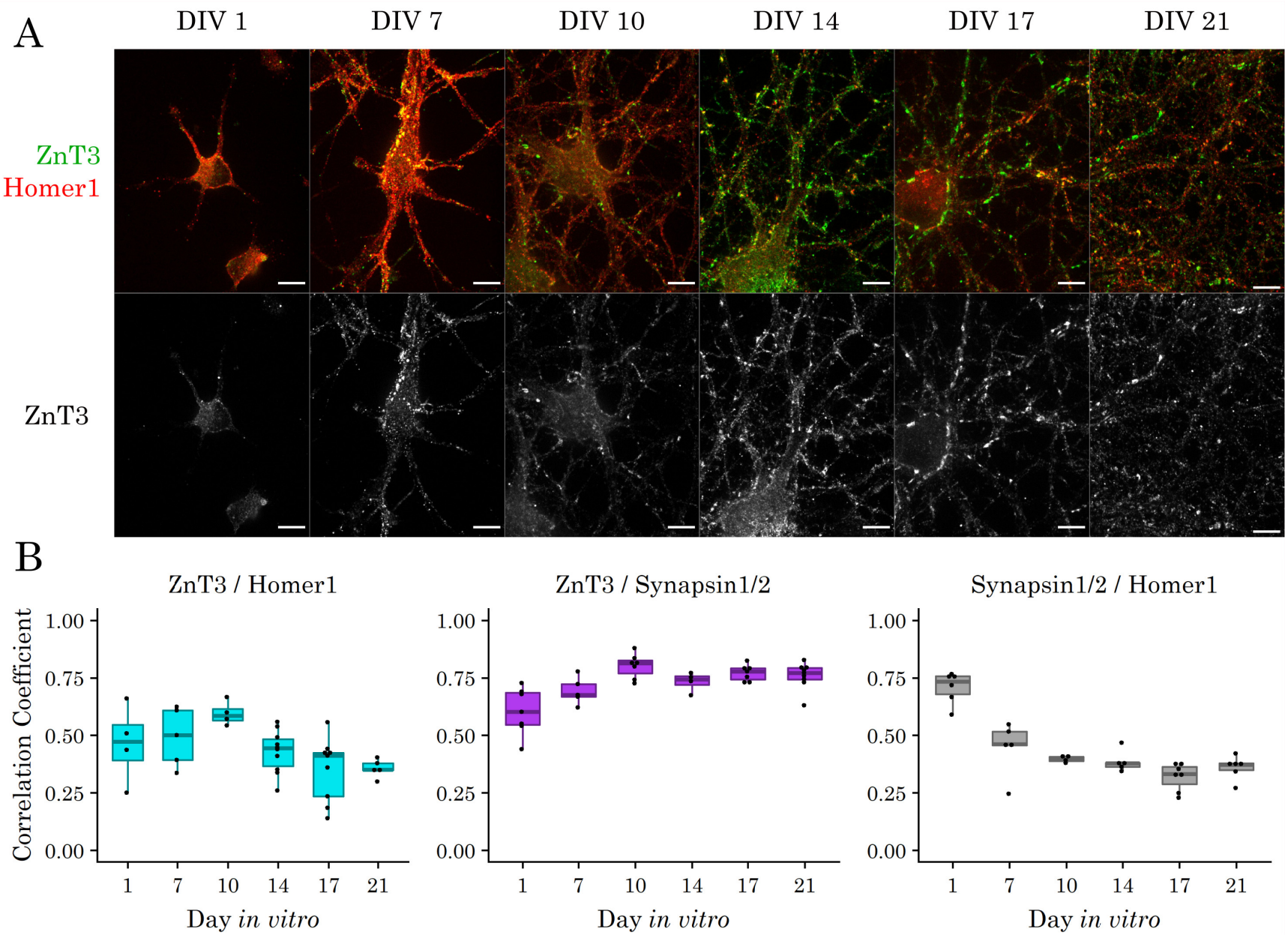
A
DIV 1
DIV 7
DIV 10
DIV 14
DIV 17
DIV 21
ZnT3
Homer1
ZnT3
B
ZnT3 / Homer1
ZnT3 / Synapsin1/2
Synapsin1/2 / Homer1
Correlation Coefficient
1.00
0.75
0.50
0.25
0.00
1
7
10
14
17
21
Day *in vitro*

2.3.3 Investigation of synaptic vesicle Zn^{2+} in dissociated neurons

Following our observation that synaptic ZnT3 is present in hippocampal neuron cultures after DIV 10, we carried out a variety of experiments to investigate whether there was direct evidence for the presence or release of synaptic Zn^{2+} in these neurons (Figures 2.9 – 2.11). In our first attempts, we applied a Timm stain, a histological stain that is commonly used to detect Zn^{2+} in brain tissue (Figure 2.9A)[491–493]. We observed significant contrast, as evidenced by the dark staining due to sulfide/silver deposition, in neurons loaded with exogenous Zn^{2+} (Figure 2.9A, Zn^{2+}/pyrithione treatment). However, we saw no clear signal corresponding to endogenous Zn^{2+} in the cell body or in processes (Figure 2.9A, untreated).

Detecting Zn^{2+} in synaptic vesicles with fluorescent dyes is not straightforward. While some literature has described the intracellular Zn^{2+}-specific dye FluoZin-3 AM as having vesicular localization[494,495], we have previously shown that FluoZin-3 AM stains various cellular compartments including the cytosol, nucleus, Golgi apparatus, and lysosome[81,496], and indeed in hippocampal neurons we see primarily a cytosolic and nuclear localization, with some aggregation in other subcellular compartments (see Figure 2.12A for FluoZin-3 AM localization). Another reported vesicle-specific Zn^{2+} fluorescent dye, SpiroZin2, largely colocalizes with lysosomes[122,496], and in our

Figure 2.5 (p. 24): Expression and localization of Zn^{2+} transporter ZnT3 in cultured neurons by immunofluorescence. (A) ZnT3 (synaptic vesicle Zn^{2+} transporter, pseudocolored green or displayed in grayscale below) and Homer1 (post-synaptic density protein, pseudocolored red) are stained at different timepoints in culture. ZnT3 increases in expression over time in culture, and shows synaptic localization starting at DIV 10. Channel intensities of all images are scaled identically. (B) 2D correlation coefficients calculated on raw immunofluorescence images. Smaller correlation coefficients are more likely to represent less colocalization. ZnT3 maintains a high correlation coefficient compared to Synapsin1/2 across the time course, whereas Synapsin1/2 compared to Homer1 and ZnT3 compared to Homer1 decrease over time. Each DIV/protein comparison is one biological replicate, with each dot representing a separate field of view within the sample. Scale bars = 10 μm.

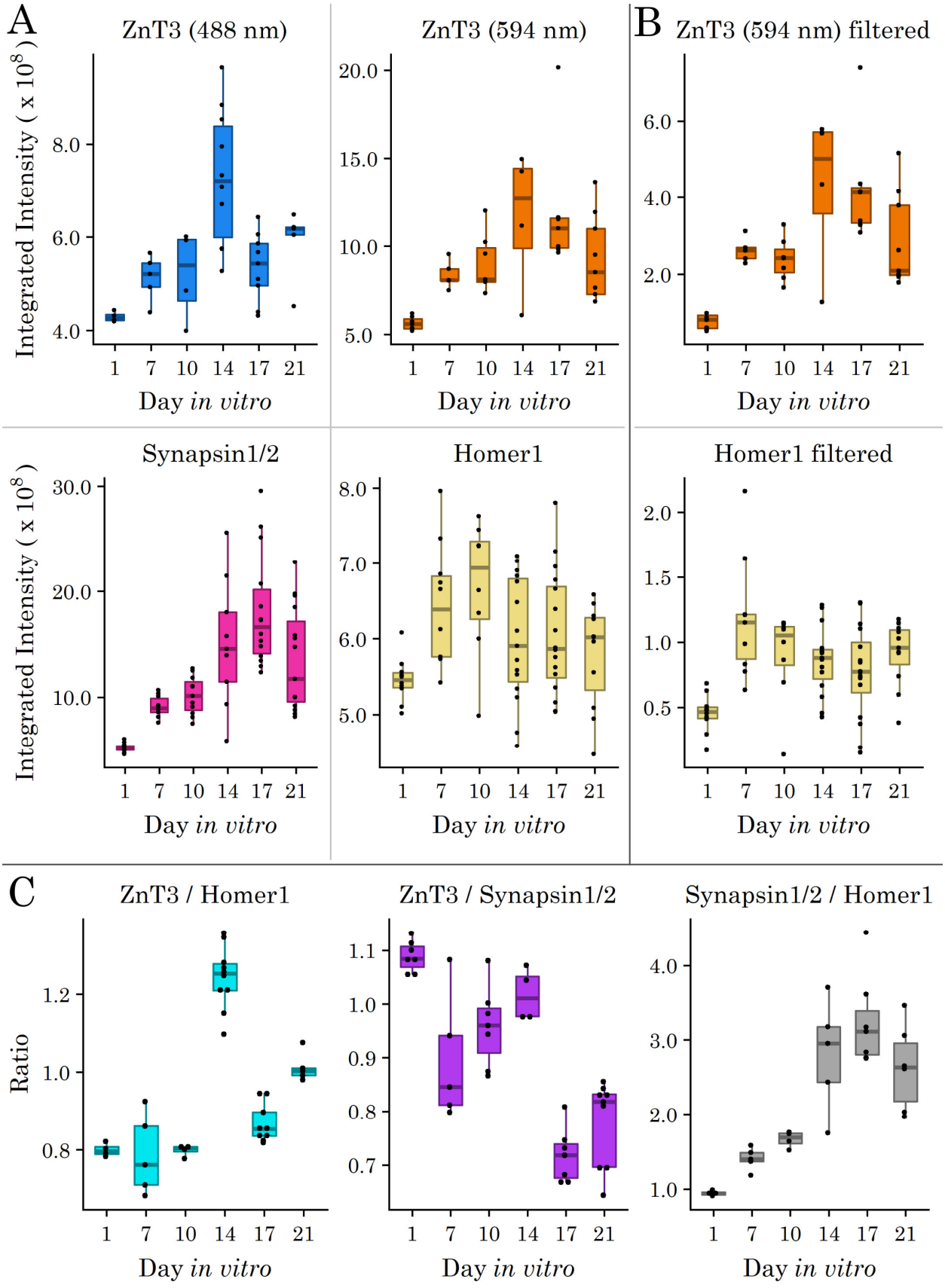
A
ZnT3 (488 nm)
ZnT3 (594 nm)
B
ZnT3 (594 nm) filtered
Integrated Intensity (x 10^8)
Day in vitro
Synapsin1/2
Homer1
Homer1 filtered
C
ZnT3 / Homer1
ZnT3 / Synapsin1/2
Synapsin1/2 / Homer1
Ratio

neuron cultures seems restricted to compartments in the cell body or rapidly trafficking along processes. Thus, FluoZin-3 AM and SpiroZin2 were deemed unsuitable for synaptic vesicle detection in our system. We also attempted to use ZIMIR, a Zn^{2+}-specific membrane dye, to quantify Zn^{2+} release upon stimulation (Figure 2.10), but were unable to show any stimulation-specific change in fluorescence.

Synaptic vesicle localization and dynamics have been previously visualized with stimulation-dependent uptake of membrane-bound FM dyes[497,498]. We adapted this technique to load synaptic vesicles with a membrane-impermeant version of FluoZin-3 (Figure 2.9B). Briefly, we electrically stimulated cells in media containing both membrane dye FM 4–64 and a high concentration of FluoZin-3. As vesicles fuse with the plasma membrane, fluorescent dyes can diffuse from the membrane or media into the vesicular lumen. We observed vesicular puncta that colocalized with FM 4–64 when this procedure was carried out with FluoZin-3 complexed with exogenous Zn^{2+} (Figure 2.9B, FluoZin-3/Zn^{2+} loaded), suggesting the soluble FluoZin-3/Zn^{2+} complex

Figure 2.6 (p. 26): Quantification of immunofluorescence signal. (A) Boxplots of integrated intensity measurements of images for each separate primary/secondary antibody combination. Synapsin1/2 and Homer1 graphs include data from two biological replicates at each timepoint, whereas each ZnT3 graph includes data from one biological replicate at each timepoint, measured with the same primary antibody and different secondary antibodies (named by wavelength). Each dot represents the integrated intensity value of one full field of view within a sample. ZnT3 and Synapsin1/2 show increased signal over time, peaking at day *in vitro* (DIV) 14. Homer1, in contrast, shows level/decreasing signal after DIV1. (B) Intensity measurement trends do not change if data is filtered. Adaptive thresholding was applied to images in MATLAB to filter background areas before integrated intensity calculation. ZnT3 (594 nm secondary antibody) and Homer1 are shown as representative examples of filtered data. Compared to the corresponding graphs in (A), the spread of the data decreases, but overall trends remain the same. Replicates are the same as in part (A). (C) Ratio measurements comparing signal within the same field of view. Ratios indicate that signal intensities for Synapsin1/2 and ZnT3 increase over time relative to Homer1, especially after DIV10, and that Synapsin1/2 intensity increases more substantially than ZnT3.

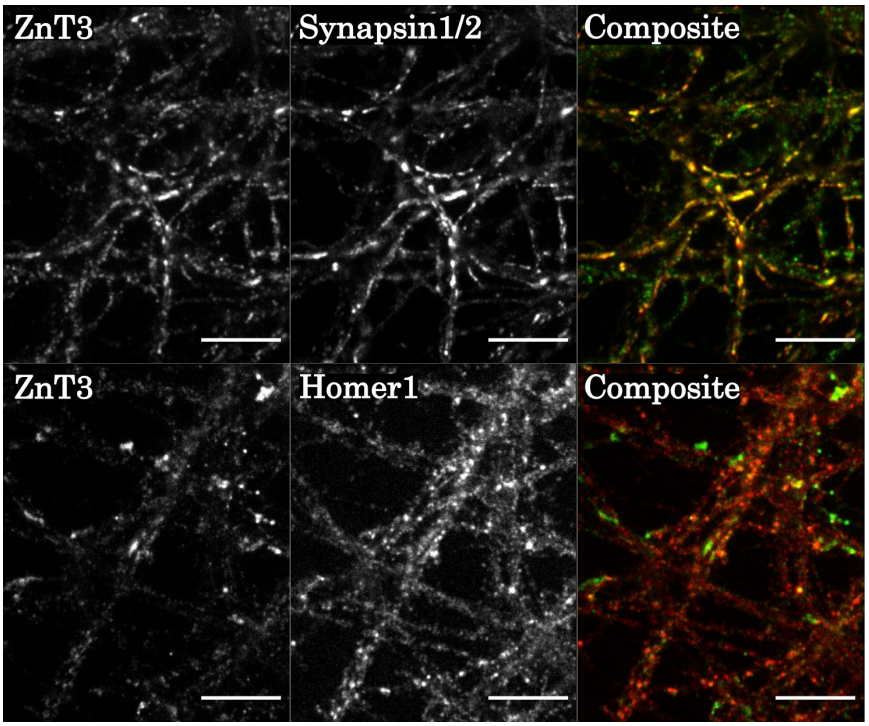

Figure 2.7: Pre-synaptic localization of ZnT3. Immunofluorescence co-staining of day *in vitro* (DIV) 10 neuron cultures for ZnT3 (green) and pre-synaptic vesicle protein Synapsin1/2 (red) shows substantial colocalization (top), whereas co-staining for ZnT3 (green) and post-synaptic protein Homer1 (red) displays little colocalization (bottom). Scale bars = 10 µm.

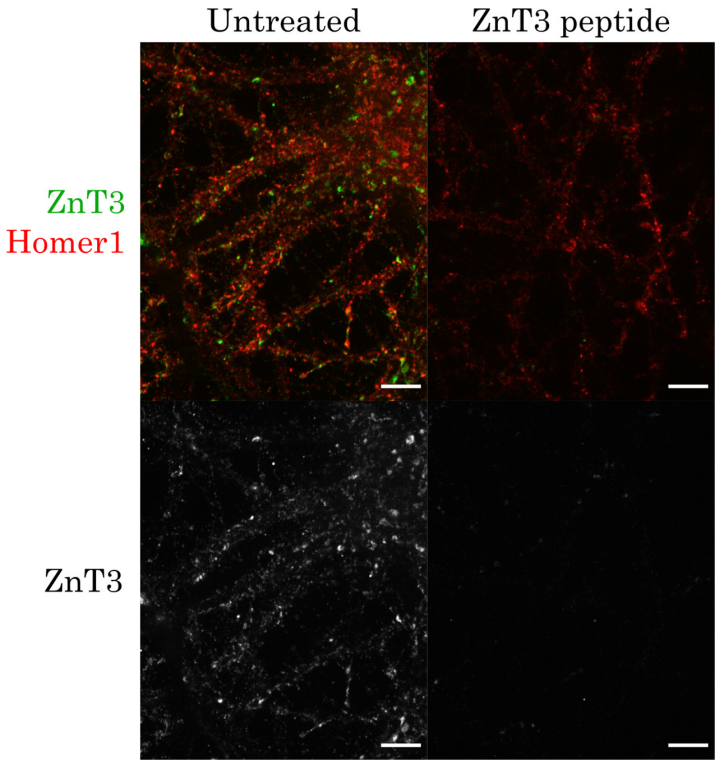

Figure 2.8: Specificity of ZnT3 immunofluorescence in DIV 10 neuron cultures. For the culture displayed on the right, ZnT3 primary antibody was pre-incubated with a peptide derived from ZnT3, which abolishes most immunofluorescence signal. Individual channel intensities of both images are scaled identically. Scale bars = 10 µm.

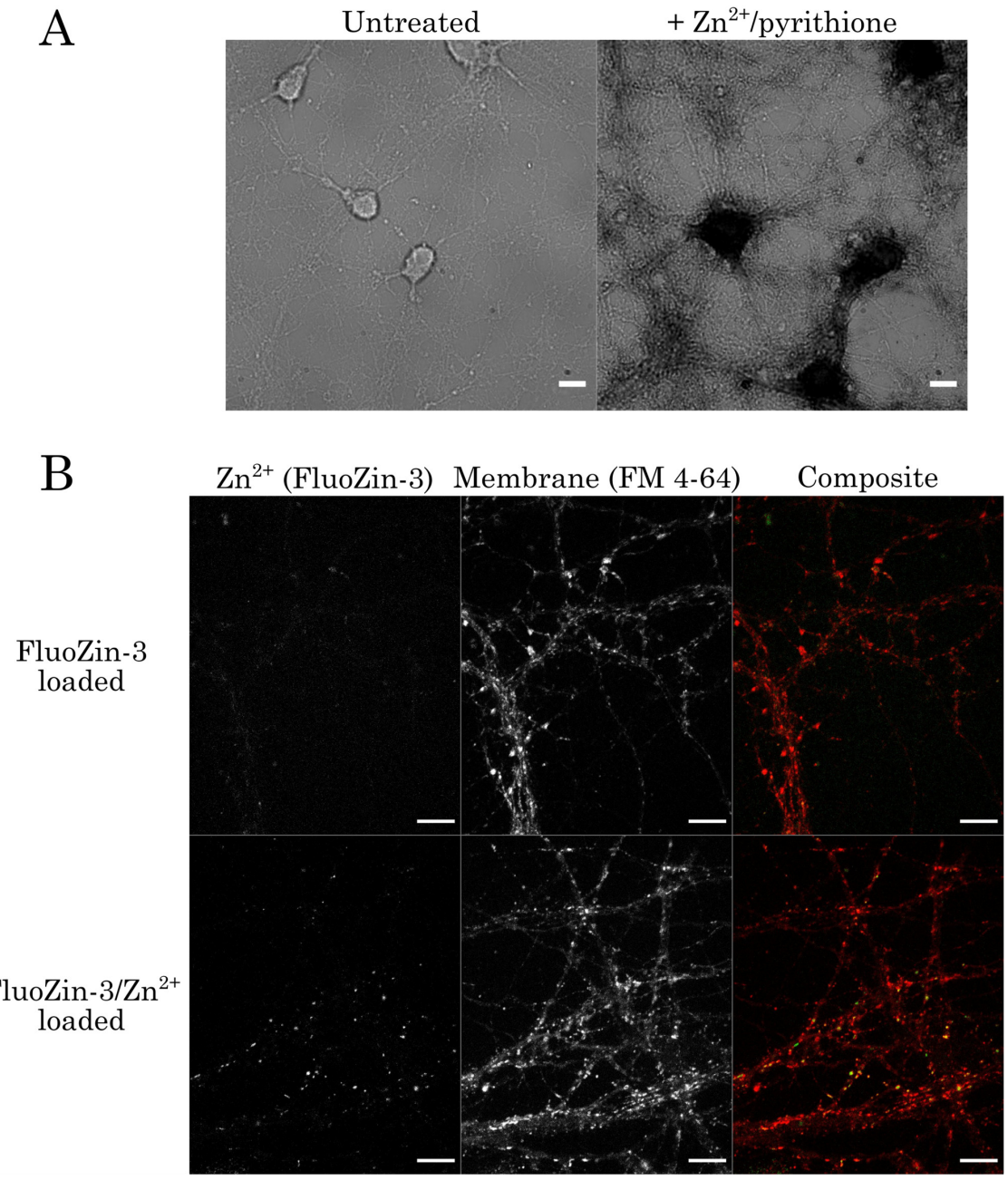

Figure 2.9: Attempts to visualize Zn^{2+} in synaptic vesicles. (A) Timm's stain of neurons at DIV 10. Cultures were stained +/− treatment with 20 µM $ZnCl_2$/2.5 µM pyrithione for 8 minutes prior to staining. Timm's stain was visible in cell bodies and processes of treated neurons (right), but not visible under endogenous Zn^{2+} conditions (left). (B) Dye loading of stimulated neurons. Cultures were electrically stimulated in the presence of extracellular fluorescent dyes FluoZin-3 (10–50 µM, green) and FM 4–64 (5 µM, red), then washed to allow visualization of internalized dye. In some samples, 10 µM $ZnCl_2$ was added to media before and during stimulation. FluoZin-3 puncta present upon co-incubation with Zn^{2+} indicate successful dye loading; however, no puncta are visible under endogenous Zn^{2+} conditions. Scale bars = 10 µm.

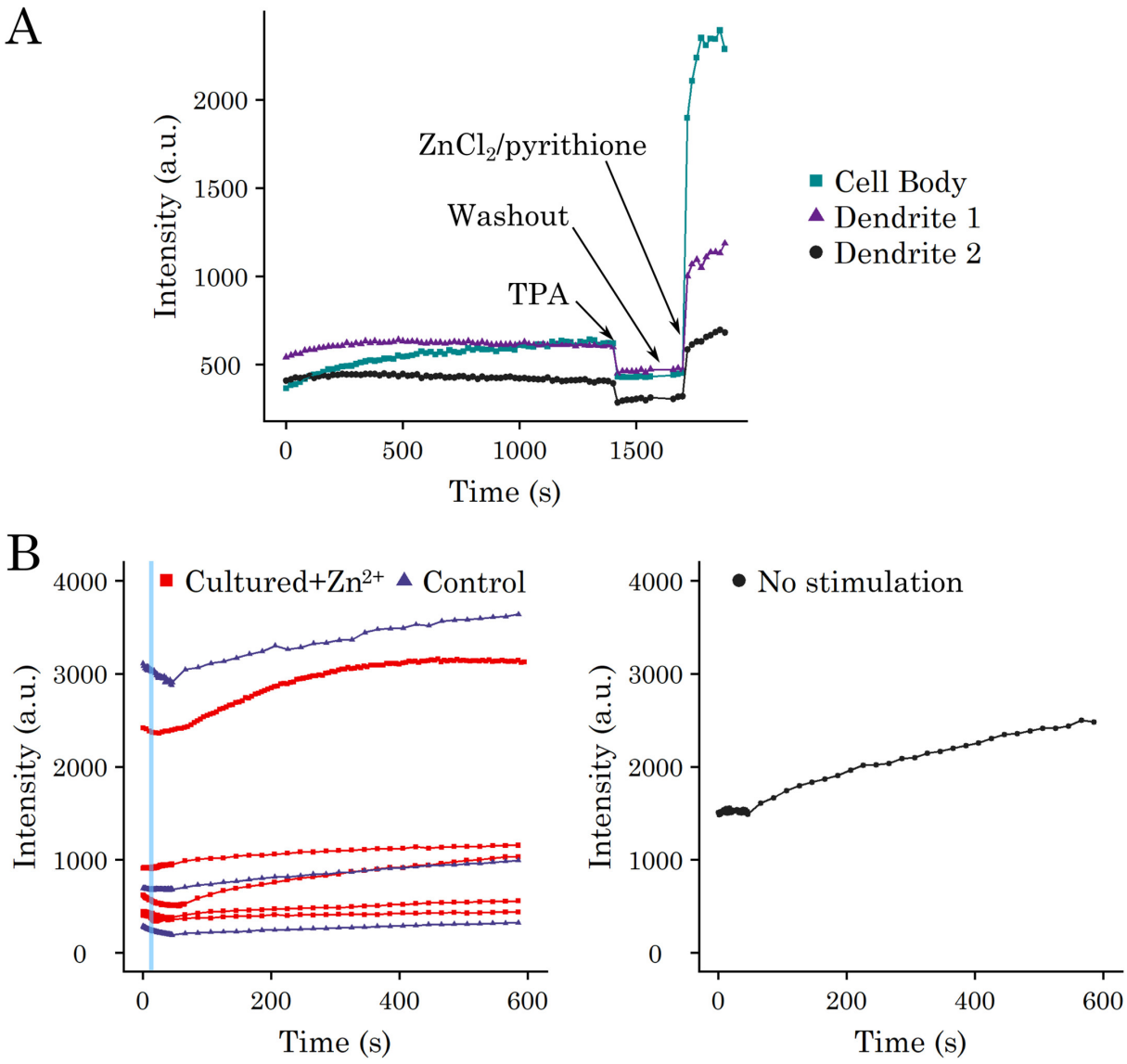

Figure 2.10: Fluorescence signal of the extracellular Zn^{2+}-specific membrane dye ZIMIR. Cultures were incubated for 20 minutes with 5 µM ZIMIR prior to imaging. (A) Exogenous Zn^{2+} perturbations of ZIMIR-incubated neurons. The dye is responsive to treatment with 10 µM TPA and 10 µM $ZnCl_2$, indicating that the observed fluorescence can change depending on the presence of extracellular Zn^{2+}. (B) ZIMIR fluorescence upon neuronal stimulation. Cells were electrically stimulated (left panel, stimulation time indicated by blue box) or imaged without application of stimulation (right panel). Electrically stimulated cells were incubated in normal media or media containing an additional 10 µM $ZnCl_2$ for 0.5-48 hours ("Cultured + Zn^{2+}" condition). Signal is variable, but generally increases over time regardless of condition. The lack of response of ZIMIR to stimulation could be due to a lack of releasable vesicular Zn^{2+} in these cultures, or it could be due to limitations in the dye itself. For example, the K_d for ZIMIR is 450 nM[499], which would be too high to allow the dye to respond effectively to Zn^{2+} release in the low nanomolar range[212].

can be taken up into vesicles upon neuron stimulation. However, in the absence of pre-loading with exogenous Zn^{2+}, the FluoZin-3 signal was extremely dim and no clear vesicular puncta were visible (Figure 2.9B, FluoZin-3 loaded). As this is an intensity-based dye, lack of signal could be due to several factors, including limited amount of dye uptake, slow dynamics of Zn^{2+} reloading after release into the extracellular space, or an increase in the K_d of FluoZin-3 for Zn^{2+} in the vesicular environment. We attempted to shift the equilibrium by adding extracellular Zn^{2+} after loading, but this had little effect on the vesicular FluoZin-3 signal (Figure 2.11). It is also possible that the amount of FluoZin-3 successfully loaded in vesicles was insufficient to compete away endogenous Zn^{2+} ions from the glutamate present in the vesicles, as glutamate likely coordinates Zn^{2+} to some extent[135,500].

Cumulatively, these experiments suggest that while dissociated hippocampal neurons do correctly express and localize ZnT3, we were unable to confirm the presence of synaptic Zn^{2+}. These results could indicate a lack of synaptic Zn^{2+}, or they could reflect limitations of the applied tools in allowing us to detect it.

2.3.4 Measurements of Zn^{2+} dynamics upon KCl stimulation

In order to visualize Zn^{2+} dynamics in excited neurons, we imaged neurons with cell-permeant Zn^{2+}-specific dye FluoZin-3 AM during stimulation with KCl (Figure 2.12). FluoZin-3 AM has been shown to be unresponsive to physiological perturbations of Ca^{2+} concentrations[499], so changes in fluorescence during neuron stimulation specifically represent Zn^{2+} dynamics. We observed that with a 10 second KCl treatment alone, neurons exhibited a small but significant rise in cytosolic Zn^{2+}, which often recovered to baseline values after the treatment was removed, although some cells had a more sustained response (Figure 2.12C,D, KCl stimulation). We

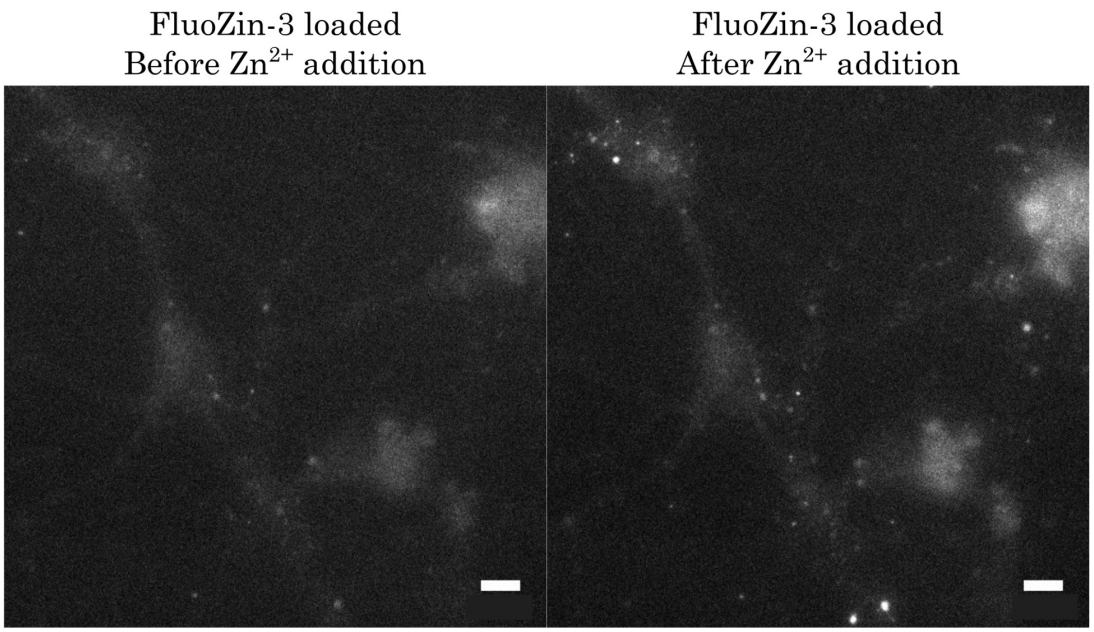

Figure 2.11: Zn^{2+} treatment of FluoZin-3 loaded neurons. Neurons loaded with FluoZin-3 by electrical stimulation were imaged (left), then treated with 50 μM $ZnCl_2$ and imaged again (right). Overall signal increases, but synaptic puncta do not appear. Scale bars = 10 μm.

detected a similar Zn^{2+} rise using the ZapCV2 sensor (Figure 2.13). With FluoZin-3 AM, we observed that this Zn^{2+} signal increased if neurons were treated with KCl in the presence of 10 μM extracellular Zn^{2+}, and the cells showed a similar variation in length of response (Figure 2.12B,C, KCl/Zn^{2+} stimulation). Mild KCl treatment thus induces an endogenous rise in cytosolic Zn^{2+} that can be potentiated by extracellular Zn^{2+} addition (Figure 2.12D). Using the *in vitro* K_d of FluoZin-3 (9.1 nM)[501], the measured rise corresponds to an increase in Zn^{2+} concentration from roughly 110 pM to 150 pM in the absence of exogenous Zn^{2+}, and from 110 pM to 220 pM in the presence of 10 μM exogenous Zn^{2+}. The estimated concentrations indicate that neurons experience a modest increase in labile Zn^{2+} upon stimulation.

2.3.5 Analysis of Zn^{2+}-dependent gene expression upon KCl stimulation

We broadly characterized the immediate transcriptional effects of the KCl-dependent Zn^{2+} increase by performing RNA-Seq on cells harvested 90 minutes after

treatment with KCl in the presence and absence of extracellular Zn^{2+} or the membrane-permeable Zn^{2+}-specific chelator TPA (Figure 2.14). We used the same 10 second KCl stimulation as our imaging experiments in order to minimize cell stress and identify transcriptional effects arising from subtle Zn^{2+} increases that may more closely mimic physiological signals than extended treatment with high concentrations of Zn^{2+}. It is well established that KCl treatment induces membrane depolarization and Ca^{2+} influx in excitable cells such as neurons. However, the KCl treatment remained constant across our conditions, and comparisons across conditions were thus representative specifically of Zn^{2+} perturbations. Differential expression analysis indicated that mild exogenous Zn^{2+} treatment during stimulation significantly alters expression of 931 genes, which can be seen as the blue dots in a volcano plot of the statistical significance vs. fold change of differentially expressed genes (Figure 2.14A,B). In contrast, KCl stimulation in the presence of TPA had no detectable effect on gene expression compared to KCl treatment alone, likely indicating that TPA had little effect on Zn^{2+} dynamics during the short time (10 sec) of stimulation. Less overall differential expression was observed between the KCl/Zn^{2+} and KCl/TPA conditions than between the KCl/Zn^{2+} and KCl conditions. This observation could result from a high degree of variability among the biological replicates for KCl/TPA and intermediate values based on principal component analysis (PCA), which resulted in fewer genes identified as differentially expressed (Figure 2.15) We note that while the number of genes whose expression is altered by Zn^{2+} perturbations is exciting, the degree of change is small, likely because of the mild Zn^{2+} perturbations and heterogeneity in both the Zn^{2+} signal (Figure 2.12) and transcriptional response (PCA in Figure 2.15). We attempted to validate the expression changes by RT-qPCR for three hits (*Slc30a3*, *Slc39a10*, and *Sik1*)

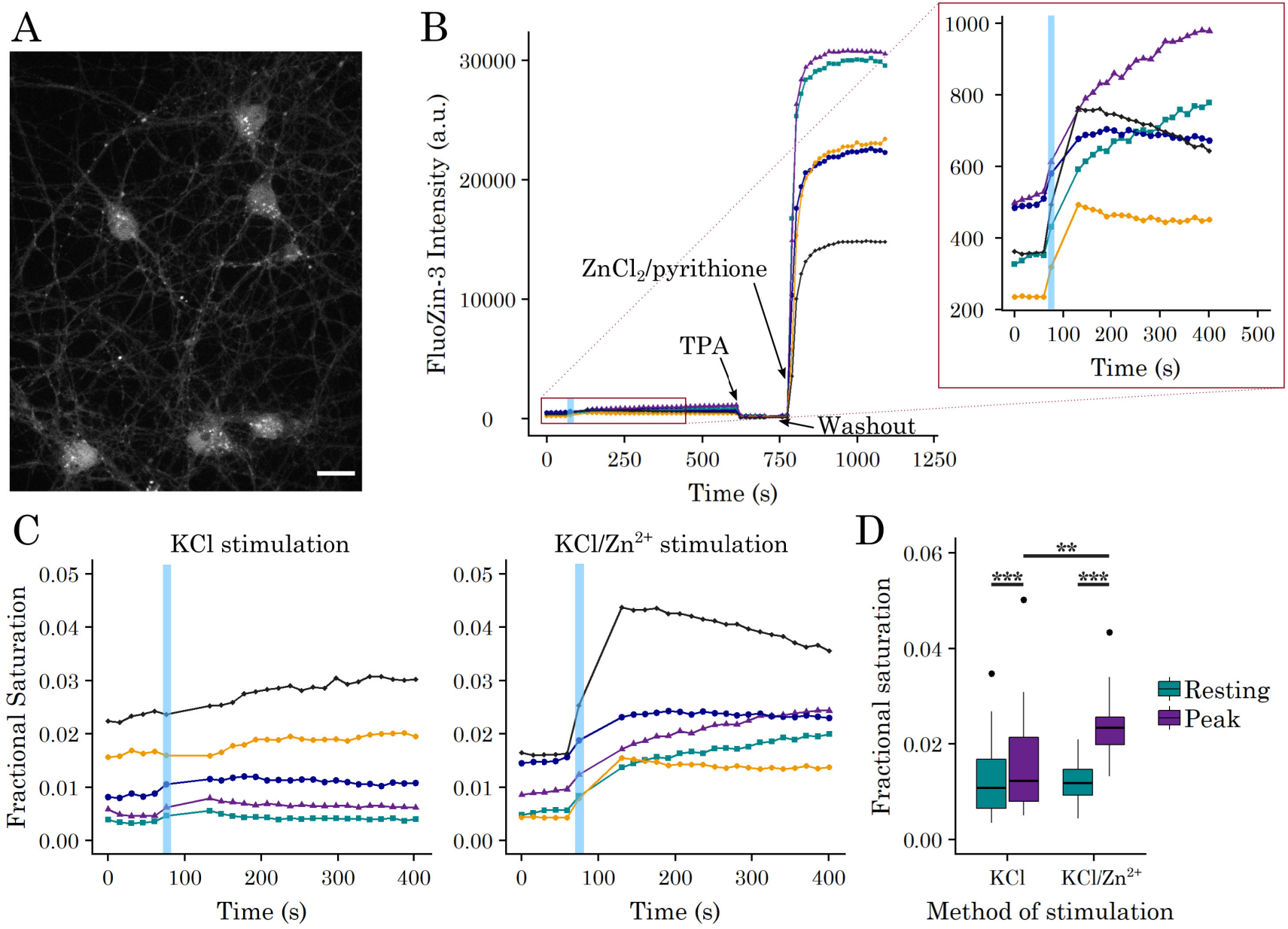
A
B
FluoZin-3 Intensity (a.u.)
30000
20000
10000
0
ZnCl2/pyrithione
TPA
Washout
0
250
500
750
1000
1250
Time (s)
1000
800
600
400
200
0
100
200
300
400
500
Time (s)
C
KCl stimulation
KCl/Zn2+ stimulation
Fractional Saturation
0.05
0.04
0.03
0.02
0.01
0.00
0
100
200
300
400
Time (s)
D
Fractional saturation
0.06
0.04
0.02
0.00
**
***
***
KCl
KCl/Zn2+
Method of stimulation
Resting
Peak

and found that we could reproduce the trend in expression for two of the three genes but the effects were not statistically significant due to small sample size (Figure 2.16).

We examined enrichment of gene ontology (GO) terms between KCl/Zn^{2+} and KCl stimulation conditions using both Gene Set Enrichment Analysis (GSEA) and the Functional Analysis tool in the DAVIDtools Suite (Figure 2.14C,D). GSEA measures whether genes in a gene set (related to a certain GO term, in this case) are distributed at random in a dataset ranked by fold change between two conditions, or whether the set genes are over-represented in either the upregulated or downregulated subsets of the dataset. In contrast, the DAVIDtools Functional Analysis tool can determine whether a certain GO term is related to more genes that are significantly upregulated than it is to genes in the genome at large. Both of these methods indicated that a larger Zn^{2+} signal upregulates expression of genes important for synaptic structure

Figure 2.12 (p. 34): Intracellular Zn^{2+} signal in stimulated neurons. (A) Image of neurons treated with FluoZin-3 AM after stimulation with KCl in the presence of 10 μM $ZnCl_2$. Scale bar = 10 μm. (B) Sample traces from a typical stimulation experiment. Each trace is derived from a region of interest within a different cell. 50 mM KCl stimulation was applied for 10 seconds (blue box) along with 10 μM $ZnCl_2$, followed by a washout period and further imaging. Samples were calibrated by addition of 10 μM Zn^{2+} chelator TPA and then 10 μM $ZnCl_2$/2.5 μM pyrithione in order to determine minimal and maximal signal for calculation of fractional saturation. Inset shows greater resolution for the time period around stimulation. Fluorescence intensity is background-corrected. (C) Sample traces from typical experiments described in (B), displayed as the calculated fractional saturation. Representative traces are shown for samples treated with KCl in the absence (left) or presence (right) of 10 μM extracellular $ZnCl_2$. For clarity, only the first 400 seconds are shown. (D) Box plot of FluoZin-3 fractional saturation levels at rest and at peak level after KCl stimulation with or without 10 μM extracellular $ZnCl_2$. n = 32 cells in 3 separate biological replicates for KCl stimulation alone and n = 18 cells in 3 separate biological replicates for the KCl/Zn^{2+} condition. Dots correspond to outliers, defined as points lying over (3^{rd} quartile + 1.5 × (interquartile range)). ***$p < 0.001$ or **$p < 0.01$ as assessed with a two-sided Wilcox Signed Rank test for paired data within conditions (KCl: test statistic V = 0, p = 4.6e-10; KCl/Zn^{2+}: test statistic V = 0, p = 7.6e-09) and a two-sided Mann-Whitney U unpaired test between the KCl and KCl/Zn^{2+} resting and peak conditions (test statistic W = 131, p = 0.0012). No significant difference between resting conditions was observed (test statistic W = 276, p = 0.818).

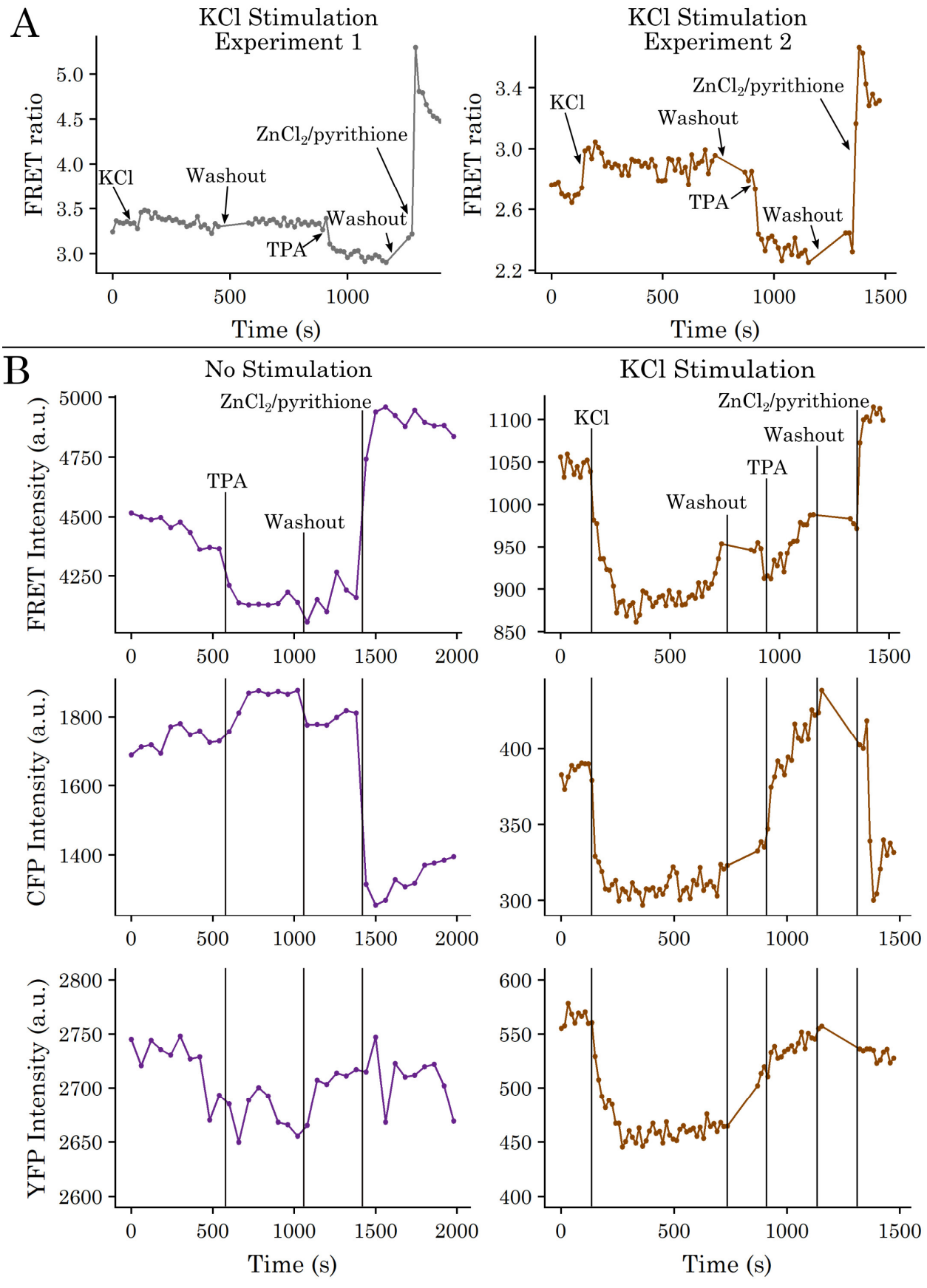
A
KCl Stimulation
Experiment 1
FRET ratio
KCl
Washout
ZnCl2/pyrithione
Washout
TPA
Time (s)
KCl Stimulation
Experiment 2
FRET ratio
KCl
Washout
ZnCl2/pyrithione
TPA
Washout
Time (s)
B
No Stimulation
KCl Stimulation
FRET Intensity (a.u.)
ZnCl2/pyrithione
TPA
Washout
KCl
CFP Intensity (a.u.)
YFP Intensity (a.u.)
Time (s)

and transmission (including *Grin2a*, *Nptn*, *Fgf13*, *Slc8a2*, *Nrxn3*, *Cnr1*, and *Grm7*), signal transduction (including *Pak7*, *Ptk2b*, *Epha4*, *Epha7*, and *Camk1d*), extracellular matrix reorganization (including *Serpine2*, *Tnr*, and *Tnc*), and cytoskeletal regulation (including *Nes*, *Dmd*, and *Arhgap35*), which corroborates observations that Zn^{2+} plays a role in neuronal plasticity.

We noted that the most upregulated gene observed upon stimulation with KCl/Zn^{2+} was ZnT3 (*Slc30a3*, Figure 2.14A), indicating that a larger Zn^{2+} signal induces neurons to shift Zn^{2+} homeostasis to expand their synaptic vesicle Zn^{2+} pool. *Slc39a10* (ZIP10), a plasma membrane-localized cytosolic Zn^{2+} importer, was also significantly upregulated, potentially allowing for more Zn^{2+} uptake from the extracellular space. In order to determine if other Zn^{2+}-binding genes were altered, we performed GSEA with gene sets related to Zn^{2+} or Zn^{2+}-binding, as derived from the Gene Ontology Consortium, the Protein Data Bank (PDB), or UniProt. None of these Zn^{2+}-related gene lists were enriched between any of our conditions, suggesting that the expression of most genes encoding for Zn^{2+}-binding proteins is not widely

Figure 2.13 (p. 36): Zn^{2+} FRET sensor experiments in KCl-stimulated neurons. (A) Two example experiments of FRET sensor recordings in neurons upon KCl treatment. Ratios correspond to the ratio of background-corrected FRET channel intensity to background-corrected CFP channel intensity in the cell body of one neuron per experiment. 50 mM KCl treatment induces a rise in FRET ratio in both experiments, and sensor in both cells subsequently responds to TPA-induced chelation of Zn^{2+} and addition of Zn^{2+}/pyrithione. (B) Example intensity traces from unstimulated (resting) and KCl-stimulated neurons. With no stimulation (left), exogenous Zn^{2+} perturbations induce reciprocal responses from FRET and CFP channels and little response in YFP fluorescence excited at 514 nm, which should be irresponsive to FRET changes. Upon KCl stimulation (right), fluorescence signals from all channels drop for the duration of the stimulation, then recover to normal levels. We have no data to indicate the cause of this behavior, although we suspect it may be due to fluorescent protein quenching by neuronal acidification upon KCl treatment. The FRET ratio data (A) supports FluoZin-3 AM experiments showing a rise in cytosolic Zn^{2+} upon depolarization with KCl. However, we were concerned about the unexpected decrease in the CFP, YFP and FRET channels upon KCl treatment (B), so we chose to use FluoZin-3 AM for quantification.

A

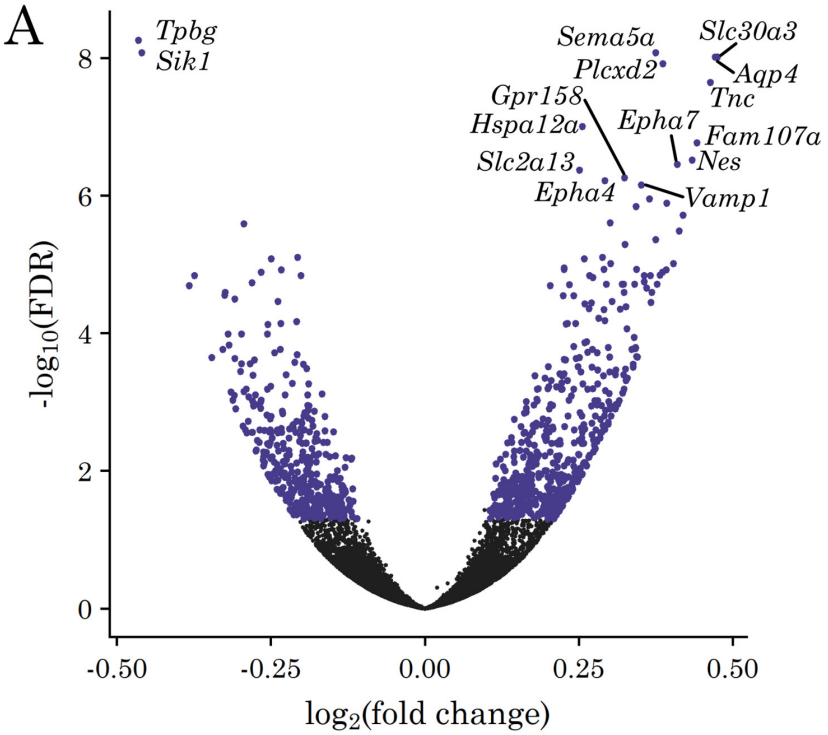

B

Condition comparison	Number of genes: Upregulated	Downregulated
KCl/Zn^{2+} vs. KCl	543	388
KCl/Zn^{2+} vs. KCl/TPA	183	99
KCl vs. KCl/TPA	0	0

C

Subset of enriched GO terms (GSEA analysis)	# genes in set	$-\log_{10}$(FDR)
Positive regulation epithelial cell regulation	138	1.4
Chemokine activity	33	1.3
Extracellular matrix binding	39	1.1
Glutathione transferase activity	33	1.1
Regulation of gliogenesis	83	1.1
Postsynapse	347	1.1
Neuron fate commitment	57	1.1
K^+ channel regulator activity	42	1.1
Intermediate filament organization	18	1.0
Excitatory synapse	178	1.0

D

Enriched GO terms, KCl/Zn^{2+} vs. KCl upregulated genes	$-\log_{10}$(FDR)
Chemical synaptic transmission	5.2
Long-term synaptic potentiation	3.6
Positive regulation GTPase activity	2.6
Cell adhesion	2.5
Signal transduction	2.3
Positive regulation synapse assembly	2.3
Positive regulation neuron projection development	1.7
Memory	1.7
Ion transmembrane transport	1.5
Learning	1.5
Response to drug	1.4
Positive regulation cell migration	1.4

Enriched KEGG pathways, KCl/Zn^{2+} vs. KCl upregulated genes	$-\log_{10}$(FDR)
cAMP signaling pathway	4.0
GABAergic synapse	3.5
Focal adhesion	3.4
Glutamatergic synapse	2.7
Retrograde endocannabinoid signaling	2.6
cGMP-PKG signaling pathway	2.1
Oxytocin signaling pathway	1.8
Proteoglycans in cancer	1.4
Enriched GO terms, KCl/Zn^{2+} vs. KCl downregulated genes	
Cholesterol biosynthetic process	4.6

altered after a mild, transient Zn^{2+} signal.

We observed several other interesting transcriptional targets of Zn^{2+} signaling, including an upregulation in several members of the MAPK pathway (*Mapk1*, *Mapk4*, *Fgfr3*, *Frs2*, *Rapgef2*, *c-Jun*) and *Fgf13*, a non-secretory growth factor that has several roles in axonal outgrowth and excitatory neurotransmission. In addition, Zn^{2+} induced transcription of many subunits of glutamate and gamma-aminobutyric acid (GABA) receptors (*Gria1*, *Gria2*, *Gria3*, *Grin2a*, *Grik4*, *Grm7*, *Gabra1*, *Gabra3*, *Gabra5*, *Gabrb3*, *Gabrd*, *Gabre*), providing further support that the observed Zn^{2+} signal may contribute to synaptic growth of both excitatory and inhibitory neurons.

The combination of imaging and sequencing data of dissociated hippocampal neurons following short KCl stimulation with or without extracellular Zn^{2+} indicates that a relatively small Zn^{2+} signal (~2-fold increase on the order of hundreds of pM) has significant and widespread effects on gene expression. Moreover, Zn^{2+}-dependent responses are involved in many processes that are essential to neuronal plasticity.

Figure 2.14 (p. 38): RNA-Seq of dissociated hippocampal neurons stimulated with and without Zn^{2+} or Zn^{2+}-specific chelator TPA. (A) Volcano plot of gene expression for all genes between KCl/Zn^{2+} and KCl stimulation conditions, providing measures of how much gene expression changed and the confidence in calling that gene differentially expressed. Positive fold changes indicate that genes were upregulated in the KCl/Zn^{2+} condition. The top 13 upregulated and 2 downregulated genes have been labeled (all genes with FDR < 10^{-6}). FDR = false discovery rate, a commonly used metric to assess significance among many hypothesis tests. Blue dots highlight all genes deemed significantly differentially expressed, with fold change magnitude > 0.1 and FDR < 0.05. (B) Number of genes differentially expressed in pairwise comparisons of conditions. (C) Gene Set Enrichment Analysis (GSEA) results examining whether sets of genes associated with certain human gene ontology terms are enriched among genes upregulated in the KCl/Zn^{2+} condition as compared to the KCl condition. These gene sets are a relevant subset of 50 gene sets found to be enriched with an FDR < 0.1. (D) Analysis of enrichment of GO terms and KEGG pathways between KCl/Zn^{2+} and KCl conditions as assessed using the DAVIDtools online functional annotation tool. Enrichment is assessed as terms/pathways being proportionally more associated with the differentially expressed genes than with the transcriptome as a whole. Listed terms and pathways were found to be enriched with FDR < 0.05. FDR = false discovery rate, GO = gene ontology, KEGG = Kyoto Encyclopedia of Genes and Genomes.

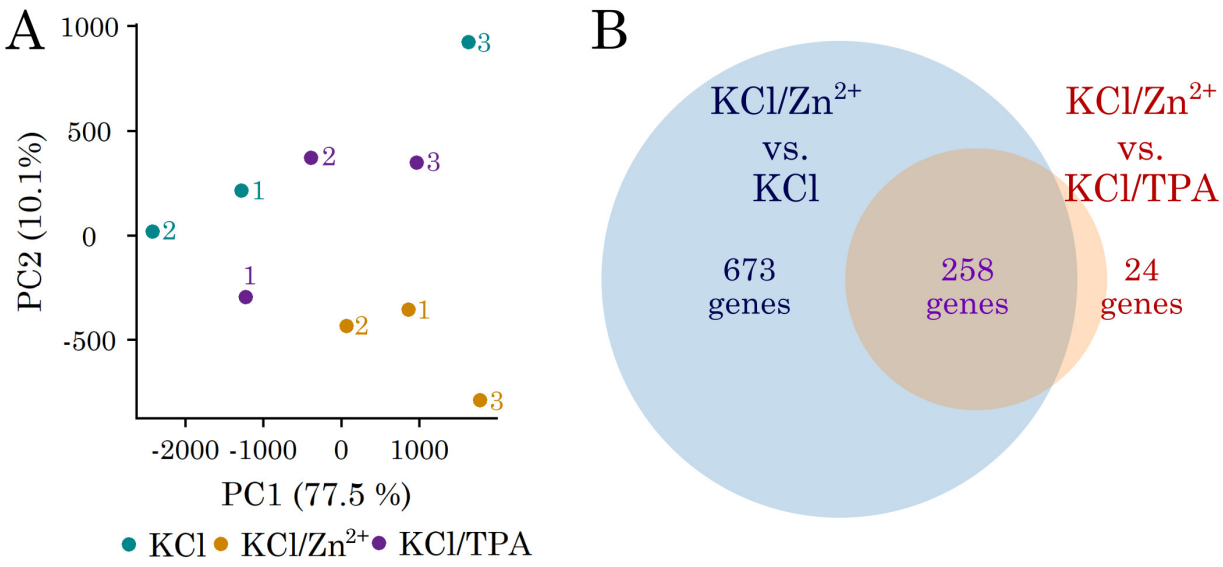

Figure 2.15: Comparison of all replicates and treatment conditions in RNA-Seq data. (A) Principle component analysis of all biological replicates in each condition. PC1 and PC2 together account for 87.6% of the variability among samples. Numbers correspond to replicate designations within conditions. Samples treated with KCl or KCl/TPA generally fall on a line distinct from the clustered KCl/Zn^{2+}-treated samples. One KCl/TPA replicate shows slightly more similarity to the KCl/Zn^{2+}-treated samples, which may be a mark of heterogeneity in Zn^{2+} status. This slightly higher variability among KCl/TPA replicates also explains the fewer number of genes called significant by DESeq2 when examining the KCl/Zn^{2+} vs. KCl/TPA comparison relative to the KCl/Zn^{2+} vs. KCl comparison, even when expression trends were similar. (B) Venn diagram of significantly differentially expressed genes between treatment comparisons. Differentially expressed genes were largely similar between treatment comparisons even though fewer were found to be significantly differentially expressed between KCl/Zn^{2+} and KCl/TPA treatments.

2.4 Discussion

In this work, we sought to characterize dissociated hippocampal cultures with respect to cytosolic and synaptic Zn^{2+}, quantify Zn^{2+} dynamics upon stimulation, and carry out an unbiased screen of the global changes in gene expression that result from Zn^{2+} dynamics to identify possible molecular players that underlie Zn^{2+}-dependent changes in neuronal functions and processes. In characterizing dissociated hippocampal neuron cultures with respect to synaptic Zn^{2+}, we showed that neurons

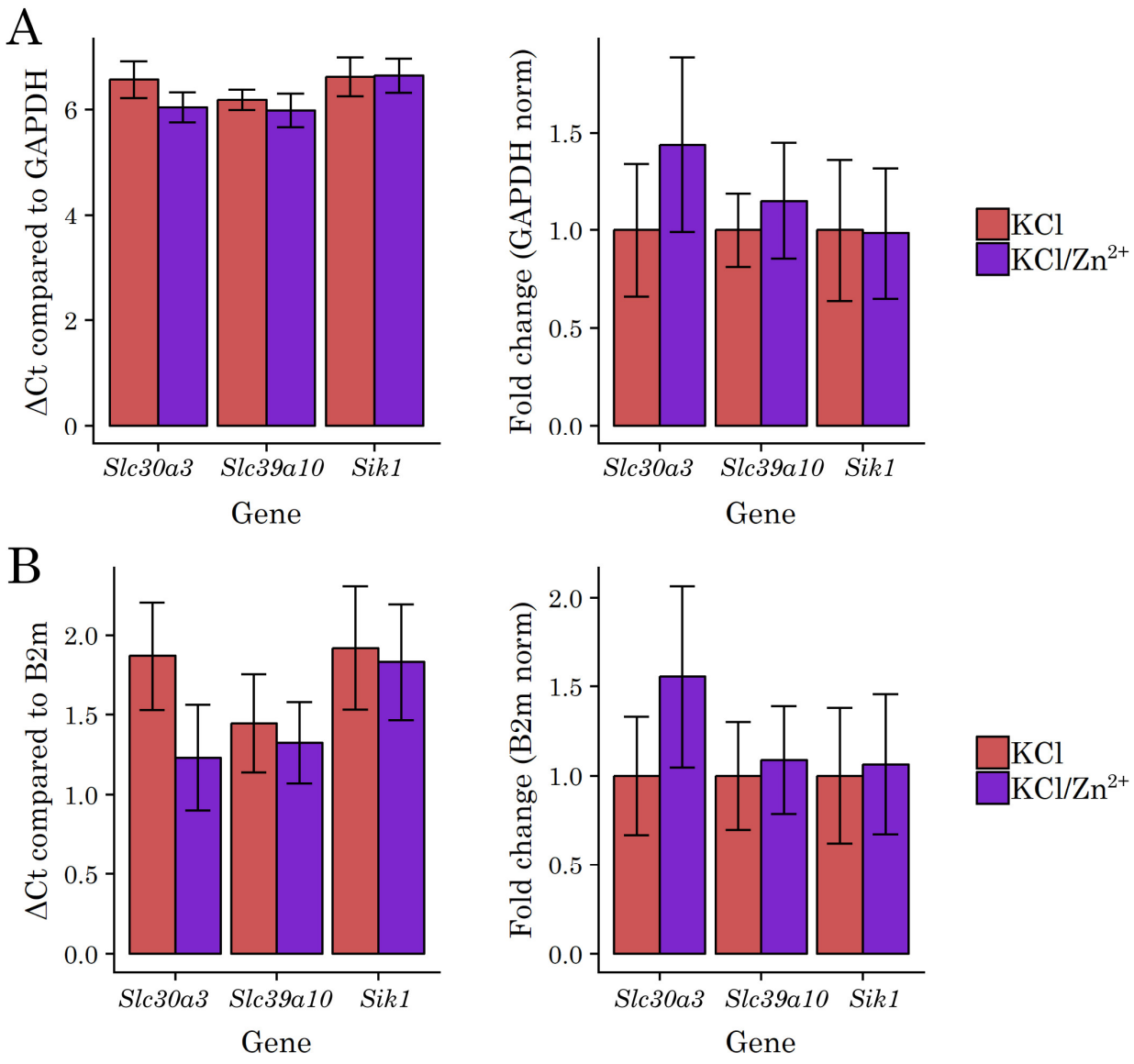

Figure 2.16: RT-qPCR of select hits from RNA-Seq experiment. ZnT3 and Zip10 were observed to increase upon KCl/Zn^{2+} treatment relative to KCl treatment in RNAseq, while Sik1 was observed to decrease. ΔCt values were generated by normalizing to GAPDH (A) or B2m (B) as an internal control, then fold changes were calculated with respect to KCl treatment. Each measurement comprises 3-4 technical replicates of each of 3 biological replicates derived from one neuron preparation. Error bars represent standard deviation of the data. Although ZnT3 and Zip10 are shown to be consistent with the direction and magnitude of changes shown in the RNA-Seq data, no samples are statistically significantly different, as the magnitude of changes are small and within error. We observed no change in Sik1 by RT-qPCR. Statistical significance was assessed by unpaired two-sided t-tests for unequal variances yielding the following statistics: GAPDH normalization, ZnT3 ($t = 1.63$, $p = 0.21$), Zip10 ($t = 0.29$, $p = 0.80$), Sik1 ($t = -0.05$, $p = 0.96$); B2m normalization, ZnT3 ($t = 2.86$, $p = 0.08$), Zip10 ($t = -0.12$, $p = 0.91$), Sik1 ($t = 0.20$, $p = 0.85$).

express and correctly localize the synaptic Zn^{2+} transporter ZnT3. However, despite using a variety of imaging tools, we were unable to determine whether the presence of this transporter actually promotes accumulation of Zn^{2+} in synaptic vesicles in dissociated neurons. These studies highlight the limitations of existing tools for defining synaptic Zn^{2+} in individual cells; the histological Timm stain did not provide sufficient contrast in isolated cells, small molecule membrane-permeable fluorescent dyes FluoZin-3 AM and SpiroZin-2 did not localize explicitly to synaptic vesicles, and extracellular probes FluoZin-3 and ZIMIR lacked sensitivity and did not yield reproducible results. These tool limitations do not provide definitive evidence that synaptic Zn^{2+} is absent from dissociated cultures. In contrast, using a different detection system, a recent study observed release of Zn^{2+} from stimulated cortical neurons and calculated the local synaptic Zn^{2+} concentration as approximately 100 nM[210], which is in accordance with previous estimates[204,208,212]. Although we could not definitively confirm the presence of synaptic Zn^{2+}, we were able to rigorously define the resting cytosolic labile Zn^{2+} concentration to be approximately 60 pM (using ZapCV2) to 110 pM (using FluoZin3 AM), and we observed a small transient rise in Zn^{2+} to roughly 150 pM upon depolarization with KCl. This transient rise in cytosolic Zn^{2+} was potentiated to approximately 220 pM when neurons were depolarized in the presence of 10 μM Zn^{2+}.

As the importance of Zn^{2+} in neurons has become more widely recognized, an increasing number of studies have focused on downstream effects of Zn^{2+} signaling, including the enhancement of long term potentiation (LTP)[354]. Several studies, however, have induced signaling changes with intensive exogenous Zn^{2+} conditions, such as 50–300 μM Zn^{2+} for time periods as long as 1 hour[337,341,502]. These conditions are likely to produce intracellular Zn^{2+} concentrations much higher than observed

physiologically *in vivo*, and have been shown to cause substantial cell stress and cell death[274,470,503].

We performed global mRNA sequencing on neurons under conditions that produced cytosolic Zn^{2+} signals that were in the sub-nanomolar range. Importantly, our results did not show an upregulation of stress-response genes, suggesting that this mild Zn^{2+} increase does not induce neuronal stress. We did observe that a subtle Zn^{2+} signal induced a significant upregulation of genes related to neurite growth and synaptic function, including many neurotransmitter receptor subunits and the Zn^{2+} transporter ZnT3. Interestingly, while Zn^{2+} has been well documented to alter the immediate responses of glutamate and GABA receptors[208,302,504,505] and has been implicated in modulating LTP in a number of electrophysiology experiments[208,242,302,354,489], to our knowledge no studies have documented a transcriptional component of Zn^{2+}-dependent synaptic regulation. It is unclear to what extent the induced intracellular Zn^{2+} signal reflects *in vivo* neuronal Zn^{2+} signals; however, our results suggest that sub-nanomolar increases in cytosolic Zn^{2+} have the potential to alter the expression of genes that have been implicated in late-phase LTP.

Another intriguing gene that was upregulated by Zn^{2+} in our neuron cultures encodes the protein FGF13, a growth factor that is highly expressed in developing cortical and hippocampal neurons. FGF13 has two main known functions. The first is that FGF13 polymerizes and stabilizes microtubules at axon growth cones[506–508], and in this capacity FGF13 upregulation contributes to the observed Zn^{2+}-dependent neurite growth induction. The second is that FGF13 limits the membrane presentation of voltage-gated sodium channels in dendritic spines, and knockout of the *Fgf13* gene leads to greater excitatory potentials and epilepsy[509,510]. ZnT3

knockout mice, which lack synaptic Zn^{2+}, are also prone to acute seizures[423,426], and while there are many potential links between Zn^{2+} and epilepsy[511], FGF13 may provide an example of how Zn^{2+}-dependent transcription could modulate neuron excitability.

Our results indicate that a transient Zn^{2+} signal has transcriptional effects in neurons. One signaling pathway likely to be involved is the MAPK pathway, which has previously been shown to be activated by Zn^{2+} [115,332,337]. We found that key components of the pathway (*Mapk1*, *Mapk4*) were upregulated upon increased cytosolic Zn^{2+}, along with other associated factors (*Epha4*, *Ephb1*, *Fgfr3*, *Rapgef2*) that have been shown to play important roles in neurite growth, branching, and guidance[512–515]. Additionally, the downstream transcription factor c-Jun (*Jun*) was significantly upregulated, although we saw no significant difference in expression of any of its binding partners (*Fos*, *FosB*, *Fosl1*, *Fosl2*, *Junb*, *Jund*)[516]. c-Jun has been implicated in signaling for axon regeneration and neuron apoptosis, but we did not observe any significant difference in expression among any of the genes normally coexpressed with *Jun* in either phenotype (*Mapk8*, *Mapk9*, *Mapk10*, *Gap43*, *Atf2*, *Atf3*, *Smad1*)[517–520]. Thus, although it seems likely that Zn^{2+} activates the MAPK pathway, which may then affect Zn^{2+}-dependent transcription through c-Jun, the mechanisms underlying these steps still require further study.

In summary, our global RNA-Seq results suggest that sub-nanomolar Zn^{2+} signals are sufficient to significantly alter gene expression in a relevant model system. Moreover, in neurons these gene expression changes correlate to physiological changes that are consistent with previous observations of the effect of Zn^{2+} on neuronal signaling.

2.5 Materials and methods

2.5.1 Neuron isolation/culture

Dishes/slides were coated overnight with 1 mg/mL Poly-D-lysine hydrobromide in 15 mM sodium borate. Glass slides for imaging were washed thoroughly and coated in 50 μM iMatrix-511 (Clontech) until neuron plating.

All animal work was approved by the Institutional Animal Care and Use Committee of CU Boulder, protocols #1407.01 and #2547 and performed in accordance with the relevant guidelines and regulations. E18 rat hippocampi were either isolated from animals or ordered from BrainBits, LLC. For animal isolation, timed pregnant Sprague Dawley rats were obtained from Charles River Laboratories. Pregnant rats were sacrificed with carbon dioxide and fetal brains were micro-dissected to isolate hippocampi. Pooled hippocampi were washed with digestion medium (1X HBSS, 10 mM HEPES, 5 μg/mL gentamicin, pH 7.2) and digested 30 min in digestion medium containing 20 U/mL papain (Worthington). Samples were then washed with plating medium (MEM, 5% FBS, 0.6% wt/vol glucose) and dissociated by sequentially passing 5–10 times through full-diameter, then half-diameter flame-polished Pasteur pipets. Cells were plated on treated slides at a density of 20,000 cells/cm^2 for imaging. Cells intended for RNA isolation were plated on treated dishes at a density of 60,000 cells/cm^2. Cells were fed 3–4 hours after plating with glial-conditioned neuron culture medium (Neurobasal Medium, 2% B27 supplement, 0.3x GlutaMAX supplement, all obtained from Thermo Fisher), and ½ media was replaced on day *in vitro* (DIV) 3, DIV 6, and DIV 13. Cultures were treated with 4 μM cytosine arabinoside from DIV 3 to DIV 6 to restrict mitotic cell proliferation. Cultures were grown in a cell culture incubator at 37 °C and 5% CO_2.

Glial cells were isolated from neonatal cortical tissue collected from neonatal rats sacrificed by decapitation with sharp scissors. Cells were dissociated as with hippocampal samples, then plated on standard cell culture dishes. Cells were fed initially and every 3–4 days with glial medium (DMEM, 5% FBS, 0.5% pen/strep) until confluent. To generate glial-conditioned medium, neuron culture medium was added to confluent glial cultures for one day, then filtered through a 0.20 μm filter prior to addition to neurons.

2.5.2 Materials

Genetically encoded Zn^{2+} Förster Resonance Energy Transfer (FRET) sensor NES-ZapCV2 was used for all resting cytosolic Zn^{2+} measurements (see RRID:Addgene_112060[521]). Sensor was either transfected 2 days prior to imaging with Lipofectamine 3000 (Thermo Fisher) according to the manufacturer's protocol, or nucleofected prior to neuron plating with a Lonza Nucleofector 2b instrument using the Rat Neuron Nucleofector Kit (Lonza) protocol. Nucleofected sensor remained fluorescent in cultures through DIV 12–13.

The following fluorescent small molecule dyes were obtained from Thermo Fisher: FluoZin-3, FluoZin-3 AM, and FM 4–64. Stock solutions of FluoZin-3 and FluoZin-3 AM were prepared at 1 mM in DMSO. Stock solutions of FM 4–64 were prepared at 5 mg/mL in water. The small molecule dye ZIMIR was obtained from VitalQuan, and stock solutions were prepared at 1 mM in DMSO.

The Zn^{2+}-specific chelator tris(2-pyridylmethyl)amine (TPA), $ZnCl_2$, chelex, and the ionophore 2-mercaptopyridine *N*-oxide (pyrithione) were purchased from Sigma-Aldrich. TPA stock solutions were prepared at 20 mM in DMSO. $ZnCl_2$ stock solutions were prepared at 1 mg/mL in water treated overnight with chelex. Pyrithione stock

solutions were prepared at 5 mM in DMSO.

For synaptic vesicle dye loading experiments, glutamate receptor antagonists 6-Cyano-7-nitroquinoxaline-2,3-dione (CNQX) and D-(−)-2-Amino-5-phosphonopentanoic acid (D-AP5) were purchased from Abcam. CNQX stock solutions were prepared at 5 mM in DMSO, while D-AP5 stock solutions were prepared at 50 mM in water. For dye quenching, advasep-7 (Biotium) was dissolved in water at a stock concentration of 100 mM.

Primary antibodies and peptide controls were purchased from Synaptic Systems: anti-ZnT3 (RRID:AB_2189665), anti-Homer1 (RRID:AB_887730), anti-Synapsin (RRID:AB_1106784), ZnT3 peptide (#197-0P). Secondary antibodies were obtained from Thermo Fisher: anti-mouse AF488 (RRID:AB_2534088), anti-guinea pig AF488 (RRID:AB_2534117), anti-rabbit AF568 (RRID:AB_2534017), anti-mouse AF594 (RRID:AB_2534091).

Resting neuron imaging media (RNIM) was formulated as follows: 145 mM NaCl, 3 mM KCl, 1.5 mM $CaCl_2$, 1 mM $MgCl_2$, 10 mM HEPES, 10 mM glucose, pH 7.4. High-potassium neuron imaging media (KNIM) was made as a 2X K^+ solution (51 mM NaCl, 97 mM KCl, 1.5 mM $CaCl_2$, 1 mM $MgCl_2$, 10 mM HEPES, 10 mM glucose, pH 7.4), which when added 1:1 to RNIM gave concentrations of 98 mM NaCl and 50 mM KCl. All media was prepared in chelex-treated water.

2.5.3 Equipment

Samples for all imaging experiments were imaged on a Nikon Ti-E spinning disc confocal microscope equipped with Nikon Elements software, Ti-E perfect focus system, Yokogawa CSU-X1 spinning disc head, Andor 888 Ultra EMCCD camera and Oko Labs enclosed environmental chamber set at 37 °C.

Samples for each type of imaging experiment except immunofluorescence experiments were also imaged on a Nikon Ti-E widefield microscope equipped with Nikon Elements software, Ti-E perfect focus system, Andor iXon3 EMCCD camera, Sutter Instruments LD-LS/30 xenon arc lamp, and Sutter Instruments Lambda 10-3 filter changer.

For electrical stimulation, an IonOptix Myopacer cell stimulator was equipped with a custom set of platinum wire electrodes. Stimulations were performed with 30 V bipolar waveform 10 ms pulses at 5 Hz for a duration of 1 minute, unless specified otherwise.

RNA extraction for next-generation sequencing was performed using a Promega Maxwell RSC Instrument.

Quantitative PCR was performed using a BIO-RAD CFX384 Real Time PCR Detection System instrument.

2.5.4 *In vitro* K_d determination

Protein purification, *in vitro* fluorescence measurements at different Zn^{2+} concentrations, and fitting to determine apparent sensor K_d were done exactly as described previously[152], with the exception that emission fluorescence intensities at 475 nm were used for λ_1 values rather than intensities at 481 nm. Fits were determined based on data from 11 titration experiments.

2.5.5 Intracellular FRET sensor calibrations

Measurements were taken on the Nikon spinning disc confocal microscope using CFP (445 nm excitation, 482/35 nm emission) and FRET (445 nm excitation, 540/30 nm emission) channels, acquiring images with a 40X (NA 0.95) air objective at 300 ms exposure, EM multiplier 300, 10 MHz camera readout speed, 20% laser power,

and binning pixels 2 × 2. Measurements were also taken on the Nikon widefield microscope using CFP (434/16 nm excitation and 470/24 nm emission) and FRET (434/16 nm excitation and 535/20 nm emission) channels, acquiring images with a 20X (NA 0.75) or 40X (NA 0.95) air objective at 4–600 ms exposure, EM multiplier 300, 1 MHz camera readout speed, with a neutral density filter (ND8) restricting lamp light to 12.5% maximum.

Neuron cultures (DIV 10–14) were washed and put in RNIM at least ten minutes prior to imaging. Baseline measurements were obtained for 5–15 minutes. Calibrations were performed by adding 10 μM TPA for 2–5 minutes, followed by wash out with RNIM and addition of 10 μM $ZnCl_2$/0.5–2 μM pyrithione. Measurements were taken for several minutes after a maximum FRET ratio was reached. For KCl stimulation experiments, KNIM was mixed 1:1 with RNIM and measurements were taken for 400–600 seconds before washing out with RNIM and performing a calibration as above.

2.5.6 Synaptic vesicle dye loading

Cultures were imaged on the Nikon spinning disc confocal microscope using GFP (FluoZin-3: 488 nm excitation, 525/50 nm emission) and GFP/RFP (FM 4–64: 488 nm excitation, 620/60 nm emission) channels, acquiring images with a 100X (NA 1.45) oil objective at 300 ms exposure, EM multiplier 300, 10 MHz camera readout speed, and 15–20% laser power. Measurements were also taken on the Nikon widefield microscope using GFP (FluoZin-3: 480/20 nm excitation and 500/20 nm emission) and GFP/RFP (FM 4–64: 480/20 nm excitation and 610/50 nm emission) channels, acquiring images with a 60X (NA 1.40) oil objective at 300 ms exposure, EM

multiplier 300, 1 MHz camera readout speed, with a neutral density filter (ND4) restricting lamp light to 25% maximum.

Neuron cultures (DIV 10–14) were incubated for 2 minutes in RNIM containing 5 μg/mL FM 4–64, 5–50 μM FluoZin-3, 10 μM CNQX, and 100 μM D-AP5. Without changing media, cultures were electrically stimulated for 1 minute, then incubated 5 minutes to accommodate compensatory endocytosis. Cells were washed twice and incubated in RNIM containing 1 mM advasep-7, 10 μM CNQX, and 100 μM D-AP5 to quench extracellular dye.

RNIM containing 50 μM $ZnCl_2$ was added to some cultures to attempt to visualize vesicles. Cultures were also further stimulated to visualize dye exocytosis with electrical stimulation, KNIM, or RNIM containing 50 μM glutamate. For positive controls, 10 μM $ZnCl_2$ was included in the initial loading solution to pre-load FluoZin-3 with Zn^{2+} before endocytosis.

2.5.7 Imaging Zn^{2+} release with ZIMIR

Cultures were imaged on the Nikon spinning disc confocal microscope using a GFP channel (488 nm excitation, 525/50 nm emission), acquiring images with a 100X (NA 1.45) oil objective at 200 ms exposure, EM multiplier 300, 10 MHz camera readout speed, and 20% laser power. Images were also acquired with a 40X (NA 0.95) air objective at 300 ms exposure, EM multiplier 300, 10 MHz camera readout speed, and 20% laser power. Some measurements were taken on the Nikon widefield microscope using a GFP channel (480/20 nm excitation and 500/20 nm emission), acquiring images with a 40X (NA 0.95) air objective at 200 ms exposure, EM multiplier 300, and a 1 MHz camera readout speed, or with a 60X (NA 1.40) oil objective at 200 ms

exposure, EM multiplier 300, 1 MHz camera readout speed, with a neutral density filter (ND4) restricting lamp light to 25% maximum.

Neuron cultures (DIV 10–14) were incubated for 20–30 minutes in 5 μM ZIMIR, then washed and imaged immediately. Electrical stimulation was applied, with stimulation protocols varied. The two most commonly used protocols were 30 V bipolar waveform 10 ms pulses at 10 Hz for a duration of 1–2 seconds, or 40 V bipolar waveform 10 ms pulses at 20 Hz for a duration of 10 seconds. Dye responsiveness was assessed by adding 10 μM TPA for 2–5 minutes, then washing out with RNIM and adding 10 μM $ZnCl_2$. In some cases, 10 μM $ZnCl_2$ was added to normal culture media for 0.5–48 hours prior to imaging, then washed out before dye incubation.

2.5.8 Intracellular Zn^{2+} measurements with FluoZin-3 AM

Measurements were taken on the Nikon spinning disc microscope using a GFP channel (488 nm excitation, 525/50 nm emission), acquiring images with a 40X (NA 0.95) air objective at 300 ms exposure, EM multiplier 300, 10 MHz camera readout speed, and 15% laser power.

Neuron cultures (DIV 10–14) were washed and incubated at room temperature in RNIM containing 5 μM FluoZin-3 AM for 30 minutes. Samples were washed in RNIM. Baseline measurements were obtained for 1 minute. Cells were then stimulated with a 10 second treatment of high K^+ by mixing KNIM 1:1 with the RNIM already present. After 10 seconds, cultures were washed 3x with RNIM and measurements taken for 15 minutes. Calibrations were performed by adding 10 μM TPA for 2 minutes, then washing out with RNIM and adding 10 μM $ZnCl_2$/0.5 μM pyrithione. Measurements were taken until several minutes after a maximum signal was observed.

2.5.9 Image analysis

FRET sensor, ZIMIR, and FluoZin-3 AM imaging experiments were analyzed with a custom MATLAB script that imports ND2 experiment files, extracts metadata, registers images, allows for manual background and cell ROI selection, and generates raw and background-subtracted average intensity measurements. FRET ratios were calculated as background-subtracted (FRET fluorescence)/(CFP fluorescence). FRET and FluoZin-3 AM calibration data were manually inspected to obtain minimum and maximum values for FRET ratios or intensity measurements, which were used to calculate fractional saturation according to the formula:

$$FS = \frac{X - F_{min}}{F_{max} - F_{min}}$$

where X is the basal or peak measurement and F_{min} and F_{max} are the minimum and maximum values of either the FRET ratio (for FRET measurements) or background-subtracted fluorescence intensity (for FluoZin-3 AM measurements). Fractional saturation was converted to an approximate intracellular Zn^{2+} concentration according to the formula:

$$[Zn^{2+}] = \frac{K_d}{\left(\frac{1}{FS} - 1\right)^{\frac{1}{n}}}$$

where K_d is the sensor dissociation constant, FS is fractional saturation as defined above, and n is the Hill coefficient (assumed to be 1 for FluoZin-3 AM).

Immunofluorescence (IF) images were decomposed by channel. Using MATLAB, images of multi-channel fluorescent beads or IF images of Homer1 and ZnT3 (594 nm secondary antibody) at DIV 6 were registered to correct for spectral anomalies between channels, then resulting registration parameters were applied to all IF images by channel. Integrated intensities were calculated on raw fluorescence of

registered images, or on images subjected to adaptive thresholding according to the built-in MATLAB function `adaptthresh` (`sensitivity = 0.25`). Two-dimensional correlation coefficients were calculated on raw fluorescence intensities of registered images using the built-in MATLAB function `corr2`.

2.5.10 RT-qPCR

For ZnT3 analysis over time, neurons at DIV 0 (extraction day) (1 replicate), DIV 1 (1 replicate), DIV7 (2 replicates), DIV 10 (2 replicates), DIV 14 (2 replicates), DIV 17 (1 replicate), and DIV 21 (1 replicate) were lysed and RNA extracted according to the Qiagen RNeasy kit protocol (Qiagen). RNA was reverse transcribed according to Protoscript II Reverse Transcriptase protocol (New England BioLabs), and quantitative PCR was performed with the TaqMan Fast Advanced Master Mix and gene-specific TaqMan assays (Applied Biosystems) according to the standard master mix protocol. TaqMan assays analyzed were Rn01472608_m1 (ZnT3), Rn01462662_g1 (GAPDH), and Rn00560865_m1 (Beta-2-microglobulin). 3–4 technical replicates were performed per sample. PCR cycle conditions were as follows: 50 °C, 2 min; 95 °C, 2 min; (95 °C, 3 s; 60 °C, 30 s) ×40 cycles.

For RNA-Seq validation analysis, neurons at DIV 14 were incubated in a 1:1 solution of RNIM/KNIM for 10 seconds, with and without the addition of 10 μM $ZnCl_2$. Each of the two conditions was performed in triplicate. After treatment, samples were placed back in the neuron culture media and incubated for 90 minutes at 37 °C and 5% CO_2. RNA extraction and reverse transcription were performed as in the previous paragraph. Quantitative PCR was performed with the TaqMan Fast Advanced Master Mix and gene-specific TaqMan assays (Applied Biosystems) according to the standard master mix protocol. TaqMan assays analyzed were Rn01472608_m1

(ZnT3), Rn01771489_m1 (ZIP10), Rn01429325_m1 (Sik1), Rn01462662_g1 (GAPDH), and Rn00560865_m1 (Beta-2-microglobulin). 3–4 technical replicates were performed per sample. Cycle conditions were as in the previous paragraph.

2.5.11 Immunofluorescence (IF)

Cultures were prepared for IF at DIV 1, 7, 10, 14, 17, and 21. Samples were fixed for 10 minutes in PBS/3.7% paraformaldehyde, then quenched in PBS/20 mM NH_4Cl for 5 minutes. Samples were blocked in PBS/10% goat serum for 30 minutes. Antibodies were diluted in PBS/2% goat serum. Samples were incubated with primary antibodies overnight and secondary antibodies for 30 minutes, with 4 × 10-minute washes between incubations. Samples were imaged on the Nikon spinning disc confocal microscope using a 100X (NA 1.45) oil objective.

Anti-ZnT3 was used as a 1:100 dilution of 1 mg/mL stock solution, and anti-Homer1 and anti-Synapsin were used as 1:200 dilutions of 1 mg/mL stock solutions. For ZnT3 peptide controls, 2.5 µg ZnT3 antibody was pre-incubated with 6 µg ZnT3 control peptide for 20 minutes prior to sample incubation. Secondary antibodies were used as 1:1000 dilutions of 2 mg/mL stock solutions.

2.5.12 Timm's stain

Neuron cultures were stained at DIV 10–14. Subsets of samples were treated prior to staining with 20–40 µM $ZnCl_2$ for 20 minutes, or with 20 µM $ZnCl_2$/2.5 µM pyrithione for 8 minutes. Samples were washed and incubated for 2 minutes in sulfide solution (0.027% Na_2S dissolved in 82 mM Tris, pH 8), then washed and fixed for 10 min in PBS/3.7% paraformaldehyde and quenched for 5 min with PBS/20 mM NH_4Cl. Samples were developed for 1 hour in developing solution prior to imaging. Developing solution was formulated by mixing aqueous solutions A (5.7 mM $AgNO_3$),

B (2% citric acid, 0.8% hydroquinone), and C (10.7% gum arabic) in the volume ratio 65:50:7 (A:B:C).

2.5.13 Sequencing and computational pipeline

Neuron cultures (DIV 14) were placed at room temperature. Media was removed and neurons incubated in a 1:1 solution of RNIM/KNIM for 10 seconds, with and without the addition of 10 μM $ZnCl_2$ or 10 μM TPA. Each of the three conditions (Stimulation, stimulation + $ZnCl_2$, stimulation + TPA) was performed in triplicate. After treatment, samples were placed back in the removed neuron culture media and incubated for 90 minutes at 37 °C and 5% CO_2. Cells were lysed and RNA extracted according to the Promega Maxwell RSC simplyRNA isolation kit. Libraries were generated according to the Bioo NextFlex Dir RNA kit and sequenced on an Illumina NextSeq 500 using a high-output 2 × 75 paired-end protocol.

Rat reference genome files (rn6), including genome fasta file and gtf gene annotation file, were downloaded from Illumina iGenomes (https://support.illumina.com/sequencing/sequencing_software/igenome.html) on 7/31/2017.

Quality control of de-multiplexed fastq files was performed using fastQC (v0.11.2, https://www.bioinformatics.babraham.ac.uk/projects/fastqc/). The first ten bases of all reads were trimmed from each separate fastq file in a single-end fashion with trimmomatic (v0.32)[522] and resulting fastq files were mapped in a paired-end fashion with tophat2 (v2.0.6, bowtie2 v2.0.2)[523] using parameters `--b2-very-sensitive -r 110 --mate-std-dev 180` and including the rn6 genes GTF file. Resultant BAM files were indexed with samtools (v0.1.18)[524].

The featureCounts function within the R package Rsubread (v1.24.2, R v3.3.0)[525]

was used to generate gene-level read counts, with parameters `GTF.featureType="exon"`, `GTP.attrType="gene_id"`, `useMetaFeatures=TRUE`, `allowMultiOverlap=FALSE`, `largestOverlap=FALSE`, `strandSpecific=2`, `isPairedEnd=TRUE`, `requireBothEndsMapped=TRUE`, `checkFragLength=TRUE`, `minFragLength=50`, `maxFragLength=60000`, `countChimericFragments=FALSE`. Differential expression analysis was performed pairwise between conditions with the R package DESeq 2 (v1.14.1, R v3.3.0)[526]. Differentially expressed genes were filtered according to a false discovery rate (p_{adj}) < 0.05, split into upregulated and downregulated genes, and analyzed with the DAVIDtools Functional Annotation Tool using default parameters (v6.8, https://david.ncifcrf.gov/)[527,528].

For GSEA analysis, gene level counts were normalized to transcripts per million (TPM). GSEA (v3.0, http://software.broadinstitute.org/gsea/index.jsp)[529,530] was then run on the TPM file with default parameters except for the following: `Collapse dataset to gene symbols = false`, `Permutation type = gene_set`, `max set size = 3000`, `min set size = 5`. Gene sets were downloaded from the Broad Institute Molecular Signatures Database (v6.2, http://software.broadinstitute.org/gsea/msigdb/index.jsp), collection C5 (GO gene sets). Gene sets for Zn^{2+}-related genes were manually curated from mouse species-filtered searches of (1) the Gene Ontology Consortium (http://www.geneontology.org/) for genes annotated with the terms “zinc ion transport”, “cellular zinc ion homeostasis”, “response to zinc ion”, “zinc ion transmembrane transport”, or “zinc ion binding”, (2) the Protein Data Bank (https://www.rcsb.org/) for all structures containing ZN, and (3) UniProt (https://www.uniprot.org/) for “zinc”.

Principal component analysis was performed on samples based on gene-level TPM values with the built-in R function prcomp (R v.3.5.1).

2.5.14 Statistical analysis and plotting

All statistical tests were performed in R (v3.5.1), and are detailed in individual figure legends. For comparison of Zn^{2+} responses to stimulation, two-sided Wilcox Signed Rank tests and two-sided Mann-Whitney U tests were used due to non-normality of original data (as assessed by a Shapiro Wilk test). Statistical tests assessing significance of differential expression were performed by the DESeq2 package, which accounts for multiple hypothesis testing corrections. Statistical tests assessing significance of GO term enrichment results were performed by the GSEA and DAVIDtools algorithms and accounted for multiple hypothesis testing corrections.

All fits and plots were generated with R (v3.5.1), using the packages ggplot2 (v3.0.0), ggrepel (v0.8.0), reshape2 (v1.4.3), extrafont (v0.17), and cowplot (v0.9.3).

2.5.15 Data availability

All raw next-generation sequencing data files and processed data files used to draw conclusions are available at the Gene Expression Omnibus, data series GSE126841.

(This page intentionally left blank)

Chapter 3

Determination of intracellular Zn^{2+} dynamics and Zn^{2+}-dependent signaling upon diverse neuronal stimulations

3.1 Publication status and author contributions

This work is unpublished. Lynn Sanford and Amy Palmer designed the study and wrote the manuscript. L.S. collected and analyzed all imaging and sequencing data.

3.2 Introduction

The pathology of many brain injuries and neurodegenerative diseases is related to the process of excitotoxicity, whereby neuronal signaling is dysregulated and excess glutamate is released at excitatory synapses[531]. The greater abundance of glutamate then causes imbalances in glutamate receptors and calcium signaling of surrounding neurons, causing accumulation of reactive oxygen and nitrogen species (ROS/RNS) and inducing stress-response pathways and/or apoptosis[532]. Furthermore, endoplasmic reticulum (ER) stress has also been observed in neurons upon a variety of insults[533–536]. Although there is some indication that ROS-induced calcium imbalances may be responsible for ER stress, the link between these two different stressors is still unclear[534,537].

High levels of intracellular Zn^{2+} have long been known to contribute to excitotoxicity in ischemic conditions[450,456,462], as well as to exacerbate neuronal stress and death in several neurodegenerative diseases[538–540]. Many different ROS/RNS,

whether generated by Ca^{2+}-induced activity of NADPH oxidase (NOX) or exogenously applied, can liberate Zn^{2+} from intracellular stores, particularly the Zn^{2+}-buffering metallothioneins[456,458,468,541–545]. Zn^{2+} has then been shown to enter mitochondria and inhibit respiratory and anti-oxidant enzymes[546,547], or to inhibit the recovery of Ca^{2+} homeostasis[458,468], both of which intensify oxidative stress and often induce apoptotic pathways. Some research has also proposed a correlation between Zn^{2+} and ER stress in a non-glutamatergic neuronal cell line, although no causal link has been shown[548].

In this study, we aimed to characterize Zn^{2+} signals in dissociated hippocampal neurons upon different types of stimulation. We found that glutamate and field electrical stimulation induced larger Zn^{2+} responses than KCl, and these responses were often heterogeneous in magnitude and duration. The differences in Zn^{2+} were unrelated to the extent of acidification in these neurons. We characterized transcriptional responses to glutamate during different Zn^{2+} perturbations using RNA-Seq, and while we saw heterogeneity in our samples, we did identify significant upregulation of ER stress response pathways in cells that exhibited greater Zn^{2+} signals. High-throughput phosphoarray analysis also provided evidence that Zn^{2+} may induce anti-apoptotic stress responses. While it is unclear whether Zn^{2+} is augmenting glutamate-induced ER stress or is involved in the response to that stress, this work confirms Zn^{2+} as a key component of excitotoxic stress.

3.3 Results

3.3.1 Quantification of Zn^{2+} signals upon different neuronal stimulations

To determine how Zn^{2+} dynamics differ depending on stimulation method, we applied KCl, glutamate, and field electrical stimulation to dissociated mouse hippocampal neuron cultures and imaged Zn^{2+} with FluoZin-3 AM. All of these

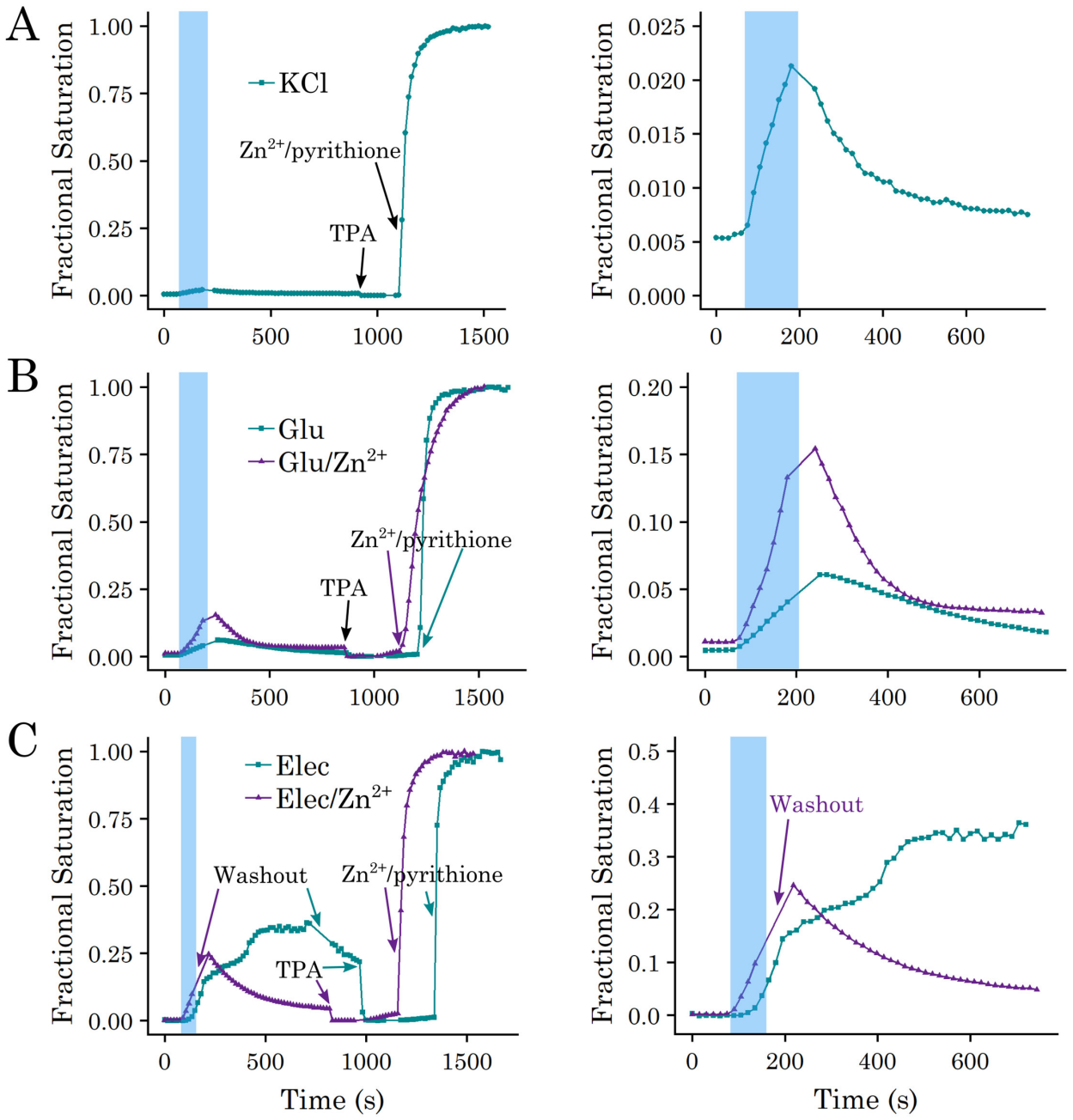

Figure 3.1: Representative FluoZin-3 AM stimulation experiments to measure cellular Zn^{2+}. Fractional saturation of FluoZin-3 is shown as determined by the full calibration shown in the left panel of each section, wherein stimulation (blue box) was followed by a period of recovery before addition of 10 μM TPA to measure minimum FluoZin-3 signal, then addition of 10 μM $ZnCl_2$/0.5 μM pyrithione to achieve maximum FluoZin-3 signal. Right-hand panels show larger views of the first 750 seconds of each experiment. FluoZin-3 responses are lowest upon KCl stimulation (A), higher upon glutamate stimulation (B), with or without co-incubation of 10 μM $ZnCl_2$, and often higher still upon electrical stimulation (C), although these responses were much more variable. Electrical stimulation also often showed more sustained responses, especially when media was not immediately replaced after stimulation.

stimulations resulted in elevated intracellular Zn^{2+}, which varied in magnitude and duration (Figures 3.1, 3.2). Generally, electrical stimulation gave rise to larger Zn^{2+} signals than glutamate stimulation, which were somewhat larger than Zn^{2+} increases observed upon KCl stimulation. While KCl and glutamate induced consistent peak Zn^{2+} signals, Zn^{2+} signals observed upon electrical stimulation were widely variable (Figure 3.2A). This is partially due to periodic failure of the electrical apparatus, leading to some cells that were not stimulated at all, but also may be due to variation in other parameters, such as exact distance of a cell from the electrodes. Furthermore, cells stimulated electrically were noticeably undergoing more stress as evidenced by blebbing toward the end of timecourses, which also may have affected the magnitude and heterogeneity of Zn^{2+} signals. Zn^{2+} signals evoked by glutamate stimulation could be intensified by the addition of exogenous Zn^{2+} (10 μM) and abrogated by the inclusion of TPA (10 μM, Figure 3.2B), allowing us to successfully modulate the magnitude of intracellular Zn^{2+} signal (Table 3.1).

3.3.2 Comparison of stimulation-dependent pH and Zn^{2+} measurements

There is evidence in the literature that Zn^{2+} signals may be due to Ca^{2+}/H^{+} exchange and subsequent acidification of neurons during stimulation, whereby acidification causes release of Zn^{2+} from cytosolic Zn^{2+}-binding proteins[281]. To determine whether the different magnitudes of Zn^{2+} signals observed upon different stimulation methods were attributable to pH changes, we imaged neurons under different stimulation conditions with the ratiometric pH-sensing small molecule dye BCECF (Figure 3.3). Comparing fluorescence ratios to standard curve ratios measured on the same day of imaging, we determined that all neurons acidified, usually to between pH 6 and pH 7 (Figure 3.4), and that the magnitude of peak Zn^{2+}

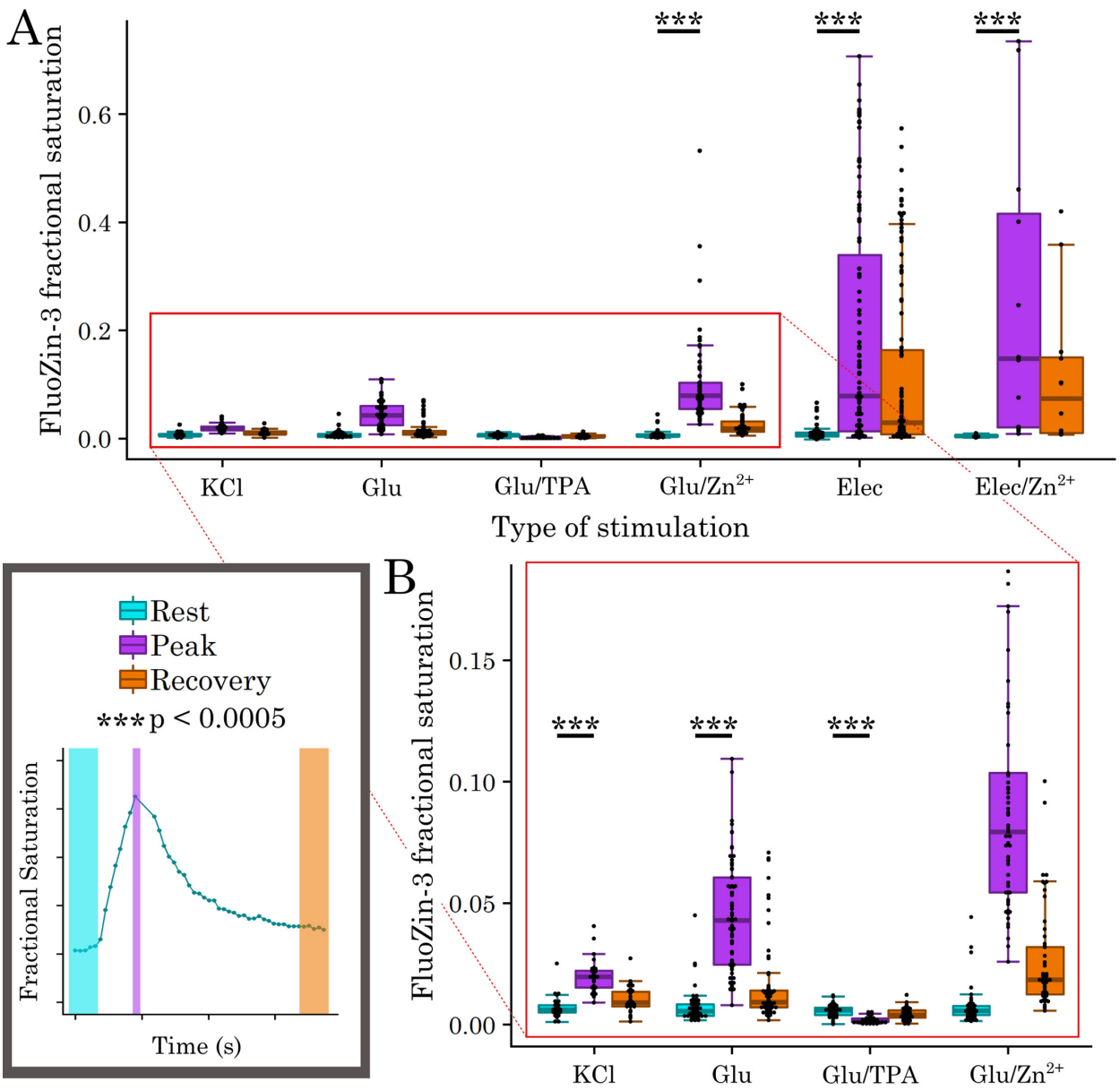

Figure 3.2: Quantification of FluoZin-3 AM signal upon different stimulation methods. The legend features an example trace diagram illustrating timepoints included in each of the measured categories (Rest, Peak, and Recovery). These timepoints were manually obtained in each experiment. (A) Box/dotplot of measured FluoZin-3 fractional saturation in different stimulation conditions. Each dot represents values obtained from an ROI in a single cell. Glu/Zn^{2+} and Elec/Zn^{2+} conditions were stimulated in the presence of 10 μM $ZnCl_2$. Electrical stimulation gave widely variable responses compared to other methods. (B) Inset providing better resolution of the smaller FluoZin-3 responses observed upon KCl and glutamate stimulation. Significance was assessed with a two-sided Wilcox Signed Rank test for paired data (KCl: n=30, test statistic V=0, p=1.9e-9; Glu: n=64, test statistic V=0, p=3.6e-12, Glu_TPA: n=45, test statistic V=983, p=2.3e-9, Glu_Zn: n=57, test statistic V=0, p=5.3e-11, Elec: n=103, test statistic V=18, p<2.2e-16, Elec_Zn: n=12, test statistic V=0, p=0.00049).

Table 3.1: Approximate Zn^{2+} concentrations observed in different stimulation conditions, as calculated from FluoZin-3 AM data.

Type of stimulation	Average resting [Zn^{2+}]	Average peak [Zn^{2+}]
KCl	70 pM ± 40 pM	180 pM ± 60 pM
Glutamate	70 pM ± 60 pM	420 pM ± 220 pM
Glutamate/Zn^{2+}	70 pM ± 70 pM	1.0 nM ± 0.8 nM
Glutamate/TPA	50 pM ± 20 pM	20 pM ± 10 pM
Electrical	80 pM ± 90 pM	2.1 nM ± 2.4 nM
Electrical/Zn^{2+}	40 pM ± 20 pM	3.0 nM ± 3.3 nM

signals in different stimulations did not correlate to the extent of neuron acidification (Figure 3.5). Interestingly, during electrical stimulation neurons were more likely to remain at low pH than in the other conditions, where there was usually some recovery in the timespan measured. This may correspond to the fact that Zn^{2+} responses were more likely to be sustained for long stretches of time upon electrical stimulation (Figure 3.1). However, the difference in magnitude of Zn^{2+} signals between glutamate and electrical stimulation could not be explained by the extent of neuron acidification. No further experiments have been conducted to determine the source of this observed difference, but given the fact that glutamate-mediated Ca^{2+} influx is known to induce production of reactive oxygen species (ROS) in neuron cultures[458,462] and symptoms of stress were observed in electrically-stimulated neurons, one possibility for differences in Zn^{2+} signals in these conditions is extent of ROS generation.

Figure 3.3 (p. 65): Representative BCECF experiments to measure cellular pH. (A) Example cells loaded with BCECF, showing signal measured at ~535 nm when excited by 488 nm (left panel) or 445 nm (center panel). The ratio of signal in relevant neuronal areas at 488 nm/445 nm excitation is displayed in the right panel. Lower BCECF ratios correspond to lower pH values (see Figure 3.4A). (B) Example traces corresponding to the signal at each excitation wavelength in the cells numbered in (A), left panel. Stimulation with 50 μM glutamate is indicated by the blue box, whereas treatment with pH 6.4 media/10 μM nigericin for calibration purposes is indicated with the orange box. Each separate experiment on a single day was treated with a different pH media to assemble a pH-BCECF ratio calibration curve. (C) Ratio of signals obtained upon different excitations for the same cells as in (B). Note the ratios converge upon pH 6.4/nigericin treatment.

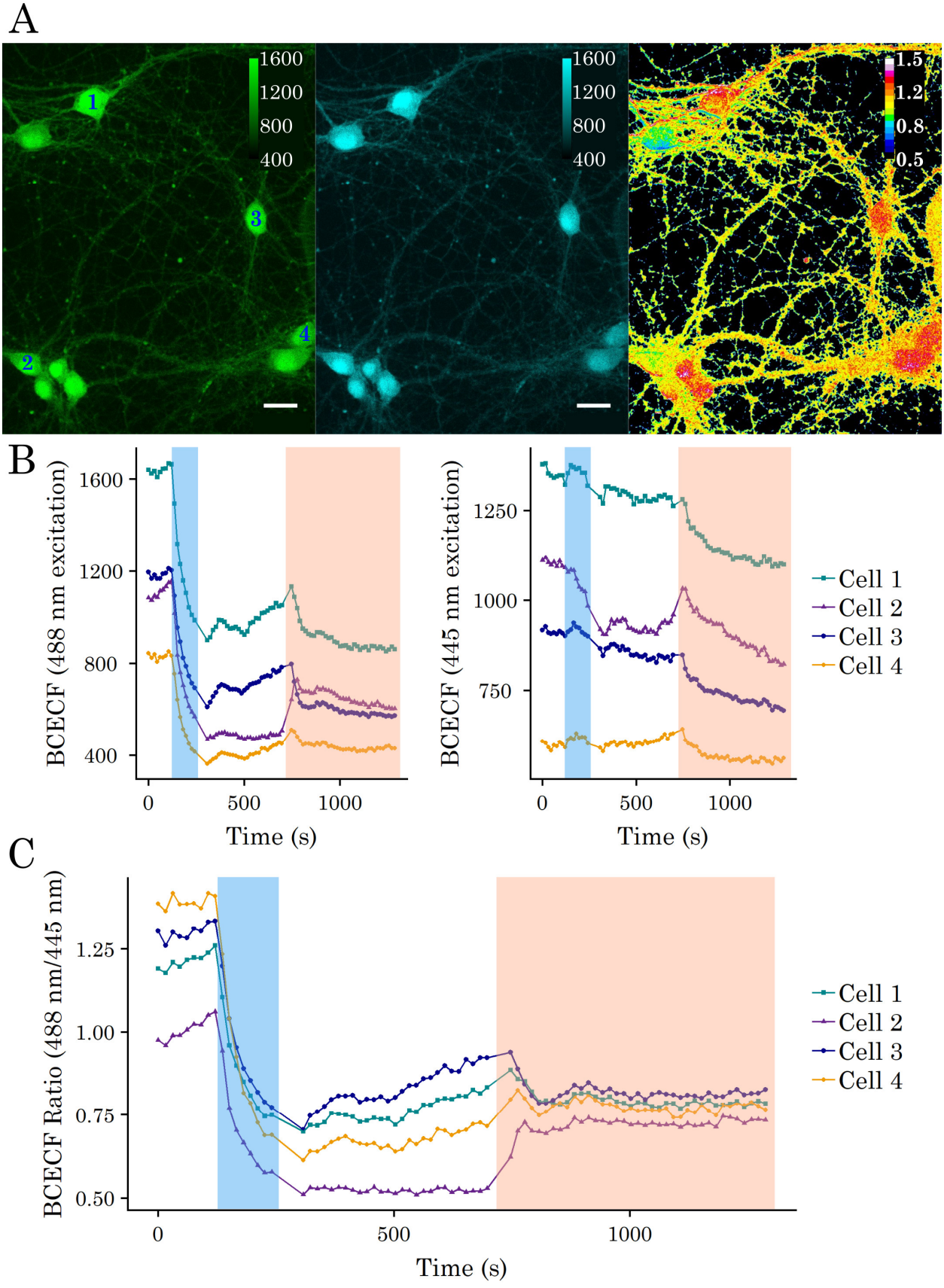
A
1600
1200
800
400
1
2
3
4
1600
1200
800
400
1.5
1.2
0.8
0.5
B
BCECF (488 nm excitation)
1600
1200
800
400
0
500
1000
Time (s)
BCECF (445 nm excitation)
1250
1000
750
0
500
1000
Time (s)
Cell 1
Cell 2
Cell 3
Cell 4
C
BCECF Ratio (488 nm/445 nm)
1.25
1.00
0.75
0.50
0
500
1000
Time (s)
Cell 1
Cell 2
Cell 3
Cell 4

3.3.3 Analysis of Zn^{2+}-dependent gene expression upon glutamate stimulation

In order to identify the transcriptional effects of Zn^{2+} signals during glutamate stimulation, we performed RNA-Seq on dissociated hippocampal neuron cultures. Neurons were exposed to a 2 minute incubation with normal media (control), media containing 50 µM glutamate ("Glu"), media containing 50 µM glutamate and 10 µM $ZnCl_2$ ("Glu/Zn^{2+}"), or media containing 50 µM glutamate and 10 µM Zn^{2+} chelator TPA ("Glu/TPA"). The two main comparison conditions were anticipated to be Glu (endogenous Zn^{2+} signal) vs. Glu/TPA (blocked Zn^{2+} signal). Surprisingly, we observed little difference between these two conditions. Principal component analysis yielded no clear clustering of any condition within any principal component (Figures 3.6, 3.7).

One possible source of variation that we considered was heterogeneity in successful neuronal stimulation; to this end, we analyzed immediate early genes (IEGs) that are known to be upregulated upon stimulation. Canonical IEGs *Jun*, *Fos*, *Egr1*, *Nr4a1*, *Npas4*, and *Fosb* did show considerable heterogeneity in upregulation upon glutamate treatment (regardless of Zn^{2+} perturbation), with some replicates

Figure 3.4 (p. 67): Quantification of BCECF signal upon different stimulation methods. (A) Calibration curve relating BCECF ratio to equilibrated pH, obtained on a single day of experiments. Each dot represents one cell in a field of view, and 1-2 experiments comprise each pH point. (B) Representative traces from Fig. 3B, marked by color where Resting, Peak, and Recovery ratio measurements were obtained. Timepoints were obtained manually in each experiment. Scale bars = 20 µm. (C) Box/dotplot of BCECF ratio measurements across stimulation conditions. Each dot represents a value from an ROI within a single cell in a field of view. All conditions show a drop in BCECF ratio upon stimulation. (D) Box/dotplot of pH across stimulation conditions, as calculated from each individual cell BCECF ratio (shown in C) via the calibration curve obtained on the day of that experiment. All stimulation methods show a significant drop in pH upon stimulation, with all except electrical stimulation then displaying some recovery toward baseline pH over the course of the timecourse. Significance was assessed with a two-sided Wilcox Signed Rank test for paired data (Glu: n=68, test statistic V=2346, p=7.8e-13, Glu/TPA: n=58, test statistic V=1711, p=3.6e-11, Glu/Zn: n=58, test statistic V=1711, p=3.6e-11, Elec: n=77, test statistic V=3003, p=2.5e-14, Elec/Zn: n=84, test statistic V=3570, p=1.7e-15).

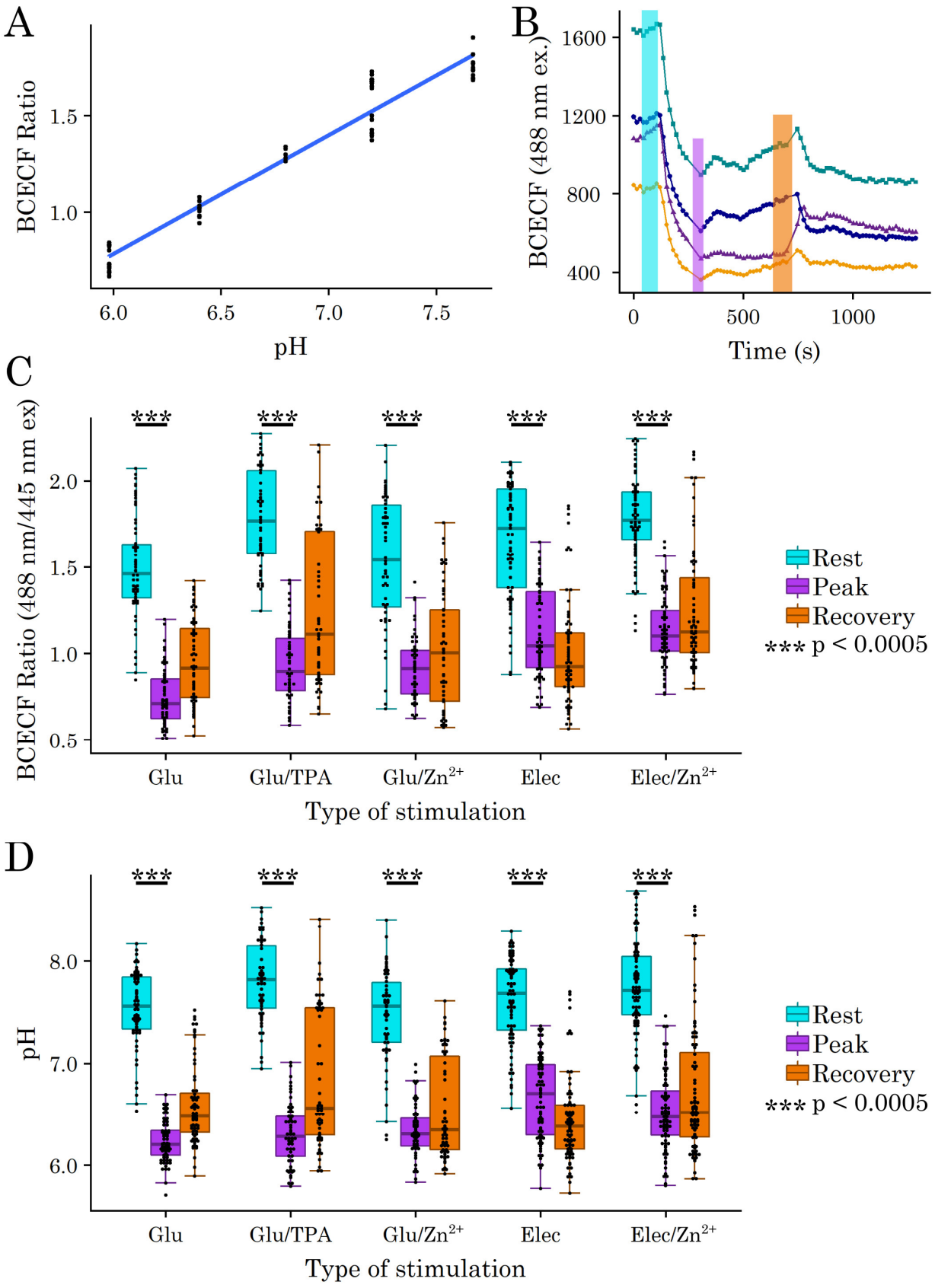
A
BCECF Ratio
1.5
1.0
6.0
6.5
7.0
7.5
pH
B
BCECF (488 nm ex.)
1600
1200
800
400
0
500
1000
Time (s)
C
BCECF Ratio (488 nm/445 nm ex)
2.0
1.5
1.0
0.5
***
Glu
Glu/TPA
Glu/Zn2+
Elec
Elec/Zn2+
Type of stimulation
Rest
Peak
Recovery
*** p < 0.0005
D
pH
8.0
7.0
6.0
***
Glu
Glu/TPA
Glu/Zn2+
Elec
Elec/Zn2+
Type of stimulation
Rest
Peak
Recovery
*** p < 0.0005

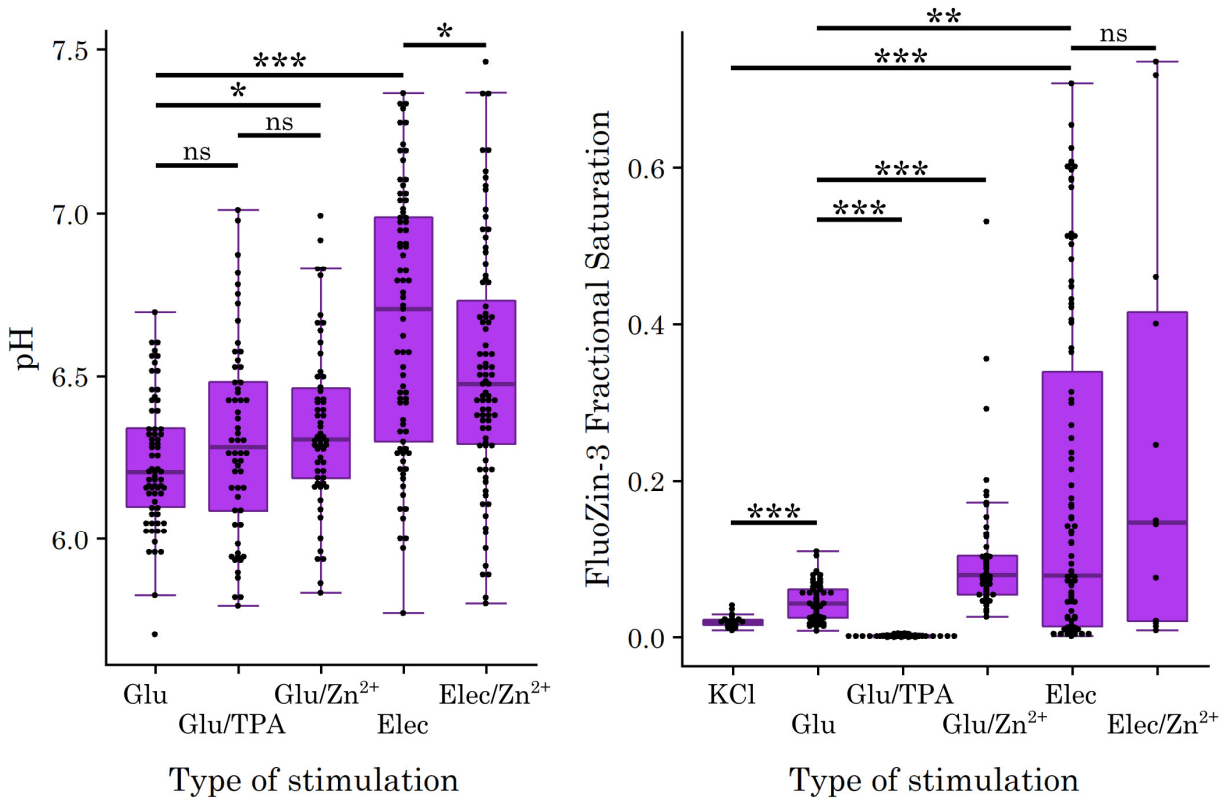

Figure 3.5: Comparison of "peak" pH (left panel) and FluoZin-3 AM (right panel) measurements across stimulation methods. "Peak" refers to the minimal (pH) or maximal (FluoZin-3) values obtained upon stimulation. Each set of data is equivalent to the peak datasets in Figs 2 and 4. While some pH differences were observed in different stimulations, especially between glutamate and electrical stimulation, these differences do not correlate with the strongly significant differences between all Zn^{2+} changes observed. * $p < 0.05$; ** $p < 0.005$, *** $p < 0.0005$. Significance was assessed with a two-sided Mann-Whitney U unpaired test for both pH (Glu vs. Glu/TPA: test statistic W=2226, p=0.21, Glu vs. Glu/Zn: test statistic W=2498, p=0.01, Glu vs. Elec: test statistic W=4223, p=2.1e-10, Glu/TPA vs. Glu/Zn: test statistic W=1543, p=0.44, Elec vs. Elec/Zn: test statistic W=3849, p=0.04) and FluoZin-3 (KCl vs. Glu: test statistic W=315, p=1.7e-07, KCl vs. Elec: test statistic W=836, p=0.00014, Glu vs. Glu/TPA: test statistic W=0, p<2.2e-16, Glu vs. Glu/Zn: test statistic W=3020, p=5.4e-10, Glu vs. Elec: test statistic W=4228, p=0.0022, Elec vs. Elec/Zn: test statistic W=521, p=0.38).

doubling expression of most of these IEGs and other replicates displaying little change (Figure 3.6C). Furthermore, other IEGs, including *Homer1* and *Egr3*, showed little change across conditions. Upon further analysis, it was determined that the six variable IEGs all contributed most significantly to PC9, which also shows some

delineation between most stimulated replicates and control replicates. Despite this evidence of heterogeneity among replicates that may be partially due to inefficiency of stimulation, no criteria could be determined upon which to deem any of the replicates outliers using principle component analysis. We also analyzed the data using hierarchical clustering (Figure 3.6B) and silhouette cluster analysis, and both of these methods deemed that one replicate of the Glu/Zn^{2+} condition was an outlier. We therefore omitted this replicate when performing further analysis.

We performed differential expression analysis of genes between different conditions in this outlier-removed dataset using the R package DESeq2. We found a gradation in expression phenotype, in that only 2 genes were significantly differentially expressed between Glu and Glu/TPA conditions, and 3 genes were significantly differentially expressed between Glu and Glu/Zn^{2+} conditions, but 763 genes were significantly differentially expressed between Glu/TPA and Glu/Zn^{2+} conditions (Figure 3.8). These results imply that glutamate treatment, which induces an intermediate Zn^{2+} signal, may also be inducing expression of Zn^{2+}-dependent genes in an intermediate fashion. However, we were not be able to resolve differences between the glutamate condition and the exogenous Zn^{2+} perturbation conditions due to heterogeneity among replicate samples.

To further investigate the differentially expressed genes between Glu/Zn^{2+} and Glu/TPA conditions, we performed gene ontology (GO) analysis using DAVIDtools (Table 3.2) and GSEA (Table 3.3). Both methods indicated that genes upregulated in the Glu/Zn^{2+} condition were significantly enriched in GO categories for ER localization, ER stress, and the unfolded protein response (UPR). Other processes implicated among upregulated genes by one of the two tools include translation and mitochondrial function, whereas some neuronal processes such as axon guidance and

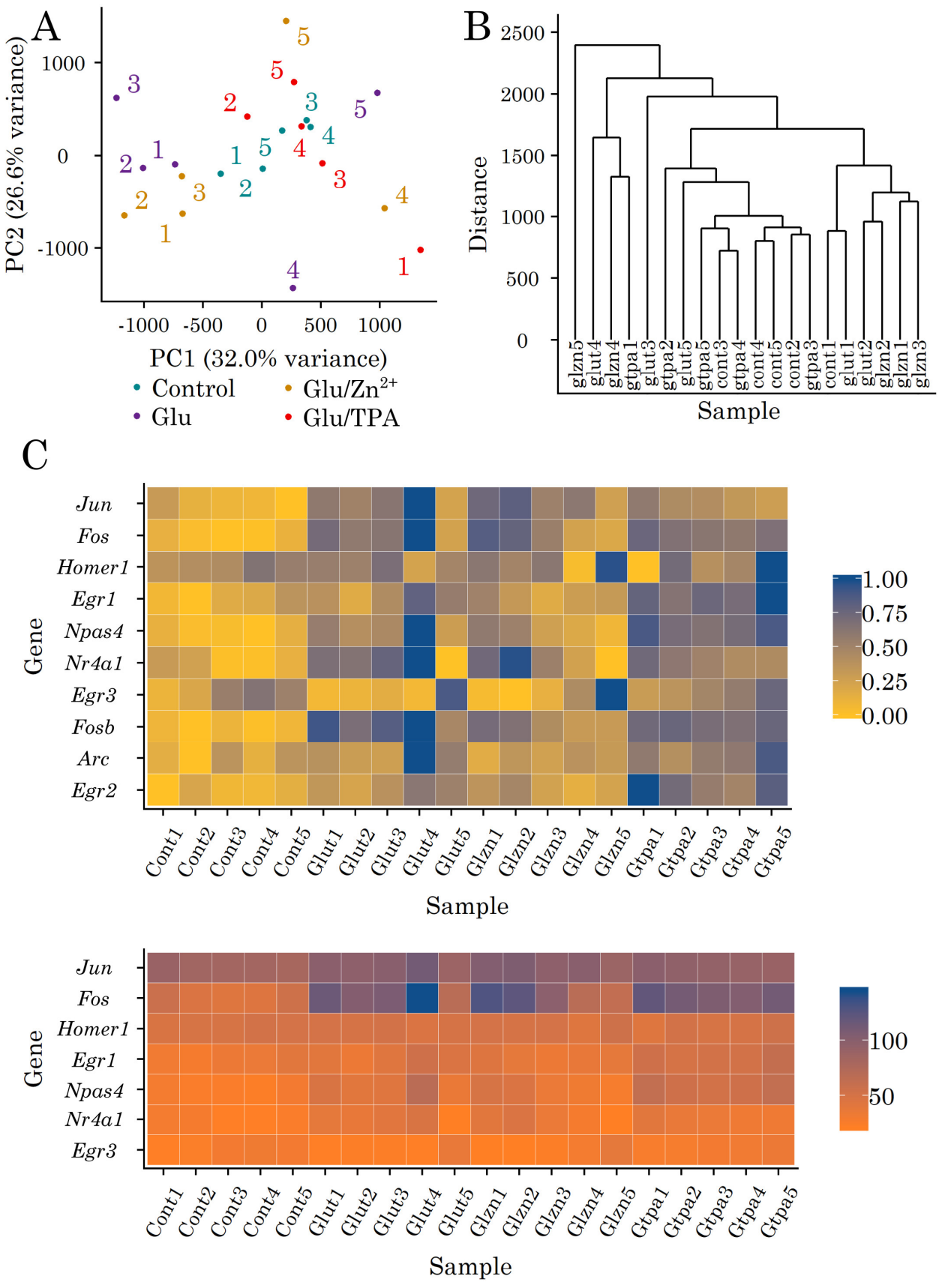
A
PC2 (26.6% variance)
1000
0
-1000
-1000 -500 0 500 1000
PC1 (32.0% variance)
Control
Glu
Glu/Zn2+
Glu/TPA
B
Distance
2500
2000
1500
1000
500
0
glzn5 glut4 glzn4 gtpa1 glut3 gtpa2 glut5 gtpa5 cont3 gtpa4 cont4 cont5 cont2 gtpa3 cont1 glut1 glut2 glzn2 glzn1 glzn3
Sample
C
Gene
Jun
Fos
Homer1
Egr1
Npas4
Nr4a1
Egr3
Fosb
Arc
Egr2
1.00
0.75
0.50
0.25
0.00
Cont1 Cont2 Cont3 Cont4 Cont5 Glut1 Glut2 Glut3 Glut4 Glut5 Glzn1 Glzn2 Glzn3 Glzn4 Glzn5 Gtpa1 Gtpa2 Gtpa3 Gtpa4 Gtpa5
Sample
Gene
Jun
Fos
Homer1
Egr1
Npas4
Nr4a1
Egr3
100
50
Cont1 Cont2 Cont3 Cont4 Cont5 Glut1 Glut2 Glut3 Glut4 Glut5 Glzn1 Glzn2 Glzn3 Glzn4 Glzn5 Gtpa1 Gtpa2 Gtpa3 Gtpa4 Gtpa5
Sample

Figure 3.6 (p. 70): Variability in RNA-Seq data. (A) Principle component analysis of all replicates. PC1 and PC2 are displayed, accounting for 58.6% of all variance across samples. No clear clustering is visible among conditions, and all stimulation conditions have some replicates clustering and some varying dramatically. (B) Dendrogram displaying hierarchical clustering distances of all replicates. Similarly to (A), no clear clustering is visible, although one replicate (glzn5) is seen to be an outlier from the rest of the samples. (C) Heat maps showing expression of canonical neuronal immediate early genes (IEGs) across replicates. The top heat map treats each gene as separate for scaling purposes, whereas the bottom heat map excludes the lowest expressing genes (average TPM < 10) and applies the same scale across all genes. Replicates in all stimulation conditions show variability in the extent of induction of these genes, perhaps providing evidence of variability in successful neuronal stimulation. Cont = control, Glut = Glu, Gtpa = Glu/TPA, Glzn = Glu/Zn^{2+}.

calcium regulation are more enriched in the Glu/TPA condition. GSEA analysis of Glu vs. Glu/TPA conditions also indicated enrichment in UPR-related genes (Table 3.3), providing further evidence that Zn^{2+} transients are important for manifestation of an ER stress response. Whether Zn^{2+} is a key agent of stress or a signaling intermediate for the stress response is still unclear.

Interestingly, there were few Zn^{2+} homeostasis genes observed to be differentially expressed among conditions. Metallothionein genes *Mt1* and *Mt2*, as well as putative plasma membrane Zn^{2+} exporter Zip11 (*Slc39a11*), were seen to be upregulated in Glu/Zn^{2+} as compared to Glu/TPA, which may indicate that the neurons are experiencing high levels of Zn^{2+}, which may require export and more extensive cytosolic Zn^{2+} buffering.

3.3.4 Comparison of Zn^{2+}-dependent gene expression upon KCl vs. glutamate stimulation

To determine whether Zn^{2+} signals act similarly in longer (2 minute) glutamate stimulation as compared to short (10 second) KCl stimulation, we compared differentially expressed genes from KCl/Zn^{2+} vs. KCl conditions (see section 2.3.5) to Glu/Zn^{2+} vs. Glu/TPA conditions (Figure 3.9). These gene sets had very little overlap,

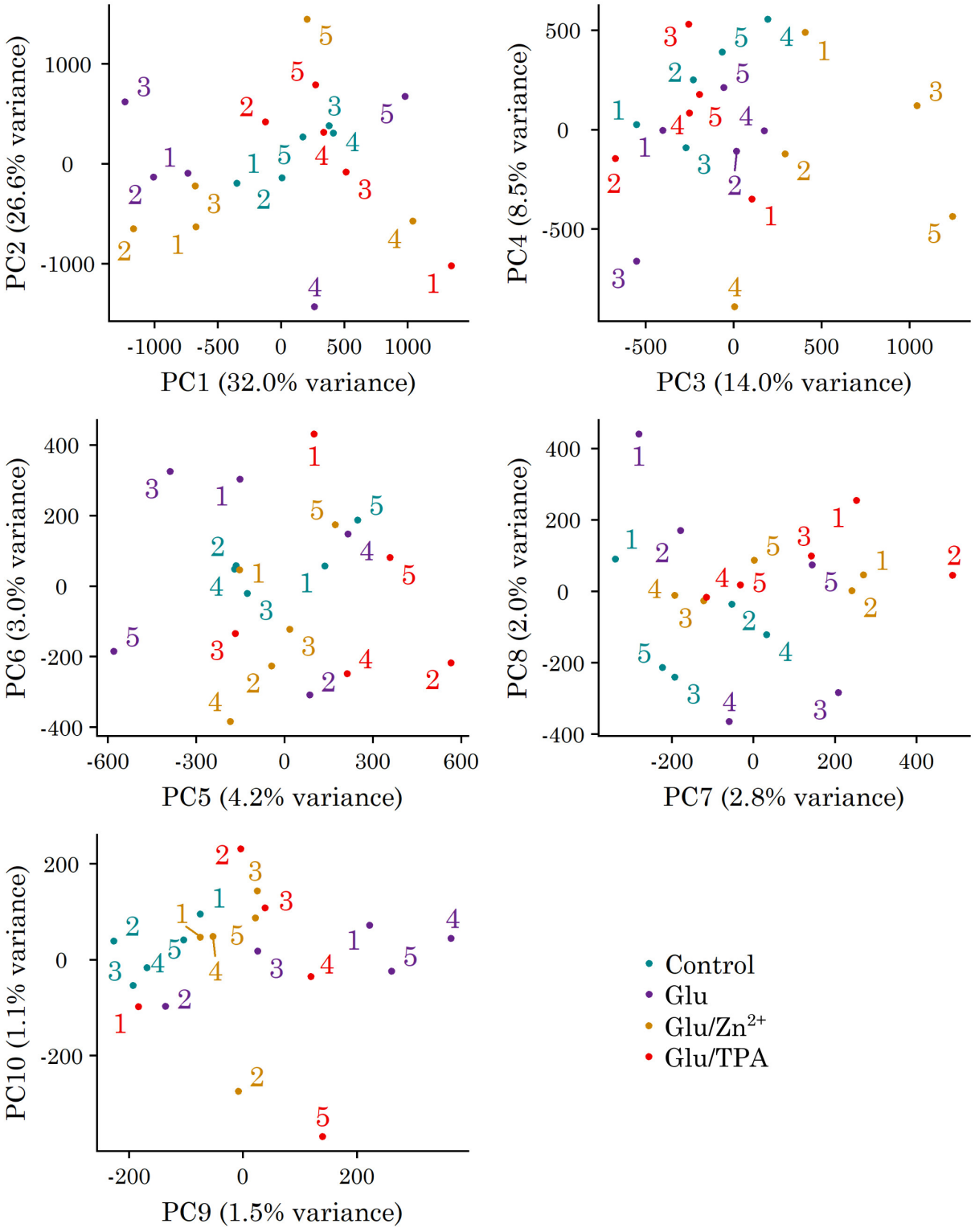

Figure 3.7: Variability in RNA-Seq data as assessed with principle component analysis. Plots are shown to visualize PC1-PC10 (PC2 vs. PC1 is the same as in Figure 6A). No clear separation is visible within any principle component.

Table 3.2: Select enriched gene ontology (GO) terms between Glu/Zn^{2+} and Glu/TPA conditions as assessed using the DAVIDtools online functional annotation tool. FDR = false discovery rate.

Upregulated in Glutamate/Zn^{2+}	# genes annotated	-$\log_{10}$(FDR)
Endoplasmic reticulum lumen	18	9.7
Endoplasmic reticulum chaperone complex	8	6.9
Endoplasmic reticulum membrane	35	5.9
Protein folding	12	2.4
Aminoacyl-tRNA ligase activity	7	1.6
Endoplasmic reticulum unfolded protein response	7	1.0
Upregulated in Glutamate/TPA		
Oxytocin signaling pathway	15	3.0
Axon guidance	14	3.0
Positive regulation of calcium-dependent exocytosis	7	3.0
Calcium transport	10	1.1

Table 3.3: Select Gene Set Enrichment Analysis (GSEA) results examining whether sets of genes associated with certain human gene ontology terms or pathways are enriched between Glu/Zn^{2+} or Glu conditions as compared to the Glu/TPA condition. FDR = false discovery rate.

Upregulated in Glutamate/Zn^{2+} vs. Glutamate/TPA	# genes in set	-$\log_{10}$(FDR)
Cellular response to topologically incorrect protein	117	1.8
Inner mitochondrial membrane protein complex	94	1.6
Ire1-mediated unfolded protein response	54	1.6
Positive regulation of fatty acid metabolic process	33	1.5
Response to endoplasmic reticulum (ER) stress	223	1.3
Negative regulation of response to ER stress	37	1.3
Mitochondrial protein complex	123	1.2
Respiratory chain	75	1.2
Negative regulation of ER stress induced intrinsic apoptotic signaling pathway	18	1.2
Phospholipase inhibitor activity	11	1.1
Response to topologically incorrect protein	156	1.1
Perk-mediated unfolded protein response	11	1.1
ERAD pathway	70	1.0
Upregulated in Glutamate/TPA vs. Glutamate/Zn^{2+}		
Type I interferon receptor binding	12	> 3
Regulation of peptidyl serine phosphorylation of stat protein	16	2.0
Upregulated in Glutamate vs. Glutamate/TPA		
Unfolded protein response	73	1.1

and most of the genes that were common to both datasets actually were upregulated in opposite Zn^{2+} conditions. This comparison is very rough (different organism, different treatment comparisons, different time of stimulation), but it does indicate that the Zn^{2+}-dependent gene expression changes during short KCl stimulation and longer glutamate stimulation are extremely different.

3.3.5 Investigation of Zn^{2+}-dependent protein phosphorylation upon glutamate stimulation

In order to determine what signaling pathways might be activated by Zn^{2+}, we performed glutamate or glutamate/TPA stimulation on neurons and collected protein lysates after 30 minutes. We then analyzed these lysates with a large phosphoarray containing 1318 antibodies to 407 different proteins and 687 unique phosphosites (Figure 3.10). This experiment was intended to be a pilot experiment, and thus we were restricted to two samples: one biological replicate per condition, with two technical replicates per phosphoarray slide. Analysis of spots on the array was hampered by variable background signals and different levels of non-specific binding, and despite using local background correction and normalizing to internal controls, we were not confident in any specific quantification (Figure 3.10A). Due to this lack of statistical power and variability of quantification, we thus treated this experiment

Figure 3.8 (p. 75): Differential expression among RNA-Seq conditions. (A) MA plots showing distribution of genes between Glu and Glu/TPA conditions (left) and between Glu/Zn^{2+} and Glu/TPA conditions (right). Each dot represents a gene, with genes that were deemed as significantly differentially expressed shown as orange. (B) Counts of differentially expressed genes between different conditions. The largest number of different genes was observed between Glu/Zn^{2+} and Glu/TPA conditions. (C) Volcano plot displaying significance of difference vs. magnitude of change for each gene between Glu/Zn^{2+} and Glu/TPA conditions. All genes passing a threshold of FDR > 1.3 and log2(FC) > 0.1 are displayed as orange. 12 genes exhibiting high significance or high fold change are labeled, as well as several genes related to ER stress (boxed).

A

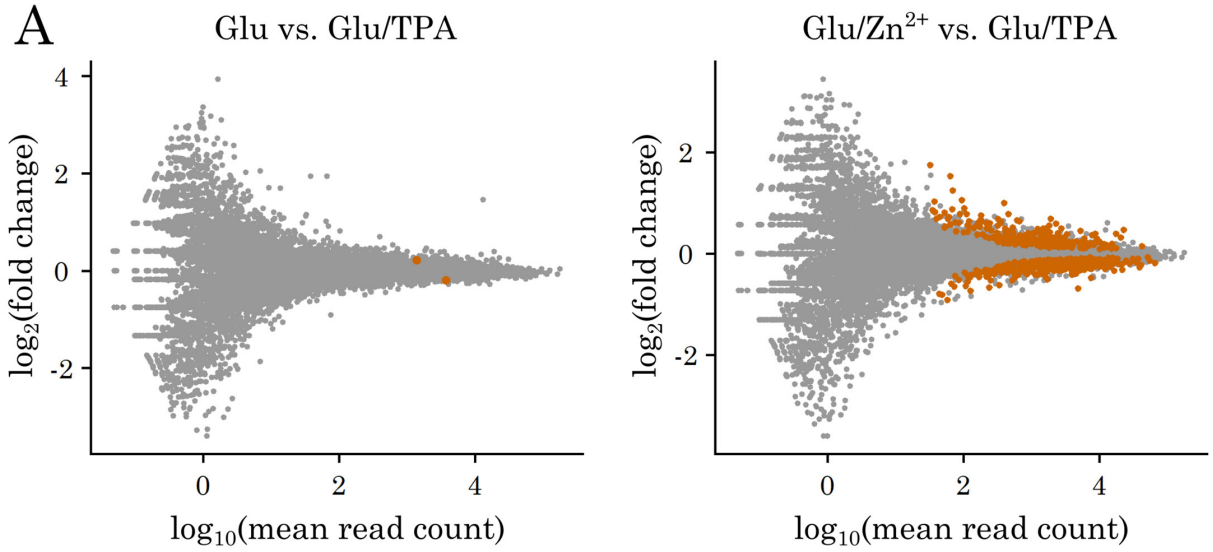

B

Condition comparison	Number of genes: Upregulated	Downregulated
Glu vs. Control	10	2
Glu/Zn^{2+} vs. Control	82	71
Glu/TPA vs. Control	10	0
Glu/Zn^{2+} vs. Glu	0	3
Glu vs. Glu/TPA	1	1
Glu/Zn^{2+} vs. Glu/TPA	311	451

C

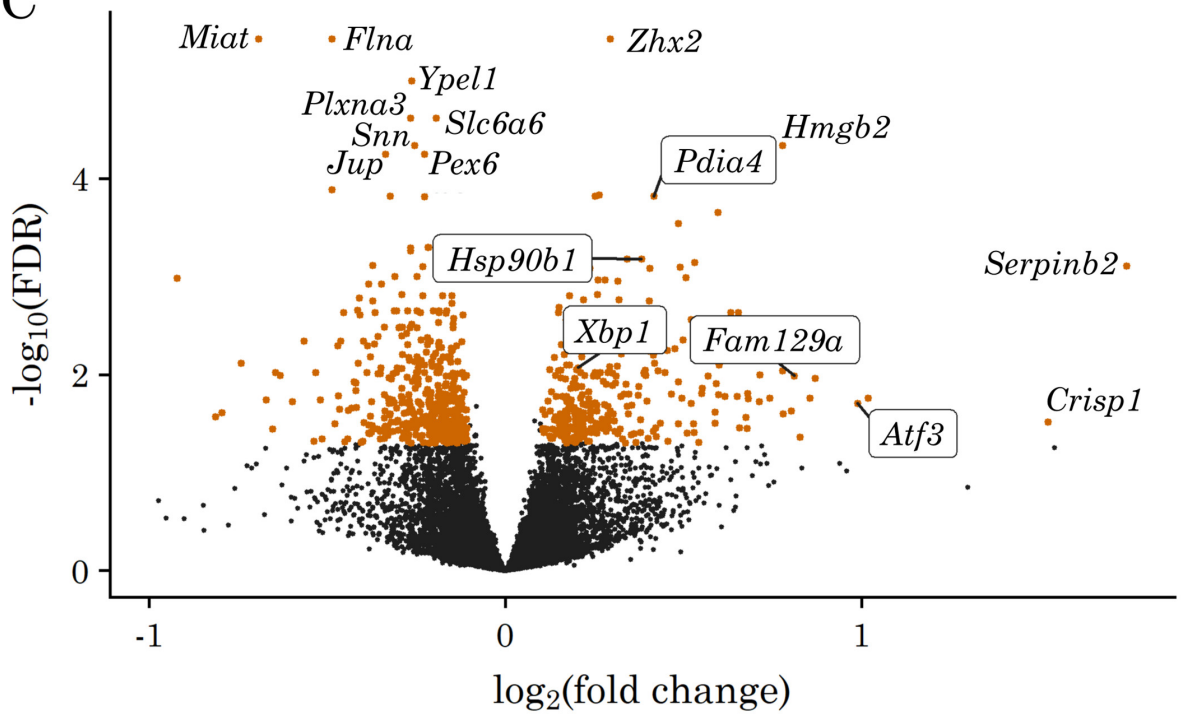

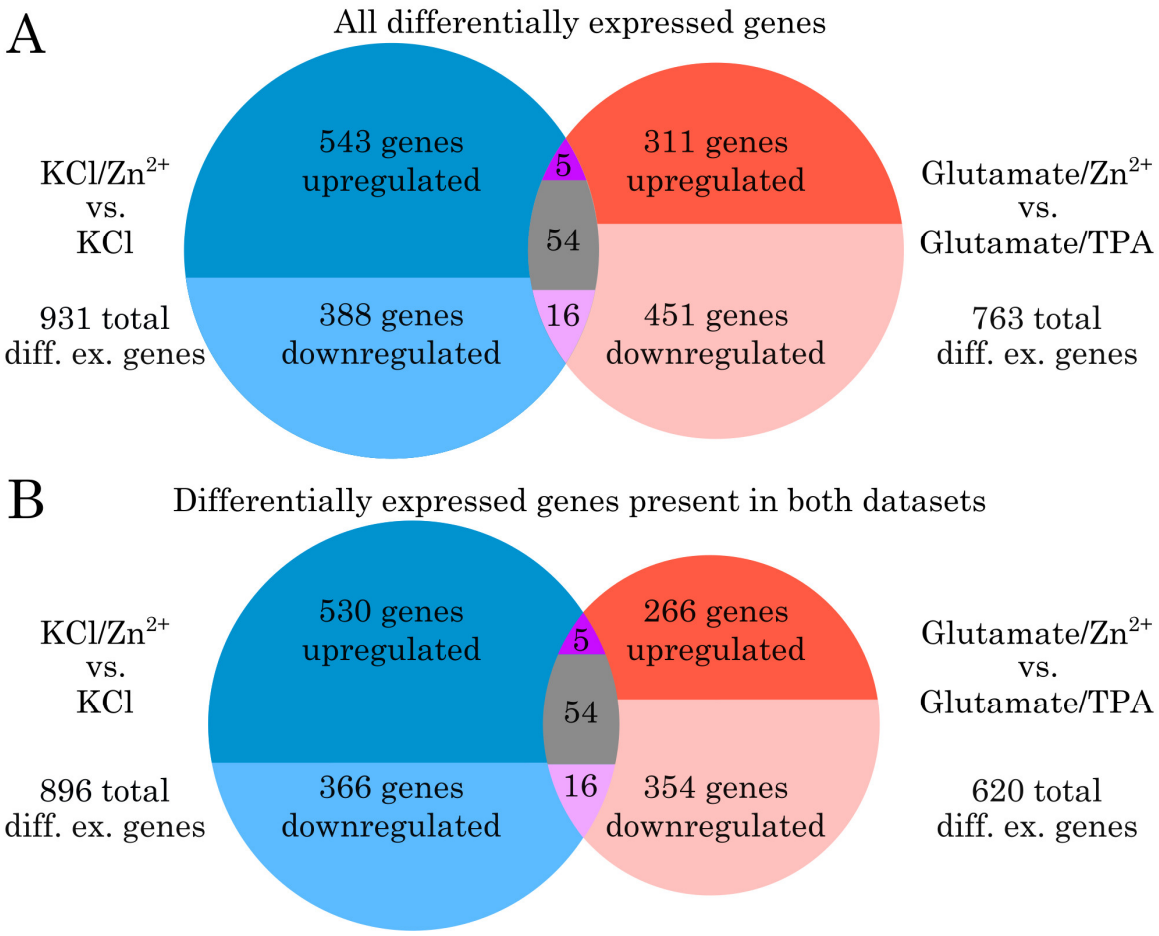

Figure 3.9: Venn diagrams comparing differentially expressed genes observed in different RNA-Seq experiments. Gene sets include (A) all differentially expressed genes seen in each experiment or (B) only differentially expressed genes that are expressed in all four conditions (DESeq2 baseMean > 1). Larger circles indicate total upregulated and downregulated genes in each experiment (KCl/Zn^{2+} vs. KCl as discussed in Chapter 2, $Glutamate/Zn^{2+}$ vs. Glutamate/TPA as discussed in this chapter). Overlap indicates how many genes were differentially expressed in both datasets and consistently upregulated (5 genes), consistently downregulated (16 genes), or regulated in different directions with relationship to Zn^{2+} status (54 genes).

as rough exploration that we intend to validate using more rigorous methods.

With these caveats, we analyzed the phosphosites that gave us the highest fold changes between the two conditions (Figure 3.10B). Most of these hits were involved in MAP kinase signaling, PI3K/AKT signaling, or NFκB signaling, with many specific phosphosites providing contradictory evidence on the overall activation of those

pathways upon Zn^{2+}-replete glutamate treatment. We posit three scenarios that may be supported by this data, none of which are mutually exclusive: 1) Zn^{2+} directly or indirectly induces NFκB-mediated anti-apoptotic stress response and inhibits apoptotic signaling; 2) the presence of Zn^{2+} induces Src activation, potentially through RTK activity, which then alters downstream MAPK and AKT signaling; 3) Zn^{2+}-altered MAPK and PKC signaling leads to cytoskeletal rearrangements and receptor localization at synapses. As described in the first scenario, the general upregulation of NFκB signaling and anti-apoptotic signaling corroborates the RNA-Seq results, and the role of Zn^{2+} in stress-related signaling and ER stress is thus a focus of ongoing research.

3.4 Discussion

In this study, we examined how different methods of stimulation of dissociated hippocampal neurons elicited diverse Zn^{2+} responses, and then we further investigated downstream consequences of glutamate stimulation in variable Zn^{2+} conditions. We found that KCl, glutamate, and field electrical stimulations generated remarkably different intracellular Zn^{2+} dynamics, and that despite literature suggesting that pH is a driving factor in glutamate-induced intracellular Zn^{2+} mobilization, the magnitudes of these differential responses failed to correlate with the extent of pH drop observed. It is possible that neurons have similarly different Ca^{2+} dynamics in these three stimulation scenarios; this is not readily apparent in the intensiometric Ca^{2+} imaging that we have done (Appendix C), but we have not performed rigorous quantification of Ca^{2+} in cells exposed to each stimulation. Variability in Ca^{2+} levels might imply that voltage is variable across conditions, leading to altered permeability of ion channels across the plasma membrane to any potential extracellular Zn^{2+}, or it could indicate that other downstream effects of Ca^{2+} could be important for Zn^{2+} mobilization. The generation of reactive oxygen/nitrogen

A

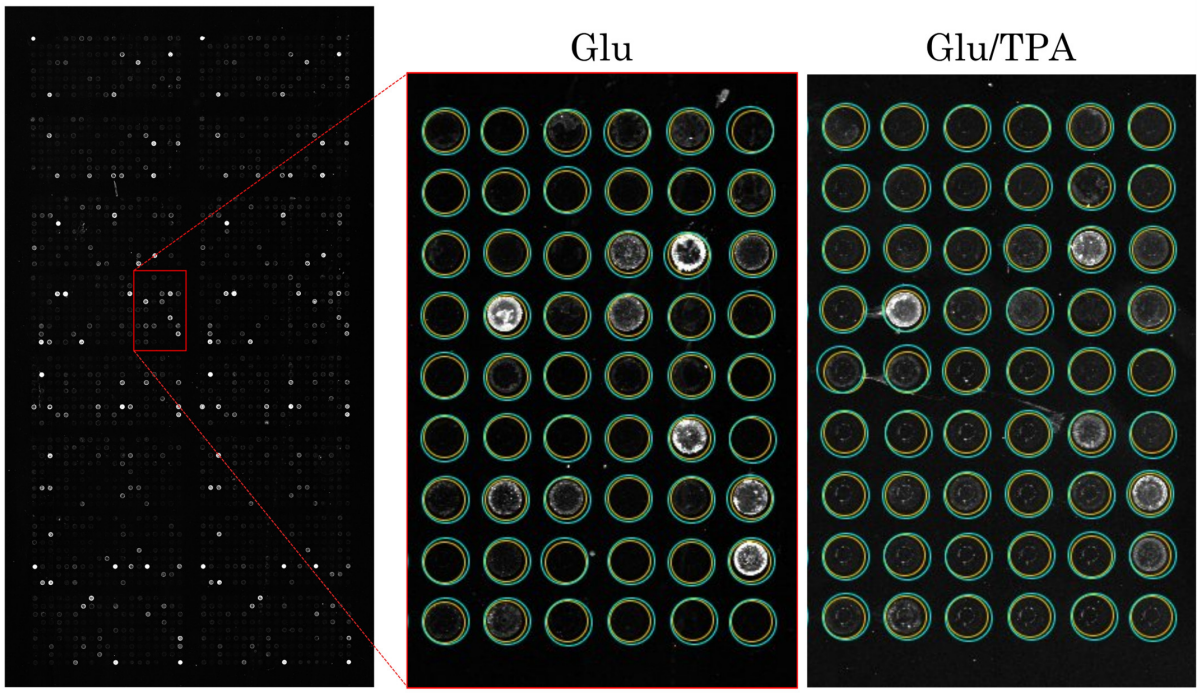

B

Phosphorylation states in Glutamate (Glu) vs. Glutamate/TPA (Glu/TPA) treatment

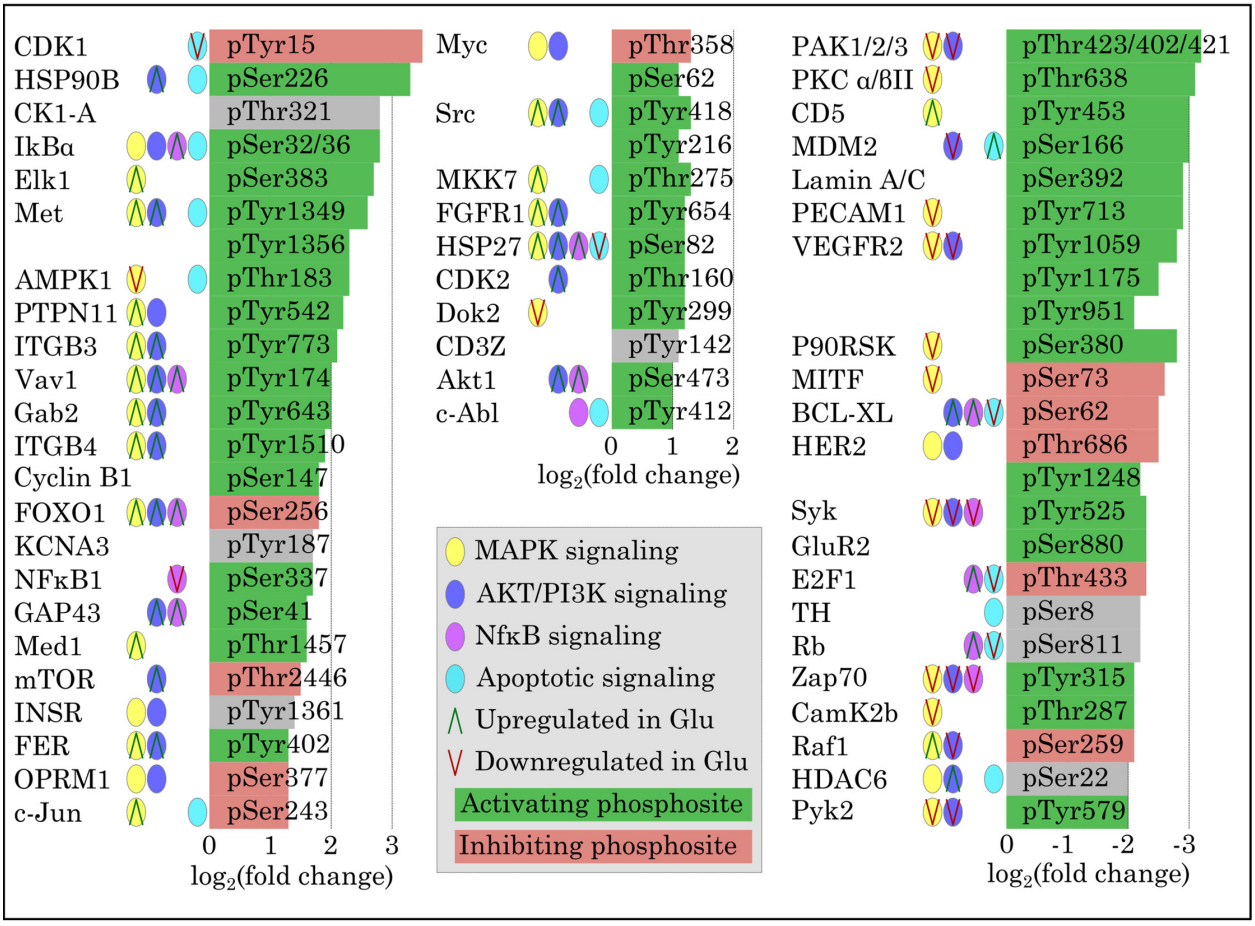

species (ROS/RNS) is another important possibility for explaining differential stimulation method-dependent Zn^{2+} dynamics. Glutamate stimulation is known to prompt ROS production[532], and ROS are known to mobilize Zn^{2+} from cytosolic metallothioneins[458,542,543], although whether the minimum timescale of this mobilization matches our observations is unclear. Some research has shown that ROS may be involved in physiological responses[282], so ROS-dependent Zn^{2+} mobilization may not necessarily be indicative of oxidative stress. However, given the visible state of stress observed over time in electrically-stimulated neurons, these cells could be experiencing higher levels of ROS, which might explain the higher peak Zn^{2+} signals observed. Furthermore, 60 mM KCl has been shown to not produce intracellular ROS[458], thus potentially explaining the limited extent of the Zn^{2+} signal we observed upon KCl stimulation. Further study of Ca^{2+} dynamics and ROS generation in neurons cultures upon stimulation will likely further clarify the different observed Zn^{2+} dynamics.

In order to determine downstream effects of Zn^{2+} signaling, we chose to use glutamate stimulation, which gave the largest consistent Zn^{2+} response as defined by

Figure 3.10 (p. 78): Analysis of phosphoarray conducted with cells stimulated with glutamate or glutamate/TPA. (A) Representative image of array areas with ROIs used for quantification. The large picture and red-boxed inset are images of the glutamate condition, whereas the right-most inset shows the same region from the glutamate/TPA array. Rings around spots (intersections of blue and yellow circles) were used to measure local background, which was then subtracted from the spot intensity (within yellow circles). Yet spot intensity itself was extremely different between the two arrays, possibly due to differences in blocking and non-specific binding, making quantification difficult. (B) Top hits from the phosphoarray comparison as assessed by fold change. All phosphosites with log2(FC) > 1 (left and center columns) or log2(FC) < 2 (right column) are displayed. The box behind each phosphosite label has a length corresponding to the log2(FC) observed and a color that illustrates whether it activates or inhibits protein function. Colored circles indicate whether the associated protein is connected to canonical signaling pathways, and arrows indicate whether the specific phosphosite(s) should upregulate or downregulate activity of that signaling pathway in the glutamate condition.

fluorescence imaging. Despite the relative consistency of Zn^{2+} signals, replicates within conditions showed substantial heterogeneity when analyzed by PCA and hierarchical clustering. There seems to be a component of this heterogeneity that may be due to less overall stimulation of some cultures, as evidenced by the lack of immediate early gene expression in several glutamate-stimulated replicates. Another source of variation in sequencing results could be the cell type composition of each culture, since they are not pure excitatory neuron cultures, although this should be minimized by the extraction method of pooling all hippocampi before dissociation and plating. We do not believe that the divergence of replicates was primarily due to disparate Zn^{2+} dynamics among cultures, due to the fact that all analysis methods indicated the replicates for the Glu/TPA condition were as variable as the rest, despite this condition showing an extremely narrow distribution of Zn^{2+} concentrations. The source of the rest of the heterogeneity is unknown.

In analyzing differential expression and enriched GO terms in the RNA-Seq data, we observed that neurons stimulated in Zn^{2+}-replete and Zn^{2+}-added conditions appeared to upregulate markers of ER stress, including genes involved in the unfolded protein response (UPR) and ER-associated degradation (ERAD). These results were somewhat surprising, as Zn^{2+} has previously been shown to exacerbate mitochondrial and ROS stress in neurons[458,468,546,547], but has only been tangentially linked to ER stress[548]. Stimulation in the presence of exogenous Zn^{2+} was also responsible for upregulation of genes related to translation and mitochondrial function, which may also be further signs of cell stress. However, oxidative stress response genes, including the transcription factor *Nrf2*, nitric oxide synthase enzymes (*Nos1/Nos2*), NADPH oxidase (*Nox1*), superoxide dismutase (*Sod1/Sod2*), thioredoxin interacting protein (*Txnip*), glutathione peroxidases (*Gpx1-Gpx4*), and

catalase (*Cat*)[480,549,550], were not observed to be upregulated. Importantly, ER stress response pathways are clearly enriched when comparing Zn^{2+}-replete and Zn^{2+}-added stimulation conditions to control neurons, but absent from comparisons between the glutamate/TPA condition and control neurons. Furthermore, glutamate stimulation of neurons in the presence of TPA seems to have preferentially upregulated genes responsible for neuron growth, given GSEA identification in the glutamate/TPA condition of pathways including axon guidance and calcium exocytosis, likely indicating a lack of stress in this condition. All of this evidence supports the hypothesis that Zn^{2+} is important for glutamate-induced cell stress, although ER stress seems to be more clearly implicated than oxidative stress, which does not coincide with the literature. It is possible that the timepoint of our sequencing was not late enough to capture a transcriptional oxidative stress response, or that the moderate Zn^{2+} dynamics resulting from the relatively mild glutamate stimulation we used did not reach a threshold for inducing oxidative stress. Either explanation, however, would also seem to preclude the ER stress we did observe, as ER stress is thought to be downstream of oxidative stress in excitotoxicity[534,537]. One further possibility is that, due to the inter-replicate variability of our sequencing samples, we may not have identified oxidative stress response genes that were upregulated less strongly than ER stress response genes. To address these possibilities, experiments are currently underway to more specifically validate the Zn^{2+}-ER stress link using benchmark ER stress assays examining XBP-1 splicing and CHOP expression, and to determine whether our stimulation conditions do induce generation of reactive oxygen species.

While the RNA-Seq results did allow us to correlate Zn^{2+} and neuronal ER stress, we were unable to elucidate whether Zn^{2+} may be causal in inducing ER stress, or if

it is an important mediator of signaling leading to stress response. One way we attempted to differentiate between these scenarios was with a high-throughput phosphoarray, with which we hoped to more clearly understand which signaling pathways are activated upon glutamate stimulation in Zn^{2+}-replete conditions. While the phosphoarray did give us some indication that the stress responses more clearly shown in the RNA-Seq data were mediated by the MAPK, PI3K/AKT, and NFκB pathways and are likely anti-apoptotic rather than pro-apoptotic, the technical and statistical limitations of the array restricted our ability to narrow our focus. Furthermore, this type of array is unlikely to provide insight into causality or sequence of events in how Zn^{2+} influences stress response.

An interesting extension of this experiment could be to assess apoptotic signaling at multiple timepoints and at varying levels of Zn^{2+}. Much of the research concerning Zn^{2+}-related oxidative stress in neurons has focused on the apoptotic endpoint following this stress[458,462,480,544,545], with few studies looking at potentially anti-apoptotic effects of Zn^{2+} [551]. However, the relatively small signals exhibited by neurons in our cultures (< 2 nM peak $[Zn^{2+}]$ upon glutamate/Zn^{2+} stimulation) are likely smaller perturbations than those induced in most of these studies, which may modulate apoptotic/anti-apoptotic signaling in different ways than previously seen. In fact, it is intriguing that some evidence of ER stress is visible upon a 6-fold increase in cytosolic Zn^{2+} as seen upon glutamate stimulation alone, whereas the 3-fold Zn^{2+} increase seen upon KCl stimulation induces pro-growth phenotypes (section 2.3.5). Further dissection of Zn^{2+}-related stress pathways and Ca^{2+} dynamics might clarify the sensitivity of this threshold.

3.5 Materials and methods

3.5.1 Neuron isolation/culture

Neuron and glial cell isolation and culture were performed as discussed in section 2.5.1 and Appendix D. No animals were used, as embryonic mouse hippocampal tissue was exclusively obtained from BrainBits, LLC, and neonatal mouse cortical tissue was obtained from the Hoeffer lab at CU Boulder.

3.5.2 Materials

The following fluorescent small molecule dyes were obtained from Thermo Fisher: FluoZin-3 AM (F24195), BCECF AM (B1150), and Fluo-4 (F14201). Stock solutions of FluoZin-3 AM were prepared at 1 mM in DMSO. Stock solutions of BCECF were prepared at 1 mM in DMSO. Stock solutions of Fluo-4 AM were prepared at 1 mM in DMSO.

The Zn^{2+}-specific chelator tris(2-pyridylmethyl)amine (TPA) (723134), $ZnCl_2$ (211273), Chelex (C7901), the ionophore 2-mercaptopyridine N-oxide (pyrithione) (188549), and the protonophore nigericin (N7143) were purchased from Sigma-Aldrich. Stock solutions were prepared as follows: TPA, 20 mM in DMSO; $ZnCl_2$, 1 mg/mL in water treated overnight with chelex; pyrithione, 5 mM in DMSO; nigericin, 1 mM in ethanol.

Resting neuron imaging media (RNIM) was formulated as follows: 145 mM NaCl, 3 mM KCl, 1.5 mM $CaCl_2$, 1 mM $MgCl_2$, 10 mM HEPES, 10 mM glucose, pH 7.4. High-potassium neuron imaging media (KNIM) was made as a 2X K^+ solution (51 mM NaCl, 97 mM KCl, 1.5 mM $CaCl_2$, 1 mM $MgCl_2$, 10 mM HEPES, 10 mM glucose, pH 7.4), which when added 1:1 to RNIM gave concentrations of 98 mM NaCl and 50 mM KCl.

3.5.3 Equipment

Samples for all imaging experiments were imaged on a Nikon Ti-E spinning disc confocal microscope equipped with Nikon Elements software, Ti-E perfect focus system, Yokogawa CSU-X1 spinning disc head, Andor 888 Ultra EMCCD camera and Oko Labs enclosed environmental chamber set at 37 °C.

For electrical stimulation, an IonOptix Myopacer cell stimulator was equipped with a custom set of platinum wire electrodes. All stimulations were performed with 30 V bipolar waveform 10 ms pulses at 5 Hz for a duration of 1 minute.

3.5.4 Stimulation-induced Zn^{2+} measurements with FluoZin-3 AM

Measurements were taken on the Nikon spinning disc microscope using a GFP channel (488 nm excitation, 525/50 nm emission), acquiring images with a 40X (NA 0.95) air objective at 300 ms exposure time, EM multiplier 300, 10 MHz camera readout speed, and 15% laser power.

Neuron cultures (DIV 10-14) were washed and incubated at room temperature in RNIM containing 5 μM FluoZin-3 AM for 30 minutes. Samples were washed 3x in RNIM. Baseline measurements were obtained for 1-3 minutes. Cells were then stimulated with one of three basic methods: 1) 2-minute treatment of high K^+ by mixing KNIM 1:1 with the RNIM already present, 2) 2-minute treatment with 50 μM glutamate, or 3) electrical stimulation (see Equipment section). For KCl or glutamate stimulation, cultures were washed 3x with RNIM and measurements taken for 15 minutes. Cultures were washed 3x with RNIM after stimulation in some electrical stimulation experiments, but not all. In + Zn^{2+} experiments, 10 μM $ZnCl_2$ was added during stimulation. In + TPA experiments, 10 μM TPA was added 1-2 minutes before stimulation and maintained through stimulation and the subsequent 15 minute

imaging period.

Calibrations were performed by adding 10 μM TPA (final concentration) for 2 minutes, then washing out with RNIM and adding 10 μM $ZnCl_2$/0.5 μM pyrithione (final concentration). Measurements were taken until several minutes after a maximum signal was observed.

3.5.5 Intracellular pH measurements with BCECF AM

Measurements were taken on the Nikon spinning disc microscope using a modified GFP channel (488 nm excitation, 2% laser power, 525-542 nm emission) and a CFP/YFP 445 ex channel (445 nm excitation, 4% laser power, 540/30 nm emission), acquiring images with a 40X (NA 0.95) air objective at 300 ms exposure time, EM multiplier 300, 10 MHz camera readout speed (for each channel).

Neuron cultures (DIV 10-14) were washed and incubated at room temperature in RNIM containing 1 μM BCECF AM for 30 minutes. Samples were washed 3x in RNIM. Baseline measurements were obtained for 1-3 minutes, then cells were stimulated by the three methods detailed in the FluoZin-3 AM section above. In + Zn^{2+} experiments, 10 μM $ZnCl_2$ was added during stimulation. In + TPA experiments, 10 μM TPA was added 1 minute before stimulation and maintained through stimulation and the subsequent 15 minute imaging period.

After each experiment, media was replaced by RNIM/10 μM nigericin buffered at a different pH, which equilibrated the intracellular and extracellular pH at a specific value. On a given day, cells in 1-2 different dishes were measured at each pH, then all data assembled to generate a relationship between ratio and pH. Buffered pH solutions were slightly different and measured precisely each day, but generally had values around pH 6.1, 6.4, 6.8, 7.3, and 7.7.

3.5.6 Image analysis

FluoZin-3 AM and BCECF imaging experiments were analyzed with a custom MATLAB script that imports ND2 experiment files, extracts metadata, registers images, allows for manual background and cell ROI selection, and generates raw and background-subtracted average intensity measurements.

For FluoZin-3 quantification, calibration data were manually inspected to obtain minimum and maximum values for intensity measurements, which were used to calculate fractional saturation according to the formula:

$$FS = \frac{X - F_{min}}{F_{max} - F_{min}}$$

where X is the resting, peak, or recovery measurement and F_{min} and F_{max} are the minimum and maximum values of the background-subtracted fluorescence intensity during TPA and Zn^{2+}/pyrithione treatments, respectively. Fractional saturation of FluoZin-3 AM was converted to an approximate intracellular Zn^{2+} concentration according to the formula:

$$[Zn^{2+}] = \frac{K_d}{\frac{1}{FS} - 1}$$

where K_d is the sensor dissociation constant (9.1 nM, Marszalek et al 2016 J Inorg Biochem) and FS is fractional saturation as defined above.

For BCECF AM quantification, BCECF ratios were calculated as (fluorescence $intensity_{488ex}$/fluorescence $intensity_{445ex}$). These ratios were converted to pH values according to the standard curve values obtained during imaging.

3.5.7 Phosphoarray and analysis

Neuron cultures (DIV14) were placed at room temperature. 1 million cells were used per condition. Media was removed and neurons incubated in RNIM (for

glutamate stimulation condition) or RNIM + 10 μM TPA (for glutamate/TPA stimulation condition) for 2 minutes. Cultures were then stimulated with RNIM + 50 μM glutamate or RNIM + 50 μM glutamate + 10 μM TPA, respectively. Neurons were washed 3x and then incubated in RNIM or RNIM + 0.5 μM TPA, respectively, for 30 minutes. Lysates were prepared and each sample was applied to a separate slide of the Phospho Explorer Array (Full Moon Biosystems PEX100) according the Antibody Array Assay Kit (KAS02). Slides were stained with Cy3-Streptavidin (GE PA43001) and sent to Full Moon Biosystems for slide scanning.

Background differed dramatically between the two slides, and thus local background correction was applied by drawing a circle of radius 15 pixels around each antibody spot, then a circle of radius 17 pixels. An effort was made to not include bright outlier pixels in the background region. The average per-pixel background signal from the background ring was adjusted to the area of the analysis ROI and subtracted from the integrated pixel intensity of the analysis ROI to obtain background-corrected signal. Spots were then filtered by requiring them to be brighter than 30% of the average intensity of three negative controls. Any proteins for which phosphosite and total protein antibody spots met this criteria had a ratio calculated as (phosphosite spot intensity)/(median of total protein spot intensities), and any that met filtering criteria in both conditions were compared.

3.5.8 Sequencing and computational pipeline

Neuron cultures (DIV 14) were placed at room temperature. For conditions with no stimulation, glutamate stimulation alone, or glutamate/Zn^{2+} stimulation, media was removed and neurons were incubated in experimental medium for 2 minutes. Experimental medium consisted of RNIM (control condition), RNIM + 50 μM

glutamate, or RNIM + 50 µM glutamate + 10 µM $ZnCl_2$. For glutamate stimulation in the presence of TPA, neuron media was removed and neurons were placed in RNIM + 10 µM TPA for 2 minutes, followed by RNIM + 50 µM glutamate + 10 µM TPA for 2 minutes, followed by RNIM + 10 µM TPA for 5 minutes. After treatment, samples were placed back in the removed neuron culture media and incubated for 90 minutes post-stimulation at 37 °C and 5% CO_2. Five replicates were performed for each of the four conditions (No stimulation, glutamate, glutamate + $ZnCl_2$, glutamate + TPA). Cells were lysed and RNA extracted according to the Qiagen RNeasy kit protocol (74106). Libraries were generated according to the TruSeq Stranded mRNA kit protocol using TruSeq RNA CD Indexes and sequenced on an Illumina NextSeq 500 using a high-output 2x75 paired-end protocol. Two sequencing runs were performed to increase read depth, and resultant fastq files for each sample were concatenated prior to downstream analysis.

Mouse reference genome files (mm10), including genome fasta file and gtf gene annotation file, were downloaded on 8/10/2018 from Illumina iGenomes (https://support.illumina.com/sequencing/sequencing_software/igenome.html).

Quality control of de-multiplexed fastq files was performed using fastQC (v0.11.5, https://www.bioinformatics.babraham.ac.uk/projects/fastqc/). Concatenated fastq files were mapped in a paired-end fashion with HISAT2 (v2.1.0[552]) using parameters `--very-sensitive --max-intronlen 50000 --rna-strandness FR` and including the rn6 genes GTF file. Resultant BAM files were sorted and indexed with samtools (v1.3.1[524]).

The featureCounts function within the R package Rsubread (v1.24.2, R v3.3.0[553]) was used to generate gene-level read counts, with parameters `GTF.featureType="exon"`, `GTP.attrType="gene_id"`,

useMetaFeatures=TRUE, allowMultiOverlap=FALSE, largestOverlap=FALSE, strandSpecific=2, isPairedEnd=TRUE, requireBothEndsMapped=TRUE, checkFragLength=TRUE, minFragLength=50, maxFragLength=60000, countChimericFragments=FALSE, autosort=TRUE. Gene-level read counts were compared pairwise between replicates to examine obvious outliers, and two genes (Rn45s and AF357359) were identified that varied widely among replicates. As these two genes express untranslated RNAs and likely represent variation in polyA enrichment, they were excluded from all downstream principle component analysis (PCA), clustering, differential expression, and GSEA analyses.

For PCA and cluster analysis, gene level counts were normalized to transcripts per million (TPM). All PCA and cluster analysis was performed in R v.3.5.3 with the package cluster (v2.0.8) or default `prcomp`, `hclust`, `cutree`, and `silhoutte` functions. A Euclidean distance matrix was calculated among all replicates and used for hierarchical clustering, then k-means clusters of 2, 3, 4, or 5 were generated for silhouette analysis. Clustering methods indicated one replicate (glzn5) of the glutamate + Zn^{2+} condition was an outlier, and thus this replicate was omitted for downstream differential expression and GSEA analyses.

Differential expression analysis was performed pairwise between conditions with the R package DESeq2 (v1.14.1, R v3.3.0[526]). Differentially expressed genes were filtered according to a false discovery rate (p_{adj}) < 0.05, split into upregulated and downregulated genes, and analyzed with the DAVIDtools Functional Annotation Tool using default parameters (v6.8, https://david.ncifcrf.gov/[527,528]).

GSEA (v3.0, http://software.broadinstitute.org/gsea/index.jsp[529,530]) was run on gene-level TPM values with default parameters except for the following: `Collapse`

`dataset to gene symbols = false`, `Permutation type = gene_set`, `max set size = 3000`, `min set size = 5`. Gene sets were downloaded from the Broad Institute Molecular Signatures Database (v6.2, http://software.broadinstitute.org/gsea/msigdb/index.jsp), collections C2 (curated gene sets) and C5 (GO gene sets).

3.5.9 Statistical analysis and plotting

All statistical tests were performed in R (v3.5.3) within RStudio (v1.2.1335), and are detailed in individual figure legends. For comparison of Zn^{2+} responses to stimulation, two-sided Wilcox Signed Rank tests and two-sided Mann-Whitney U tests were used due to non-normality of original data (as assessed by a Shapiro Wilk test). Statistical tests assessing significance of differential expression are performed by the DESeq2 package and account for multiple hypothesis testing corrections. Statistical tests assessing significance of GO term enrichment results are performed by the GSEA and DAVIDtools algorithms and account for multiple hypothesis testing corrections.

All fits and plots were generated with R (v3.5.3) within RStudio (v1.2.1335), using the packages ggplot2 (v3.1.1), ggrepel (v0.8.0), ggpubr(v0.2), reshape2 (v1.4.3), extrafont (v0.17), dplyr(v0.8.0.1), and cowplot (v0.9.4).

Chapter 4

Future explorations of Zn^{2+}-dependent neuronal signaling

4.1 Further investigation of Zn^{2+}-dependent signaling in dissociated neurons

In our examination of Zn^{2+} signaling in neurons, we took a somewhat naïve approach which led to some very interesting implications. Originally, we wanted to explore global Zn^{2+}-dependent changes in neurons, so we quickly defined stimulation conditions that we knew did induce intracellular Zn^{2+} changes (10 second KCl treatment) and performed RNA-Seq. After finding that gene expression did not change rapidly or dramatically, as our fold changes were extremely small, we then more rigorously tested stimulation conditions and looked for larger Zn^{2+} signals. This led us to perform a similar RNA-Seq experiment using a 2 minute glutamate treatment that induced larger Zn^{2+} signals, yet the resulting gene expression changes were still small and the results even more variable. RNA extraction at later timepoints could enhance our ability to discriminate differences, although it could also include secondary effects that may be hard to parse. Ultimately, these mild changes are likely indicative that Zn^{2+} signals do alter gene expression, but not drastically. The best way to increase our signal to noise in looking at these changes would be to do nascent transcription sequencing, such as PRO-Seq, which would require many more neurons than we usually grow, or potentially use ATAC-Seq as a

proxy for nascent transcription. These would allow us to focus more specifically on Zn^{2+}-related transcriptional changes after stimulation. Ideally these techniques would also give us higher resolution in looking at Zn^{2+}-dependent transcription changes that would allow us to specifically probe endogenous Zn^{2+} signals rather than rely on larger changes induced by stimulation in the presence of exogenous Zn^{2+}.

Despite the fact that different stimulation conditions did not give us a cleaner sequencing experiment, the contrast in differentially expressed genes was striking. There are a variety of factors that are different between these two experiments, including organism, stimulation chemical, stimulation duration, and maximum intracellular Zn^{2+} concentration. It would be fascinating to control for several more of these factors in order to determine whether the growth vs. stress phenotypes are truly Zn^{2+}-dependent. One possible way to do this would be to perform RNA-Seq/PRO-Seq or phosphoarrays/phosphoproteomics on neurons after KCl or glutamate stimulation in different concentrations of both extracellular and cell-permeable Zn^{2+} chelators. If the resolution of detection were high enough, we could ideally identify a titratable Zn^{2+} response, and establish a threshold between Zn^{2+}-dependent induction of growth or stress. Further imaging-based exploration of Ca^{2+} and ROS signaling in these different conditions would also help us define confounding variables, and potentially look at crosstalk between Zn^{2+} and other stimulation-dependent intracellular signaling.

4.2 Expansion of exploratory methods to brain slices

Our original plan for my graduate work was to establish global sequencing methods in a system where we could rigorously define Zn^{2+} dynamics (dissociated neurons) and then to apply these methods to a more physiological system. Much of

the work concerning Zn^{2+} signaling in neurons has been conducted in brain slices for compelling reasons. Slices, if properly prepared, preserve endogenous synaptic Zn^{2+} and retain neural connectivity, meaning that presynaptic and postsynaptic Zn^{2+}-dependent signaling can be meaningfully dissected. Furthermore, conditions and tools have been established in slices for a number of different stimulation paradigms with different Zn^{2+} perturbations. Using these protocols, we could stimulate a region in the hippocampus in different Zn^{2+} conditions and then collect downstream neurons for sequencing or phosphorylation analysis, using bulk RNA-Seq, single-cell RNA-Seq, ATAC-Seq, or phosphoproteomics. This would ideally allow us to determine whether the Zn^{2+}-dependent cell growth and stress phenotypes that we see in our dissociated neurons are also present in neurons with synaptic connections developed *in vivo* and endogenous synaptic Zn^{2+}, and would contextualize many other brain slice-based experiments investigating Zn^{2+} in neurobiology.

(This page intentionally left blank)

Bibliography

1. Maret, W. The Metals in the Biological Periodic System of the Elements: Concepts and Conjectures. *Int. J. Mol. Sci.* **17**, (2016).

2. Williams, R. J. P. The biochemistry of zinc. *Polyhedron* **6**, 61–69 (1987).

3. Andreini, C., Bertini, I. & Rosato, A. Metalloproteomes: a bioinformatic approach. *Acc. Chem. Res.* **42**, 1471–1479 (2009).

4. Maret, W. Zinc coordination environments in proteins determine zinc functions. *J. Trace Elem. Med. Biol. Organ Soc. Miner. Trace Elem. GMS* **19**, 7–12 (2005).

5. Csopak, H. The specific binding of zinc(II) to alkaline phosphatase of Escherichia coli. *Eur. J. Biochem. FEBS* **7**, 186–192 (1969).

6. Fedotova, A. A., Bonchuk, A. N., Mogila, V. A. & Georgiev, P. G. C_2H_2 Zinc Finger Proteins: The Largest but Poorly Explored Family of Higher Eukaryotic Transcription Factors. *Acta Naturae* **9**, 47–58 (2017).

7. Michel, S. L. J. & Besold, A. N. The Neural Zinc Finger Factor/Myelin Transcription Factor Proteins: metal binding, fold and function. *Biochemistry* (2015). doi:10.1021/bi501371a

8. Schmitges, F. W. *et al.* Multiparameter functional diversity of human C2H2 zinc finger proteins. *Genome Res.* (2016). doi:10.1101/gr.209643.116

9. Reddi, A. R., Pawlowska, M. & Gibney, B. R. Evaluation of the Intrinsic Zn(II) Affinity of a Cys_3His_1 Site in the Absence of Protein Folding Effects. *Inorg. Chem.* (2015). doi:10.1021/acs.inorgchem.5b00718

10. Andreini, C., Banci, L., Bertini, I. & Rosato, A. Counting the zinc-proteins encoded in the human genome. *J. Proteome Res.* **5**, 196–201 (2006).

11. Patel, K., Kumar, A. & Durani, S. Analysis of the structural consensus of the zinc coordination centers of metalloprotein structures. *Biochim. Biophys. Acta* **1774**, 1247–1253 (2007).

12. Valasatava, Y., Andreini, C. & Rosato, A. Hidden relationships between metalloproteins unveiled by structural comparison of their metal sites. *Sci. Rep.* **5**, 9486 (2015).

13. Yao, S., Flight, R. M., Rouchka, E. C. & Moseley, H. N. B. A less biased analysis of metalloproteins reveals novel zinc coordination geometries. *Proteins* (2015). doi:10.1002/prot.24834

14. Wuehler, S. E., Peerson, J. M. & Brown, K. H. Use of national food balance data to estimate the adequacy of zinc in national food supplies: methodology and regional estimates. *Public Health Nutr.* **8**, 812–819 (2005).

15. Plum, L. M., Rink, L. & Haase, H. The Essential Toxin: Impact of Zinc on Human Health. *Int. J. Environ. Res. Public. Health* **7**, 1342–1365 (2010).

16. Drobinskaya, I., Neumaier, F., Pereverzev, A., Hescheler, J. & Schneider, T. Diethyldithiocarbamate-mediated zinc ion chelation reveals role of Cav2.3 channels in glucagon secretion. *Biochim. Biophys. Acta* (2015). doi:10.1016/j.bbamcr.2015.01.001

17. Zhang, T., Sui, D. & Hu, J. Structural insights of ZIP4 extracellular domain critical for optimal zinc transport. *Nat. Commun.* **7**, 11979 (2016).

18. Ohashi, W. *et al.* Zinc Transporter SLC39A7/ZIP7 Promotes Intestinal Epithelial Self-Renewal by Resolving ER Stress. *PLoS Genet.* **12**, e1006349 (2016).

19. Guthrie, G. J. *et al.* Influence of ZIP14 (slc39A14) on intestinal zinc processing and barrier function. *Am. J. Physiol. Gastrointest. Liver Physiol.* ajpgi.00021.2014 (2014). doi:10.1152/ajpgi.00021.2014

20. Limpongsanurak, W., Kuptanon, C., Singhamatr, P., Singalavanija, S. & Sirisutthisuwan, S. SLC39A4 mutation in zinc deficiency patients. *J. Med. Assoc. Thail. Chotmaihet Thangphaet* **97 Suppl 6**, S14-19 (2014).

21. Anzilotti, C. *et al.* An essential role for the Zn^{2+} transporter ZIP7 in B cell development. *Nat. Immunol.* (2019). doi:10.1038/s41590-018-0295-8

22. Golan, Y., Kambe, T. & Assaraf, Y. G. The role of the zinc transporter SLC30A2/ZnT2 in transient neonatal zinc deficiency. *Met. Integr. Biometal Sci.* (2017). doi:10.1039/c7mt00162b

23. Kumar, L. *et al.* Altered expression of two zinc transporters, SLC30A5 and SLC30A6, underlies a mammary gland disorder of reduced zinc secretion into milk. *Genes Nutr.* **10**, 487 (2015).

24. Petkovic, V., Miletta, M. C., Eblé, A., Flück, C. E. & Mullis, P.-E. Alteration of ZnT5-Mediated Zinc Import into the Early Secretory Pathway Affects the Secretion of Growth Hormone from Rat Pituitary Cells. *Horm. Res. Paediatr.* (2014). doi:10.1159/000365924

25. Hojyo, S. & Fukada, T. 5: Zinc transporters and signaling in physiology and pathogenesis. *Arch. Biochem. Biophys.* (2016). doi:10.1016/j.abb.2016.06.020

26. Inoue, Y. *et al.* ZIP2, a zinc transporter, is associated with keratinocyte differentiation. *J. Biol. Chem.* (2014). doi:10.1074/jbc.M114.560821

27. Taylor, K. M. *et al.* Zinc transporter ZIP10 forms a heteromer with ZIP6 which regulates embryonic development and cell migration. *Biochem. J.* (2016). doi:10.1042/BCJ20160388

28. Tuschl, K. *et al.* Mutations in SLC39A14 disrupt manganese homeostasis and cause childhood-onset parkinsonism-dystonia. *Nat. Commun.* **7**, 11601 (2016).

29. Quadri, M. *et al.* Mutations in SLC30A10 Cause Parkinsonism and Dystonia with Hypermanganesemia, Polycythemia, and Chronic Liver Disease. *Am. J. Hum. Genet.* **90**, 467–477 (2012).

30. Pickrell, J. K. *et al.* Detection and interpretation of shared genetic influences on 42 human traits. *Nat. Genet.* **48**, 709–717 (2016).

31. Nowak, G., Szewczyk, B. & Pilc, A. Zinc and depression. An update. *Pharmacol. Rep. PR* **57**, 713–718 (2005).

32. Atrian, S. & Capdevila, M. Metallothionein-protein interactions. *Biomol. Concepts* **4**, 143–160 (2013).

33. Vela, G. *et al.* Zinc in Gut-Brain Interaction in Autism and Neurological Disorders. *Neural Plast.* **2015**, 972791 (2015).

34. Adam, P. *et al.* Metallothioneins and Prion-and Amyloid-Related Diseases. *J. Alzheimers Dis. JAD* (2016). doi:10.3233/JAD-150984

35. Capasso, M., Jeng, J.-M., Malavolta, M., Mocchegiani, E. & Sensi, S. L. Zinc dyshomeostasis: a key modulator of neuronal injury. *J. Alzheimers Dis. JAD* **8**, 93–108; discussion 209-215 (2005).

36. Kim, T. D., Paik, S. R., Yang, C. H. & Kim, J. Structural changes in alpha-synuclein affect its chaperone-like activity in vitro. *Protein Sci. Publ. Protein Soc.* **9**, 2489–2496 (2000).

37. Li, C., Meng, L., Li, X., Li, D. & Jiang, L.-H. Non-NMDAR neuronal Ca(2+)-permeable channels in delayed neuronal death and as potential therapeutic

targets for ischemic brain damage. *Expert Opin. Ther. Targets* **19**, 879–892 (2015).

38. Kanninen, K. M. *et al.* Increased zinc and manganese in parallel with neurodegeneration, synaptic protein changes and activation of Akt/GSK3 signaling in ovine CLN6 neuronal ceroid lipofuscinosis. *PloS One* **8**, e58644 (2013).

39. Zhao, L. *et al.* The zinc transporter ZIP12 regulates the pulmonary vascular response to chronic hypoxia. *Nature* **524**, 356–360 (2015).

40. Mutai, H., Miya, F., Fujii, M., Tsunoda, T. & Matsunaga, T. Attenuation of Progressive Hearing Loss in DBA/2J Mice by Reagents that Affect Epigenetic Modifications Is Associated with Up-Regulation of the Zinc Importer Zip4. *PloS One* **10**, e0124301 (2015).

41. Hamon, R. *et al.* Zinc and Zinc Transporters in Macrophages and Their Roles in Efferocytosis in COPD. *PloS One* **9**, e110056 (2014).

42. Cheng, X. *et al.* SLC39A6 Promotes Aggressiveness of Esophageal Carcinoma Cells by Increasing Intracellular Levels of Zinc, Activating Phosphatidylinositol 3-kinase Signaling, and Upregulating Genes That Regulate Metastasis. *Gastroenterology* (2017). doi:10.1053/j.gastro.2017.02.006

43. Thomas, P., Dong, J., Berg, A. H. & Pang, Y. Identification and characterization of membrane androgen receptors in the ZIP9 zinc transporter subfamily: II. Role of human ZIP9 in testosterone-induced prostate and breast cancer cell apoptosis. *Endocrinology* en20141201 (2014). doi:10.1210/en.2014-1201

44. Gu, H. F. Genetic, Epigenetic and Biological Effects of Zinc Transporter (SLC30A8) in Type 1 and Type 2 Diabetes. *Curr. Diabetes Rev.* (2015).

45. Myers, S. A. Zinc transporters and zinc signaling: new insights into their role in type 2 diabetes. *Int. J. Endocrinol.* **2015**, 167503 (2015).

46. Adulcikas, J., Sonda, S., Norouzi, S., Sohal, S. S. & Myers, S. Targeting the Zinc Transporter ZIP7 in the Treatment of Insulin Resistance and Type 2 Diabetes. *Nutrients* **11**, (2019).

47. Tamaki, M. *et al.* The diabetes-susceptible gene SLC30A8/ZnT8 regulates hepatic insulin clearance. *J. Clin. Invest.* **123**, 4513–4524 (2013).

48. Liu, Y. *et al.* Characterization of Zinc Influx Transporters (ZIPs) in Pancreatic Beta Cells: Roles in Regulating Cytosolic Zinc Homeostasis and Insulin Secretion. *J. Biol. Chem.* (2015). doi:10.1074/jbc.M115.640524

49. Yi, B., Huang, G. & Zhou, Z.-G. Current and Future Clinical Applications of Zinc Transporter-8 in Type 1 Diabetes Mellitus. *Chin. Med. J. (Engl.)* **128**, 2387–2394 (2015).

50. Maxel, T. *et al.* The zinc transporter Zip14 (SLC39a14) affects Beta-cell Function: Proteomics, Gene expression, and Insulin secretion studies in INS-1E cells. *Sci. Rep.* **9**, 8589 (2019).

51. Byun, H.-R., Choi, J. A. & Koh, J.-Y. The role of metallothionein-3 in streptozotocin-induced beta-islet cell death and diabetes in mice. *Met. Integr. Biometal Sci.* (2014). doi:10.1039/c4mt00143e

52. Khrenova, M. G., Savitsky, A. P., Topol, I. A. & Nemukhin, A. V. Exploration of the Zinc Finger Motif in Controlling Activity of Matrix Metalloproteinases. *J. Phys. Chem. B* (2014). doi:10.1021/jp5088702

53. Holubova, M. *et al.* KRAS NF-κB is involved in the development of zinc resistance and reduced curability in prostate cancer. *Met. Integr. Biometal Sci.* (2014). doi:10.1039/c4mt00065j

54. Nedumpully-Govindan, P., Yang, Y., Andorfer, R., Cao, W. & Ding, F. Promotion or Inhibition of Islet Amyloid Polypeptide Aggregation by Zinc Coordination Depends on Its Relative Concentration. *Biochemistry* (2015). doi:10.1021/acs.biochem.5b00891

55. Manna, P. T. *et al.* TRPM2-mediated intracellular Zn^{2+} release triggers pancreatic ß-cell death. *Biochem. J.* **466**, 537–546 (2015).

56. Jeong, J. *et al.* Promotion of vesicular zinc efflux by ZIP13 and its implications for spondylocheiro dysplastic Ehlers-Danlos syndrome. *Proc. Natl. Acad. Sci. U. S. A.* **109**, E3530-3538 (2012).

57. Slepchenko, K. G., Lu, Q. & Li, Y. V. Zinc wave during the treatment of hypoxia is required for initial reactive oxygen species activation in mitochondria. *Int. J. Physiol. Pathophysiol. Pharmacol.* **8**, 44–51 (2016).

58. Istrate, A. N. *et al.* Interplay of histidine residues of the Alzheimer's disease Aß peptide governs its Zn-induced oligomerization. *Sci. Rep.* **6**, 21734 (2016).

59. Schulte, M., Mattay, D., Kriegel, S., Hellwig, P. & Friedrich, T. Inhibition of the Escherichia coli respiratory complex I by Zn^{2+}. *Biochemistry* (2014). doi:10.1021/bi5009276

60. Ma, L., Terwilliger, A. & Maresso, A. W. Iron and zinc exploitation during bacterial pathogenesis. *Met. Integr. Biometal Sci.* (2015). doi:10.1039/c5mt00170f

61. Cunden, L. S., Gaillard, A. & Nolan, E. M. Calcium Ions Tune the Zinc-Sequestering Properties and Antimicrobial Activity of Human S100A12. *Chem. Sci. R. Soc. Chem. 2010* **7**, 1338–1348 (2016).

62. Capdevila, D. A., Wang, J. & Giedroc, D. P. Bacterial Strategies to Maintain Zinc Metallostasis at the Host-Pathogen Interface. *J. Biol. Chem.* (2016). doi:10.1074/jbc.R116.742023

63. Ammendola, S. *et al.* Zinc is required to ensure the expression of flagella and the ability to form biofilms in Salmonella enterica sv Typhimurium. *Met. Integr. Biometal Sci.* **8**, 1131–1140 (2016).

64. Rahman, M. T. & Karim, M. M. Metallothionein: a Potential Link in the Regulation of Zinc in Nutritional Immunity. *Biol. Trace Elem. Res.* (2017). doi:10.1007/s12011-017-1061-8

65. Kapetanovic, R. *et al.* Salmonella employs multiple mechanisms to subvert the TLR-inducible zinc-mediated antimicrobial response of human macrophages. *FASEB J. Off. Publ. Fed. Am. Soc. Exp. Biol.* (2016). doi:10.1096/fj.201500061

66. Bonaventura, P., Lamboux, A., Albarède, F. & Miossec, P. A Feedback Loop between Inflammation and Zn Uptake. *PloS One* **11**, e0147146 (2016).

67. Read, S. A. *et al.* Zinc is a potent and specific inhibitor of IFN-λ3 signalling. *Nat. Commun.* **8**, 15245 (2017).

68. Gao, H., Dai, W., Zhao, L., Min, J. & Wang, F. The Role of Zinc and Zinc Homeostasis in Macrophage Function. *J. Immunol. Res.* **2018**, 6872621 (2018).

69. Fukada, T., Hojyo, S., Hara, T. & Takagishi, T. Revisiting the old and learning the new of zinc in immunity. *Nat. Immunol.* (2019). doi:10.1038/s41590-019-0319-z

70. Haase, H. *et al.* Zinc Signals Are Essential for Lipopolysaccharide-Induced Signal Transduction in Monocytes. *J. Immunol.* **181**, 6491–6502 (2008).

71. Krezel, A., Hao, Q. & Maret, W. The zinc/thiolate redox biochemistry of metallothionein and the control of zinc ion fluctuations in cell signaling. *Arch. Biochem. Biophys.* **463**, 188–200 (2007).

72. Gilston, B. A. *et al.* Structural and Mechanistic Basis of Zinc Regulation Across the E. coli Zur Regulon. *PLoS Biol* **12**, e1001987 (2014).

73. Choi, S. & Bird, A. J. Zinc'ing sensibly: controlling zinc homeostasis at the transcriptional level. *Met. Integr. Biometal Sci.* **6**, 1198–1215 (2014).

74. Hardyman, J. E. J. *et al.* Zinc sensing by metal-responsive transcription factor 1 (MTF1) controls metallothionein and ZnT1 expression to buffer the sensitivity of the transcriptome response to zinc. *Met. Integr. Biometal Sci.* (2016). doi:10.1039/c5mt00305a

75. Eide, D. J. Zinc transporters and the cellular trafficking of zinc. *Biochim. Biophys. Acta* **1763**, 711–722 (2006).

76. Kambe, T., Tsuji, T., Hashimoto, A. & Itsumura, N. The Physiological, Biochemical, and Molecular Roles of Zinc Transporters in Zinc Homeostasis and Metabolism. *Physiol. Rev.* **95**, 749–784 (2015).

77. Ho, E. *et al.* Zinc transporter expression in zebrafish (Danio rerio) during development. *Comp. Biochem. Physiol. Toxicol. Pharmacol. CBP* **155**, 26–32 (2012).

78. Kimura, T. & Kambe, T. The Functions of Metallothionein and ZIP and ZnT Transporters: An Overview and Perspective. *Int. J. Mol. Sci.* **17**, (2016).

79. Krężel, A. & Maret, W. The biological inorganic chemistry of zinc ions. *Arch. Biochem. Biophys.* **611**, 3–19 (2016).

80. Petering, D. H. & Mahim, A. Proteomic High Affinity Zn^{2+} Trafficking: Where Does Metallothionein Fit in? *Int. J. Mol. Sci.* **18**, 1289 (2017).

81. Qin, Y. *et al.* Direct comparison of a genetically encoded sensor and small molecule indicator: implications for quantification of cytosolic Zn(2+). *ACS Chem. Biol.* **8**, 2366–2371 (2013).

82. Hessels, A. M. & Merkx, M. Simple Method for Proper Analysis of FRET Sensor Titration Data and Intracellular Imaging Experiments Based on Isosbestic Points. *ACS Sens.* **1**, 498–502 (2016).

83. Krężel, A. & Maret, W. Zinc-buffering capacity of a eukaryotic cell at physiological pZn. *JBIC J. Biol. Inorg. Chem.* **11**, 1049–1062 (2006).

84. Baltaci, A. K., Yuce, K. & Mogulkoc, R. Zinc Metabolism and Metallothioneins. *Biol. Trace Elem. Res.* (2017). doi:10.1007/s12011-017-1119-7

85. Artells, E., Palacios, Ò., Capdevila, M. & Atrian, S. Mammalian MT1 and MT2 metallothioneins differ in their metal binding abilities. *Metallomics* **5**, 1397–1410 (2013).

86. Colvin, R. A. *et al.* Insights into Zn^{2+} homeostasis in neurons from experimental and modeling studies. *AJP Cell Physiol.* **294**, C726–C742 (2008).

87. Pinter, T. B. J. & Stillman, M. J. The Zinc Balance: Competitive Zinc Metalation of Carbonic Anhydrase and Metallothionein 1A. *Biochemistry* (2014). doi:10.1021/bi5008673

88. Levaot, N. & Hershfinkel, M. How cellular Zn^{2+} signaling drives physiological functions. *Cell Calcium* **75**, 53–63 (2018).

89. Maret, W. Molecular aspects of human cellular zinc homeostasis: redox control of zinc potentials and zinc signals. *Biometals Int. J. Role Met. Ions Biol. Biochem. Med.* **22**, 149–157 (2009).

90. Syring, K. E. *et al.* Combined Deletion of Slc30a7 and Slc30a8 Unmasks a Critical Role for ZnT8 in Glucose-Stimulated Insulin Secretion. *Endocrinology* en20161573 (2016). doi:10.1210/en.2016-1573

91. Miao, X. *et al.* Zinc homeostasis in the metabolic syndrome and diabetes, Zinc homeostasis in the metabolic syndrome and diabetes. *Front. Med.* **7**, 31–52 (2013).

92. Miyai, T. *et al.* Zinc transporter SLC39A10/ZIP10 facilitates antiapoptotic signaling during early B-cell development. *Proc. Natl. Acad. Sci. U. S. A.* (2014). doi:10.1073/pnas.1323549111

93. Cohen, L., Sekler, I. & Hershfinkel, M. The zinc sensing receptor, ZnR/GPR39, controls proliferation and differentiation of colonocytes and thereby tight junction formation in the colon. *Cell Death Dis.* **5**, e1307 (2014).

94. Lin, R. S., Rodriguez, C., Veillette, A. & Lodish, H. F. Zinc Is Essential for Binding of p56 lck to CD4 and CD8α. *J. Biol. Chem.* **273**, 32878–32882 (1998).

95. Dierichs, L., Kloubert, V. & Rink, L. Cellular zinc homeostasis modulates polarization of THP-1-derived macrophages. *Eur. J. Nutr.* (2017). doi:10.1007/s00394-017-1491-2

96. Rice, J. M., Zweifach, A. & Lynes, M. A. Metallothionein regulates intracellular zinc signaling during CD4(+) T cell activation. *BMC Immunol.* **17**, 13 (2016).

97. Woodier, J., Rainbow, R. D., Stewart, A. J. & Pitt, S. J. Intracellular Zinc Modulates Cardiac Ryanodine Receptor-mediated Calcium Release. *J. Biol. Chem.* **290**, 17599–17610 (2015).

98. Thokala, S., Bodiga, V. L., Kudle, M. R. & Bodiga, S. Comparative Response of Cardiomyocyte ZIPs and ZnTs to Extracellular Zinc and TPEN. *Biol. Trace Elem. Res.* (2019). doi:10.1007/s12011-019-01671-0

99. Billur, D. *et al.* Interplay Between Cytosolic Free Zn(2+) and Mitochondrion Morphological Changes in Rat Ventricular Cardiomyocytes. *Biol. Trace Elem. Res.* **174**, 177–188 (2016).

100. Kong, B. Y. *et al.* Maternally-derived zinc transporters ZIP6 and ZIP10 drive the mammalian oocyte-to-egg transition. *Mol. Hum. Reprod.* (2014). doi:10.1093/molehr/gau066

101. McGinnis, L. A., Lee, H. J., Robinson, D. N. & Evans, J. P. MAPK3/1 (ERK1/2) and Myosin Light Chain Kinase in Mammalian Eggs Affect Myosin-II Function and Regulate the Metaphase II State in a Calcium- and Zinc-Dependent Manner. *Biol. Reprod.* (2015). doi:10.1095/biolreprod.114.127027

102. Kong, B. Y. *et al.* The inorganic anatomy of the mammalian preimplantation embryo and the requirement of zinc during the first mitotic divisions. *Dev. Dyn. Off. Publ. Am. Assoc. Anat.* (2015). doi:10.1002/dvdy.24285

103. Que, E. L. *et al.* Quantitative mapping of zinc fluxes in the mammalian egg reveals the origin of fertilization-induced zinc sparks. *Nat. Chem.* **7**, 130–139 (2015).

104. Shimizu, Y., Koyama, R. & Kawamoto, T. Rho kinase-dependent desensitization of GPR39; a unique mechanism of GPCR downregulation. *Biochem. Pharmacol.* **140**, 105–114 (2017).

105. Sunuwar, L., Gilad, D. & Hershfinkel, M. The zinc sensing receptor, ZnR/GPR39, in health and disease. *Front. Biosci. Landmark Ed.* **22**, 1469–1492 (2017).

106. Xiong, Y. *et al.* Zinc binds to and directly inhibits protein phosphatase 2A in vitro. *Neurosci. Bull.* (2015). doi:10.1007/s12264-014-1519-z

107. Krezel, A. & Maret, W. Thionein/metallothionein control Zn(II) availability and the activity of enzymes. *J. Biol. Inorg. Chem. JBIC Publ. Soc. Biol. Inorg. Chem.* **13**, 401–409 (2008).

108. Bellomo, E., Hogstrand, C. & Maret, W. Redox and zinc signalling pathways converging on protein tyrosine phosphatases. *Free Radic. Biol. Med.* **75 Suppl 1**, S9 (2014).

109. Maret, W. Inhibitory zinc sites in enzymes. *Biometals Int. J. Role Met. Ions Biol. Biochem. Med.* **26**, 197–204 (2013).

110. Brautigan, D. L., Bornstein, P. & Gallis, B. Phosphotyrosyl-protein phosphatase. Specific inhibition by Zn. *J. Biol. Chem.* **256**, 6519–6522 (1981).

111. Dagbay, K. *et al.* A multipronged approach for compiling a global map of allosteric regulation in the apoptotic caspases. *Methods Enzymol.* **544**, 215–249 (2014).

112. Jakob, U., Eser, M. & Bardwell, J. C. Redox switch of hsp33 has a novel zinc-binding motif. *J. Biol. Chem.* **275**, 38302–38310 (2000).

113. Nimmanon, T., Ziliotto, S., Morris, S., Flanagan, L. & Taylor, K. M. Phosphorylation of zinc channel ZIP7 drives MAPK, PI3K and mTOR growth and proliferation signalling. *Met. Integr. Biometal Sci.* **9**, 471–481 (2017).

114. Hönscheid, A., Dubben, S., Rink, L. & Haase, H. Zinc differentially regulates mitogen-activated protein kinases in human T cells. *J. Nutr. Biochem.* **23**, 18–26 (2012).

115. Jang, Y. *et al.* NO mobilizes intracellular Zn^{2+} via cGMP/PKG signaling pathway and prevents mitochondrial oxidant damage in cardiomyocytes. *Cardiovasc. Res.* **75**, 426–433 (2007).

116. Zhao, Y., Feresin, R. G., Falcon-Perez, J. M. & Salazar, G. Differential Targeting of SLC30A10/ZnT10 Heterodimers to Endolysosomal Compartments Modulates EGF-induced MEK/ERK1/2 Activity. *Traffic Cph. Den.* (2016). doi:10.1111/tra.12371

117. Jarosz, M., Olbert, M., Wyszogrodzka, G., Młyniec, K. & Librowski, T. Antioxidant and anti-inflammatory effects of zinc. Zinc-dependent NF-κB signaling. *Inflammopharmacology* (2017). doi:10.1007/s10787-017-0309-4

118. Stand, F., Rosoff, B., Williams, G. L. & Spencer, H. Tissue Distribution Studies of Ionic and Chelated Zn65 in Mice. *J. Pharmacol. Exp. Ther.* **138**, 399–404 (1962).

119. Claiborne, B. J., Rea, M. A. & Terrian, D. M. Detection of zinc in isolated nerve terminals using a modified Timm's sulfide-silver method. *J. Neurosci. Methods* **30**, 17–22 (1989).

120. Du, P. & Lippard, S. J. A highly selective turn-on colorimetric, red fluorescent sensor for detecting mobile zinc in living cells. *Inorg. Chem.* **49**, 10753–10755 (2010).

121. Loas, A., Radford, R. J. & Lippard, S. J. Addition of a second binding site increases the dynamic range but alters the cellular localization of a red fluorescent probe for mobile zinc. *Inorg. Chem.* **53**, 6491–6493 (2014).

122. Rivera-Fuentes, P. *et al.* A Far-Red Emitting Probe for Unambiguous Detection of Mobile Zinc in Acidic Vesicles and Deep Tissue. *Chem. Sci. R. Soc. Chem. 2010* **6**, 1944–1948 (2015).

123. Shi, Y. *et al.* A novel dual-emission ratiometric fluorescent nanoprobe for sensing and intracellular imaging of Zn^{2+}. *Biosens. Bioelectron.* **61**, 397–403 (2014).

124. Liu, Z. *et al.* In vivo ratiometric Zn^{2+} imaging in zebrafish larvae using a new visible light excitable fluorescent sensor. *Chem. Commun.* **50**, 1253–1255 (2014).

125. Iniya, M., Jeyanthi, D., Krishnaveni, K., Mahesh, A. & Chellappa, D. Triazole based ratiometric fluorescent probe for Zn^{2+} and its application in bioimaging. *Spectrochim. Acta. A. Mol. Biomol. Spectrosc.* **120**, 40–46 (2014).

126. Sreenath, K., Yuan, Z., Allen, J. R., Davidson, M. W. & Zhu, L. A Fluorescent Indicator for Imaging Lysosomal Zinc(II) with Förster Resonance Energy Transfer (FRET)-Enhanced Photostability and a Narrow Band of Emission. *Chem. Weinh. Bergstr. Ger.* (2014). doi:10.1002/chem.201403479

127. Santhakumar, H. *et al.* Real Time Imaging and Dynamics of Hippocampal Zn^{2+} under Epileptic Condition Using a Ratiometric Fluorescent Probe. *Sci. Rep.* **8**, 9069 (2018).

128. Nolan, E. M. & Lippard, S. J. Small-Molecule Fluorescent Sensors for Investigating Zinc Metalloneurochemistry. *Acc. Chem. Res.* **42**, 193–203 (2008).

129. Carpenter, M. C., Lo, M. N. & Palmer, A. E. Techniques for measuring cellular zinc. *Arch. Biochem. Biophys.* (2016). doi:10.1016/j.abb.2016.08.018

130. Karim, M. R. & Petering, D. H. Newport Green, a fluorescent sensor of weakly bound cellular Zn(2+): competition with proteome for Zn(2.). *Met. Integr. Biometal Sci.* (2015). doi:10.1039/c5mt00167f

131. Nolan, E. M. *et al.* Zinspy Sensors with Enhanced Dynamic Range for Imaging Neuronal Cell Zinc Uptake and Mobilization. *J. Am. Chem. Soc.* **128**, 15517–15528 (2006).

132. Komatsu, K., Kikuchi, K., Kojima, H., Urano, Y. & Nagano, T. Selective zinc sensor molecules with various affinities for Zn^{2+}, revealing dynamics and regional distribution of synaptically released Zn^{2+} in hippocampal slices. *J. Am. Chem. Soc.* **127**, 10197–10204 (2005).

133. Carter, K. P., Young, A. M. & Palmer, A. E. Fluorescent sensors for measuring metal ions in living systems. *Chem. Rev.* **114**, 4564–4601 (2014).

134. Meeusen, J. W., Nowakowski, A. & Petering, D. H. Reaction of metal-binding ligands with the zinc proteome: zinc sensors and N,N,N',N'-tetrakis(2-pyridylmethyl)ethylenediamine. *Inorg. Chem.* **51**, 3625–3632 (2012).

135. Marszałek, I., Goch, W. & Bal, W. Ternary Zn(II) Complexes of FluoZin-3 and the Low Molecular Weight Component of the Exchangeable Cellular Zinc Pool. *Inorg. Chem.* (2018). doi:10.1021/acs.inorgchem.8b00489

136. Nowakowski, A. B., Meeusen, J. W., Menden, H., Tomasiewicz, H. & Petering, D. H. Chemical-Biological Properties of Zinc Sensors TSQ and Zinquin: Formation of Sensor-Zn-Protein Adducts versus Zn(Sensor)2 Complexes. *Inorg. Chem.* (2015). doi:10.1021/acs.inorgchem.5b01535

137. Snitsarev, V. *et al.* Fluorescent detection of Zn(2+)-rich vesicles with Zinquin: mechanism of action in lipid environments. *Biophys. J.* **80**, 1538–1546 (2001).

138. Kay, A. R. & Tóth, K. Influence of location of a fluorescent zinc probe in brain slices on its response to synaptic activation. *J. Neurophysiol.* **95**, 1949–1956 (2006).

139. Kay, A. R. Imaging synaptic zinc: promises and perils. *Trends Neurosci.* **29**, 200–206 (2006).

140. Sanford, L. & Palmer, A. Recent Advances in Development of Genetically Encoded Fluorescent Sensors. *Methods Enzymol.* **589**, 1–49 (2017).

141. Qin, Y., Sammond, D. W., Braselmann, E., Carpenter, M. C. & Palmer, A. E. Development of an optical Zn^{2+} probe based on a single fluorescent protein. *ACS Chem. Biol.* (2016). doi:10.1021/acschembio.6b00442

142. Fudge, D. H., Black, R., Son, L., LeJeune, K. & Qin, Y. Optical Recording of Zn^{2+} Dynamics in the Mitochondrial Matrix and Intermembrane Space with the GZnP2 Sensor. *ACS Chem. Biol.* **13**, 1897–1905 (2018).

143. Chen, Z.-J. & Ai, H.-W. Single Fluorescent Protein-Based Indicators for Zinc Ion (Zn^{2+}). *Anal. Chem.* (2016). doi:10.1021/acs.analchem.6b01653

144. Dittmer, P. J., Miranda, J. G., Gorski, J. A. & Palmer, A. E. Genetically encoded sensors to elucidate spatial distribution of cellular zinc. *J. Biol. Chem.* **284**, 16289–16297 (2009).

145. Lindenburg, L. H., Hessels, A. M., Ebberink, E. H. T. M., Arts, R. & Merkx, M. Robust red FRET sensors using self-associating fluorescent domains. *ACS Chem. Biol.* **8**, 2133–2139 (2013).

146. Miranda, J. G. *et al.* New alternately colored FRET sensors for simultaneous monitoring of Zn^{2+} in multiple cellular locations. *PloS One* **7**, e49371 (2012).

147. Qin, Y., Dittmer, P. J., Park, J. G., Jansen, K. B. & Palmer, A. E. Measuring steady-state and dynamic endoplasmic reticulum and Golgi Zn^{2+} with genetically encoded sensors. *Proc. Natl. Acad. Sci. U. S. A.* **108**, 7351–7356 (2011).

148. Vinkenborg, J. L. *et al.* Genetically encoded FRET sensors to monitor intracellular Zn^{2+} homeostasis. *Nat. Methods* **6**, 737–740 (2009).

149. Aper, S. J. A., Dierickx, P. & Merkx, M. Dual readout BRET/FRET-sensors for measuring intracellular zinc. *ACS Chem. Biol.* (2016). doi:10.1021/acschembio.6b00453

150. Hessels, A. M. *et al.* eZinCh-2: a versatile, genetically-encoded FRET sensor for cytosolic and intra-organelle Zn^{2+} imaging. *ACS Chem. Biol.* (2015). doi:10.1021/acschembio.5b00211

151. Park, J. G., Qin, Y., Galati, D. F. & Palmer, A. E. New sensors for quantitative measurement of mitochondrial Zn(2+). *ACS Chem. Biol.* **7**, 1636–1640 (2012).

152. Carter, K. P., Carpenter, M. C., Fiedler, B., Jimenez, R. & Palmer, A. E. Critical Comparison of FRET-Sensor Functionality in the Cytosol and Endoplasmic Reticulum and Implications for Quantification of Ions. *Anal. Chem.* (2017). doi:10.1021/acs.analchem.7b02933

153. Frederickson, C. J. & Danscher, G. Zinc-containing neurons in hippocampus and related CNS structures. *Prog. Brain Res.* **83**, 71–84 (1990).

154. Danscher, G. The autometallographic zinc-sulphide method. A new approach involving in vivo creation of nanometer-sized zinc sulphide crystal lattices in zinc-enriched synaptic and secretory vesicles. *Histochem. J.* **28**, 361–373 (1996).

155. Slomianka, L. Neurons of origin of zinc-containing pathways and the distribution of zinc-containing boutons in the hippocampal region of the rat. *Neuroscience* **48**, 325–352 (1992).

156. Pe´rez-Clausell, J. & Danscher, G. Intravesicular localization of zinc in rat telencephalic boutons. A histochemical study. *Brain Res.* **337**, 91–98 (1985).

157. Czupryn, A. & Skangiel-Kramska, J. Distribution of synaptic zinc in the developing mouse somatosensory barrel cortex. *J. Comp. Neurol.* **386**, 652–660 (1997).

158. Brown, C. E. & Dyck, R. H. Distribution of zincergic neurons in the mouse forebrain. *J. Comp. Neurol.* **479**, 156–167 (2004).

159. Garrett, B. & Slomianka, L. Postnatal development of zinc-containing cells and neuropil in the visual cortex of the mouse. *Anat. Embryol. (Berl.)* **186**, 487–496 (1992).

160. Land, P. W. & Shamalla-Hannah, L. Transient expression of synaptic zinc during development of uncrossed retinogeniculate projections. *J. Comp. Neurol.* **433**, 515–525 (2001).

161. Masters, B. A. *et al.* Metallothionein III is expressed in neurons that sequester zinc in synaptic vesicles. *J. Neurosci.* **14**, 5844–5857 (1994).

162. Mizukawa, K., Tseng, I. M. & Otsuka, N. Quantitative electron microscopic analysis of postnatal development of zinc-positive nerve endings in the rat amygdala using Timm's sulphide silver technique. *Brain Res. Dev. Brain Res.* **50**, 197–203 (1989).

163. Wang, Z., Danscher, G., Kim, Y. K., Dahlstrom, A. & Mook Jo, S. Inhibitory zinc-enriched terminals in the mouse cerebellum: double-immunohistochemistry for zinc transporter 3 and glutamate decarboxylase. *Neurosci. Lett.* **321**, 37–40 (2002).

164. Rubio, M. E. & Juiz, J. M. Chemical anatomy of excitatory endings in the dorsal cochlear nucleus of the rat: differential synaptic distribution of aspartate aminotransferase, glutamate, and vesicular zinc. *J. Comp. Neurol.* **399**, 341–358 (1998).

165. Zirpel, L. & Parks, T. N. Zinc inhibition of group I mGluR-mediated calcium homeostasis in auditory neurons. *J. Assoc. Res. Otolaryngol. JARO* **2**, 180–187 (2001).

166. Danscher, G. *et al.* Inhibitory zinc-enriched terminals in mouse spinal cord. *Neuroscience* **105**, 941–947 (2001).

167. Velázquez, R. A., Cai, Y., Shi, Q. & Larson, A. A. The distribution of zinc selenite and expression of metallothionein-III mRNA in the spinal cord and dorsal root ganglia of the rat suggest a role for zinc in sensory transmission. *J. Neurosci. Off. J. Soc. Neurosci.* **19**, 2288–2300 (1999).

168. Schrøder, H. D., Danscher, G., Jo, S. M. & Su, H. Zinc-enriched boutons in rat spinal cord. *Brain Res.* **868**, 119–122 (2000).

169. Wang, Z., Danscher, G., Mook Jo, S., Shi, Y. & Schrøder, H. D. Retrograde tracing of zinc-enriched (ZEN) neuronal somata in rat spinal cord. *Brain Res.* **900**, 80–87 (2001).

170. Akagi, T., Kaneda, M., Ishii, K. & Hashikawa, T. Differential subcellular localization of zinc in the rat retina. *J. Histochem. Cytochem. Off. J. Histochem. Soc.* **49**, 87–96 (2001).

171. Ugarte, M. & Osborne, N. N. Zinc in the retina. *Prog. Neurobiol.* **64**, 219–249 (2001).

172. Wang, Z.-Y., Li, J.-Y., Danscher, G. & Dahlström, A. Localization of zinc-enriched neurons in the mouse peripheral sympathetic system. *Brain Res.* **928**, 165–174 (2002).

173. Frederickson, C. J. *et al.* Synaptic release of zinc from brain slices: factors governing release, imaging, and accurate calculation of concentration. *J. Neurosci. Methods* **154**, 19–29 (2006).

174. Ramos, P. *et al.* Anatomical Region Differences and Age-Related Changes in Copper, Zinc, and Manganese Levels in the Human Brain. *Biol. Trace Elem. Res.* 1–12 (2014). doi:10.1007/s12011-014-0093-6

175. Slomianka, L. & Geneser, F. A. Postnatal development of zinc-containing cells and neuropil in the hippocampal region of the mouse. *Hippocampus* **7**, 321–340 (1997).

176. Sanchez-Andres, J. V. *et al.* Zinc-positive presynaptic boutons of the rabbit hippocampus during early postnatal development. *Brain Res. Dev. Brain Res.* **103**, 171–183 (1997).

177. Saito, T. *et al.* Deficiencies of hippocampal Zn and ZnT3 accelerate brain aging of Rat. *Biochem. Biophys. Res. Commun.* **279**, 505–511 (2000).

178. Palmiter, R. D., Cole, T. B., Quaife, C. J. & Findley, S. D. ZnT-3, a putative transporter of zinc into synaptic vesicles. *Proc. Natl. Acad. Sci. U. S. A.* **93**, 14934–14939 (1996).

179. Wenzel, H. J., Cole, T. B., Born, D. E., Schwartzkroin, P. A. & Palmiter, R. D. Ultrastructural localization of zinc transporter-3 (ZnT-3) to synaptic vesicle membranes within mossy fiber boutons in the hippocampus of mouse and monkey. *Proc. Natl. Acad. Sci. U. S. A.* **94**, 12676–12681 (1997).

180. Lee, J.-Y., Kim, J. S., Byun, H.-R., Palmiter, R. D. & Koh, J.-Y. Dependence of the histofluorescently reactive zinc pool on zinc transporter-3 in the normal brain. *Brain Res.* **1418**, 12–22 (2011).

181. Liguz-Lecznar, M., Nowicka, D., Czupryn, A. & Skangiel-Kramska, J. Dissociation of synaptic zinc level and zinc transporter 3 expression during postnatal development and after sensory deprivation in the barrel cortex of mice. *Brain Res. Bull.* **66**, 106–113 (2005).

182. Árus, D., Dancs, Á., Nagy, N. V. & Gajda, T. A comparative study on the possible zinc binding sites of the human ZnT3 zinc transporter protein. *Dalton Trans. Camb. Engl. 2003* **42**, 12031–12040 (2013).

183. Chi, Z.-H. *et al.* Zinc transporter 3 immunohistochemical tracing of sprouting mossy fibres. *Neurochem. Int.* **52**, 1305–1309 (2008).

184. Ebadi, M. *et al.* Expression and regulation of brain metallothionein. *Neurochem. Int.* **27**, 1–22 (1995).

185. Vašák, M. & Meloni, G. Mammalian Metallothionein-3: New Functional and Structural Insights. *Int. J. Mol. Sci.* **18**, (2017).

186. Ebadi, M., Murrin, L. C. & Pfeiffer, R. F. Hippocampal zinc thionein and pyridoxal phosphate modulate synaptic functions. *Ann. N. Y. Acad. Sci.* **585**, 189–201 (1990).

187. Sekler, I. *et al.* Distribution of the zinc transporter ZnT-1 in comparison with chelatable zinc in the mouse brain. *J. Comp. Neurol.* **447**, 201–209 (2002).

188. Qin, Y., Thomas, D., Fontaine, C. P. & Colvin, R. A. Silencing of ZnT1 reduces Zn^{2+} efflux in cultured cortical neurons. *Neurosci. Lett.* **450**, 206–210 (2009).

189. Sindreu, C., Bayés, À., Altafaj, X. & Pérez-Clausell, J. Zinc transporter-1 concentrates at the postsynaptic density of hippocampal synapses. *Mol. Brain* **7**, 16 (2014).

190. Mellone, M. *et al.* Zinc transporter-1 (ZNT-1): a novel NMDA receptor-binding protein at postsynaptic density. *J. Neurochem.* (2014). doi:10.1111/jnc.12968

191. Karol, N. *et al.* Zinc homeostatic proteins in the CNS are regulated by crosstalk between extracellular and intracellular zinc. *J. Cell. Physiol.* **224**, 567–574 (2010).

192. McCormick, D. A. Chapter 12 - Membrane Potential and Action Potential. in *From Molecules to Networks (Third Edition)* (eds. Byrne, J. H., Heidelberger, R. & Waxham, M. N.) 351–376 (Academic Press, 2014). doi:10.1016/B978-0-12-397179-1.00012-9

193. Purves, D. *et al.* Chemical Synapses. *Neurosci. 2nd Ed.* (2001).

194. Purves, D. *et al.* Glutamate Receptors. *Neurosci. 2nd Ed.* (2001).

195. Ruiz, A., Walker, M. C., Fabian-Fine, R. & Kullmann, D. M. Endogenous zinc inhibits GABA(A) receptors in a hippocampal pathway. *J. Neurophysiol.* **91**, 1091–1096 (2004).

196. Wall, M. J. Actions of zinc at mature Golgi cell to granule cell synapses in cerebellum of rats and mice. *Neurosci. Lett.* **367**, 101–104 (2004).

197. Salazar, G., Craige, B., Love, R., Kalman, D. & Faundez, V. Vglut1 and ZnT3 co-targeting mechanisms regulate vesicular zinc stores in PC12 cells. *J. Cell Sci.* **118**, 1911–1921 (2005).

198. Frederickson, C. J., Suh, S. W., Silva, D., Frederickson, C. J. & Thompson, R. B. Importance of zinc in the central nervous system: the zinc-containing neuron. *J. Nutr.* **130**, 1471S–83S (2000).

199. Wellenreuther, G., Cianci, M., Tucoulou, R., Meyer-Klaucke, W. & Haase, H. The ligand environment of zinc stored in vesicles. *Biochem. Biophys. Res. Commun.* **380**, 198–203 (2009).

200. Budde, T., Minta, A., White, J. A. & Kay, A. R. Imaging free zinc in synaptic terminals in live hippocampal slices. *Neuroscience* **79**, 347–358 (1997).

201. Varea, E., Ponsoda, X., Molowny, A., Danscher, G. & Lopez-Garcia, C. Imaging synaptic zinc release in living nervous tissue. *J. Neurosci. Methods* **110**, 57–63 (2001).

202. Quinta-Ferreira, M. E., Matias, C. M., Arif, M. & Dionísio, J. C. Measurement of presynaptic zinc changes in hippocampal mossy fibers. *Brain Res.* **1026**, 1–10 (2004).

203. Qian, J. & Noebels, J. L. Visualization of transmitter release with zinc fluorescence detection at the mouse hippocampal mossy fibre synapse. *J. Physiol.* **566**, 747–758 (2005).

204. Li, Y., Hough, C. J., Suh, S. W., Sarvey, J. M. & Frederickson, C. J. Rapid translocation of Zn(2+) from presynaptic terminals into postsynaptic hippocampal neurons after physiological stimulation. *J. Neurophysiol.* **86**, 2597–2604 (2001).

205. Ketterman, J. K. & Li, Y. V. Presynaptic evidence for zinc release at the mossy fiber synapse of rat hippocampus. *J. Neurosci. Res.* **86**, 422–434 (2008).

206. Khan, M. *et al.* Two-photon imaging of Zn^{2+} dynamics in mossy fiber boutons of adult hippocampal slices. *Proc. Natl. Acad. Sci. U. S. A.* **111**, 6786–6791 (2014).

207. Blakemore, L. J., Tomat, E., Lippard, S. J. & Trombley, P. Q. Zinc released from olfactory bulb glomeruli by patterned electrical stimulation of the olfactory nerve. *Met. Integr. Biometal Sci.* **5**, 208–213 (2013).

208. Vergnano, A. M. *et al.* Zinc Dynamics and Action at Excitatory Synapses. *Neuron* **82**, 1101–1114 (2014).

209. Matias, C. M., Dionísio, J. C., Saggau, P. & Quinta-Ferreira, M. Activation of group II metabotropic glutamate receptors blocks zinc release from hippocampal mossy fibers. *Biol. Res.* **47**, 73 (2014).

210. Anand, A. *et al.* The Extracellular Zn^{2+} Concentration Surrounding Excited Neurons Is High Enough to Bind Amyloid-ß Revealed by a Nanowire Transistor. *Small* **14**, 1704439 (2018).

211. Kay, A. R. Evidence for chelatable zinc in the extracellular space of the hippocampus, but little evidence for synaptic release of Zn. *J. Neurosci. Off. J. Soc. Neurosci.* **23**, 6847–6855 (2003).

212. Quinta-Ferreira, M. E. *et al.* Modelling zinc changes at the hippocampal mossy fiber synaptic cleft. *J. Comput. Neurosci.* 1–15 (2016). doi:10.1007/s10827-016-0620-x

213. Assaf, S. Y. & Chung, S. H. Release of endogenous Zn^{2+} from brain tissue during activity. *Nature* **308**, 734–736 (1984).

214. Traynelis, S. F. *et al.* Glutamate Receptor Ion Channels: Structure, Regulation, and Function. *Pharmacol. Rev.* **62**, 405–496 (2010).

215. Sirrieh, R. E., MacLean, D. M. & Jayaraman, V. A conserved structural mechanism of NMDA receptor inhibition: A comparison of ifenprodil and zinc. *J. Gen. Physiol.* (2015). doi:10.1085/jgp.201511422

216. Choi, Y. B. & Lipton, S. A. Identification and mechanism of action of two histidine residues underlying high-affinity Zn^{2+} inhibition of the NMDA receptor. *Neuron* **23**, 171–180 (1999).

217. Mayer, M. L., Vyklicky, L. & Westbrook, G. L. Modulation of excitatory amino acid receptors by group IIB metal cations in cultured mouse hippocampal neurones. *J. Physiol.* **415**, 329–350 (1989).

218. Peters, S., Koh, J. & Choi, D. W. Zinc selectively blocks the action of N-methyl-D-aspartate on cortical neurons. *Science* **236**, 589–593 (1987).

219. Westbrook, G. L. & Mayer, M. L. Micromolar concentrations of Zn^{2+} antagonize NMDA and GABA responses of hippocampal neurons. *Nature* **328**, 640–643 (1987).

220. Chen, N., Moshaver, A. & Raymond, L. A. Differential sensitivity of recombinant N-methyl-D-aspartate receptor subtypes to zinc inhibition. *Mol. Pharmacol.* **51**, 1015–1023 (1997).

221. Vogt, K., Mellor, J., Tong, G. & Nicoll, R. The actions of synaptically released zinc at hippocampal mossy fiber synapses. *Neuron* **26**, 187–196 (2000).

222. Molnár, P. & Nadler, J. V. Synaptically-released zinc inhibits N-methyl-D-aspartate receptor activation at recurrent mossy fiber synapses. *Brain Res.* **910**, 205–207 (2001).

223. Erreger, K. & Traynelis, S. F. Allosteric interaction between zinc and glutamate binding domains on NR2A causes desensitization of NMDA receptors. *J. Physiol.* **569**, 381–393 (2005).

224. Amico-Ruvio, S. A., Murthy, S. E., Smith, T. P. & Popescu, G. K. Zinc effects on NMDA receptor gating kinetics. *Biophys. J.* **100**, 1910–1918 (2011).

225. Romero-Hernandez, A., Simorowski, N., Karakas, E. & Furukawa, H. Molecular Basis for Subtype Specificity and High-Affinity Zinc Inhibition in the GluN1-GluN2A NMDA Receptor Amino-Terminal Domain. *Neuron* **92**, 1324–1336 (2016).

226. Ueno, S. *et al.* Mossy fiber Zn^{2+} spillover modulates heterosynaptic N-methyl-D-aspartate receptor activity in hippocampal CA3 circuits. *J. Cell Biol.* **158**, 215–220 (2002).

227. Smart, T. G., Hosie, A. M. & Miller, P. S. Zn^{2+} ions: modulators of excitatory and inhibitory synaptic activity. *Neurosci. Rev. J. Bringing Neurobiol. Neurol. Psychiatry* **10**, 432–442 (2004).

228. Suwa, H., Saint-Amant, L., Triller, A., Drapeau, P. & Legendre, P. High-affinity zinc potentiation of inhibitory postsynaptic glycinergic currents in the zebrafish hindbrain. *J. Neurophysiol.* **85**, 912–925 (2001).

229. Laube, B. *et al.* Modulation by zinc ions of native rat and recombinant human inhibitory glycine receptors. *J. Physiol.* **483 (Pt 3)**, 613–619 (1995).

230. Laube, B. Potentiation of inhibitory glycinergic neurotransmission by Zn^{2+}: a synergistic interplay between presynaptic P2X2 and postsynaptic glycine receptors. *Eur. J. Neurosci.* **16**, 1025–1036 (2002).

231. Hirzel, K. *et al.* Hyperekplexia phenotype of glycine receptor alpha1 subunit mutant mice identifies Zn(2+) as an essential endogenous modulator of glycinergic neurotransmission. *Neuron* **52**, 679–690 (2006).

232. Perez-Rosello, T., Anderson, C. T., Ling, C., Lippard, S. J. & Tzounopoulos, T. Tonic Zinc Inhibits Spontaneous Neuronal Firing in Dorsal Cochlear Nucleus Principal Neurons by Enhancing Glycinergic Neurotransmission. *Neurobiol. Dis.* (2015). doi:10.1016/j.nbd.2015.03.012

233. Martina, M., Mozrzymas, J. W., Strata, F. & Cherubini, E. Zinc modulation of bicuculline-sensitive and -insensitive GABA receptors in the developing rat hippocampus. *Eur. J. Neurosci.* **8**, 2168–2176 (1996).

234. Berger, T., Schwarz, C., Kraushaar, U. & Monyer, H. Dentate gyrus basket cell GABAA receptors are blocked by Zn^{2+} via changes of their desensitization kinetics: an in situ patch-clamp and single-cell PCR study. *J. Neurosci. Off. J. Soc. Neurosci.* **18**, 2437–2448 (1998).

235. Barberis, A., Petrini, E. M., Cherubini, E. & Mozrzymas, J. W. Allosteric interaction of zinc with recombinant alpha(1)beta(2)gamma(2) and alpha(1)beta(2) GABA(A) receptors. *Neuropharmacology* **43**, 607–618 (2002).

236. Hosie, A. M., Dunne, E. L., Harvey, R. J. & Smart, T. G. Zinc-mediated inhibition of GABA(A) receptors: discrete binding sites underlie subtype specificity. *Nat. Neurosci.* **6**, 362–369 (2003).

237. Dreixler, J. C. & Leonard, J. P. Effects of external calcium on zinc modulation of AMPA receptors. *Brain Res.* **752**, 170–174 (1997).

238. Blakemore, L. J. & Trombley, P. Q. Diverse modulation of olfactory bulb AMPA receptors by zinc. *Neuroreport* **15**, 919–923 (2004).

239. Kreitzer, M. A., Birnbaum, A. D., Qian, H. & Malchow, R. P. Pharmacological characterization, localization, and regulation of ionotropic glutamate receptors in skate horizontal cells. *Vis. Neurosci.* **26**, 375–387 (2009).

240. Zhang, D.-Q., Ribelayga, C., Mangel, S. C. & McMahon, D. G. Suppression by zinc of AMPA receptor-mediated synaptic transmission in the retina. *J. Neurophysiol.* **88**, 1245–1251 (2002).

241. Armstrong, N. & Gouaux, E. Mechanisms for activation and antagonism of an AMPA-sensitive glutamate receptor: crystal structures of the GluR2 ligand binding core. *Neuron* **28**, 165–181 (2000).

242. Kalappa, B. I. & Tzounopoulos, T. Context-Dependent Modulation of Excitatory Synaptic Strength by Synaptically Released Zinc. *eNeuro* **4**, (2017).

243. Mott, D. D., Benveniste, M. & Dingledine, R. J. pH-dependent inhibition of kainate receptors by zinc. *J. Neurosci. Off. J. Soc. Neurosci.* **28**, 1659–1671 (2008).

244. Veran, J. *et al.* Zinc potentiates GluK3 glutamate receptor function by stabilizing the ligand binding domain dimer interface. *Neuron* **76**, 565–578 (2012).

245. Xie, X. & Smart, T. G. Giant GABAB-mediated synaptic potentials induced by zinc in the rat hippocampus: paradoxical effects of zinc on the GABAB receptor. *Eur. J. Neurosci.* **5**, 430–436 (1993).

246. Swaminath, G., Steenhuis, J., Kobilka, B. & Lee, T. W. Allosteric modulation of beta2-adrenergic receptor by Zn(2+). *Mol. Pharmacol.* **61**, 65–72 (2002).

247. Moroni, M. *et al.* Non-agonist-binding subunit interfaces confer distinct functional signatures to the alternate stoichiometries of the alpha4beta2 nicotinic receptor: an alpha4-alpha4 interface is required for Zn^{2+} potentiation. *J. Neurosci. Off. J. Soc. Neurosci.* **28**, 6884–6894 (2008).

248. Barrondo, S. & Sallés, J. Allosteric modulation of 5-HT(1A) receptors by zinc: Binding studies. *Neuropharmacology* **56**, 455–462 (2009).

249. Spiridon, M., Kamm, D., Billups, B., Mobbs, P. & Attwell, D. Modulation by zinc of the glutamate transporters in glial cells and cones isolated from the tiger salamander retina. *J. Physiol.* **506 (Pt 2)**, 363–376 (1998).

250. Mitrovic, A. D., Plesko, F. & Vandenberg, R. J. Zn(2+) inhibits the anion conductance of the glutamate transporter EEAT4. *J. Biol. Chem.* **276**, 26071–26076 (2001).

251. Ju, P., Aubrey, K. R. & Vandenberg, R. J. Zn^{2+} inhibits glycine transport by glycine transporter subtype 1b. *J. Biol. Chem.* **279**, 22983–22991 (2004).

252. Cohen-Kfir, E., Lee, W., Eskandari, S. & Nelson, N. Zinc inhibition of gamma-aminobutyric acid transporter 4 (GAT4) reveals a link between excitatory and inhibitory neurotransmission. *Proc. Natl. Acad. Sci. U. S. A.* **102**, 6154–6159 (2005).

253. Gruss, M., Mathie, A., Lieb, W. R. & Franks, N. P. The two-pore-domain K(+) channels TREK-1 and TASK-3 are differentially modulated by copper and zinc. *Mol. Pharmacol.* **66**, 530–537 (2004).

254. Imbrici, P., D'Adamo, M. C., Cusimano, A. & Pessia, M. Episodic ataxia type 1 mutation F184C alters Zn^{2+}-induced modulation of the human K^+ channel Kv1.4-Kv1.1/Kvbeta1.1. *Am. J. Physiol. Cell Physiol.* **292**, C778-787 (2007).

255. Gu, Y., Barry, J. & Gu, C. Kv3 channel assembly, trafficking and activity are regulated by zinc through different binding sites. *J. Physiol.* **591**, 2491–2507 (2013).

256. Gao, H. *et al.* Intracellular zinc activates KCNQ channels by reducing their dependence on phosphatidylinositol 4,5-bisphosphate. *Proc. Natl. Acad. Sci. U. S. A.* **114**, E6410–E6419 (2017).

257. Hershfinkel, M. *et al.* Intracellular zinc inhibits KCC2 transporter activity. *Nat. Neurosci.* **12**, 725–727 (2009).

258. Anastassov, I., Shen, W., Ripps, H. & Chappell, R. L. Zinc modulation of calcium activity at the photoreceptor terminal: a calcium imaging study. *Exp. Eye Res.* **112**, 37–44 (2013).

259. Traboulsie, A. *et al.* Subunit-specific modulation of T-type calcium channels by zinc. *J. Physiol.* **578**, 159–171 (2007).

260. Shcheglovitov, A. *et al.* Molecular and biophysical basis of glutamate and trace metal modulation of voltage-gated Ca(v)2.3 calcium channels. *J. Gen. Physiol.* **139**, 219–234 (2012).

261. Kovács, G. *et al.* Modulation of P2X7 purinergic receptor activity by extracellular Zn^{2+} in cultured mouse hippocampal astroglia. *Cell Calcium* **75**, 1–13 (2018).

262. Colvin, R. A. Zinc inhibits Ca^{2+} transport by rat brain Na^{+}/Ca^{2+} exchanger. *Neuroreport* **9**, 3091–3096 (1998).

263. Heiliger, E. *et al.* N-cadherin-mediated cell adhesion is regulated by extracellular Zn(2+). *Met. Integr. Biometal Sci.* (2015). doi:10.1039/c4mt00300d

264. Tsvetkov, P. O. *et al.* Functional Status of Neuronal Calcium Sensor-1 Is Modulated by Zinc Binding. *Front. Mol. Neurosci.* **11**, 459 (2018).

265. Sensi, S. L. *et al.* Measurement of Intracellular Free Zinc in Living Cortical Neurons: Routes of Entry. *J. Neurosci.* **17**, 9554–9564 (1997).

266. Minami, A. *et al.* Inhibition of presynaptic activity by zinc released from mossy fiber terminals during tetanic stimulation. *J. Neurosci. Res.* **83**, 167–176 (2006).

267. Suh, S. W. Detection of zinc translocation into apical dendrite of CA1 pyramidal neuron after electrical stimulation. *J. Neurosci. Methods* **177**, 1–13 (2009).

268. Inoue, K., O'Bryant, Z. & Xiong, Z.-G. Zinc-permeable ion channels: effects on intracellular zinc dynamics and potential physiological/pathophysiological significance. *Curr. Med. Chem.* **22**, 1248–1257 (2015).

269. Yin, H. Z. & Weiss, J. H. Zn(2+) permeates Ca(2+) permeable AMPA/kainate channels and triggers selective neural injury. *Neuroreport* **6**, 2553–2556 (1995).

270. Yin, H. Z., Ha, D. H., Carriedo, S. G. & Weiss, J. H. Kainate-stimulated Zn^{2+} uptake labels cortical neurons with Ca^{2+}-permeable AMPA/kainate channels. *Brain Res.* **781**, 45–56 (1998).

271. Weiss, J. H., Hartley, D. M., Koh, J. Y. & Choi, D. W. AMPA receptor activation potentiates zinc neurotoxicity. *Neuron* **10**, 43–49 (1993).

272. Sensi, S. L., Yin, H. Z. & Weiss, J. H. Glutamate triggers preferential Zn^{2+} flux through Ca^{2+} permeable AMPA channels and consequent ROS production. *Neuroreport* **10**, 1723–1727 (1999).

273. Jia, Y., Jeng, J.-M., Sensi, S. L. & Weiss, J. H. Zn^{2+} currents are mediated by calcium-permeable AMPA/Kainate channels in cultured murine hippocampal neurones. *J. Physiol.* **543**, 35–48 (2002).

274. Koh, J. Y. & Choi, D. W. Zinc toxicity on cultured cortical neurons: involvement of N-methyl-D-aspartate receptors. *Neuroscience* **60**, 1049–1057 (1994).

275. Freund, W. D. & Reddig, S. AMPA/Zn(2+)-induced neurotoxicity in rat primary cortical cultures: involvement of L-type calcium channels. *Brain Res.* **654**, 257–264 (1994).

276. Yin, H. Z., Sensi, S. L., Ogoshi, F. & Weiss, J. H. Blockade of Ca^{2+}-permeable AMPA/kainate channels decreases oxygen-glucose deprivation-induced Zn^{2+} accumulation and neuronal loss in hippocampal pyramidal neurons. *J. Neurosci. Off. J. Soc. Neurosci.* **22**, 1273–1279 (2002).

277. Colvin, R. A. Characterization of a plasma membrane zinc transporter in rat brain. *Neurosci. Lett.* **247**, 147–150 (1998).

278. Colvin, R. A., Davis, N., Nipper, R. W. & Carter, P. A. Evidence for a zinc/proton antiporter in rat brain. *Neurochem. Int.* **36**, 539–547 (2000).

279. Emmetsberger, J. *et al.* Tissue plasminogen activator alters intracellular sequestration of zinc through interaction with the transporter ZIP4. *J. Neurosci. Off. J. Soc. Neurosci.* **30**, 6538–6547 (2010).

280. Qian, J. *et al.* Knockout of Zn transporters Zip-1 and Zip-3 attenuates seizure-induced CA1 neurodegeneration. *J. Neurosci. Off. J. Soc. Neurosci.* **31**, 97–104 (2011).

281. Kiedrowski, L. Proton-dependent zinc release from intracellular ligands. *J. Neurochem.* **130**, 87–96 (2014).

282. Oswald, M. C. W., Garnham, N., Sweeney, S. T. & Landgraf, M. Regulation of neuronal development and function by ROS. *Febs Lett.* **592**, 679–691 (2018).

283. Thomas, R. C. The plasma membrane calcium ATPase (PMCA) of neurones is electroneutral and exchanges 2 H^+ for each Ca^{2+} or Ba^{2+} ion extruded. *J. Physiol.* **587**, 315–327 (2009).

284. Schwiening, C. J. & Willoughby, D. Depolarization-induced pH microdomains and their relationship to calcium transients in isolated snail neurones. *J. Physiol.* **538**, 371–382 (2002).

285. Rathje, M. *et al.* AMPA receptor pHluorin-GluA2 reports NMDA receptor-induced intracellular acidification in hippocampal neurons. *Proc. Natl. Acad. Sci. U. S. A.* **110**, 14426–14431 (2013).

286. Rossano, A. J., Kato, A., Minard, K. I., Romero, M. F. & Macleod, G. T. Na^+ /H^+ exchange via the Drosophila vesicular glutamate transporter mediates activity-induced acid efflux from presynaptic terminals. *J. Physiol.* **595**, 805–824 (2017).

287. Rossano, A. J., Chouhan, A. K. & Macleod, G. T. Genetically encoded pH-indicators reveal activity-dependent cytosolic acidification of Drosophila motor nerve termini in vivo. *J. Physiol.* **591**, 1691–1706 (2013).

288. Zhan, R. Z. *et al.* NMDA induces a biphasic change in intracellular pH in rat hippocampal slices. *Brain Res.* **760**, 179–186 (1997).

289. Kiedrowski, L. Cytosolic acidification and intracellular zinc release in hippocampal neurons. *J. Neurochem.* **121**, 438–450 (2012).

290. Kiedrowski, L. Neuronal acid-induced [Zn(2+)]i elevations calibrated using the low-affinity ratiometric probe FuraZin-1. *J. Neurochem.* (2015). doi:10.1111/jnc.13282

291. Adamo, A. M. *et al.* Early Developmental Marginal Zinc Deficiency Affects Neurogenesis Decreasing Neuronal Number and Altering Neuronal Specification in the Adult Rat Brain. *Front. Cell. Neurosci.* **13**, 62 (2019).

292. Yu, X., Ren, T. & Yu, X. Disruption of calmodulin-dependent protein kinase II α/brain-derived neurotrophic factor (α-CaMKII/BDNF) signalling is associated with zinc deficiency-induced impairments in cognitive and synaptic plasticity. *Br. J. Nutr.* **110**, 2194–2200 (2013).

293. Jiang, Y.-G. *et al.* Depressed hippocampal MEK/ERK phosphorylation correlates with impaired cognitive and synaptic function in zinc-deficient rats. *Nutr. Neurosci.* **14**, 45–50 (2011).

294. Takeda, A., Suzuki, M., Tempaku, M., Ohashi, K. & Tamano, H. Influx of extracellular Zn(2+) into the hippocampal CA1 neurons is required for cognitive performance via long-term potentiation. *Neuroscience* **304**, 209–216 (2015).

295. Frederickson, R. E., Frederickson, C. J. & Danscher, G. In situ binding of bouton zinc reversibly disrupts performance on a spatial memory task. *Behav. Brain Res.* **38**, 25–33 (1990).

296. Takeda, A., Sawashita, J., Takefuta, S., Ohnuma, M. & Okada, S. Role of zinc released by stimulation in rat amygdala. *J. Neurosci. Res.* **57**, 405–410 (1999).

297. Takeda, A., Sakurada, N., Kanno, S., Minami, A. & Oku, N. Response of extracellular zinc in the ventral hippocampus against novelty stress. *J. Neurochem.* **99**, 670–676 (2006).

298. Ceccom, J., Bouhsira, E., Halley, H., Daumas, S. & Lassalle, J. M. Differential needs of zinc in the CA3 area of dorsal hippocampus for the consolidation of contextual fear and spatial memories. *Learn. Mem. Cold Spring Harb. N* **20**, 348–351 (2013).

299. Takeda, A. *et al.* Intracellular Zn(2+) signaling in the dentate gyrus is required for object recognition memory. *Hippocampus* (2014). doi:10.1002/hipo.22322

300. Cole, T. B., Wenzel, H. J., Kafer, K. E., Schwartzkroin, P. A. & Palmiter, R. D. Elimination of zinc from synaptic vesicles in the intact mouse brain by disruption of the ZnT3 gene. *Proc. Natl. Acad. Sci. U. S. A.* **96**, 1716–1721 (1999).

301. Cole, T. B., Martyanova, A. & Palmiter, R. D. Removing zinc from synaptic vesicles does not impair spatial learning, memory, or sensorimotor functions in the mouse. *Brain Res.* **891**, 253–265 (2001).

302. Pan, E. *et al.* Vesicular zinc promotes presynaptic and inhibits postsynaptic long-term potentiation of mossy fiber-CA3 synapse. *Neuron* **71**, 1116–1126 (2011).

303. Adlard, P. A., Parncutt, J. M., Finkelstein, D. I. & Bush, A. I. Cognitive Loss in Zinc Transporter-3 Knock-Out Mice: A Phenocopy for the Synaptic and Memory Deficits of Alzheimer's Disease? *J. Neurosci.* **30**, 1631–1636 (2010).

304. Martel, G., Hevi, C., Friebely, O., Baybutt, T. & Shumyatsky, G. P. Zinc transporter 3 is involved in learned fear and extinction, but not in innate fear. *Learn. Mem.* **17**, 582–590 (2010).

305. Thackray, S. E., McAllister, B. B. & Dyck, R. H. Behavioral characterization of female zinc transporter 3 (ZnT3) knockout mice. *Behav. Brain Res.* **321**, 36–49 (2017).

306. Patrick Wu, H.-P. & Dyck, R. H. Signaling by Synaptic Zinc is Required for Whisker-Mediated, Fine Texture Discrimination. *Neuroscience* **369**, 242–247 (2018).

307. McAllister, B. B., Wright, D. K., Wortman, R. C., Shultz, S. R. & Dyck, R. H. Elimination of vesicular zinc alters the behavioural and neuroanatomical effects of social defeat stress in mice. *Neurobiol. Stress* **9**, 199–213 (2018).

308. Anderson, C. T., Kumar, M., Xiong, S. & Tzounopoulos, T. Cell-specific gain modulation by synaptically released zinc in cortical circuits of audition. *eLife* **6**, e29893 (2017).

309. Kumar, M., Xiong, S., Tzounopoulos, T. & Anderson, C. T. Fine Control of Sound Frequency Tuning and Frequency Discrimination Acuity by Synaptic Zinc Signaling in Mouse Auditory Cortex. *J. Neurosci. Off. J. Soc. Neurosci.* **39**, 854–865 (2019).

310. Land, P. W. & Akhtar, N. D. Experience-dependent alteration of synaptic zinc in rat somatosensory barrel cortex. *Somatosens. Mot. Res.* **16**, 139–150 (1999).

311. Quaye, V. L., Shamalla-Hannah, L. & Land, P. W. Experience-dependent alteration of zinc-containing circuits in somatosensory cortex of the mouse. *Brain Res. Dev. Brain Res.* **114**, 283–287 (1999).

312. Czupryn, A. & Skangiel-Kramska, J. Differential response of synaptic zinc levels to sensory deprivation in the barrel cortex of young and adult mice. *Exp. Brain Res.* **141**, 567–572 (2001).

313. Czupryn, A. & Skangiel-Kramska, J. Deprivation and denervation differentially affect zinc-containing circuitries in the barrel cortex of mice. *Brain Res. Bull.* **55**, 287–295 (2001).

314. Nakashima, A. S. & Dyck, R. H. Dynamic, experience-dependent modulation of synaptic zinc within the excitatory synapses of the mouse barrel cortex. *Neuroscience* **170**, 1015–1019 (2010).

315. Brown, C. E. & Dyck, R. H. Rapid, experience-dependent changes in levels of synaptic zinc in primary somatosensory cortex of the adult mouse. *J. Neurosci. Off. J. Soc. Neurosci.* **22**, 2617–2625 (2002).

316. Brown, C. E. & Dyck, R. H. Experience-dependent regulation of synaptic zinc is impaired in the cortex of aged mice. *Neuroscience* **119**, 795–801 (2003).

317. Dyck, R. H., Chaudhuri, A. & Cynader, M. S. Experience-dependent regulation of the zincergic innervation of visual cortex in adult monkeys. *Cereb. Cortex N. Y. N 1991* **13**, 1094–1109 (2003).

318. Brown, C. E. & Dyck, R. H. Modulation of synaptic zinc in barrel cortex by whisker stimulation. *Neuroscience* **134**, 355–359 (2005).

319. Nakashima, A. S. & Dyck, R. H. Enhanced plasticity in zincergic, cortical circuits after exposure to enriched environments. *J. Neurosci. Off. J. Soc. Neurosci.* **28**, 13995–13999 (2008).

320. Xie, X. M. & Smart, T. G. A physiological role for endogenous zinc in rat hippocampal synaptic neurotransmission. *Nature* **349**, 521–524 (1991).

321. Lopantsev, V., Wenzel, H. J., Cole, T. B., Palmiter, R. D. & Schwartzkroin, P. A. Lack of vesicular zinc in mossy fibers does not affect synaptic excitability of CA3 pyramidal cells in zinc transporter 3 knockout mice. *Neuroscience* **116**, 237–248 (2003).

322. Grauert, A., Engel, D. & Ruiz, A. J. Endogenous zinc depresses GABAergic transmission via T-type Ca(2+) channels and broadens the time window for integration of glutamatergic inputs in dentate granule cells. *J. Physiol.* **592**, 67–86 (2014).

323. Kodirov, S. A. *et al.* Synaptically released zinc gates long-term potentiation in fear conditioning pathways. *Proc. Natl. Acad. Sci. U. S. A.* **103**, 15218–15223 (2006).

324. Takeda, A., Minami, A., Seki, Y. & Oku, N. Differential effects of zinc on glutamatergic and GABAergic neurotransmitter systems in the hippocampus. *J. Neurosci. Res.* **75**, 225–229 (2004).

325. Minami, A., Takeda, A., Yamaide, R. & Oku, N. Relationship between zinc and neurotransmitters released into the amygdalar extracellular space. *Brain Res.* **936**, 91–94 (2002).

326. Takeda, A., Fuke, S., Tsutsumi, W. & Oku, N. Negative modulation of presynaptic activity by zinc released from Schaffer collaterals. *J. Neurosci. Res.* **85**, 3666–3672 (2007).

327. Lavoie, N. *et al.* Vesicular zinc regulates the Ca^{2+} sensitivity of a subpopulation of presynaptic vesicles at hippocampal mossy fiber terminals. *J. Neurosci. Off. J. Soc. Neurosci.* **31**, 18251–18265 (2011).

328. Khulusi, S. S., Brown, M. W. & Wright, D. M. Zinc and paired-pulse potentiation in the hippocampus. *Brain Res.* **363**, 152–155 (1986).

329. Sim, J. A. & Cherubini, E. Submicromolar concentrations of zinc irreversibly reduce a calcium-dependent potassium current in rat hippocampal neurons in vitro. *Neuroscience* **36**, 623–629 (1990).

330. Kresse, W. *et al.* Zinc ions are endogenous modulators of neurotransmitter-stimulated capacitative Ca^{2+} entry in both cultured and in situ mouse astrocytes. *Eur. J. Neurosci.* **21**, 1626–1634 (2005).

331. Takeda, A. *et al.* Zinc release from Schaffer collaterals and its significance. *Brain Res. Bull.* **68**, 442–447 (2006).

332. Sindreu, C., Palmiter, R. D. & Storm, D. R. Zinc transporter ZnT-3 regulates presynaptic Erk1/2 signaling and hippocampus-dependent memory. *Proc. Natl. Acad. Sci. U. S. A.* **108**, 3366–3370 (2011).

333. Park, J. A. & Koh, J. Y. Induction of an immediate early gene egr-1 by zinc through extracellular signal-regulated kinase activation in cortical culture: its role in zinc-induced neuronal death. *J. Neurochem.* **73**, 450–456 (1999).

334. Liu, J. *et al.* Depletion of intracellular zinc down-regulates expression of Uch-L1 mRNA and protein, and CREB mRNA in cultured hippocampal neurons. *Nutr. Neurosci.* **11**, 96–102 (2008).

335. Besser, L. *et al.* Synaptically released zinc triggers metabotropic signaling via a zinc-sensing receptor in the hippocampus. *J. Neurosci. Off. J. Soc. Neurosci.* **29**, 2890–2901 (2009).

336. Perez-Rosello, T. *et al.* Synaptic Zn^{2+} inhibits neurotransmitter release by promoting endocannabinoid synthesis. *J. Neurosci. Off. J. Soc. Neurosci.* **33**, 9259–9272 (2013).

337. Huang, Y. Z., Pan, E., Xiong, Z.-Q. & McNamara, J. O. Zinc-Mediated Transactivation of TrkB Potentiates the Hippocampal Mossy Fiber-CA3 Pyramid Synapse. *Neuron* **57**, 546–558 (2008).

338. Li, C., Dabrowska, J., Hazra, R. & Rainnie, D. G. Synergistic activation of dopamine D1 and TrkB receptors mediate gain control of synaptic plasticity in the basolateral amygdala. *PloS One* **6**, e26065 (2011).

339. Lee, Y. *et al.* Characterization of the zinc-induced Shank3 interactome of mouse synaptosome. *Biochem. Biophys. Res. Commun.* (2017). doi:10.1016/j.bbrc.2017.10.143

340. Grabrucker, A. M. *et al.* Concerted action of zinc and ProSAP/Shank in synaptogenesis and synapse maturation. *EMBO J.* **30**, 569–581 (2011).

341. Tao-Cheng, J.-H., Toy, D., Winters, C. A., Reese, T. S. & Dosemeci, A. Zinc Stabilizes Shank3 at the Postsynaptic Density of Hippocampal Synapses. *PloS One* **11**, e0153979 (2016).

342. Arons, M. H. *et al.* Shank3 Is Part of a Zinc-Sensitive Signaling System That Regulates Excitatory Synaptic Strength. *J. Neurosci. Off. J. Soc. Neurosci.* **36**, 9124–9134 (2016).

343. Hoffman, L., Li, L., Alexov, E., Sanabria, H. & Waxham, M. N. Cytoskeletal-like Filaments of Ca(2+)-Calmodulin-Dependent Protein Kinase II Are Formed in a Regulated and Zn(2+)-Dependent Manner. *Biochemistry* **56**, 2149–2160 (2017).

344. Perrin, L. *et al.* Zinc and Copper Effects on Stability of Tubulin and Actin Networks in Dendrites and Spines of Hippocampal Neurons. *ACS Chem. Neurosci.* (2017). doi:10.1021/acschemneuro.6b00452

345. Meighan, P. C., Meighan, S. E., Davis, C. J., Wright, J. W. & Harding, J. W. Effects of matrix metalloproteinase inhibition on short- and long-term plasticity of schaffer collateral/CA1 synapses. *J. Neurochem.* **102**, 2085–2096 (2007).

346. Purves, D. *et al.* Long-Term Synaptic Potentiation. *Neurosci. 2nd Ed.* (2001).

347. Castillo, P. E. Presynaptic LTP and LTD of excitatory and inhibitory synapses. *Cold Spring Harb. Perspect. Biol.* **4**, (2012).

348. Lu, Y. M. *et al.* Endogenous Zn(2+) is required for the induction of long-term potentiation at rat hippocampal mossy fiber-CA3 synapses. *Synap. N. Y. N* **38**, 187–197 (2000).

349. Quinta-Ferreira, M. E. & Matias, C. M. Tetanically released zinc inhibits hippocampal mossy fiber calcium, zinc and synaptic responses. *Brain Res.* **1047**, 1–9 (2005).

350. Li, Y., Hough, C. J., Frederickson, C. J. & Sarvey, J. M. Induction of mossy fiber --> Ca3 long-term potentiation requires translocation of synaptically released Zn^{2+}. *J. Neurosci. Off. J. Soc. Neurosci.* **21**, 8015–8025 (2001).

351. Lüscher, C. & Malenka, R. C. NMDA Receptor-Dependent Long-Term Potentiation and Long-Term Depression (LTP/LTD). *Cold Spring Harb. Perspect. Biol.* **4**, (2012).

352. Izumi, Y., Auberson, Y. P. & Zorumski, C. F. Zinc modulates bidirectional hippocampal plasticity by effects on NMDA receptors. *J. Neurosci. Off. J. Soc. Neurosci.* **26**, 7181–7188 (2006).

353. Ma, J. Y. & Zhao, Z. Q. The effects of Zn^{2+} on long-term potentiation of C fiber-evoked potentials in the rat spinal dorsal horn. *Brain Res. Bull.* **56**, 575–579 (2001).

354. Tamano, H., Nishio, R. & Takeda, A. Involvement of intracellular Zn^{2+} signaling in LTP at perforant pathway-CA1 pyramidal cell synapse. *Hippocampus* **27**, 777–783 (2017).

355. Kim, T.-Y., Hwang, J.-J., Yun, S. H., Jung, M. W. & Koh, J.-Y. Augmentation by zinc of NMDA receptor-mediated synaptic responses in CA1 of rat hippocampal slices: mediation by Src family tyrosine kinases. *Synap. N. Y. N* **46**, 49–56 (2002).

356. Izumi, Y., Tokuda, K. & Zorumski, C. F. Long-term potentiation inhibition by low-level N-methyl-D-aspartate receptor activation involves calcineurin, nitric oxide, and p38 mitogen-activated protein kinase. *Hippocampus* **18**, 258–265 (2008).

357. Takeda, A., Fuke, S., Ando, M. & Oku, N. Positive modulation of long-term potentiation at hippocampal CA1 synapses by low micromolar concentrations of zinc. *Neuroscience* **158**, 585–591 (2009).

358. Sullivan, J. A. *et al.* Zinc enhances hippocampal long-term potentiation at CA1 synapses through NR2B containing NMDA receptors. *PloS One* **13**, e0205907 (2018).

359. Ha, H. T. T. *et al.* Shank and Zinc Mediate an AMPA Receptor Subunit Switch in Developing Neurons. *Front. Mol. Neurosci.* **11**, 405 (2018).

360. Helgager, J., Huang, Y. Z. & Mcnamara, J. O. Brain-derived neurotrophic factor but not vesicular zinc promotes TrkB activation within mossy fibers of mouse hippocampus in vivo. *J. Comp. Neurol.* **522**, 3885–3899 (2014).

361. Danscher, G. *et al.* Increased amount of zinc in the hippocampus and amygdala of Alzheimer's diseased brains: a proton-induced X-ray emission spectroscopic analysis of cryostat sections from autopsy material. *J. Neurosci. Methods* **76**, 53–59 (1997).

362. Lovell, M. A., Smith, J. L., Xiong, S. & Markesbery, W. R. Alterations in zinc transporter protein-1 (ZnT-1) in the brain of subjects with mild cognitive impairment, early, and late-stage Alzheimer's disease. *Neurotox. Res.* **7**, 265–271 (2005).

363. Lee, J.-Y. *et al.* Apolipoprotein E ablation decreases synaptic vesicular zinc in the brain. *Biometals Int. J. Role Met. Ions Biol. Biochem. Med.* **23**, 1085–1095 (2010).

364. Beyer, N. *et al.* Zinc transporter mRNA levels in Alzheimer's disease postmortem brain. *J. Alzheimers Dis. JAD* **29**, 863–873 (2012).

365. Bjorklund, N. L. *et al.* Absence of amyloid ß oligomers at the postsynapse and regulated synaptic Zn^{2+} in cognitively intact aged individuals with Alzheimer's disease neuropathology. *Mol. Neurodegener.* **7**, 23 (2012).

366. Bjorklund, N. L., Sadagoparamanujam, V.-M. & Taglialatela, G. Selective, quantitative measurement of releasable synaptic zinc in human autopsy hippocampal brain tissue from Alzheimer's disease patients. *J. Neurosci. Methods* **203**, 146–151 (2012).

367. Nakashima, A. S., Oddo, S., Laferla, F. M. & Dyck, R. H. Experience-dependent regulation of vesicular zinc in male and female 3xTg-AD mice. *Neurobiol. Aging* **31**, 605–613 (2010).

368. Stoltenberg, M. *et al.* Amyloid plaques arise from zinc-enriched cortical layers in APP/PS1 transgenic mice and are paradoxically enlarged with dietary zinc deficiency. *Neuroscience* **150**, 357–369 (2007).

369. Lee, J.-Y., Cho, E., Seo, J.-W., Hwang, J. J. & Koh, J.-Y. Alteration of the cerebral zinc pool in a mouse model of Alzheimer disease. *J. Neuropathol. Exp. Neurol.* **71**, 211–222 (2012).

370. Lee, J.-Y., Cole, T. B., Palmiter, R. D., Suh, S. W. & Koh, J.-Y. Contribution by synaptic zinc to the gender-disparate plaque formation in human Swedish mutant APP transgenic mice. *Proc. Natl. Acad. Sci. U. S. A.* **99**, 7705–7710 (2002).

371. Lee, S.-J., Seo, B.-R. & Koh, J.-Y. Metallothionein-3 modulates the amyloid ß endocytosis of astrocytes through its effects on actin polymerization. *Mol. Brain* **8**, 84 (2015).

372. Flinn, J. M., Bozzelli, P. L., Adlard, P. A. & Railey, A. M. Spatial memory deficits in a mouse model of late-onset Alzheimer's disease are caused by zinc supplementation and correlate with amyloid-beta levels. *Front. Aging Neurosci.* **6**, 174 (2014).

373. Li, X., Xie, B., Dong, X. & Sun, Y. Bifunctionality of Iminodiacetic Acid-Modified Lysozyme on Inhibiting Zn^{2+}-Mediated Amyloid ß-Protein Aggregation. *Langmuir ACS J. Surf. Colloids* **34**, 5106–5115 (2018).

374. Xu, L. *et al.* Coupling of Zinc-Binding and Secondary Structure in Non-Fibrillar Aß40 Peptide Oligomerization. *J. Chem. Inf. Model.* (2015). doi:10.1021/acs.jcim.5b00063

375. Hane, F. T., Hayes, R., Lee, B. Y. & Leonenko, Z. Effect of Copper and Zinc on the Single Molecule Self-Affinity of Alzheimer's Amyloid-ß Peptides. *PloS One* **11**, e0147488 (2016).

376. Shi, H., Kang, B. & Lee, J. Y. Zn(2+) effect on structure and residual hydrophobicity of amyloid ß-peptide monomers. *J. Phys. Chem. B* **118**, 10355–10361 (2014).

377. Xu, L., Wang, X. & Wang, X. Effects of Zn^{2+} binding on the structural and dynamic properties of amyloid ß peptide associated with Alzheimer's disease: Asp1 or Glu11? *ACS Chem. Neurosci.* **4**, 1458–1468 (2013).

378. Branch, T., Barahona, M., Dodson, C. A. & Ying, L. Kinetic Analysis Reveals the Identity of Aß-Metal Complex Responsible for the Initial Aggregation of Aß in the Synapse. *ACS Chem. Neurosci.* **8**, 1970–1979 (2017).

379. Deshpande, A., Kawai, H., Metherate, R., Glabe, C. G. & Busciglio, J. A role for synaptic zinc in activity-dependent Abeta oligomer formation and accumulation at excitatory synapses. *J. Neurosci. Off. J. Soc. Neurosci.* **29**, 4004–4015 (2009).

380. Abramovitch-Dahan, C. *et al.* Amyloid ß attenuates metabotropic zinc sensing receptor, mZnR/GPR39, dependent Ca(2+) , ERK1/2 and Clusterin signaling in neurons. *J. Neurochem.* (2016). doi:10.1111/jnc.13760

381. Whitfield, D. R. *et al.* Assessment of ZnT3 and PSD95 protein levels in Lewy body dementias and Alzheimer's disease: association with cognitive impairment. *Neurobiol. Aging* (2014). doi:10.1016/j.neurobiolaging.2014.06.015

382. Tamano, H., Nishio, R., Morioka, H. & Takeda, A. Extracellular Zn^{2+} Influx into Nigral Dopaminergic Neurons Plays a Key Role for Pathogenesis of 6-Hydroxydopamine-Induced Parkinson's Disease in Rats. *Mol. Neurobiol.* **56**, 435–443 (2019).

383. Gardner, B. *et al.* Metal concentrations and distributions in the human olfactory bulb in Parkinson's disease. *Sci. Rep.* **7**, 10454 (2017).

384. Yang, T.-C. *et al.* Cell death caused by the synergistic effects of zinc and dopamine is mediated by a stress sensor gene Gadd45b - implication in the pathogenesis of Parkinson's disease. *J. Neurochem.* **139**, 120–133 (2016).

385. Leal, S. S., Cristóvão, J. S., Biesemeier, A., Cardoso, I. & Gomes, C. M. Aberrant zinc binding to immature conformers of metal-free copper-zinc superoxide dismutase triggers amorphous aggregation. *Met. Integr. Biometal Sci.* (2015). doi:10.1039/c4mt00278d

386. Crow, J. P., Sampson, J. B., Zhuang, Y., Thompson, J. A. & Beckman, J. S. Decreased zinc affinity of amyotrophic lateral sclerosis-associated superoxide dismutase mutants leads to enhanced catalysis of tyrosine nitration by peroxynitrite. *J. Neurochem.* **69**, 1936–1944 (1997).

387. Kaneko, M. *et al.* Zinc transporters ZnT3 and ZnT6 are downregulated in the spinal cords of patients with sporadic amyotrophic lateral sclerosis. *J. Neurosci. Res.* (2014). doi:10.1002/jnr.23491

388. Perez-Becerril, C., Morris, A. G., Mortimer, A., McKenna, P. J. & de Belleroche, J. Allelic variants in the zinc transporter-3 gene, SLC30A3, a candidate gene identified from gene expression studies, show gender-specific association with schizophrenia. *Eur. Psychiatry J. Assoc. Eur. Psychiatr.* **29**, 172–178 (2014).

389. Grabrucker, S. *et al.* Zinc deficiency dysregulates the synaptic ProSAP/Shank scaffold and might contribute to autism spectrum disorders. *Brain J. Neurol.* **137**, 137–152 (2014).

390. Lee, E.-J. *et al.* Trans-synaptic zinc mobilization improves social interaction in two mouse models of autism through NMDAR activation. *Nat. Commun.* **6**, 7168 (2015).

391. Młyniec, K., Budziszewska, B., Holst, B., Ostachowicz, B. & Nowak, G. GPR39 (Zinc Receptor) Knockout Mice Exhibit Depression-Like Behavior and CREB/BDNF Down-Regulation in the Hippocampus. *Int. J. Neuropsychopharmacol. Off. Sci. J. Coll. Int. Neuropsychopharmacol. CINP* (2014). doi:10.1093/ijnp/pyu002

392. Młyniec, K., Gaweł, M. & Nowak, G. Study of antidepressant drugs in GPR39 (zinc receptor(-/-)) knockout mice, showing no effect of conventional antidepressants, but effectiveness of NMDA antagonists. *Behav. Brain Res.* (2015). doi:10.1016/j.bbr.2015.03.053

393. Młyniec, K. *et al.* Immune malfunction in the GPR39 zinc receptor of knockout mice: Its relationship to depressive disorder. *J. Neuroimmunol.* **291**, 11–17 (2016).

394. Tena-Campos, M. *et al.* Zinc Is Involved in Depression by Modulating G Protein-Coupled Receptor Heterodimerization. *Mol. Neurobiol.* (2015). doi:10.1007/s12035-015-9153-y

395. Sowa-Kućma, M. *et al.* Chronic treatment with zinc and antidepressants induces enhancement of presynaptic/extracellular zinc concentration in the rat prefrontal cortex. *Amino Acids* **40**, 249–258 (2011).

396. Doboszewska, U. *et al.* Zinc deficiency in rats is associated with up-regulation of hippocampal NMDA receptor. *Prog. Neuropsychopharmacol. Biol. Psychiatry* (2014). doi:10.1016/j.pnpbp.2014.09.013

397. Manosso, L. M. *et al.* Antidepressant-like effect of zinc is dependent on signaling pathways implicated in BDNF modulation. *Prog. Neuropsychopharmacol. Biol. Psychiatry* **59C**, 59–67 (2015).

398. Szewczyk, B. *et al.* Activation of mTOR dependent signaling pathway is a necessary mechanism of antidepressant-like activity of zinc. *Neuropharmacology* **99**, 517–526 (2015).

399. Omar, N. N. & Tash, R. F. Fluoxetine coupled with zinc in a chronic mild stress model of depression: Providing a reservoir for optimum zinc signaling and neuronal remodeling. *Pharmacol. Biochem. Behav.* **160**, 30–38 (2017).

400. Nguyen, M., Vendier, L., Stigliani, J.-L., Meunier, B. & Robert, A. Structures of the Copper and Zinc Complexes of PBT2, a Chelating Agent Evaluated as Potential Drug for Neurodegenerative Diseases: Structures of the Copper and Zinc Complexes of PBT2, a Chelating Agent Evaluated as Potential Drug for Neurodegenerative Diseases. *Eur. J. Inorg. Chem.* **2017**, 600–608 (2017).

401. Quillinan, N., Herson, P. S. & Traystman, R. J. Neuropathophysiology of Brain Injury. *Anesthesiol. Clin.* **34**, 453–464 (2016).

402. Bano, D. & Ankarcrona, M. Beyond the critical point: An overview of excitotoxicity, calcium overload and the downstream consequences. *Neurosci. Lett.* **663**, 79–85 (2018).

403. Takeda, A., Hirate, M., Tamano, H. & Oku, N. Zinc movement in the brain under kainate-induced seizures. *Epilepsy Res.* **54**, 123–129 (2003).

404. Kitamura, Y. *et al.* Release of vesicular Zn^{2+} in a rat transient middle cerebral artery occlusion model. *Brain Res. Bull.* **69**, 622–625 (2006).

405. Kitamura, Y. *et al.* In vivo measurement of presynaptic Zn^{2+} release during forebrain ischemia in rats. *Biol. Pharm. Bull.* **29**, 821–823 (2006).

406. Doering, P. *et al.* Changes in the vesicular zinc pattern following traumatic brain injury. *Neuroscience* **150**, 93–103 (2007).

407. Carter, R. E., Aiba, I., Dietz, R. M., Sheline, C. T. & Shuttleworth, C. W. Spreading depression and related events are significant sources of neuronal Zn^{2+} release and accumulation. *J. Cereb. Blood Flow Metab. Off. J. Int. Soc. Cereb. Blood Flow Metab.* **31**, 1073–1084 (2011).

408. Pereno, G. L. & Beltramino, C. A. Timed changes of synaptic zinc, synaptophysin and MAP2 in medial extended amygdala of epileptic animals are suggestive of reactive neuroplasticity. *Brain Res.* **1328**, 130–138 (2010).

409. Domínguez, M. I., Blasco-Ibáñez, J. M., Crespo, C., Marqués-Marí, A. I. & Martínez-Guijarro, F. J. Zinc chelation during non-lesioning overexcitation results in neuronal death in the mouse hippocampus. *Neuroscience* **116**, 791–806 (2003).

410. Takeda, A., Hirate, M., Tamano, H., Nisibaba, D. & Oku, N. Susceptibility to kainate-induced seizures under dietary zinc deficiency. *J. Neurochem.* **85**, 1575–1580 (2003).

411. Côté, A. *et al.* Cell type-specific action of seizure-induced intracellular zinc accumulation in the rat hippocampus. *J. Physiol.* **566**, 821–837 (2005).

412. Kitamura, Y. *et al.* Protective effect of zinc against ischemic neuronal injury in a middle cerebral artery occlusion model. *J. Pharmacol. Sci.* **100**, 142–148 (2006).

413. Domínguez, M.-I. *et al.* Neural overexcitation and implication of NMDA and AMPA receptors in a mouse model of temporal lobe epilepsy implying zinc chelation. *Epilepsia* **47**, 887–899 (2006).

414. Aquilani, R., Sessarego, P., Iadarola, P., Barbieri, A. & Boschi, F. Nutrition for brain recovery after ischemic stroke: an added value to rehabilitation. *Nutr. Clin. Pract. Off. Publ. Am. Soc. Parenter. Enter. Nutr.* **26**, 339–345 (2011).

415. Qiu, M. *et al.* Zinc mediates the neuronal activity-dependent anti-apoptotic effect. *PloS One* **12**, e0182150 (2017).

416. Koh, J. Y. & Choi, D. W. Zinc alters excitatory amino acid neurotoxicity on cortical neurons. *J. Neurosci. Off. J. Soc. Neurosci.* **8**, 2164–2171 (1988).

417. Williamson, A. & Spencer, D. Zinc reduces dentate granule cell hyperexcitability in epileptic humans. *Neuroreport* **6**, 1562–1564 (1995).

418. Bancila, V., Nikonenko, I., Dunant, Y. & Bloc, A. Zinc inhibits glutamate release via activation of pre-synaptic K channels and reduces ischaemic damage in rat hippocampus. *J. Neurochem.* **90**, 1243–1250 (2004).

419. Anastassov, I., Ripps, H. & Chappell, R. L. Cytoprotection by endogenous zinc in the vertebrate retina. *J. Neurochem.* **129**, 249–255 (2014).

420. Cope, E. C., Morris, D. R., Gower-Winter, S. D., Brownstein, N. C. & Levenson, C. W. Effect of zinc supplementation on neuronal precursor proliferation in the rat hippocampus after traumatic brain injury. *Exp. Neurol.* (2016). doi:10.1016/j.expneurol.2016.02.017

421. Elsas, S.-M., Hazany, S., Gregory, W. L. & Mody, I. Hippocampal zinc infusion delays the development of afterdischarges and seizures in a kindling model of epilepsy. *Epilepsia* **50**, 870–879 (2009).

422. Aras, M. A., Hara, H., Hartnett, K. A., Kandler, K. & Aizenman, E. Protein kinase C regulation of neuronal zinc signaling mediates survival during preconditioning. *J. Neurochem.* **110**, 106–117 (2009).

423. Cole, T. B., Robbins, C. A., Wenzel, H. J., Schwartzkroin, P. A. & Palmiter, R. D. Seizures and neuronal damage in mice lacking vesicular zinc. *Epilepsy Res.* **39**, 153–169 (2000).

424. Doering, P. *et al.* Chemical blocking of zinc ions in CNS increases neuronal damage following traumatic brain injury (TBI) in mice. *PloS One* **5**, e10131 (2010).

425. Aiba, I., Carlson, A. P., Sheline, C. T. & Shuttleworth, C. W. Synaptic release and extracellular actions of Zn^{2+} limit propagation of spreading depression and related events in vitro and in vivo. *J. Neurophysiol.* **107**, 1032–1041 (2012).

426. Hildebrand, M. S. *et al.* Loss of synaptic Zn(2+) transporter function increases risk of febrile seizures. *Sci. Rep.* **5**, 17816 (2015).

427. Noh, K. M., Kim, Y. H. & Koh, J. Y. Mediation by membrane protein kinase C of zinc-induced oxidative neuronal injury in mouse cortical cultures. *J. Neurochem.* **72**, 1609–1616 (1999).

428. Canzoniero, L. M., Turetsky, D. M. & Choi, D. W. Measurement of intracellular free zinc concentrations accompanying zinc-induced neuronal death. *J. Neurosci. Off. J. Soc. Neurosci.* **19**, RC31 (1999).

429. Kim, Y. H., Kim, E. Y., Gwag, B. J., Sohn, S. & Koh, J. Y. Zinc-induced cortical neuronal death with features of apoptosis and necrosis: mediation by free radicals. *Neuroscience* **89**, 175–182 (1999).

430. Lin, D. D., Cohen, A. S. & Coulter, D. A. Zinc-induced augmentation of excitatory synaptic currents and glutamate receptor responses in hippocampal CA3 neurons. *J. Neurophysiol.* **85**, 1185–1196 (2001).

431. Wang, H. *et al.* Excessive zinc chloride induces murine photoreceptor cell death via reactive oxygen species and mitochondrial signaling pathway. *J. Inorg. Biochem.* **187**, 25–32 (2018).

432. Frederickson, C. J., Hernandez, M. D. & McGinty, J. F. Translocation of zinc may contribute to seizure-induced death of neurons. *Brain Res.* **480**, 317–321 (1989).

433. Koh, J. Y. *et al.* The role of zinc in selective neuronal death after transient global cerebral ischemia. *Science* **272**, 1013–1016 (1996).

434. Suh, S. W. *et al.* Evidence that synaptically-released zinc contributes to neuronal injury after traumatic brain injury. *Brain Res.* **852**, 268–273 (2000).

435. Suh, S. W., Thompson, R. B. & Frederickson, C. J. Loss of vesicular zinc and appearance of perikaryal zinc after seizures induced by pilocarpine. *Neuroreport* **12**, 1523–1525 (2001).

436. Lee, J.-M. *et al.* Zinc translocation accelerates infarction after mild transient focal ischemia. *Neuroscience* **115**, 871–878 (2002).

437. Revuelta, M., Castaño, A., Machado, A., Cano, J. & Venero, J. L. Kainate-induced zinc translocation from presynaptic terminals causes neuronal and astroglial cell death and mRNA loss of BDNF receptors in the hippocampal formation and amygdala. *J. Neurosci. Res.* **82**, 184–195 (2005).

438. Sensi, S. L., Rockabrand, E. & Canzoniero, L. M. T. Acidosis enhances toxicity induced by kainate and zinc exposure in aged cultured astrocytes. *Biogerontology* **7**, 367–374 (2006).

439. Lavoie, N. *et al.* Extracellular chelation of zinc does not affect hippocampal excitability and seizure-induced cell death in rats. *J. Physiol.* **578**, 275–289 (2007).

440. Dietz, R. M., Weiss, J. H. & Shuttleworth, C. W. Zn^{2+} influx is critical for some forms of spreading depression in brain slices. *J. Neurosci. Off. J. Soc. Neurosci.* **28**, 8014–8024 (2008).

441. Sheline, C. T., Zhou, Y. & Bai, S. Light-induced photoreceptor and RPE degeneration involve zinc toxicity and are attenuated by pyruvate, nicotinamide, or cyclic light. *Mol. Vis.* **16**, 2639–2652 (2010).

442. Wang, W.-M. *et al.* The Zinc Ion Chelating Agent TPEN Attenuates Neuronal Death/apoptosis Caused by Hypoxia/ischemia Via Mediating the Pathophysiological Cascade Including Excitotoxicity, Oxidative Stress, and Inflammation. *CNS Neurosci. Ther.* (2015). doi:10.1111/cns.12428

443. Qi, Z. *et al.* Zinc contributes to acute cerebral ischemia-induced blood-brain barrier disruption. *Neurobiol. Dis.* **95**, 12–21 (2016).

444. Li, Y. *et al.* Mobile zinc increases rapidly in the retina after optic nerve injury and regulates ganglion cell survival and optic nerve regeneration. *Proc. Natl. Acad. Sci. U. S. A.* **114**, E209–E218 (2017).

445. Medvedeva, Y. V., Ji, S. G., Yin, H. Z. & Weiss, J. H. Differential Vulnerability of CA1 versus CA3 Pyramidal Neurons After Ischemia: Possible Relationship to Sources of Zn^{2+} Accumulation and Its Entry into and Prolonged Effects on Mitochondria. *J. Neurosci. Off. J. Soc. Neurosci.* **37**, 726–737 (2017).

446. Zhang, F. *et al.* TPEN, a Specific Zn(2+) Chelator, Inhibits Sodium Dithionite and Glucose Deprivation (SDGD)-Induced Neuronal Death by Modulating Apoptosis, Glutamate Signaling, and Voltage-Gated K(+) and Na(+) Channels. *Cell. Mol. Neurobiol.* **37**, 235–250 (2017).

447. Trakhtenberg, E. F. *et al.* Zinc chelation and Klf9 knockdown cooperatively promote axon regeneration after optic nerve injury. *Exp. Neurol.* **300**, 22–29 (2018).

448. Choi, J. A., Kim, Y. J., Seo, B.-R., Koh, J.-Y. & Yoon, Y. H. Potential Role of Zinc Dyshomeostasis in Matrix Metalloproteinase-2 and -9 Activation and Photoreceptor Cell Death in Experimental Retinal Detachment. *Invest. Ophthalmol. Vis. Sci.* **59**, 3058–3068 (2018).

449. Zhao, L., Liu, Q., Ma, S., Zhang, Y. & Liang, P. TPEN Attenuates Neural Autophagy Induced by Synaptically-released Zinc Translocation and Improves Histological Outcomes after Traumatic Brain Injury in Rats. *Ann. Clin. Lab. Sci.* **48**, 446–452 (2018).

450. Lee, J. Y., Cole, T. B., Palmiter, R. D. & Koh, J. Y. Accumulation of zinc in degenerating hippocampal neurons of ZnT3-null mice after seizures: evidence against synaptic vesicle origin. *J. Neurosci. Off. J. Soc. Neurosci.* **20**, RC79 (2000).

451. Chen, D. *et al.* Neuroprotective Effect of ZnT3 Knockout on Subarachnoid Hemorrhage. *Transl. Neurosci.* **9**, 26–32 (2018).

452. Bai, S., Sheline, C. R., Zhou, Y. & Sheline, C. T. A reduced zinc diet or zinc transporter 3 knockout attenuate light induced zinc accumulation and retinal degeneration. *Exp. Eye Res.* **108**, 59–67 (2013).

453. Erickson, J. C., Hollopeter, G., Thomas, S. A., Froelick, G. J. & Palmiter, R. D. Disruption of the metallothionein-III gene in mice: analysis of brain zinc, behavior, and neuron vulnerability to metals, aging, and seizures. *J. Neurosci. Off. J. Soc. Neurosci.* **17**, 1271–1281 (1997).

454. Medvedeva, Y. V., Lin, B., Shuttleworth, C. W. & Weiss, J. H. Intracellular Zn^{2+} accumulation contributes to synaptic failure, mitochondrial depolarization, and cell death in an acute slice oxygen-glucose deprivation model of ischemia. *J. Neurosci. Off. J. Soc. Neurosci.* **29**, 1105–1114 (2009).

455. Carter, R. E., Weiss, J. H. & Shuttleworth, C. W. Zn^{2+} chelation improves recovery by delaying spreading depression-like events. *Neuroreport* **21**, 1060–1064 (2010).

456. Clausen, A., McClanahan, T., Ji, S. G. & Weiss, J. H. Mechanisms of rapid reactive oxygen species generation in response to cytosolic Ca^{2+} or Zn^{2+} loads in cortical neurons. *PloS One* **8**, e83347 (2013).

457. Dong, W. *et al.* Reduction of zinc accumulation in mitochondria contributes to decreased cerebral ischemic injury by normobaric hyperoxia treatment in an experimental stroke model. *Exp. Neurol.* (2015). doi:10.1016/j.expneurol.2015.04.005

458. Granzotto, A. & Sensi, S. L. Intracellular zinc is a critical intermediate in the excitotoxic cascade. *Neurobiol. Dis.* (2015). doi:10.1016/j.nbd.2015.04.010

459. Yang, J. S., Perveen, S., Ha, T. J., Kim, S. Y. & Yoon, S. H. Cyanidin-3-glucoside inhibits glutamate-induced Zn^{2+} signaling and neuronal cell death in cultured rat hippocampal neurons by inhibiting Ca^{2+}-induced mitochondrial depolarization and formation of reactive oxygen species. *Brain Res.* **1606**, 9–20 (2015).

460. Medvedeva, Y. V. & Weiss, J. H. Intramitochondrial Zn^{2+} accumulation via the Ca^{2+} uniporter contributes to acute ischemic neurodegeneration. *Neurobiol. Dis.* **68**, 137–144 (2014).

461. Cuajungco, M. P. & Lees, G. J. Nitric oxide generators produce accumulation of chelatable zinc in hippocampal neuronal perikarya. *Brain Res.* **799**, 118–129 (1998).

462. Bossy-Wetzel, E. *et al.* Crosstalk between nitric oxide and zinc pathways to neuronal cell death involving mitochondrial dysfunction and p38-activated K^+ channels. *Neuron* **41**, 351–365 (2004).

463. Kim, S. *et al.* Disparate roles of zinc in chemical hypoxia-induced neuronal death. *Front. Cell. Neurosci.* **9**, 1 (2015).

464. Hung, H.-H. *et al.* Dopamine elevates intracellular zinc concentration in cultured rat embryonic cortical neurons through the cAMP-nitric oxide signaling cascade. *Mol. Cell. Neurosci.* **82**, 35–45 (2017).

465. Babu, C. S., Lee, Y.-M., Dudev, T. & Lim, C. Modeling Zn^{2+} release from metallothionein. *J. Phys. Chem. A* **118**, 9244–9252 (2014).

466. Lebrun, V. *et al.* Efficient Oxidation and Destabilization of Zn(Cys)4 Zinc Fingers by Singlet Oxygen. *Angew. Chem. Int. Ed Engl.* (2014). doi:10.1002/anie.201405333

467. Lebrun, V. *et al.* Reactivity of a Zn(Cys)2 (His)2 Zinc Finger with Singlet Oxygen: Oxidation Directed toward Cysteines but not Histidines. *Chem. Weinh. Bergstr. Ger.* (2015). doi:10.1002/chem.201501749

468. Park, S. E. *et al.* Contribution of Zinc-Dependent Delayed Calcium Influx via TRPC5 in Oxidative Neuronal Death and its Prevention by Novel TRPC Antagonist. *Mol. Neurobiol.* **56**, 2822–2835 (2019).

469. Dineley, K. E., Devinney, M. J., 2nd, Zeak, J. A., Rintoul, G. L. & Reynolds, I. J. Glutamate mobilizes [Zn^{2+}] through Ca^{2+} -dependent reactive oxygen species accumulation. *J. Neurochem.* **106**, 2184–2193 (2008).

470. Sheline, C. T., Behrens, M. M. & Choi, D. W. Zinc-induced cortical neuronal death: contribution of energy failure attributable to loss of NAD(+) and inhibition of glycolysis. *J. Neurosci. Off. J. Soc. Neurosci.* **20**, 3139–3146 (2000).

471. Zhao, Y. *et al.* Synergistic Interaction Between Zinc and Reactive Oxygen Species Amplifies Ischemic Brain Injury in Rats. *Stroke* **49**, 2200–2210 (2018).

472. Sensi, S. L. *et al.* Modulation of mitochondrial function by endogenous Zn^{2+} pools. *Proc. Natl. Acad. Sci. U. S. A.* **100**, 6157–6162 (2003).

473. Sensi, S. L., Ton-That, D. & Weiss, J. H. Mitochondrial sequestration and Ca(2+)-dependent release of cytosolic Zn(2+) loads in cortical neurons. *Neurobiol. Dis.* **10**, 100–108 (2002).

474. Ji, S. G. & Weiss, J. H. Zn^{2+}-induced disruption of neuronal mitochondrial function: Synergism with Ca^{2+}, critical dependence upon cytosolic Zn^{2+} buffering, and contributions to neuronal injury. *Exp. Neurol.* **302**, 181–195 (2018).

475. Yin, H. Z. *et al.* Rapid Intramitochondrial Zn^{2+} Accumulation in CA1 Hippocampal Pyramidal Neurons After Transient Global Ischemia: A Possible Contributor to Mitochondrial Disruption and Cell Death. *J. Neuropathol. Exp. Neurol.* **78**, 655–664 (2019).

476. Sensi, S. L., Yin, H. Z. & Weiss, J. H. AMPA/kainate receptor-triggered Zn^{2+} entry into cortical neurons induces mitochondrial Zn^{2+} uptake and persistent mitochondrial dysfunction. *Eur. J. Neurosci.* **12**, 3813–3818 (2000).

477. Sensi, S. L., Yin, H. Z., Carriedo, S. G., Rao, S. S. & Weiss, J. H. Preferential Zn^{2+} influx through Ca^{2+}-permeable AMPA/kainate channels triggers prolonged mitochondrial superoxide production. *Proc. Natl. Acad. Sci. U. S. A.* **96**, 2414–2419 (1999).

478. Min, Y. K., Lee, J. E. & Chung, K. C. Zinc induces cell death in immortalized embryonic hippocampal cells via activation of Akt-GSK-3beta signaling. *Exp. Cell Res.* **313**, 312–321 (2007).

479. Lee, J. Y. *et al.* Induction by synaptic zinc of heat shock protein-70 in hippocampus after kainate seizures. *Exp. Neurol.* **161**, 433–441 (2000).

480. Malairaman, U., Dandapani, K. & Katyal, A. Effect of Ca2EDTA on Zinc Mediated Inflammation and Neuronal Apoptosis in Hippocampus of an In Vivo Mouse Model of Hypobaric Hypoxia. *PloS One* **9**, e110253 (2014).

481. Cortese, M. M., Suschek, C. V., Wetzel, W., Kröncke, K.-D. & Kolb-Bachofen, V. Zinc protects endothelial cells from hydrogen peroxide via Nrf2-dependent stimulation of glutathione biosynthesis. *Free Radic. Biol. Med.* **44**, 2002–2012 (2008).

482. Lee, S. R. Critical Role of Zinc as Either an Antioxidant or a Prooxidant in Cellular Systems. *Oxidative Medicine and Cellular Longevity* (2018). doi:10.1155/2018/9156285

483. Takeda, A., Kanno, S., Sakurada, N., Ando, M. & Oku, N. Attenuation of hippocampal mossy fiber long-term potentiation by low micromolar concentrations of zinc. *J. Neurosci. Res.* **86**, 2906–2911 (2008).

484. McAllister, B. B. & Dyck, R. H. Zinc Transporter 3 (ZnT3) and Vesicular Zinc in Central Nervous System Function. *Neurosci. Biobehav. Rev.* doi:10.1016/j.neubiorev.2017.06.006

485. Kim, A. M. *et al.* Zinc sparks are triggered by fertilization and facilitate cell cycle resumption in mammalian eggs. *ACS Chem. Biol.* **6**, 716–723 (2011).

486. Paoletti, P., Ascher, P. & Neyton, J. High-affinity zinc inhibition of NMDA NR1-NR2A receptors. *J. Neurosci. Off. J. Soc. Neurosci.* **17**, 5711–5725 (1997).

487. Horenstein, J. & Akabas, M. H. Location of a high affinity Zn^{2+} binding site in the channel of alpha1beta1 gamma-aminobutyric acidA receptors. *Mol. Pharmacol.* **53**, 870–877 (1998).

488. Kalappa, B. I., Anderson, C. T., Goldberg, J. M., Lippard, S. J. & Tzounopoulos, T. AMPA receptor inhibition by synaptically released zinc. *Proc. Natl. Acad. Sci. U. S. A.* (2015). doi:10.1073/pnas.1512296112

489. Takeda, A. *et al.* Maintained LTP and Memory Are Lost by Zn^{2+} Influx into Dentate Granule Cells, but Not Ca^{2+} Influx. *Mol. Neurobiol.* **55**, 1498–1508 (2018).

490. Martel, G., Hevi, C., Kane-Goldsmith, N. & Shumyatsky, G. P. Zinc transporter ZnT3 is involved in memory dependent on the hippocampus and perirhinal cortex. *Behav. Brain Res.* **223**, 233–238 (2011).

491. Frederickson, C. J., Rampy, B. A., Reamy-Rampy, S. & Howell, G. A. Distribution of histochemically reactive zinc in the forebrain of the rat. *J. Chem. Neuroanat.* **5**, 521–530 (1992).

492. Seress, L. & Gallyas, F. The use of a sodium tungstate developer markedly improves the electron microscopic localization of zinc by the Timm method. *J. Neurosci. Methods* **100**, 33–39 (2000).

493. Stoltenberg, M. *et al.* Immersion autometallographic tracing of zinc ions in Alzheimer beta-amyloid plaques. *Histochem. Cell Biol.* **123**, 605–611 (2005).

494. Hwang, J. J., Lee, S.-J., Kim, T.-Y., Cho, J.-H. & Koh, J.-Y. Zinc and 4-hydroxy-2-nonenal mediate lysosomal membrane permeabilization induced by H2O2 in cultured hippocampal neurons. *J. Neurosci. Off. J. Soc. Neurosci.* **28**, 3114–3122 (2008).

495. McCormick, N., Velasquez, V., Finney, L., Vogt, S. & Kelleher, S. L. X-ray fluorescence microscopy reveals accumulation and secretion of discrete intracellular zinc pools in the lactating mouse mammary gland. *PloS One* **5**, e11078 (2010).

496. Han, Y., Goldberg, J. M., Lippard, S. J. & Palmer, A. E. Superiority of SpiroZin2 Versus FluoZin-3 for monitoring vesicular Zn^{2+} allows tracking of lysosomal Zn^{2+} pools. *Sci. Rep.* **8**, 15034 (2018).

497. Ryan, T. A. *et al.* The kinetics of synaptic vesicle recycling measured at single presynaptic boutons. *Neuron* **11**, 713–724 (1993).

498. Pyle, J. L., Kavalali, E. T., Choi, S. & Tsien, R. W. Visualization of synaptic activity in hippocampal slices with FM1-43 enabled by fluorescence quenching. *Neuron* **24**, 803–808 (1999).

499. Li, D. *et al.* Imaging dynamic insulin release using a fluorescent zinc indicator for monitoring induced exocytotic release (ZIMIR). *Proc. Natl. Acad. Sci. U. S. A.* **108**, 21063–21068 (2011).

500. Krężel, A. & Maret, W. The biological inorganic chemistry of zinc ions. *Arch. Biochem. Biophys.* (2016). doi:10.1016/j.abb.2016.04.010

501. Marszałek, I. *et al.* Revised stability constant, spectroscopic properties and binding mode of Zn(II) to FluoZin-3, the most common zinc probe in life sciences. *J. Inorg. Biochem.* **161**, 107–114 (2016).

502. Poddar, R., Rajagopal, S., Shuttleworth, C. W. & Paul, S. Zn^{2+}-dependent activation of the Trk signaling pathway induces phosphorylation of the brain-enriched tyrosine phosphatase STEP: molecular basis for Zn^{2+}-induced ERK MAPK activation. *J. Biol. Chem.* (2015). doi:10.1074/jbc.M115.663468

503. Lobner, D. *et al.* Zinc-induced neuronal death in cortical neurons. *Cell. Mol. Biol. Noisy--Gd. Fr.* **46**, 797–806 (2000).

504. Casagrande, S., Valle, L., Cupello, A. & Robello, M. Modulation by Zn(2+) and Cd(2+) of GABA(A) receptors of rat cerebellum granule cells in culture. *Eur. Biophys. J. EBJ* **32**, 40–46 (2003).

505. Marchetti, C. Interaction of metal ions with neurotransmitter receptors and potential role in neurodiseases. *Biometals Int. J. Role Met. Ions Biol. Biochem. Med.* (2014). doi:10.1007/s10534-014-9791-y

506. Wu, Q.-F. *et al.* Fibroblast Growth Factor 13 Is a Microtubule-Stabilizing Protein Regulating Neuronal Polarization and Migration. *Cell* **149**, 1549–1564 (2012).

507. Yao, D. L. *et al.* Pretreatment with intravenous FGF-13 reduces infarct volume and ameliorates neurological deficits following focal cerebral ischemia in rats. *Brain Res.* **818**, 140–146 (1999).

508. Li, J. *et al.* Lentivirus Mediating FGF13 Enhances Axon Regeneration after Spinal Cord Injury by Stabilizing Microtubule and Improving Mitochondrial Function. *J. Neurotrauma* **35**, 548–559 (2018).

509. Puranam, R. S. *et al.* Disruption of Fgf13 Causes Synaptic Excitatory–Inhibitory Imbalance and Genetic Epilepsy and Febrile Seizures Plus. *J. Neurosci.* **35**, 8866–8881 (2015).

510. Pablo, J. L., Wang, C., Presby, M. M. & Pitt, G. S. Polarized localization of voltage-gated Na^+ channels is regulated by concerted FGF13 and FGF14 action. *Proc. Natl. Acad. Sci.* **113**, E2665–E2674 (2016).

511. Doboszewska, U. *et al.* Zinc signaling and epilepsy. *Pharmacol. Ther.* (2018). doi:10.1016/j.pharmthera.2018.08.013

512. Nolt, M. J. *et al.* EphB controls NMDA receptor function and synaptic targeting in a subunit-specific manner. *J. Neurosci. Off. J. Soc. Neurosci.* **31**, 5353–5364 (2011).

513. Liu, B. P., Cafferty, W. B. J., Budel, S. O. & Strittmatter, S. M. Extracellular regulators of axonal growth in the adult central nervous system. *Philos. Trans. R. Soc. Lond. B. Biol. Sci.* **361**, 1593–1610 (2006).

514. Kang, W. & Hébert, J. M. FGF Signaling Is Necessary for Neurogenesis in Young Mice and Sufficient to Reverse Its Decline in Old Mice. *J. Neurosci. Off. J. Soc. Neurosci.* **35**, 10217–10223 (2015).

515. Mayanagi, T., Yasuda, H. & Sobue, K. PSD-Zip70 Deficiency Causes Prefrontal Hypofunction Associated with Glutamatergic Synapse Maturation Defects by Dysregulation of Rap2 Activity. *J. Neurosci. Off. J. Soc. Neurosci.* **35**, 14327–14340 (2015).

516. Raivich, G. & Behrens, A. Role of the AP-1 transcription factor c-Jun in developing, adult and injured brain. *Prog. Neurobiol.* **78**, 347–363 (2006).

517. Zhou, F.-Q., Walzer, M. A. & Snider, W. D. Turning on the machine: genetic control of axon regeneration by c-Jun. *Neuron* **43**, 1–2 (2004).

518. Pearson, A. G. *et al.* ATF3 enhances c-Jun-mediated neurite sprouting. *Brain Res. Mol. Brain Res.* **120**, 38–45 (2003).

519. Fagoe, N. D., Attwell, C. L., Kouwenhoven, D., Verhaagen, J. & Mason, M. R. J. Overexpression of ATF3 or the combination of ATF3, c-Jun, STAT3 and Smad1 promotes regeneration of the central axon branch of sensory neurons but without synergistic effects. *Hum. Mol. Genet.* **24**, 6788–6800 (2015).

520. Yuan, Z. *et al.* Opposing roles for ATF2 and c-Fos in c-Jun-mediated neuronal apoptosis. *Mol. Cell. Biol.* **29**, 2431–2442 (2009).

521. Fiedler, B. L. *et al.* Droplet Microfluidic Flow Cytometer For Sorting On Transient Cellular Responses Of Genetically-Encoded Sensors. *Anal. Chem.* (2016). doi:10.1021/acs.analchem.6b03235

522. Bolger, A. M., Lohse, M. & Usadel, B. Trimmomatic: a flexible trimmer for Illumina sequence data. *Bioinforma. Oxf. Engl.* **30**, 2114–2120 (2014).

523. Kim, D. *et al.* TopHat2: accurate alignment of transcriptomes in the presence of insertions, deletions and gene fusions. *Genome Biol.* **14**, R36 (2013).

524. Li, H. *et al.* The Sequence Alignment/Map format and SAMtools. *Bioinforma. Oxf. Engl.* **25**, 2078–2079 (2009).

525. Liao, Y., Smyth, G. K. & Shi, W. The Subread aligner: fast, accurate and scalable read mapping by seed-and-vote. *Nucleic Acids Res.* **41**, e108 (2013).

526. Love, M. I., Huber, W. & Anders, S. Moderated estimation of fold change and dispersion for RNA-seq data with DESeq2. *Genome Biol.* **15**, 550 (2014).

527. Huang, D. W., Sherman, B. T. & Lempicki, R. A. Bioinformatics enrichment tools: paths toward the comprehensive functional analysis of large gene lists. *Nucleic Acids Res.* **37**, 1–13 (2009).

528. Huang, D. W., Sherman, B. T. & Lempicki, R. A. Systematic and integrative analysis of large gene lists using DAVID bioinformatics resources. *Nat. Protoc.* **4**, 44–57 (2009).

529. Subramanian, A. *et al.* Gene set enrichment analysis: a knowledge-based approach for interpreting genome-wide expression profiles. *Proc. Natl. Acad. Sci. U. S. A.* **102**, 15545–15550 (2005).

530. Mootha, V. K. *et al.* PGC-1alpha-responsive genes involved in oxidative phosphorylation are coordinately downregulated in human diabetes. *Nat. Genet.* **34**, 267–273 (2003).

531. Lai, T. W., Zhang, S. & Wang, Y. T. Excitotoxicity and stroke: identifying novel targets for neuroprotection. *Prog. Neurobiol.* **115**, 157–188 (2014).

532. Fan, J., Dawson, T. M. & Dawson, V. L. Cell Death Mechanisms of Neurodegeneration. in *Neurodegenerative Diseases: Pathology, Mechanisms, and Potential Therapeutic Targets* (eds. Beart, P., Robinson, M., Rattray, M. & Maragakis, N. J.) 403–425 (Springer International Publishing, 2017). doi:10.1007/978-3-319-57193-5_16

533. Thornton, C., Baburamani, A. A., Kichev, A. & Hagberg, H. Oxidative stress and endoplasmic reticulum (ER) stress in the development of neonatal hypoxic–ischaemic brain injury. *Biochem. Soc. Trans.* **45**, 1067–1076 (2017).

534. Park, S. J. *et al.* DISC1 Modulates Neuronal Stress Responses by Gate-Keeping ER-Mitochondria Ca^{2+} Transfer through the MAM. *Cell Rep.* **21**, 2748–2759 (2017).

535. He, Q. *et al.* Titanium dioxide nanoparticles induce mouse hippocampal neuron apoptosis via oxidative stress- and calcium imbalance-mediated endoplasmic reticulum stress. *Environ. Toxicol. Pharmacol.* **63**, 6–15 (2018).

536. Gao, Z. *et al.* Trehalose inhibits H2O2-induced autophagic death in dopaminergic SH-SY5Y cells via mitigation of ROS-dependent endoplasmic reticulum stress and AMPK activation. *Int. J. Med. Sci.* **15**, 1014–1024 (2018).

537. Hayashi, T. *et al.* Damage to the endoplasmic reticulum and activation of apoptotic machinery by oxidative stress in ischemic neurons. *J. Cereb. Blood Flow Metab. Off. J. Int. Soc. Cereb. Blood Flow Metab.* **25**, 41–53 (2005).

538. Yuan, Y., Niu, F., Liu, Y. & Lu, N. Zinc and its effects on oxidative stress in Alzheimer's disease. *Neurol. Sci.* **35**, 923–928 (2014).

539. Tamano, H., Morioka, H., Nishio, R., Takeuchi, A. & Takeda, A. AMPA-induced extracellular Zn^{2+} influx into nigral dopaminergic neurons causes movement disorder in rats. *Neurotoxicology* (2018). doi:10.1016/j.neuro.2018.08.008

540. Chauhan, A. K., Mittra, N., Singh, B. K. & Singh, C. Inhibition of glutathione S-transferase-pi triggers c-jun N-terminal kinase-dependent neuronal death in Zn-induced Parkinsonism. *Mol. Cell. Biochem.* **452**, 95–104 (2019).

541. Aizenman, E. *et al.* Induction of Neuronal Apoptosis by Thiol Oxidation. *J. Neurochem.* **75**, 1878–1888 (2000).

542. Lee, S.-J., Seo, B.-R., Choi, E.-J. & Koh, J.-Y. The role of reciprocal activation of cAbl and Mst1 in the Oxidative death of cultured astrocytes. *Glia* **62**, 639–648 (2014).

543. Stork, C. J. & Li, Y. V. Elevated Cytoplasmic Free Zinc and Increased Reactive Oxygen Species Generation in the Context of Brain Injury. in *Brain Edema XVI: Translate Basic Science into Clinical Practice* (eds. Applegate, R. L., Chen, G., Feng, H. & Zhang, J. H.) 347–353 (Springer International Publishing, 2016). doi:10.1007/978-3-319-18497-5_60

544. Zhang, Y. *et al.* Intracellular Zinc Release and ERK Phosphorylation Are Required Upstream of 12-Lipoxygenase Activation in Peroxynitrite Toxicity to Mature Rat Oligodendrocytes. *J. Biol. Chem.* **281**, 9460–9470 (2006).

545. Pan, R., Chen, C., Liu, W.-L. & Liu, K.-J. Zinc promotes the death of hypoxic astrocytes by upregulating hypoxia-induced hypoxia-inducible factor-1alpha expression via poly(ADP-ribose) polymerase-1. *CNS Neurosci. Ther.* **19**, 511–520 (2013).

546. Gazaryan, I. G., Krasinskaya, I. P., Kristal, B. S. & Brown, A. M. Zinc Irreversibly Damages Major Enzymes of Energy Production and Antioxidant Defense Prior to Mitochondrial Permeability Transition. *J. Biol. Chem.* **282**, 24373–24380 (2007).

547. Sharpley, M. S. & Hirst, J. The inhibition of mitochondrial complex I (NADH:ubiquinone oxidoreductase) by Zn^{2+}. *J. Biol. Chem.* **281**, 34803–34809 (2006).

548. Tanaka, K.-I. & Kawahara, M. Copper Enhances Zinc-Induced Neurotoxicity and the Endoplasmic Reticulum Stress Response in a Neuronal Model of Vascular Dementia. *Front. Neurosci.* **11**, 58 (2017).

549. Wu, C. *et al.* MiRNAs regulate oxidative stress related genes via binding to the 3′ UTR and TATA-box regions: a new hypothesis for cataract pathogenesis. *BMC Ophthalmol.* **17**, 142 (2017).

550. Hybertson, B. M., Gao, B., Bose, S. K. & McCord, J. M. Oxidative stress in health and disease: The therapeutic potential of Nrf2 activation. *Mol. Aspects Med.* **32**, 234–246 (2011).

551. Bao, B., Prasad, A. S., Beck, F. W. J. & Sarkar, F. H. Zinc up-regulates NF-κB activation via phosphorylation of IκB in HUT-78 (Th0) cells. *FEBS Lett.* **581**, 4507–4511 (2007).

552. Kim, D., Langmead, B. & Salzberg, S. L. HISAT: a fast spliced aligner with low memory requirements. *Nat. Methods* **12**, 357–360 (2015).

553. Liao, Y., Smyth, G. K. & Shi, W. featureCounts: an efficient general purpose program for assigning sequence reads to genomic features. *Bioinforma. Oxf. Engl.* **30**, 923–930 (2014).

554. Baltaci, A. K. & Yuce, K. Zinc Transporter Proteins. *Neurochem. Res.* (2017). doi:10.1007/s11064-017-2454-y

555. Strand, O. A. H. *et al.* Synthesis and initial in vitro biological evaluation of two new zinc-chelating compounds: comparison with TPEN and PAC-1. *Bioorg. Med. Chem.* **21**, 5175–5181 (2013).

556. Goglia, A. G. & Toettcher, J. E. A bright future: optogenetics to dissect the spatiotemporal control of cell behavior. *Curr. Opin. Chem. Biol.* **48**, 106–113 (2019).

557. Taslimi, A. *et al.* An optimized optogenetic clustering tool for probing protein interaction and function. *Nat. Commun.* **5**, 4925 (2014).

558. Bonger, K. M., Rakhit, R., Payumo, A. Y., Chen, J. K. & Wandless, T. J. General Method for Regulating Protein Stability with Light. *ACS Chem. Biol.* **9**, 111–115 (2014).

559. Maret, W. Zinc and the zinc proteome. *Met. Ions Life Sci.* **12**, 479–501 (2013).

560. Zhu, J. & Weng, Z. FAST: a novel protein structure alignment algorithm. *Proteins* **58**, 618–627 (2005).

561. Andreini, C., Bertini, I. & Cavallaro, G. Minimal functional sites allow a classification of zinc sites in proteins. *PloS One* **6**, e26325 (2011).

562. Kawabata, T. MATRAS: A program for protein 3D structure comparison. *Nucleic Acids Res.* **31**, 3367–3369 (2003).

563. Papadopoulos, E. *et al.* Solution structure and biophysical properties of MqsA, a Zn-containing antitoxin from Escherichia coli. *Biochim. Biophys. Acta* **1824**, 1401–1408 (2012).

564. Sikorska, M., Krężel, A. & Otlewski, J. Femtomolar Zn^{2+} affinity of LIM domain of PDLIM1 protein uncovers crucial contribution of protein-protein interactions to protein stability. *J. Inorg. Biochem.* **115**, 28–35 (2012).

565. Hirose, J. *et al.* Characterization of the metal-substituted dipeptidyl peptidase III (rat liver). *Biochemistry* **40**, 11860–11865 (2001).

566. McCall, K. A. & Fierke, C. A. Probing determinants of the metal ion selectivity in carbonic anhydrase using mutagenesis. *Biochemistry* **43**, 3979–3986 (2004).

567. Müller, H. N. & Skerra, A. Grafting of a high-affinity Zn(II)-binding site on the beta-barrel of retinol-binding protein results in enhanced folding stability and enables simplified purification. *Biochemistry* **33**, 14126–14135 (1994).

568. Hasler, D. W., Jensen, L. T., Zerbe, O., Winge, D. R. & Vasák, M. Effect of the two conserved prolines of human growth inhibitory factor (metallothionein-3) on

its biological activity and structure fluctuation: comparison with a mutant protein. *Biochemistry* **39**, 14567–14575 (2000).

569. Voordouw, G., Milo, C. & Roche, R. S. The determination of the binding constant of metalloenzymes for their active site metal ion from ligand inhibition data. Theoretical analysis and application to the inhibition of thermolysin by 1,10-phenanthroline. *Anal. Biochem.* **70**, 313–326 (1976).

570. Sellin, S. & Mannervik, B. Metal dissociation constants for glyoxalase I reconstituted with Zn^{2+}, Co^{2+}, Mn^{2+}, and Mg^{2+}. *J. Biol. Chem.* **259**, 11426–11429 (1984).

571. diTargiani, R. C., Lee, S. J., Wassink, S. & Michel, S. L. J. Functional characterization of iron-substituted tristetraprolin-2D (TTP-2D, NUP475-2D): RNA binding affinity and selectivity. *Biochemistry* **45**, 13641–13649 (2006).

572. Payne, J. C., Rous, B. W., Tenderholt, A. L. & Godwin, H. A. Spectroscopic determination of the binding affinity of zinc to the DNA-binding domains of nuclear hormone receptors. *Biochemistry* **42**, 14214–14224 (2003).

573. Berkovits, H. J. & Berg, J. M. Metal and DNA binding properties of a two-domain fragment of neural zinc finger factor 1, a CCHC-type zinc binding protein. *Biochemistry* **38**, 16826–16830 (1999).

574. Bal, W., Schwerdtle, T. & Hartwig, A. Mechanism of nickel assault on the zinc finger of DNA repair protein XPA. *Chem. Res. Toxicol.* **16**, 242–248 (2003).

575. Posewitz, M. C. & Wilcox, D. E. Properties of the Sp1 zinc finger 3 peptide: coordination chemistry, redox reactions, and metal binding competition with metallothionein. *Chem. Res. Toxicol.* **8**, 1020–1028 (1995).

576. Berg, J. M. & Merkle, D. L. On the metal ion specificity of zinc finger proteins. *J. Am. Chem. Soc.* **111**, 3759–3761 (1989).

577. Pedone, P. V. *et al.* The single Cys2-His2 zinc finger domain of the GAGA protein flanked by basic residues is sufficient for high-affinity specific DNA binding. *Proc. Natl. Acad. Sci. U. S. A.* **93**, 2822–2826 (1996).

578. Kleemann, S. G., Keung, W. M. & Riordan, J. F. Metal binding to angiotensin converting enzyme: implications for the metal binding site. *J. Inorg. Biochem.* **26**, 93–106 (1986).

579. Tashiro, S., Caaveiro, J. M. M., Wu, C.-X., Hoang, Q. Q. & Tsumoto, K. Thermodynamic and structural characterization of the specific binding of Zn(II) to human protein DJ-1. *Biochemistry* **53**, 2218–2220 (2014).

(This page intentionally left blank)

Appendix A

Optogenetic tools for modulating intracellular Zn^{2+}

A.1 Introduction

The study of Zn^{2+} in cells is often hampered by inefficient or toxic methods of Zn^{2+} perturbation. The complexity of the Zn^{2+} transport and intracellular buffering system complicates efforts to modulate cytosolic or organelle-bound Zn^{2+} pools through genetic knockout or knockdown methods[71,75,554]. Addition of exogenous Zn^{2+}, Zn^{2+} chelators such as *N*,*N*,*N*′,*N*′-tetrakis(2-pyridinylmethyl)-1,2-ethanediamine (TPEN), and ionophores such as pyrithione can perturb intracellular Zn^{2+}, but do so with variable dynamics and can have secondary toxic effects, as observed by the Palmer lab and others[334,555]. Better methods for rapid alteration of intracellular Zn^{2+} would be useful for furthering research into Zn^{2+} homeostasis and signaling.

In recent years, a variety of tools have been developed to quickly and specifically alter protein localization, function, expression, or degradation using light[556]. Collectively, these are known as optogenetic tools, and they have valuable implications for perturbing and manipulating systems without the addition of exogenous chemicals. We sought to try to develop tools to modulate intracellular Zn^{2+} through two separate optogenetic platforms. The first was the Cry2olig-Cib1 platform, which was developed from the *Arabidopsis* photoreceptor Cry2[557]. Upon blue light stimulation, Cry2olig monomers aggregate and bind to a binding partner

called Cib1. These two separate functions of the Cry2olig construct could allow for a variety of different protein engineering strategies to modulate Zn^{2+}. The second platform that we attempted to develop was that of the LOV24 degron, in which a blue-light sensitive light-oxygen-voltage (LOV) domain undergoes a conformational change upon blue light irradiation to expose a degron domain, targeting the attached protein to the proteosome for degradation[558].

The most obvious target protein for manipulation of cytosolic Zn^{2+} was one of the isoforms of the highly expressed Zn^{2+} buffering protein metallothionein (MT), which can bind up to seven Zn^{2+} ions and act as a source of or sink for Zn^{2+}, depending on the homeostatic needs of the cell[71]. We therefore generated constructs linking MT to Cry2olig and to the LOV24 degron. In the case of the LOV24 degron, we hypothesized that light-induced degradation of MT would release some protein-bound Zn^{2+} and increase cytosolic Zn^{2+} levels. The expected end result of inducing MT clustering with Cry2olig was less clear, as such clustering could sequester Zn^{2+} in smaller cytosolic regions, release Zn^{2+} due to electrostatic interactions within clusters, or fail to alter metallothionein binding at all. We thus treated the MT-Cry2olig experiments as useful exploratory work before we attempted to develop other more rationalized (but more complicated) approaches.

Ultimately, while we successfully generated constructs linking MT to each of these two optogenetic tools, and we were able to verify blue light activation of the MT-Cry2olig construct, we observed no perturbation in intracellular Zn^{2+}.

A.2 Results

In order to generate MT optogenetic constructs, we needed an MT gene, the optogenetic domain, and a selection marker. We simultaneously performed cloning

with both *Mt1*, a ubiquitously expressed MT, and *Mt3*, which has a much more restricted pattern of expression and is selectively enriched in the brain[161]. The selection marker we chose was mNeptune2.5, which is a fluorescent protein that is red-shifted compared to mCherry (maximum excitation at 599 nm). With this, we thought that it might be possible to activate the optogenetic construct with blue light, independently measure Zn^{2+} using a green-red Zn^{2+} FRET sensor, and verify activation/degradation with mNeptune2.5. This was not an accurate assumption, as both of the selected optogenetic domains are activated by light up to ~490 nm and thus are activated upon GFP excitation, but it was the original intention upon construct design. Using these building blocks, we successfully cloned constructs with the *Mt1* gene, each optogenetic domain, and mNeptune2.5, as well as created

Table A.1: Constructs either purchased from Addgene (with associated ID), or cloned in this project. Intermediate tags are included that could potentially be used in other projects to tag other proteins.

Plasmid/construct	Addgene ID	Useful intermediates
CRY2olig-mCherry*	60032	
pcDNA3.1 MT1 Cry2olig mNeptune2.5		pcDNA3.1 Cry2 mNeptune2.5 (no stop) pcDNA3.1 MT1 Cry2 (no stop) pcDNA3.1 MT3 Cry2 (no stop) pcDNA3.1 Cry2 (no stop) pcDNA3.1 MT1 (no stop) pcDNA3.1 MT3 (no stop)
pmGFP CIBN (delta NLS)¥	26867	
pBMN HA-YFP-LOV24	49570	
pcDNA3.1 mNeptune2.5 MT1 LOV24		pcDNA3.1 LOV24 (no start)

*This construct is the Cry2 sequence (GenBank AY057440.1) with the following mutations: M367V, I476T, E490G

¥This construct is residues 1-515 of the Cib1 sequence (GenBank NM119618.3) with the following mutations: K93A, R94A, K106A, K107A

plasmids with a variety of useful intermediates for further work that might use MTs or these optogenetic domains (Table A.1).

While cloning, we attempted to recapitulate the published methods for activating each of the optogenetic constructs. In the case of Cry2olig/Cib1, imaging of cotransfected constructs successfully reproduced both the binding of Cry2olig to Cib1 and the clustering of Cry2olig (Figure A.1). Both of these phenotypes were reversible over the course of ~10 minutes with no light exposure (data not shown). Conversely, activation of the LOV24 degron could not be reproduced with our experimental equipment. The original paper used constant illumination with a custom-made array of blue aquarium lights to induce LOV24-YFP degradation[558]. As we had no such array, we tried a variety of methods for activation, including close-range illumination with a blacklight flashlight, constant exposure to a low-power 488 nm microscope laser, and illumination under a UV bacterial colony screen light. No clear decrease in fluorescence was observed using any method (data not shown). Thus, despite the successful cloning of the MT1 LOV24 construct, no further work was done using this optogenetic tool.

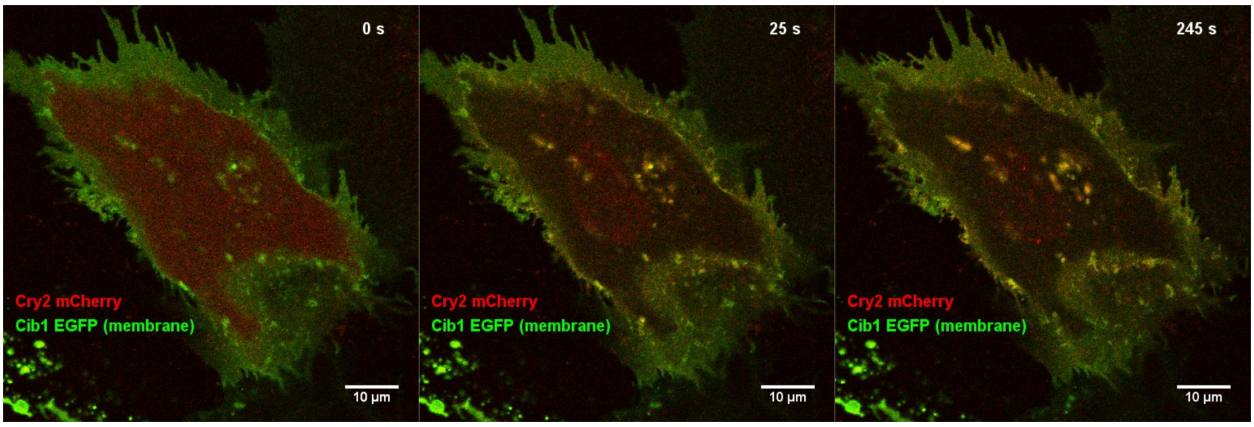

Figure A.1: Reproducing Cry2/Cib1 aggregation and binding data. At the beginning of the timecourse (left), Cry2olig (red) is diffuse throughout the cytosol and has no colocalization with Cib1 (green). In less than 30s (with the only Cry2 activation being imaging of GFP), Cry2 is seen to have moved to colocalize with Cib1. Further imaging reveals the formation of Cry2 aggregate clusters, most visible in the nucleus where there is no Cib1 present.

As we could reproduce the Cry2olig/Cib1 phenotypes seen in the literature, we imaged our cloned MT1 Cry2olig construct alone and in conjunction with a cyan-yellow Zn^{2+} FRET sensor (Figure A.2). Simultaneous imaging of CFP, YFP FRET, and mNeptune2.5 successfully activated the aggregation of the MT1 Cry2olig protein (Figure A.2A). However, FRET ratios did not change during this process in any experiment, at least on the time scale of 10-20 minutes (Figure A.2B). Further work is required to more fully investigate the properties of this construct.

A.3 Discussion

In developing optogenetic tools for modulating intracellular Zn^{2+}, we cloned constructs that linked MT1 to each of two different optogenetic domains/proteins. The MT1 Cry2olig construct successfully clustered upon blue light irradiation (CFP excitation laser), but we observed no corresponding change in FRET ratio within 20 minutes of this clustering. One possible explanation for this is that the large repository of MT in the cell compensates for any changes in the smaller MT pool present in the overexpressed construct. In order to assess this possibility as a confounding factor, orthogonal coding of MT1 in our constructs could allow us to simultaneously knockdown endogenous MTs. Our primary explanation for this lack of Zn^{2+} change, however, is that the aggregation of the Cry2olig proteins (498 residues), which are much larger than MT1 (61 residues), has little steric or electrostatic effect on the attached MT1 proteins, and thus has little effect on their coordination of Zn^{2+}. If this is true, a platform redesign may be necessary to affect MT in a meaningful way. One possible avenue for continuing with this specific construct is attaching a disulfide isomerase to Cib1, which may then be brought into close enough proximity to the MT by Cry2olig activation to catalyze disulfide bond

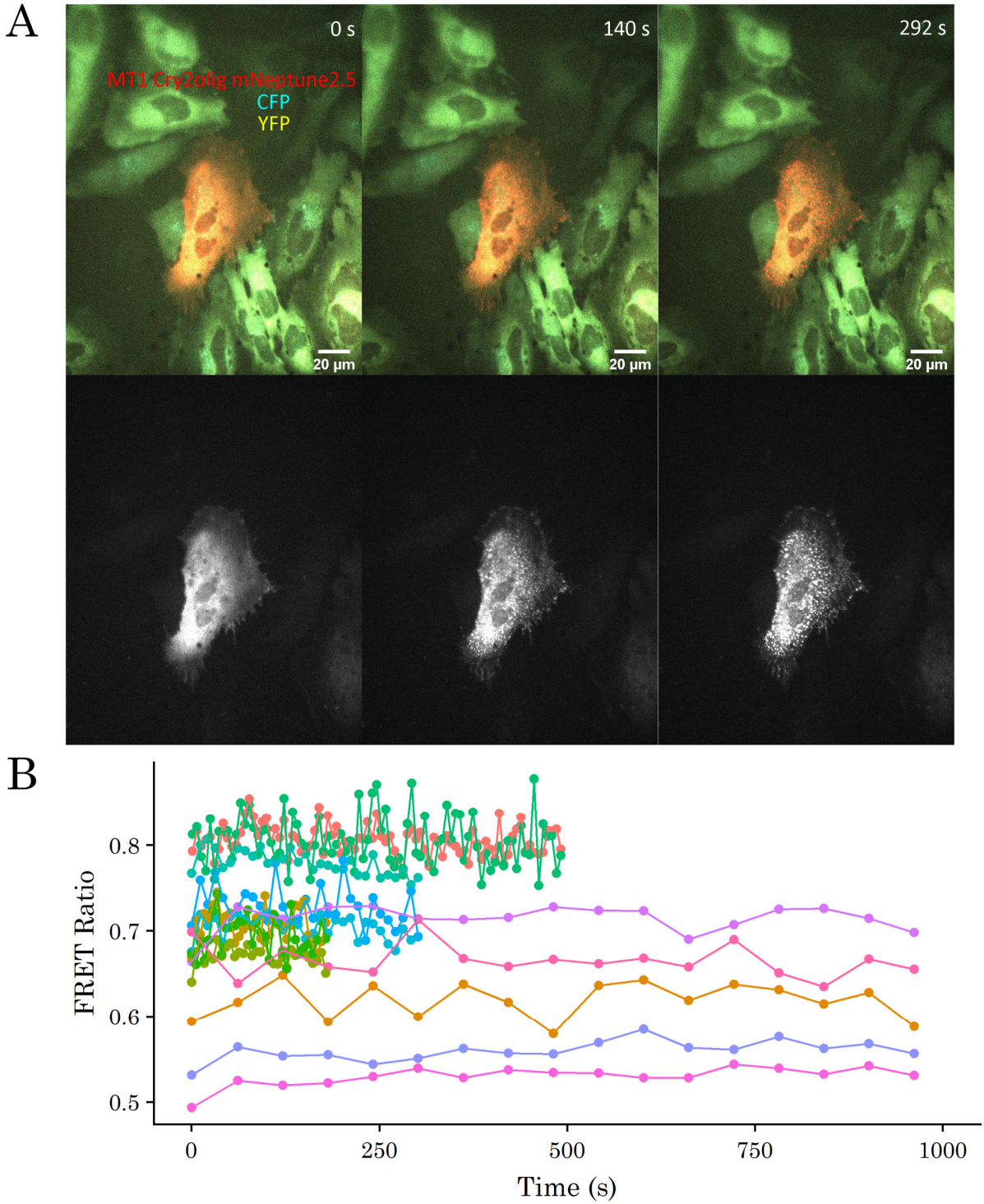

Figure A.2: MT1 Cry2 imaging in HeLa cells containing Zn^{2+} FRET sensor NES ZapCV2. (A) Representative cell containing the NES ZapCV2 FRET sensor (CFP/YFP channels) and the MT1 Cry2olig mNeptune2.5 construct. As seen more easily in the mNeptune2.5 grayscale image below, the construct aggregates over time. (B) No change in FRET ratio was seen over time, despite construct aggregation. Two different frame rates were used to attempt to see short and long scale dynamics.

formation and therefore restrict cysteine-based Zn^{2+} binding sites in the MT.

We were unable to recapitulate activation of the LOV24 degron with our experimental equipment. It is unclear whether this is solely a problem with our experimental equipment, and thus whether this project could be continued with a more specific blue light apparatus that has an appropriate power and wavelength composition, or whether this reflects a lack in robustness of the tool itself. In our different attempts to reproduce degradation, we also reflected on the utility of a tool that requires such intensive exposure over a long (~30 minute) period, and whether such conditions may induce unwanted phototoxic side effects, as well as photobleach any sensors present in the cell. Thus, while the MT1 LOV24 construct could still be a potentially interesting avenue of study, it also comes with important caveats to consider in future experiments.

A.4 Methods

Most of the imaging for this section was performed on a Nikon Ti-E spinning disc confocal microscope equipped with Nikon Elements software, Ti-E perfect focus system, Yokogawa CSU-X1 spinning disc head, and Andor 888 Ultra EMCCD camera. Some LOV24-YFP experiments were performed on a Nikon Ti-E widefield microscope equipped with Nikon Elements software, Ti-E perfect focus system, Andor iXon3 EMCCD camera, Sutter Instruments LD-LS/30 xenon arc lamp, and Sutter Instruments Lambda 10-3 filter changer. Some Cry2/Cib1 clustering verification experiments were also performed on a Nikon A1R laser scanning confocal microscope.

All NES-ZapCV2/MT1 Cry2olig experiments were conducted by imaging HeLa cells with genomically integrated NES-ZapCV2 and transiently transfected MT1 Cry2olig. Some attempts were made to aim a 405 nm laser to stimulate specific cells

with Cry2/Cib1 experiments when imaging on the laser scanning confocal microscope. However, all NES-ZapCV2/MT1 Cry2olig experiments involved finding transfected cells solely through red channel imaging (594 nm laser excitation), then stimulating cells by normal FRET sensor imaging with the 445 nm laser (see section 2.5.5) in addition to monitoring mNeptune fluorescence.

The following were used in attempts to induce LOV24-YFP degradation: a Mag-Lite blacklight flashlight at ~1/2 inch from cells for about 30 minutes, the spinning disk 488 nm microscope laser at 5% power for a constant 5 min exposure, and a UV bacterial colony screen light (395/40), under which cells were moved between each imaging frame (~10 minute timepoints). Normal YFP imaging conditions were used in all of these experiments, and no degradation was identified.

Appendix B

Computational analysis of protein Zn^{2+} affinities

B.1 Publication status and author contributions

This appendix was originally prepared as a report detailing a semester-long project for the course MCDB 5314: Algorithms for Molecular Biology, authored by Lynn Sanford, Samarpita Debnath, and Kyle Rooney. L.S. designed the study. All authors analyzed and interpreted data and wrote the manuscript.

B.2 Abstract

Zinc-binding proteins compose a large portion of mammalian proteomes and are essential for virtually all cellular functions. These proteins have widely varying affinities for zinc. We attempted to determine through structural alignment whether full-length proteins or zinc-binding sites of proteins with known zinc affinity had shared characteristics. Using the structural alignment algorithms FAST and MATRAS we created alignments of 21 full-length proteins and 18 minimal functional sites consisting of amino acid residues in a small sphere directly around the zinc atom. We found no pattern of basic similarity among proteins with similar zinc affinities, and therefore could not determine any specific characteristics of sites with specific affinities for zinc.

B.3 Introduction

Zinc is the second most common transition metal in cells and is essential for all life. About 10% of proteins (~2500-3000) in humans are predicted to bind zinc in its ionic form (Zn^{2+}) in order to perform their function[559]. Regulation of Zn^{2+} is important for proper protein function and problems with this regulation (either deficiency or excess) are implicated in developmental impairments and diseases, such as neurodegenerative diseases, diabetes, and cancer[559].

Many proteins bind Zn^{2+} in order to maintain a proper three dimensional structure, and in enzymes it is often necessary for catalytic activity. Depending on the particular binding site, a protein has a specific affinity for Zn^{2+} [559]. This matters because the concentration of Zn^{2+} in cells can change. As it does, the sets of proteins that bind it may change according to their particular affinities. The goal of our project was to determine by structural analysis whether certain Zn^{2+} binding sites could be matched with affinities in order to try to hypothesize at different Zn^{2+} concentrations what proteins bind the ion and are therefore functional.

Problem statement

To find zinc-binding affinities of proteins based on structural alignments of zinc-binding domains.

Problem Description

On visual inspection, we concluded that sequence-based alignment is very unlikely to produce any results, because zinc-binding sites with same linear sequence of amino acids and similar sequence separation have affinities that differ widely. Also, zinc-binding sites with significantly different linear sequence have same

affinities.

Hence, we analyzed structural data of Zn^{2+}-binding proteins with known Zn^{2+} affinities and looked for patterns in their binding sites. There were a few things about the structure of Zn^{2+}-binding domains which we thought might influence the Zn^{2+}-binding affinity of the domain.

- *Coordination geometry:* Zn^{2+} ions are typically coordinated by 4 electron-rich atoms like oxygen or nitrogen. These atoms (as components of amino acids) can have different orientations relative to each other in three-dimensional space that might be characteristic based on affinity.
- *Types of amino acids surrounding binding site:* Zn^{2+}-coordinating amino acids almost always consist of cysteine, histidine, aspartate, or glutamate. There may be other types of amino acids that are more likely to stabilize these coordinating residues that may have patterns characteristic of affinity.
- *Secondary structure:* Certain secondary structures of the protein at specific distances from the Zn^{2+} ion may affect affinity.

B.4 Methods

The data for this project was entirely derived from the publicly accessible database Protein Data Bank (PDB) and the biochemical literature.

All possible Zn^{2+}-binding affinity data for individual proteins was accumulated from the literature. After pruning proteins that had multiple Zn^{2+}-binding sites, we developed a test set of 21 proteins for which structural data were available. The full-length proteins were aligned pairwise in an all-against-all fashion using the

structural alignment algorithm FAST (http://biowulf.bu.edu/FAST/index.htm)[560]. Similarity scores were then analyzed with regard to zinc affinity.

We then defined a minimal functional site (MFS) containing only amino acids directly surrounding the Zn^{2+} site. This was done according to a procedure previously described in which all residues are included that contain atoms within a threshold distance of residues coordinating the Zn^{2+} ion[561]. The radius of the MFS site was tested at 2.5 and 10 angstroms, and 10 angstroms was determined to provide a sufficient amount of information for structural alignment. MFS sites for 18 proteins were divided into three groups based on affinity (dissociation constant (K_d) values in the fM, pM, and nM ranges). Multiple sequence alignments were performed within each affinity group using the structural alignment algorithm MATRAS, and outputs were analyzed based on calculated similarity scores and the same criteria as applied to the analysis of full-length proteins above (Figure B.1)[562].

Assessment

We followed the below assessment plan to validate our project:

1. To determine consensus features of zinc binding sites: The consensus features developed for a specific affinity should align with the entire seed set with all affinities.
2. To define the minimal functional site: The radius should allow for the inclusion of enough residues to align but should not include residues outside of the immediate zinc-binding vicinity.
3. To validate the minimal functional sites: The atoms included in the MFS output should overlay with the same atoms in the original PDB structure file. Each MFS will be slightly different depending on how tightly packed the protein is around the zinc ion, but it will always correspond to the original

structure.

4. To validate if the MFS are well aligned using MATRAS: Similar structures, such as those conserved binding domains in the same protein, will provide high similarity scores.
5. To validate the similarity scores and to come up with correlation with affinity: MFS sites with similar affinities will have high similarity scores.

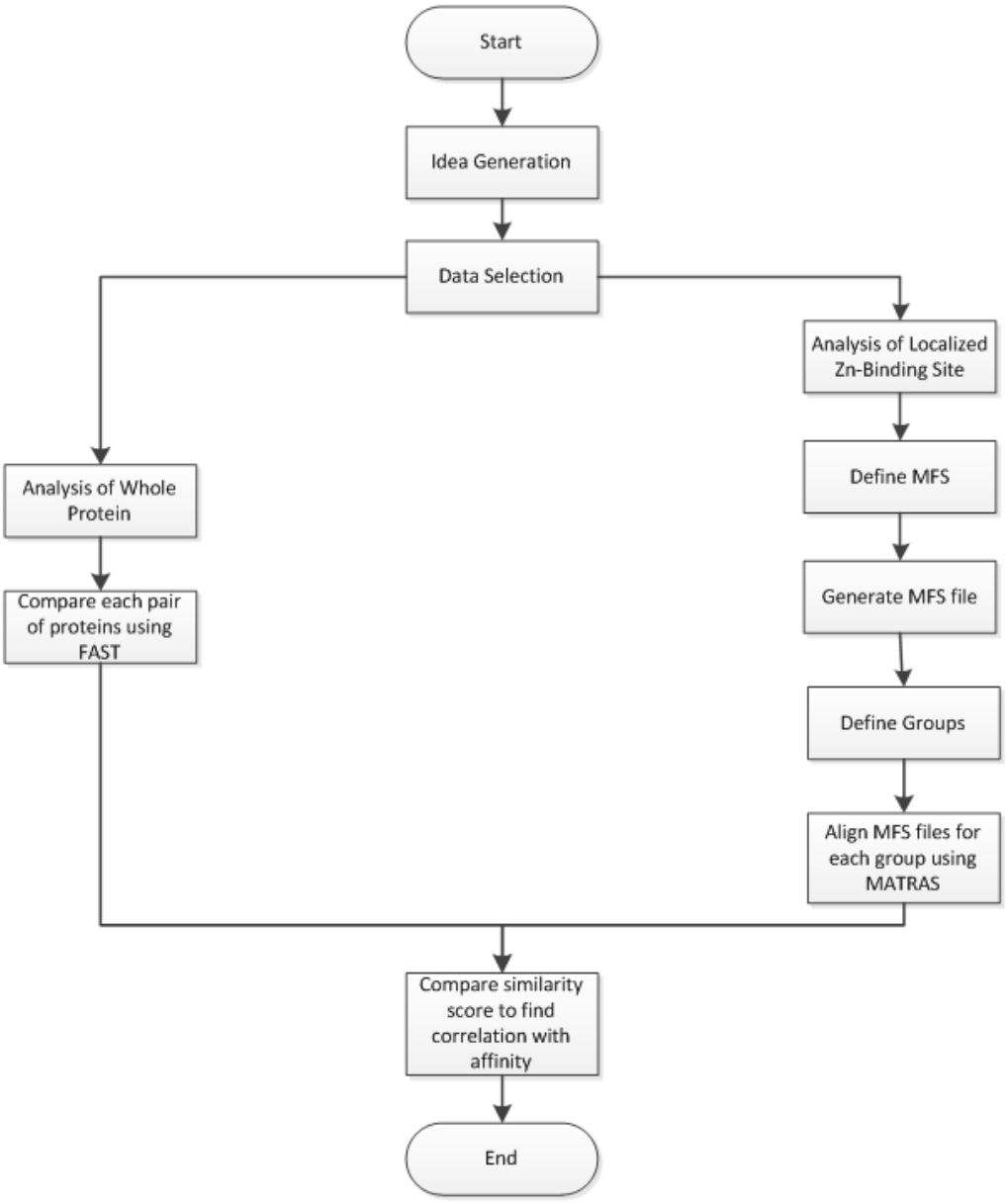

Figure B.1: Flow chart depicting workflow for this study

Innovativeness of approach

We used FAST in a new way that has not been attempted; we examined specific residues to find zinc binding affinities and attempted to correspond these with other zinc binding proteins to classify our list of proteins within different levels of affinities.

We also used MATRAS in a new way that has not been attempted; we aligned specific residues (situated in the vicinity of 10 angstroms from Zn^{2+}) to find similarity between zinc binding sites and not entire proteins.

B.5 Results

Protein affinity data was accumulated from the literature, yielding a set of 21 proteins for which there were also structural data available (Table B.1). These represented different classes of proteins from different organisms, and the zinc binding sites displayed diversity in sequence, function, and binding affinity.

Table B.1: Proteins used for structural zinc binding site analysis

Protein	Binding residues	Function	Kd (M)	Organism	PDB Structure	Reference
Antitoxin MqsA	CCCC	Structural	1.00E-15	E. coli	3GN5	563
Hsp33	CCCC	Enzyme	1.00E-15	E. coli	1HW7	112
PDZ and LIM domain protein 1 – LIM domain	CCHC/CCCH	Structural	3.16E-15	Human	1X62	564
Superoxide dismutase	HHHD	Structural	4.00E-14	Human	1PU0	386
Dipeptidyl peptidase III	HHE	Enzyme	5.01E-13	Human	3FVY	565
Human carbonic anhydrase	HHH	Enzyme	1.00E-12	Human	1CA2	566
Alkaline phosphatase	DDH/DHH	Enzyme	2.00E-12	E. coli	1ALK	5
Mammalian serum retinol-binding protein	HHH	Structural	2.00E-12	Human	1CRB	567
Metallothionein MT3	CCCC	Regulatory	3.17E-12	Human	4MT2	568
Thermolysin	HHE	Enzyme	5.00E-12	B. thermoproteolyticus	5TLN	569
Lactoylglutathione lyase	QE/EH	Enzyme	2.50E-11	Human	1FRO	570
Tristetraprolin	CCCH	Structural	6.30E-11	Mouse	1M9O	571
Human estrogen receptor a	CCCC/CCCC	Structural	1.00E-10	Human	1HCQ	572
Neural zinc finger factor 1	CCHC	Structural	1.26E-10	Rattus	1PXE	573
Xeroderma pigmentosum group A complementing protein XPAzf	CCCC	Structural	1.58E-10	Human	1XPA	574
Glucocorticoid receptor a	CCCC	Structural	2.00E-10	Rattus	1GLU	572
Transcription factor Sp1–3	CCHH	Structural	6.31E-10	Human	1VA2	575
TFIIIA	CCHH	Structural	3.16E-09	Xenopus	1UN6	576
GAGA	CCHH	Structural	5.01E-09	Drosophila	1YUI	577
Angiotensin converting enzyme	HHE	Enzyme	6.31E-09	Human	1O8A	578
DJ-1	CE	?	6.00E-07	Human	4P35	579

B.5.1 FAST analysis of whole proteins

Every protein was aligned pairwise with FAST in an all-vs-all manner, yielding 210 pairings. Of these, 32 pairings yielded some result (Table B.2). These alignments mostly consisted of regions less than 30 amino acids.

From the list of 21 proteins in Table 1, only 12 found matches in the FAST search, with only three results over a score of 1. The majority of the proteins found their highest score when paired with the GAGA protein(1YUI), which has one of the highest Zinc K_d values of 5.01 nM. There was a total of 64 matches found in the FAST search, with repeats from each protein, coming out to a total of 32 matches in FAST. The GAGA protein and metallothionein MT3 (4MT2) were the only proteins with more than 10 total matches.

When further analyzed, only three results yielded a similarity score of greater than 1, which indicated that few of the thirty alignment results were of good quality. Of the three results mentioned, two contained alignments that did not include the zinc-binding site of either protein. The third, an alignment of TFIIIA and GAGA, did align part of the zinc binding sites. These two proteins are both transcription factors with very similar zinc-binding sites, so some amount of similarity between them is not surprising. However, the few meaningful results generated by this process indicated as a whole that the alignment of full zinc-binding proteins is not a useful approach to determining any similarities between zinc-binding sites.

B.5.2 MATRAS analysis of minimal functional sites (MFS) for zinc-binding domains

We wrote a C program to find out the MFS. This program takes PDB files as input and generates one MFS file for each Zn^{2+} ion from entire PDB file as input. As we

Table B.2: Protein results in FAST search

Proteins	# of Matches	Highest Score	Highest Score Matched Protein
1CA2	3	0.475	1YUI
1CRB	6	1.059	1HW7
1GLU	4	0.7856	1YUI
1HCQ	2	0.463	1YUI
1HW7	4	1.059	1CRB
1UN6	2	1.018	1YUI
1XPA	8	1.009	1YUI
1YUI	12	1.018	1UN6
3GN5	3	0.9867	1YUI
4MT2	11	0.4067	1XPA
4P35	4	0.8736	1YUI
5TLN	2	0.497	1YUI

used proteins having multiple zinc-binding sites, this gave us more than 50 MFS files. Each MFS had 200 atoms belonging to more than 10 residues on an average.

Proteins were split into three groups according to zinc affinity. For groups containing proteins with multiple MFS outputs (multiple zinc binding sites), MFS outputs were restricted to ten randomly chosen sites (ensuring that at least one site from each protein was included), as ten files is the maximum input for MATRAS (Table B.3).

The output for MATRAS multiple alignments yielded both the actual alignments (in sequence and structural form) and RDIS similarity scores (Figure B.2). Group 1 MFS sites showed some similarity along segments of the peptide backbone, as seen in Figure B.2A. However, the sites overall showed variable amounts of similarity (Figure B.2C). The only two pairwise alignments with similarity scores above 5% were between two different sites from the same protein. Group 2 shows a similar lack of similarity between MFS in different proteins (Figure B.3). This implies that

different proteins that are known to have femtomolar (Group 1) or picomolar (Group 2) affinity for zinc have very little structural similarity within a 10 angstrom radius of the zinc atom.

Table B.3: MFS sites used for multiple sequence alignment

Group 1				Group 2				Group 3			
ID #	Code	Protein	K_d for Zn	ID #	Code	Protein	K_d for Zn	ID #	Code	Protein	K_d for Zn
1	1HW7	Hsp33	1.0 fM	1	1ALK_6611	Alkaline Phosphatase	2.0 pM	1	1GLU_2034	Glucocorticoid Receptor A	0.2 nM
2	1PU0_11152	Superoxide Dismutase	40 fM	2	1ALK_6612	Alkaline Phosphatase	2.0 pM	2	1HCQ_3714	Estrogen Receptor A	0.1 nM
3	1X62_1169	PDZ and LIM Domain Protein 1	3.2 fM	3	1ALK_6619	Alkaline Phosphatase	2.0 pM	3	1M9O	Tristetraprolin	63 pM
4	1X62_1170	PDZ and LIM Domain Protein 1	3.2 fM	4	1ALK_6620	Alkaline Phosphatase	2.0 pM	4	1O8A	Angiotensin Converting Enzyme	6.3 nM
5	3GN5_A	Antitoxin MqsA	1.0 fM	5	1CA2	Carbonic Anhydrase	1.0 pM	5	1PXE	Neural Zinc Finger Factor 1	0.1 nM
6	3GN5_b	Antitoxin MqsA	1.0 fM	6	1CRB_1104	Serum Retinol-Binding Protein	2.0 pM	6	1UN6_4523	TFIIIA	3.2 nM
				7	1CRB_1105	Serum Retinol-Binding Protein	2.0 pM	7	1UN6_4531	TFIIIA	3.2 nM
				8	4MT2_410	Metallothionein 3	3.2 pM	8	1VA2	Transcription Factor Sp1-3	0.6 nM
				9	4MT2_411	Metallothionein 3	3.2 pM	9	1XPA	Xeroderma Pigmentosum Group A Complementing Protein	0.2 nM
				10	5TLN	Thermolysin	5.0 pM	10	1YUI	GAGA	5.0 nM

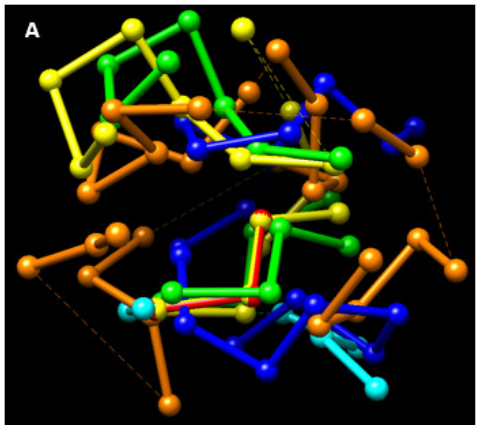

B

```
[AVE_SECSTR]  ccttcbccccsssccccccctcccttttccccctttc
up13910_5     ------------VCCEES------------------:43
up13910_6     KCPV------CHQGEMYC-VHCEES------------:43
up13910_1     ----------CTC-------------------------:234
up13910_2     ----FHVPH----FNRKH-GGRH--VGDLGLGSTKTG:138
up13910_3     ---------MCDKCGTGI-VHRH--PECY--------:42
up13910_4     ---------VCTDCGTNI-YCEK--HA----------:69
```

C

[RDIS(%)]	1HW7	1PUO_11152	1X62_1169	1X62_1170	3GN5_A	3GN5_B
1HW7	0.000	0.000	1.200	1.600	-0.700	1.000
1PUO_11152	0.000	0.000	4.300	1.600	0.000	1.400
1X62_1169	1.200	4.300	0.000	19.000	0.700	4.200
1X62_1170	1.600	1.600	19.000	0.000	0.900	-2.200
3GN5_A	-0.700	0.000	0.700	0.900	0.000	5.300
3GN5_B	1.000	1.400	4.200	-2.200	5.300	0.000

Figure B.2: Analysis of multiple MFS sites with MATRAS, Group 1 (fM). (A) Superimposed structural alignment of α carbons of residues in the MFS sites. Each color represents a distinct MFS site. (B) Alignment shown in sequence format. Numbers after underscore in ID correspond with MFS sites in Table 3. (C) Heat map of RDIS similarity scores. Red, yellow, and green represent lowest, medium, and highest similarity scores, respectively.

Figure B.3: Analysis of multiple MFS sites with MATRAS, Group 2 (pM).(A) Superimposed structural alignment of α carbons of residues in the MFS sites. Each color represents a distinct MFS site. (B) Alignment shown in sequence format. Numbers after underscore in ID correspond with MFS sites in Table 3. (C) Heat map of RDIS similarity scores. Red, yellow, and green represent lowest, medium, and highest similarity scores, respectively.

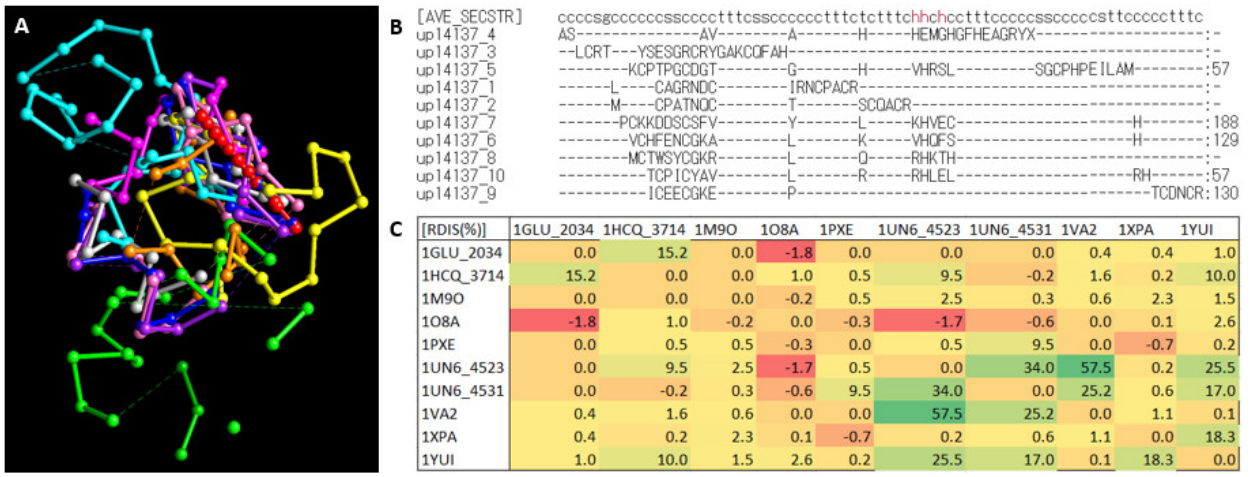

Figure B.4: Analysis of multiple MFS sites with MATRAS, Group 3 (nM). (A) Superimposed structural alignment of α carbons of residues in the MFS sites. Each color represents a distinct MFS site. (B) Alignment shown in sequence format. Numbers after underscore in ID correspond with MFS sites in Table 3. (C) Heat map of RDIS similarity scores. Red, yellow, and green represent lowest, medium, and highest similarity scores, respectively.

Group 3 shows somewhat more similarity among MFS from several member proteins, but is inconsistent in which proteins are similar (Figure B.4). Many of the transcription factors (glucocorticoid receptor A, estrogen receptor A, TFIIIA, transcription factor Sp1-3, GAGA) have relatively high levels of similarity when compared pairwise with certain others, but not all others. For example, the MFS from transcription factor Sp1-3 (1VA2) showed the highest structural similarity to both zinc sites derived from TFIIIA (1UN6) but no similarity to the MFS from GAGA (1YUI). These inconsistencies and the overall amount of neutral or negative similarity scores within this group led us to similarly conclude that zinc-binding sites of proteins with approximately nanomolar affinity for zinc have no cohesive structural similarity.

B.6 Discussion

Analysis of full-length zinc-binding proteins with FAST and of minimal functional sites with MATRAS both indicated that we could not correlate structural features of these proteins to zinc affinity.

Several caveats exist in these approaches. The first involves the set of proteins used as a seed set. It is difficult to measure protein zinc affinity, as oxygen-rich environments may perturb zinc binding sites and exact zinc concentrations are difficult to formulate due to widespread zinc contamination. This reality has severely restricted the number of data points that were available to us to use. If more data were available in the literature, it could allow us to expand this study by utilizing different categories of proteins. Structural similarities that are hinted at in the Group 3 MATRAS analysis could become more clear with a larger sample size.

A second main caveat involves the algorithms used in this study. Both FAST and MATRAS align the α or β carbon atoms of amino acid residues. This is useful for a full-length protein structural alignment because considering all atoms would be very computationally expensive. But especially in analyzing much smaller MFS sites, another structural alignment algorithm that considered the positions of side chains and angles present between atoms of the peptide backbone might yield much more useful information about elements that are important in strength of zinc binding. Several other algorithms were explored over the course of this study, but due to compatibility issues with input data or software difficulties were not implemented.

One other explanation for the lack of similarity found in this study was that the static structural information present in PDB data did not allow for us to visualize the dynamics that might be important for determining zinc affinities. The nature of this study did not allow for us to address this possibility, as other types of experimental data would be necessary.

Appendix C

Ca^{2+} imaging of neuron stimulations

C.1 Quantification of Ca^{2+} signals

In order to determine whether neurons were successfully stimulated, Ca^{2+} imaging was performed with the small molecule dye Fluo-4 AM in all conditions, in both mouse and rat neurons.

No rigorous quantification was done in most cases. Several full calibrations were performed after KCl and KCl/Zn^{2+} treatments in rat neurons, and similar calibrations were attempted after glutamate stimulation in mouse neurons, but minima were not reached, possibly due to age/stability of reagents. Not enough experiments were performed with full calibrations to quantify fractional saturation changes upon stimulation, which normally aids in controlling for cell-to-cell variability in dye loading and cell shape. Only $\Delta F/F$ values from resting to peak levels were calculated (Figure C.1), and given the lack of replicates and the caveats associated with such quantification, we do not believe we have enough quantitative data to determine whether there are any differences in Ca^{2+} signals depending on stimulation method. Furthermore, validation with a lower affinity sensor may also be necessary, given that some traces indicate that stimulation-dependent Ca^{2+} changes may cause the Fluo-4 sensor to approach saturation.

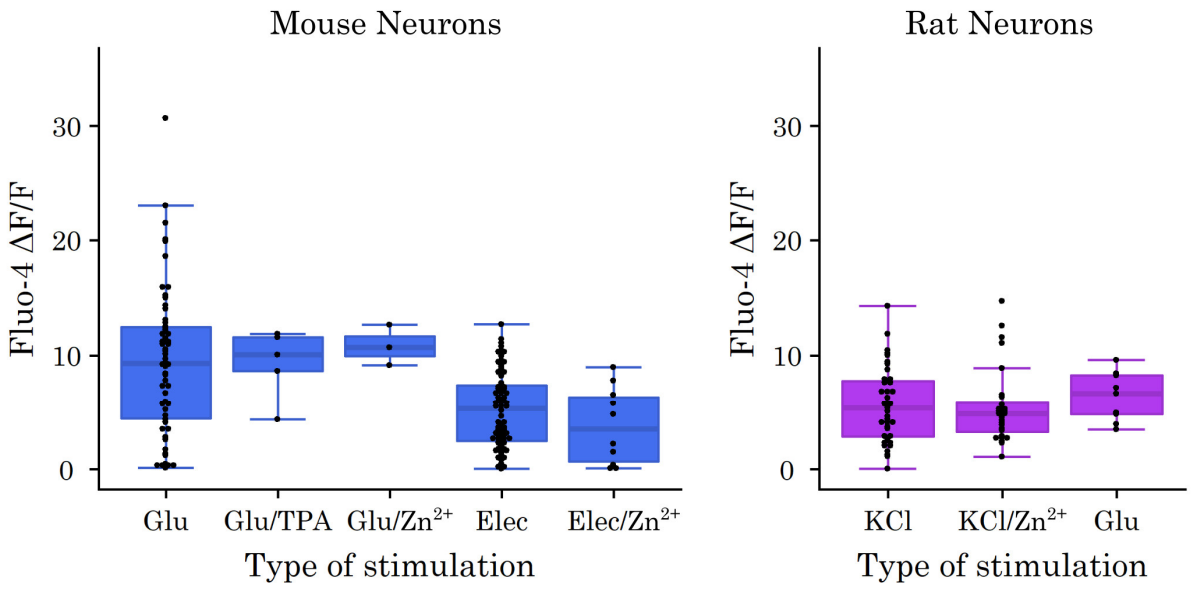

Figure C.1: Quantification of Ca^{2+} imaging in neurons with the small molecule indicator Fluo-4 AM. Plotted ΔF/F values were calculated as (peak intensity upon stimulation – resting intensity)/(resting intensity). Each dot represents a cell in a field of view.

C.2 Ca^{2+} imaging traces

The following figures (Figures C.2 through C.11) show traces obtained from Fluo4 AM Ca^{2+} imaging experiments. In all cases, stimulation is represented by a blue box, with other relevant media changes labeled. Stimulation and organism are labeled in the upper right of each plot. Concentrations were as follows for all experiments: glutamate = 50 μM, TPA = 10 μM, $ZnCl_2$ = 10 μM, $CaCl_2$ = 10 mM, ionomycin = 5-10 μM, EGTA = 5-10 mM, EDTA = 10 mM.

Electrical experiments had no media changes until indicated, meaning some were not washed after stimulation (which seems to change the extent of signal). Electrical stimulation in all cases was a 10 ms bipolar waveform, 30 V, 5 Hz, 60 seconds, although in some experiments electrodes were adjusted during stimulation, which altered Ca^{2+} signals, and in some cases electrodes may not have been correctly connected.

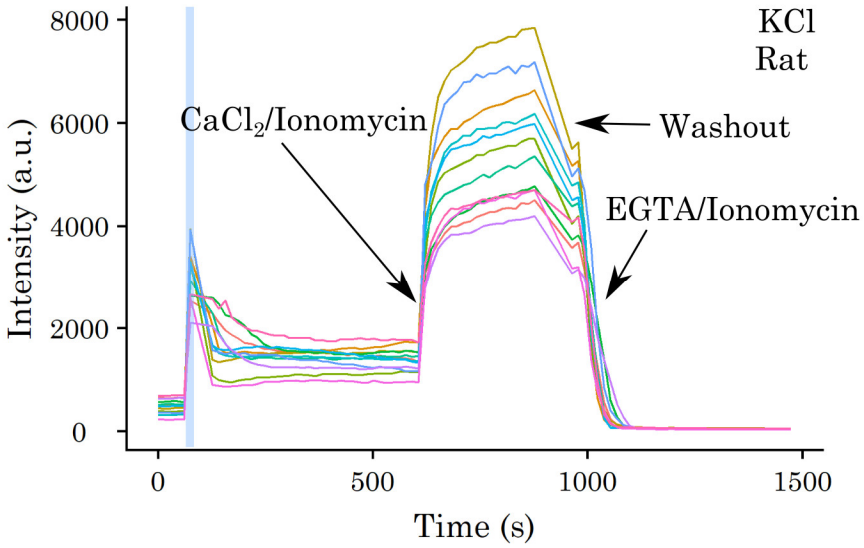

Figure C.2: Ca^{2+} imaging in rat neurons with KCl stimulation (1 of 2).

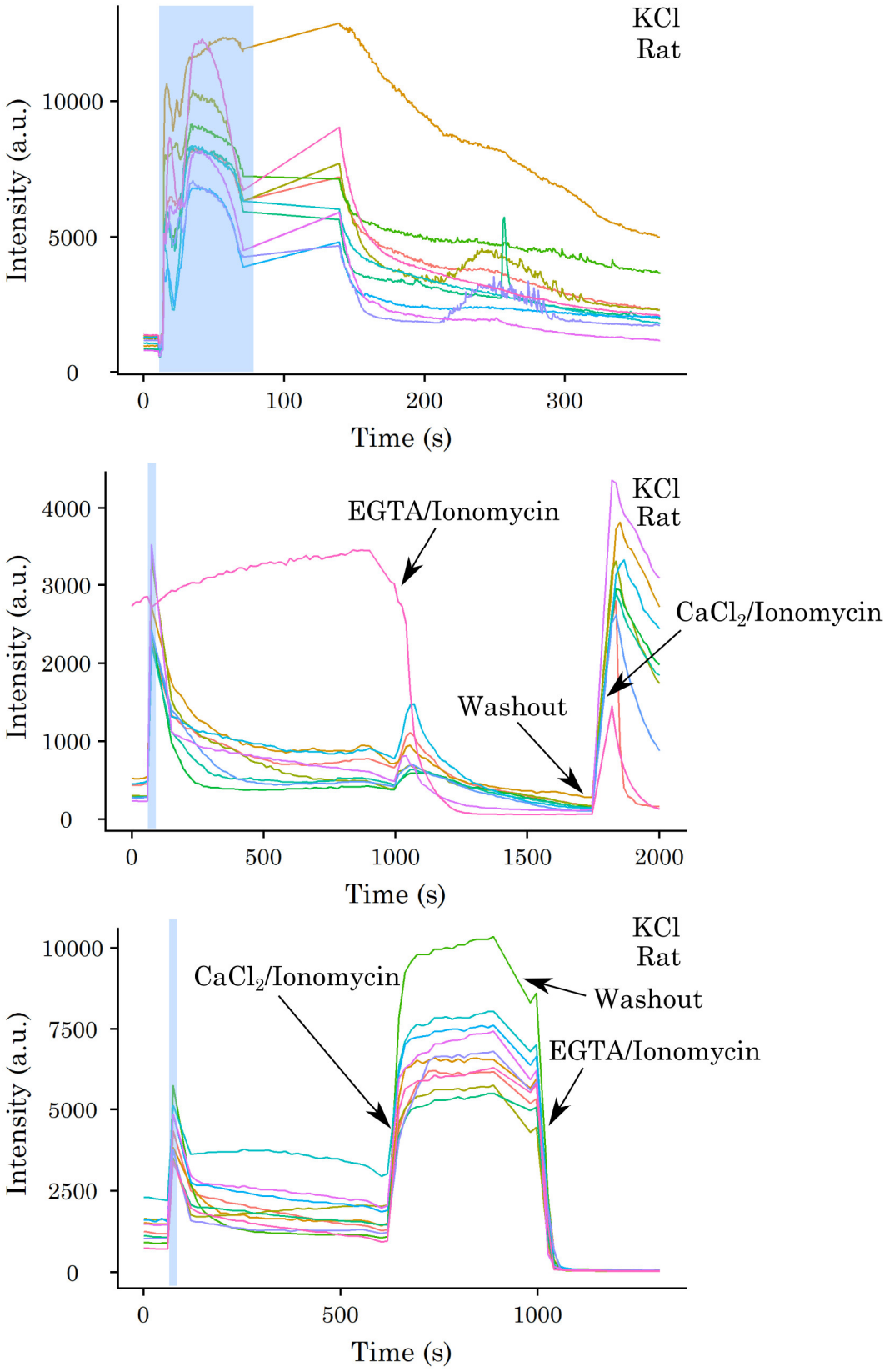

Figure C.3: Ca^{2+} imaging in rat neurons with KCl stimulation (2 of 2).

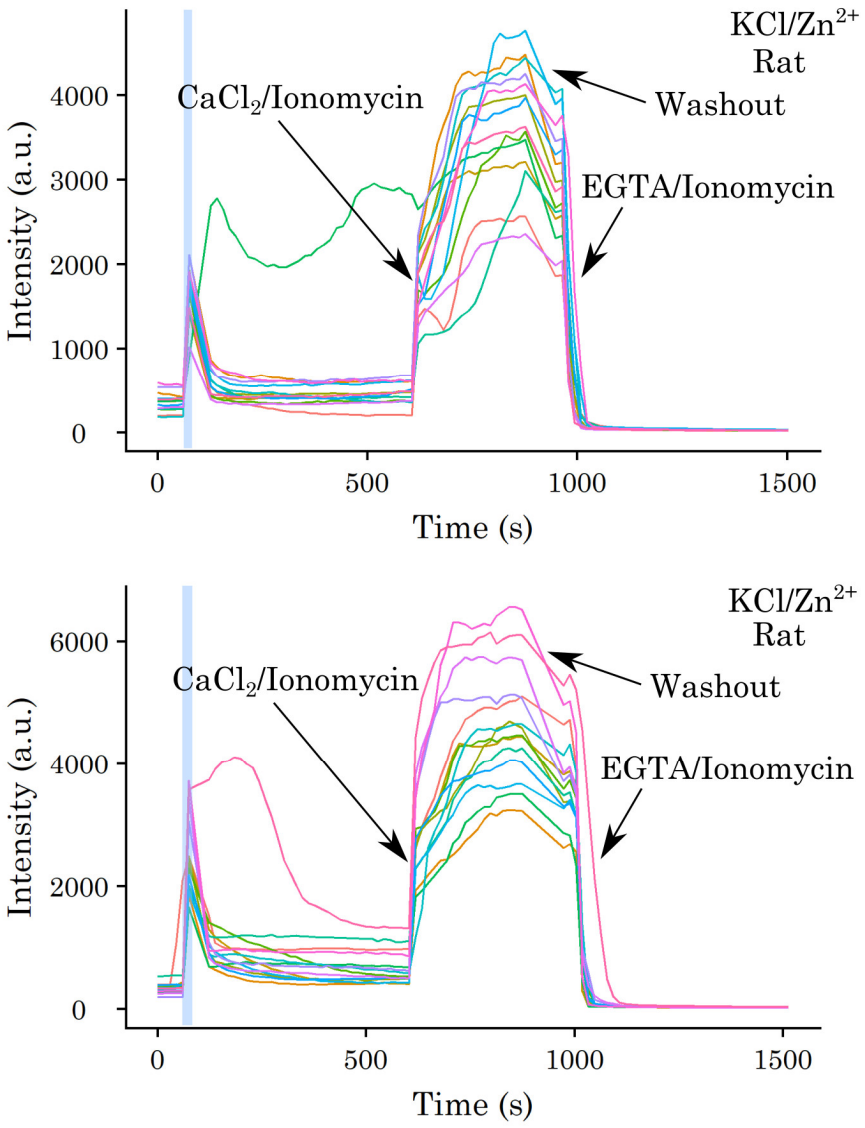

Figure C.4: Ca^{2+} imaging in rat neurons with KCl/Zn^{2+} stimulation

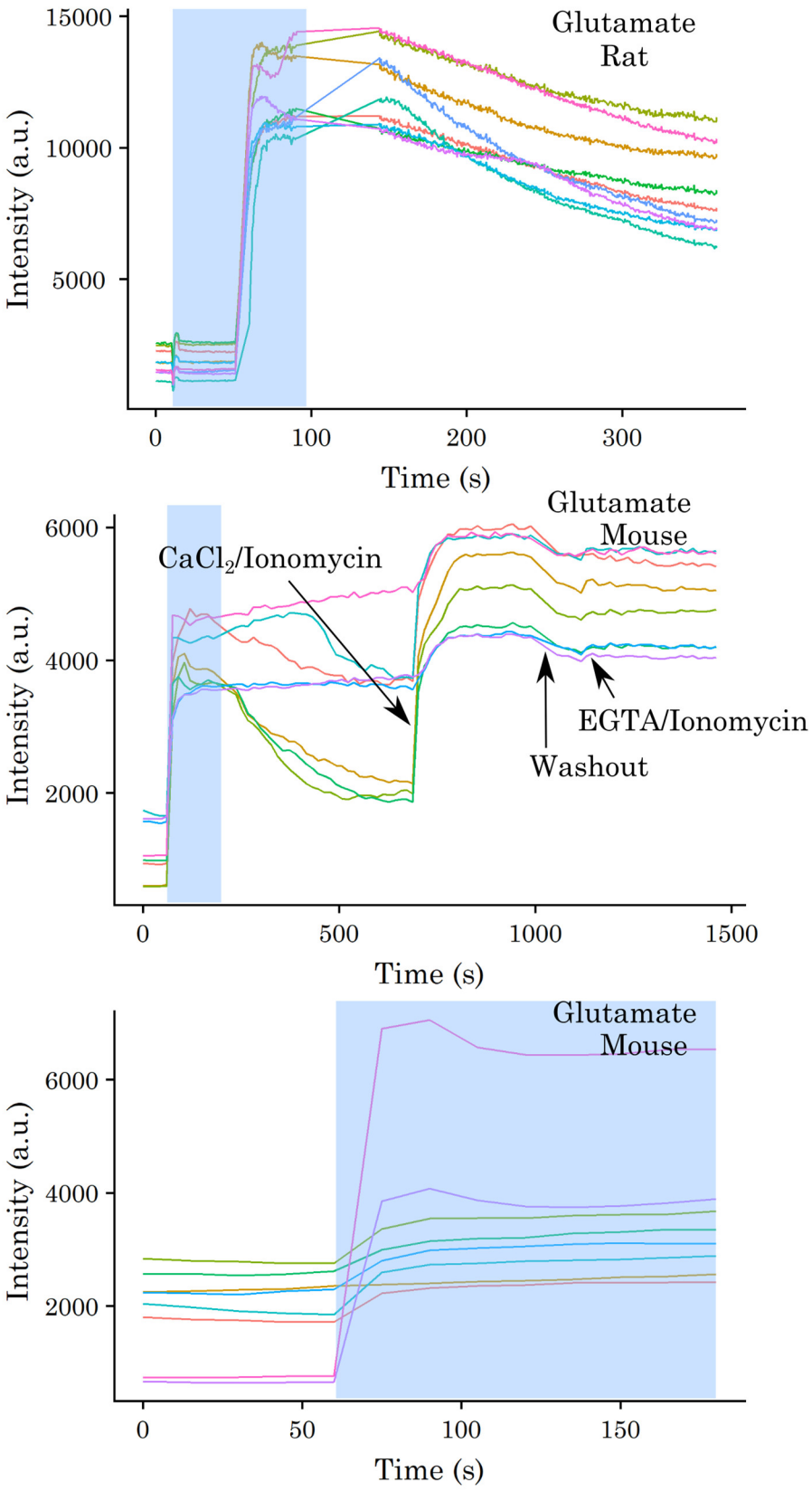

Figure C.5: Ca^{2+} imaging in rat and mouse neurons with glutamate stimulation (1 of 3).

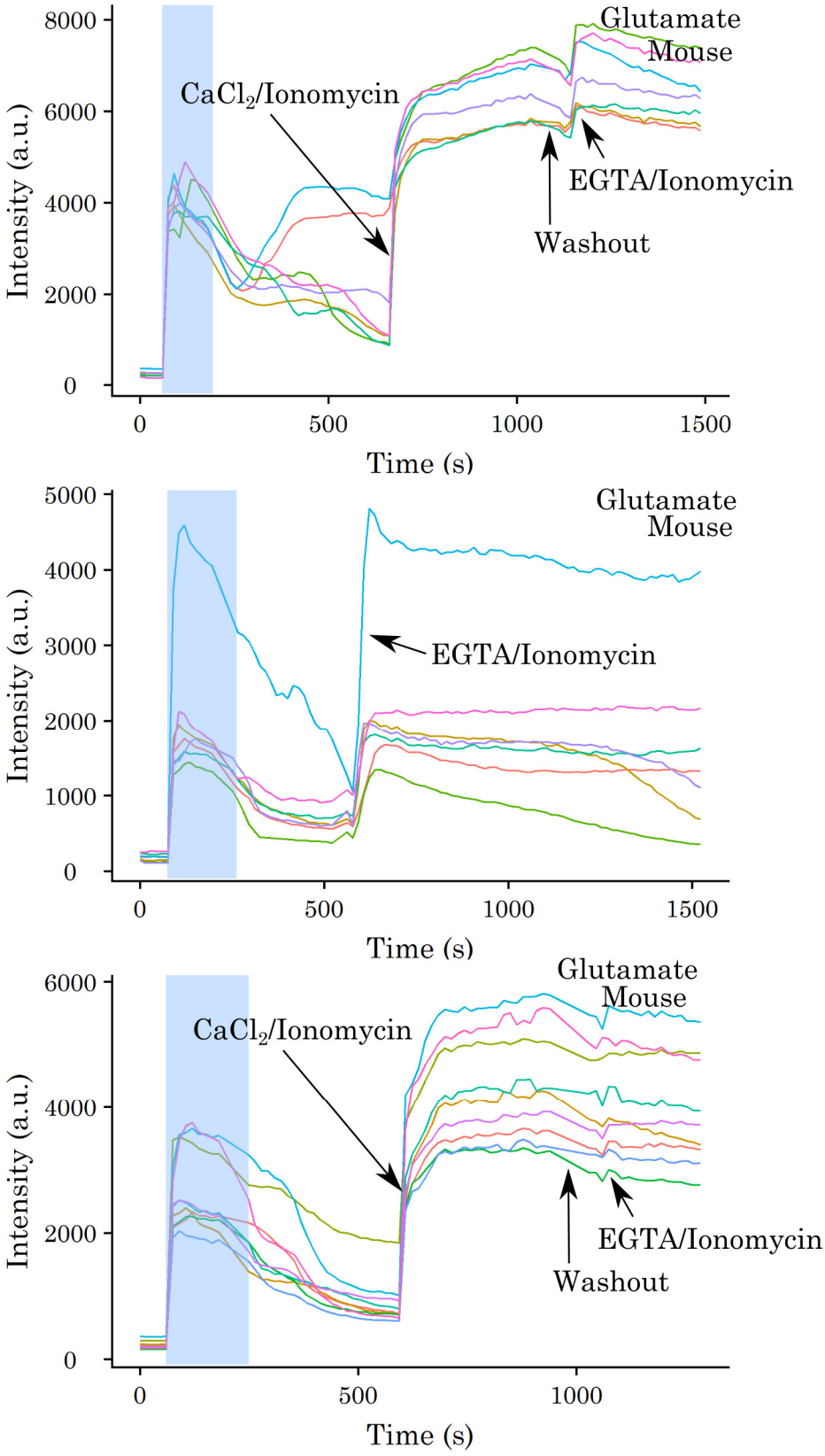

Figure C.6: Ca^{2+} imaging in mouse neurons with glutamate stimulation (2 of 3).

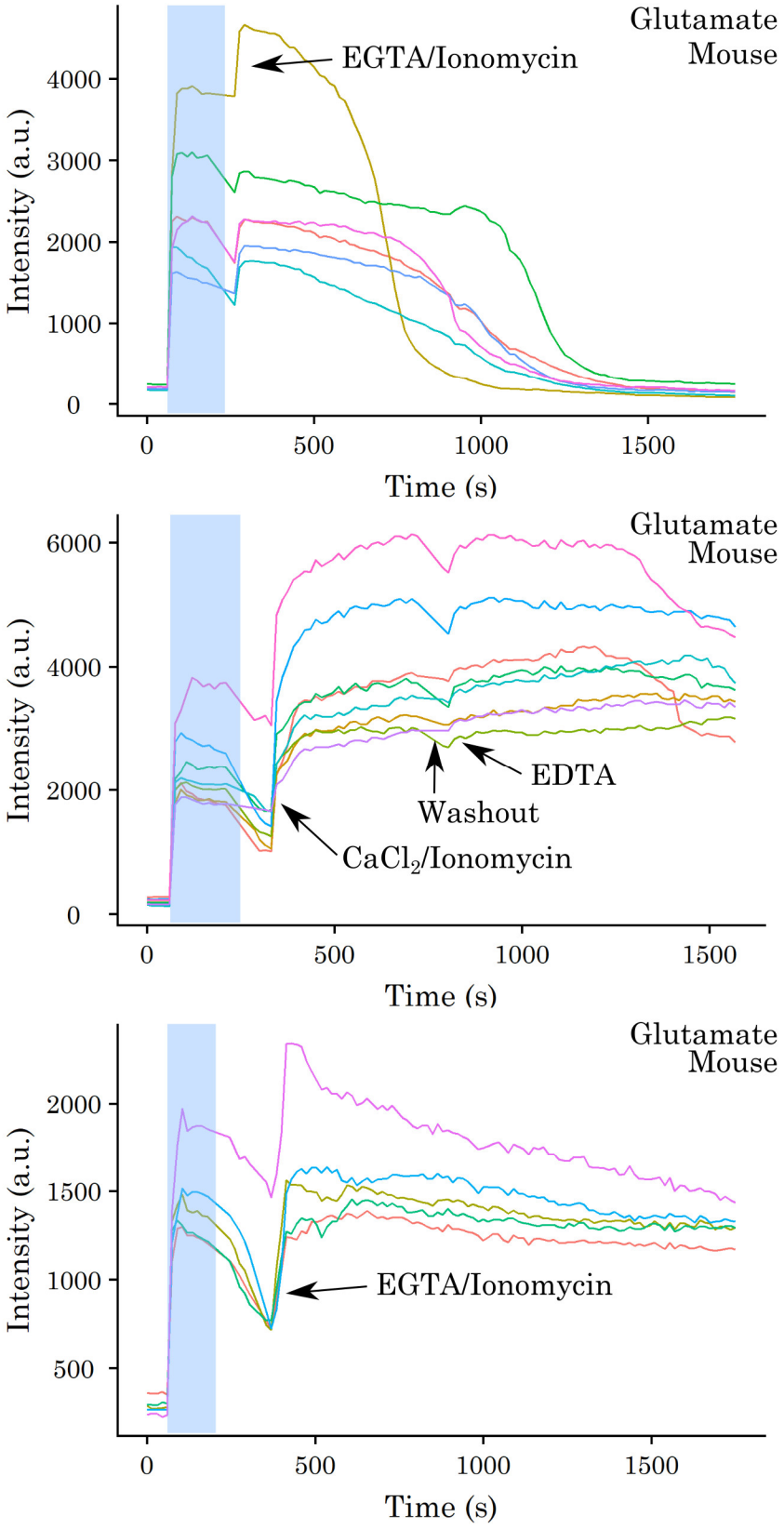

Figure C.7: Ca^{2+} imaging in mouse neurons with glutamate stimulation (3 of 3).

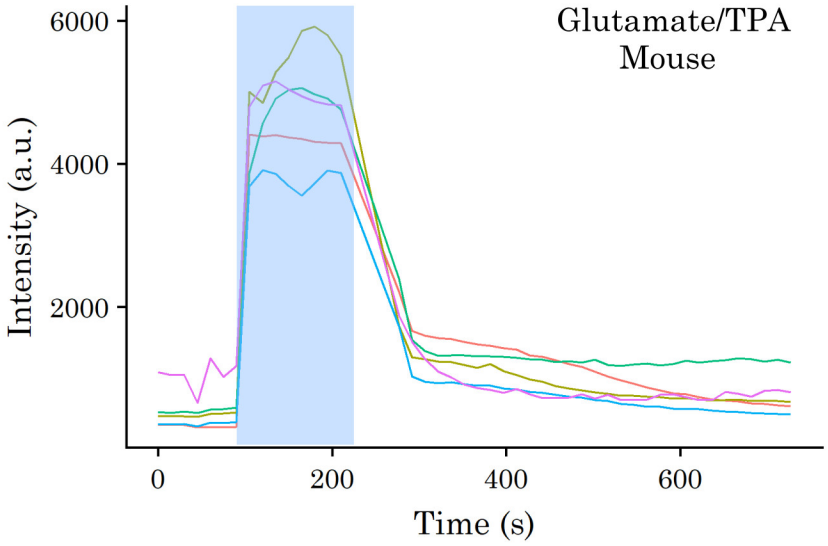

Figure C.8: Ca^{2+} imaging in mouse neurons with glutamate/TPA stimulation.

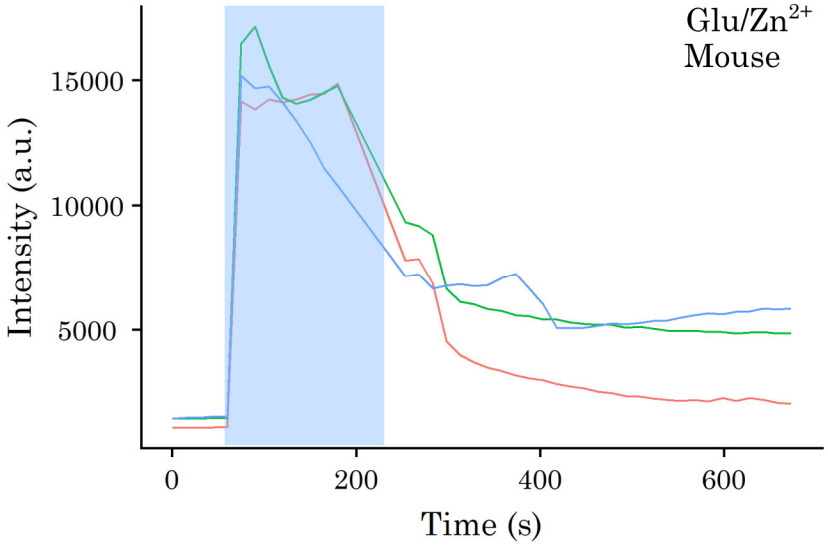

Figure C.9: Ca^{2+} imaging in mouse neurons with glutamate/Zn^{2+} stimulation

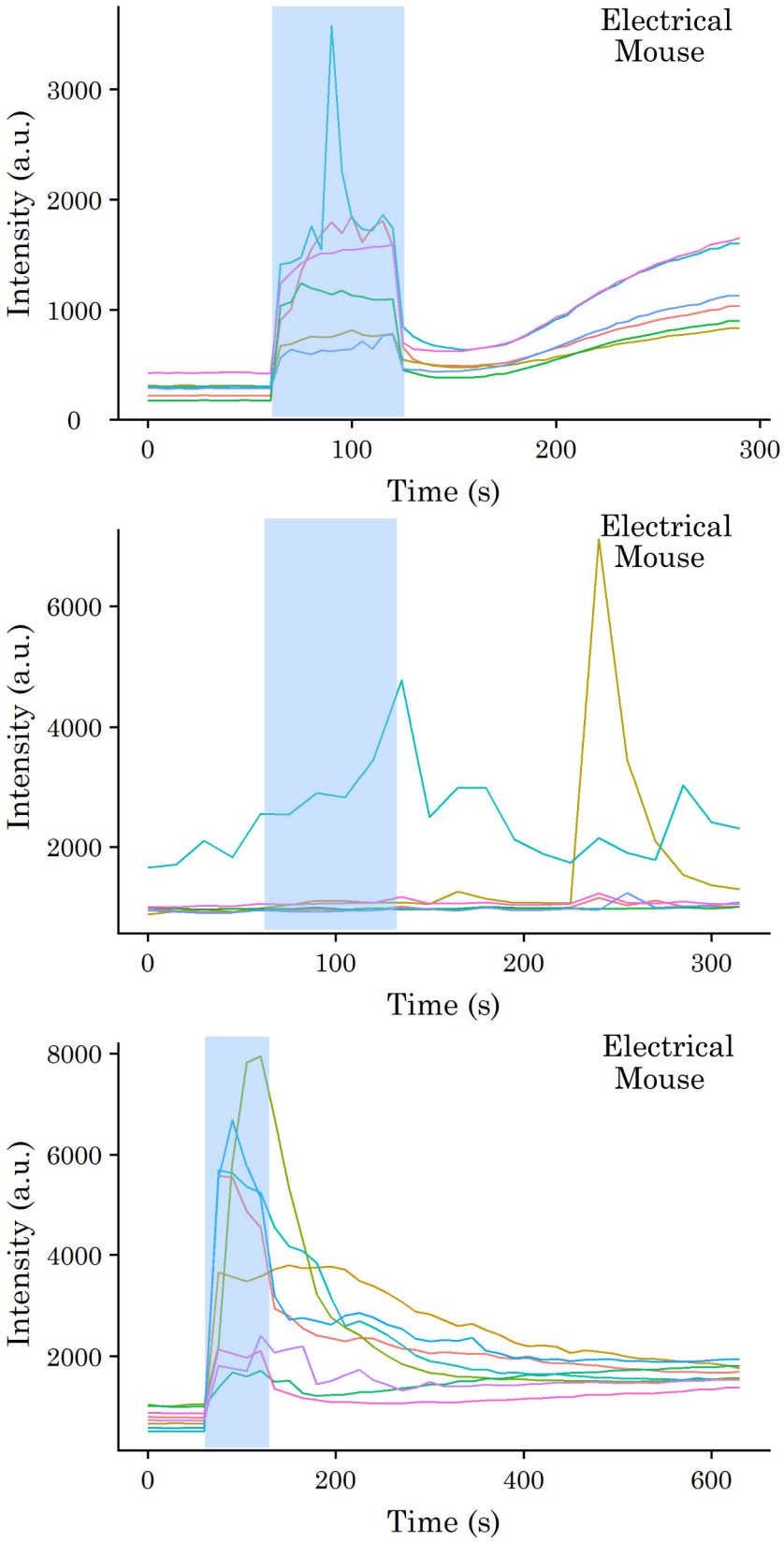

Figure C.10: Ca^{2+} imaging in mouse neurons with electrical stimulation (1 of 3).

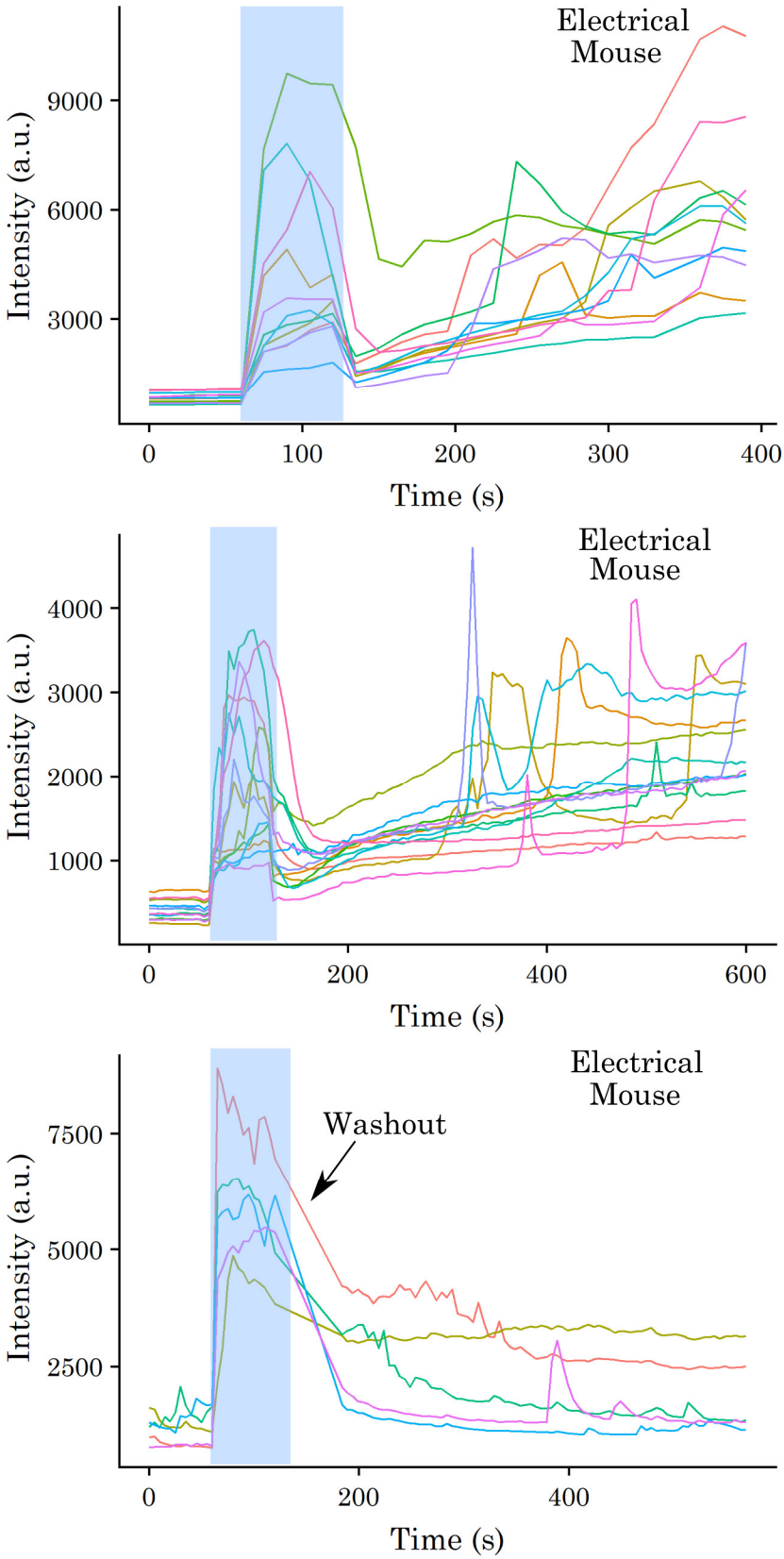

Figure C.11: Ca^{2+} imaging in mouse neurons with electrical stimulation (2 of 3).

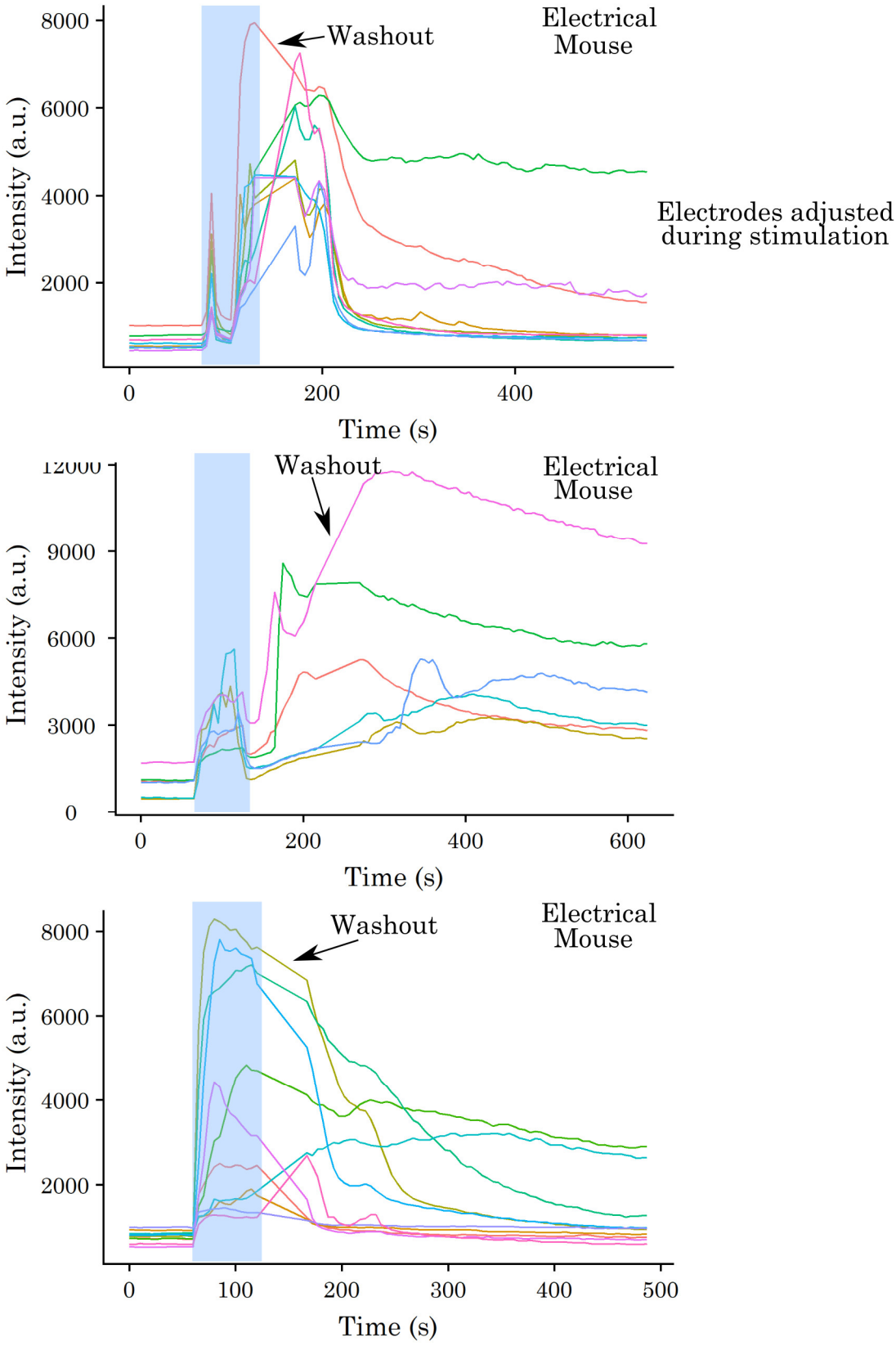

Figure C.12: Ca^{2+} imaging in mouse neurons with electrical stimulation (3 of 3).

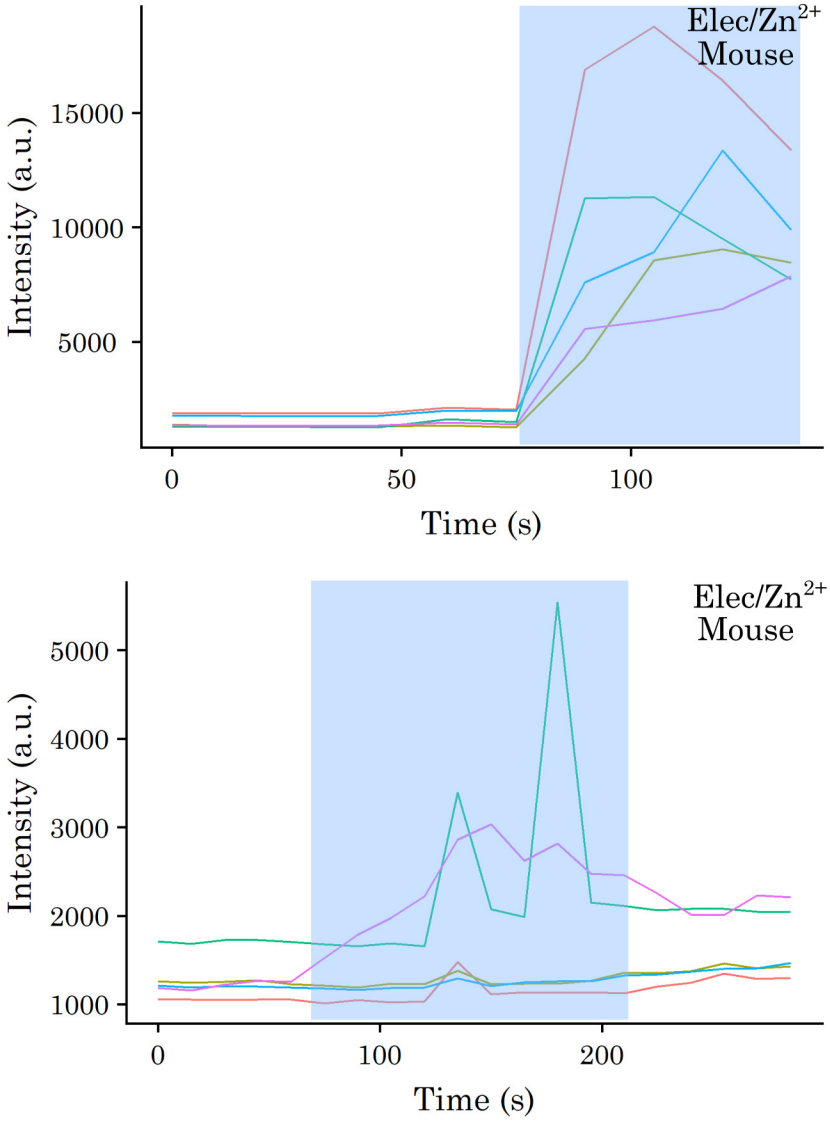

Figure C.13: Ca^{2+} imaging in mouse neurons with electrical/Zn^{2+} stimulation.

(This page intentionally left blank)

Appendix D

Detailed protocols and computational analysis procedures

D.1 Rat embryonic neuron isolation protocol

- **Materials**
  - Equipment
    - Dissecting scissors, various sizes
    - Scalpel handle and surgical blades
    - Forceps, various sizes
    - Petri dishes (sterile)
    - Needles (sterile)
    - Pasteur pipettes
    - pH meter and reagents
    - Laminar flow hood, able to accommodate a dissecting microscope
    - Tissue culture incubator
    - Water bath
    - Dissecting microscope
    - Centrifuge
  - Reagents
    - 10X HBSS (no Ca^{2+} or Mg^{2+}) (Life/Invitrogen 14185-052)
    - 1 M HEPES (Life/Invitrogen 15630-080)

- Gentamycin, 50 mg/mL (Life/Invitrogen 15750-060)
- MEM with Earle's Salts and L-glutamine (Life/Invitrogen 11095-080)
- D-Glucose (Sigma G8769-100ML)
- Fetal Bovine Serum (See cell culture for details)
- Papain, 1000 U/mL (Worthington, LS003126)
- DNase (Sigma D4527-10KU)
- Poly-D-lysine hydrobromide (Sigma P0899-10MG)
- Sodium borate
- Laminan: iMatrix-511 (Clontech T303)
- Neurobasal Medium (Life/Invitrogen 21103-049)
- GlutaMAX-I supplement (Life/Invitrogen 35050-061)
- B-27 supplement (Life/Invitrogen 17504-001)
- MilliQ H_2O
- 70% ethanol

- **Procedure**

- 1) Prepare solutions

  - 1.1) Dissection medium, 500 mL (calcium, magnesium, and bicarbonate-free HBSS with HEPES)

    - Components
      - 50 mL 10X HBSS
      - 5 mL 1 M HEPES buffer, pH 7.3
      - 50 µL gentamycin (50 mg/mL)
    - pH to 7.2
    - Bring to 500 mL with milliQ H_2O
    - Filter sterilize

- Store in 50 mL aliquots at -20 °C

- 1.2) Neuron plating medium, 250 mL (MEM supplemented with glucose and 5% FBS)
  - Components
    - 1.5 g glucose (0.6% wt/vol) – 3.33 mL 45% glucose stock
    - 12.5 mL fetal bovine serum
    - About 234.2 mL MEM with Earle's Salts and L-glutamine (up to 150 mL)
  - Filter sterilize
  - Store at 4 °C
- 1.3) Digestion solution, 30 mL (Dissection medium containing papain)
  - Prepare shortly before dissociation
  - Components
    - Dissection medium (HBSS)
    - Papain, 1000 U/mL, 100 µL per 5 mL dissection medium
  - Heat at 37 °C for 10-30 min and filter (0.2 µm) once papain has dissolved
  - Keep in 37 °C water bath
- 1.4) DNase I solution
  - Prepare at 1 mg/mL in HBSS
  - Filter sterilize
  - Aliquot, store at -20 °C
  - Thaw before dissection, keep in 37 °C water bath
- 1.5) Poly-D-lysine coating solution
  - Stock: prepare at 10 mg/mL in 150 mM sodium borate (10X)
  - Filter sterilize
  - Aliquot in 600 µL, store at -20 °C

- Make working dilution at 1 mg/mL in sterile mqH_2O immediately before coating

- 1.6) Laminin coating solution
  - Laminin is iMatrix-511 from Clontech
  - Prepare at 50 µg/mL in sterile H_2O immediately before coating
    - 25 µg/mL works most of the time, although is sometimes slightly patchy; 50 µg/mL works well every time
- 1.7) Neuron culture medium, 500 mL
  - Components
    - 500 mL Neurobasal medium
    - 1.5 mL GlutaMAX-I supplement
    - 10 mL B-27 supplement
  - Filter sterilize
  - Store at 4 °C

- 2) Prepare equipment
  - 2.1) Pasteur pipettes
    - Flame polish Pasteur pipettes to be normal diameter, but smoothed around tip
    - Flame polish Pasteur pipettes to have a tip diameter half the normal
  - 2.2) Autoclave tools
    - Place scissors, forceps, and Pasteur pipettes (normal and smaller diameter) in disposable autoclave bags
    - Autoclave

- 3) Coat plates

- 3.1) **At least 2 days before** isolation, incubate imaging dishes in 1 mg/mL poly-D-lysine (PDL) solution overnight at 4 °C
  - Ideally about a week before
- 3.2) **The day after PDL incubation** wash dishes 3-4 times with sterile H_2O
  - Coat with 50 µg/mL laminin (iMatrix-511) overnight at 4 °C
  - Ideally leave in laminin at 4 °C for about a week – better results
- 3.3) Aspirate laminin solution immediately before plating (step 7.3)

- If getting hippocampi from Brain Bits, skip to step 6)

- 4) Animal dissection (30 min)
  - 4.1) Euthanize pregnant rat with CO_2 and secondary euthanasia according to animal protocol
  - 4.2) In animal facility, dissect out uterus onto a sterile petri dish and remove fetuses
  - 4.3) Decapitate fetuses with sharp sterile scissors
  - 4.4) Place heads in ice-cold neuron plating media and move to cell culture facility
- 5) Brain dissection (2-2.5 hrs)
  - 5.1) Place head in a sterile petri dish with cold dissection medium
  - 5.2) Cut scalp and skull along midline and use forceps to pull back skull and expose brain
  - 5.3) Remove brain and keep in cold neuron plating medium **on ice** until microdissection
  - 5.4) For each brain, rinse with ice-cold dissection medium and transfer to a small, sterile petri dish containing 10 mL dissection medium
    - Switch out dish/media every so often to keep as cold as possible

- 5.5) Using a dissecting microscope, remove meninges with forceps
- 5.6) Dissect out hippocampus with forceps and needles and transfer to a 15 mL conical with neuron plating medium **on ice**

- 6) Prepare cell suspension (1-1.5 hrs)
  - 6.1) Wash hippocampi 2X with room temperature dissection medium
    - Each wash – spin 5 min at 300 rpm in room temperature centrifuge **or** let tissue settle
    - During washes/settling make digestion solution
  - 6.2) Remove dissection medium and add 10 mL digestion solution
    - If only a couple hippocampi, can use 5 mL; if whole extraction use 10 mL
  - 6.3) Incubate at 37°C for 15 min with occasional gentle inversion
  - 6.4) Add DNase I solution (100 µL per every 2 mL) to break DNA released by digestion and incubate 15 min at 37°C
    - I usually only do this if nucleofecting, otherwise hasn't seemed to affect viability
    - If no DNase I incubation, do full 30 min incubation with digestion solution
  - 6.5) Take tube out of incubator and centrifuge at 300 rpm for 5 minutes at room temperature
    - Depending on digestions, sometimes this isn't a strong enough centrifugation – go up from here in terms of speed
  - 6.6) Aspirate enzyme solution and wash tissue 2X with 4 mL neuron plating medium to neutralize remaining enzyme
    - Each wash – spin 5 min at 300 rpm at room temperature (see note on 6.5)
    - After washes resuspend in ~1-1.5 mL neuron plating medium (smaller volume better for dissociation)

- 6.7) Dissociate hippocampi by pipetting 5-10 times with a normal Pasteur pipette, then 5-10 times with a half-diameter Pasteur pipette
  - Expel the suspension forcefully against the bottom of the tube to minimize foaming
  - Pipet only enough times to homogenize cells
  - By the end there should be no chunks of tissue left
- 6.8) For full extraction, pass the cell suspension into a new 50 mL conical through a 40 µm cell strainer
  - This helps remove some fibers/clumps present in the tissue
  - Flow a couple mL plating media over top of cell strainer to wash through as many as possible
  - This is generally not necessary for a couple of hippocampi

- 7) Plate cells (outside of nucleofected samples) (0.5-2 hours, depending on #/variety of plates)
  - 7.1) Determine cell density and total yield
    - Yield should be approximately 400,000 – 500,000 cells per hippocampus
    - Viability should be greater than 85%
  - 7.2) Adjust cell density
  - 7.3) Add desired number of cells to center of imaging dishes
    - Imaging dishes **must be** coated
    - Plate no more than 10^5 per dish – I've found a good density for imaging at 10-20 days is 20,000 cells/dish
  - 7.4) Add desired number of cells to 6-well plates/dishes
  - 7.5) After about 10 min (once neurons have adhered), add 1-2 mL neuron plating medium

- 8) Nucleofect cells with Amaxa system (optional)
  - 8.1) Pipette 4-5 million cells into microcentrifuge tube
    - Keep any other cells not resuspended in warm neuron plating medium
  - 8.2) Spin cells at 100 x g in microcentrifuge for 10 min, RT
  - 8.3) Aspirate media with a pipette tip
  - 8.4) Add 100 µL nucleofection buffer (with supplement added) and 1-3 µg plasmid DNA
  - 8.5) Pipet cell/DNA mixture into nucleofection cuvette
    - Make sure there's no bubbles and that it evenly covers the bottom of the cuvette
  - 8.6) Put cuvette into nucleofector and run protocol
    - Protocol: Neuron, rat hippocampal (Saved setting O-003)
  - 8.7) Remove cuvette back into the hood and add 500 µL pre-equilibrated RPMI
    - Incubate in 37 °C for at least 10 minutes for recovery step
  - 8.8) Adjust volume and plate cells as in 7.2) – 7.5)
- 9) Re-feed cells and maintain culture
  - 9.1) After 2-4 hours transfer to neuron culture medium, ideally with some portion glial-fed (see notes)
  - 9.2) Two days after plating, add cytosine arabinoside (1-ß-D-arabinofuranosylcytosine) to a final concentration of 5 µM to curb glial proliferation
  - 9.3) After 2-3 days change 1/2 existing medium
  - 9.4) Every subsequent 7 days change 1/3-1/2 of existing medium

- **Notes**
  - For step 6.8 the diameter of the flame-polished Pasteur pipettes is very

important – too narrow will damage cells and too wide will not fully dissociate the tissue

- Neuron culture medium for initial plating/re-feeding can be filtered from glial cultures for more nutrients
  - Glial cells can be extracted from neonate cortical tissue as in steps 5) and 6)
  - Glial cells should be plated at a couple million/10 cm plate, grown to confluence, and frozen
  - Fresh neuron culture medium should be added to the glial cultures the day before neuron feeding
  - Glial-fed media should be filtered before addition to cultures

D.2 Image analysis procedures

The MATLAB image analysis script that was used for analysis of all timecourse imaging data is deposited on my GitHub account (https://github.com/lynn-sanford). All prerequisites for running this script are detailed in the first section of the script; the most important prerequisites are MATLAB version 2016b or later and the "bfmatlab" package from BioFormats (http://downloads.openmicroscopy.org/bio-formats/). User input is obtained periodically throughout the script on the number of files/channels/ROIs to use in order to be as flexible as possible. Cell segmentation is not performed, as neurons do not lend themselves to automated cell segmentation, so manual ROIs are requested. FRET calculations can be automated. The script outputs some microscopy metadata, all analysis parameters necessary for reproduction of analysis, graphs of background and background-subtracted intensities for each channel, FRET ratio data if requested, image containing ROI locations, and a .csv file containing average intensities of background and all ROIs in each frame.

D.3 RNA-Seq analysis pipeline scripts

All referenced scripts used for short-read sequence analysis have been deposited on my GitHub account (https://github.com/lynn-sanford).